#### WARSAW UNIVERSITY OF TECHNOLOGY

## Ph.D.

# Thesis

Discipline of Science: Physical Sciences/

Field of Science: Natural Sciences

## Jakub Zdziebłowski M.Sc.

Application of chalcogenide semiconductors in artificial neuromorphic devices

Supervisor

Ph.D Paweł Zabierowski

### Abstract

The subject of this doctoral dissertation was to investigate the application of chalcogenide semiconductors, specifically cadmium indium sulphide (CdIn<sub>2</sub>S<sub>4</sub>), as an active layer material in neuromorphic devices. Extensive electrical and optoelectronic studies of the selected chalcogenide were first conducted for this very purpose. The main goal was to analyse the energetic structure of native defects present in the material, to investigate the dependence on stoichiometry and processing after deposition of the compound, and to clarify issues related to the presence of native metastable defects. Based on the conducted experiments, defect-controlled mechanisms governing optoelectronic processes were deduced, and thus a model describing the material properties was formulated. In the next step, based on the obtained model, the synthesis and material characterisation of thin CdIn<sub>2</sub>S<sub>4</sub> films with the desired parameters were carried out. Thenceforth, several neuromorphic devices were constructed based on the grown layers. The final stage of the work included the characterisation of the devices and experiments examining their synaptic properties. Devices of the type obtained in this work have been shown to exhibit promising performance; therefore, establishing the possibility of using metastable defects as a source of neuromorphic behaviour, allowing the potential application of chalcogenides in neuromorphic computing in the post-Moore era.

## Keywords:

neuromorphic devices, memristor, chalcogenide semiconductors, metastable defects, spinel

#### Streszczenie

Przedmiotem niniejszej rozprawy doktorskiej było zbadanie zagadnienia zastosowania półprzewodników chalkogenkowych, precyzyjnie siarczku indowo-kadmowego (CdIn2S4 w roli materiału aktywnego w urządzeniach neuromorficznych. W tym celu, w pierwszej kolejności przeprowadzono ekstensywne badania elektryczne oraz optoelektroniczne wybranego chalkogenku. Głównym ich celem była analiza struktury energetycznej obecnych w materiale rodzimych defektów, zbadanie zależności od stechiometrii i przetwarzania po osadzaniu związku, a także wyjaśnienie kwestii związanych z obecnymi rodzimymi defektami metastabilnymi. Na podstawie przeprowadzonych eksperymentów zdołano wydedukować kontrolowane defektami mechanizmy rządzące procesami optoelektronicznymi i tym samym sformułować model opisujący właściwości materiału. W kolejnym kroku, w oparciu o uzyskany model, przeprowadzono syntezę oraz badania materiałowe cienkich warstw CdIn2S4 o pożądanych parametrach, a następnie na ich bazie skonstruowano szereg urządzeń neuromorficznych. Ostatni etap prac obejmował charakteryzację wykonanych urządzeń oraz przeprowadzenie eksperymentów bada jących ich właściwości synaptyczne. Urządzenia uzyskane w niniejszej pracy wykazały obiecującą wydajność, pokazując możliwość wykorzystania defektów metastabilnych jako źródła właściwości neuromorficznych, co z kolei wskazuje na potencjalne zastosowanie chalkogenków w obliczeniach neuromorficznych w erze post-Moore'a.

## Słowa kluczowe:

urządzenia neuromorficzne, memrystor, półprzewodniki chalkgenkowe, defekty metastabilne, spinel

## Contents

P	Preface				
1	Introduction				
2	On the neuromorphic devices				
	2.1	The M	Memristor	13	
		2.1.1	Criticism of the memristor	19	
	2.2	Biolog	gical archetypes	21	
	2.3	Towar	ds neuromorphic devices	25	
	2.4	Existi	ng technologies	30	
	2.5	Challe	enges	36	
3	Theoretical matters				
	3.1	1 Metastable defects		41	
	3.2	Metho	ods of semiconductor investigation	50	
		3.2.1	Thermally Stimulated Current (TSC)	50	
		3.2.2	AC conductivity	53	
		3.2.3	Photoconductivity processes	61	
		3.2.4	Metal-semiconductor junctions	75	
	3.3	Electrical characterization of memristive devices		85	
		3.3.1	Neuromorphic behaviour	86	
		3.3.2	The memristor test	90	
	3.4	Thin-	film deposition	92	

#### CONTENTS

4	Intr	oducti	ion to the $\mathrm{CdIn}_2\mathrm{S}_4$	95			
	4.1	Introd	luction	. 95			
	4.2	Litera	ture review	. 96			
		4.2.1	Structural properties	. 96			
		4.2.2	Photoluminescence	. 99			
		4.2.3	Photoconductivity	. 101			
		4.2.4	Conductivity and electrical properties	. 102			
		4.2.5	Complex defects	. 102			
		4.2.6	Memory effects	. 104			
	4.3	Wrapp	ping up the literature	. 105			
5	$A \; Study \; in \; Spinel - { m investigation \; of \; the \; CdIn_2S_4}$						
	5.1	The o	bject of study	. 112			
	5.2	Optica	al measurements	. 115			
		5.2.1	Photoluminescence	. 115			
	5.3	ical measurements	. 120				
		5.3.1	DC conductivity vs temperature	. 121			
		5.3.2	Current-voltage characteristics	. 126			
		5.3.3	Thermally stimulated current	. 127			
		5.3.4	$\sigma(\omega)$ measurements	. 133			
	5.4 Photocurrent measurements		current measurements	. 139			
		5.4.1	Lux-Ampere/PITCS measurement	. 139			
		5.4.2	PITCS-wavelength measurement	. 150			
		5.4.3	Bandgap determination	. 157			
	5.5	Invest	igation of metastable phenomena	. 159			
		5.5.1	Persistent photoconductivity	. 160			
		5.5.2	Persistent photosensitivity	. 165			
	5.6	The fu	ıll picture	. 170			
	5.7	questions	. 178				
		5.7.1	Real values of mobility	. 178			

#### CONTENTS

		5.7.2	Blocking contacts	179		
		5.7.3	Facticity of the $\sigma_{AC}$ measurement	180		
		5.7.4	Case of non-exponential current transients	181		
		5.7.5	Uncertainty of the bandgap values	181		
	5.8	Model	l predictions and further work	182		
6	Towards the devices – growth and analysis of $CdIn_2S_4$ thin films 18					
	6.1	Objec	tives	188		
	6.2	Thin films' growth				
	6.3	3 Thin films' analysis		195		
		6.3.1	Composition	195		
		6.3.2	X-ray diffraction spectra	198		
		6.3.3	Photoluminescence	203		
	6.4	Concl	uding remarks and future work	214		
7	Memristive devices 21					
	7.1	Device	es' design $\dots$	217		
	7.2	Polytices' characterisation				
		7.2.1	General observations	225		
		7.2.2	Principle of operation	232		
		7.2.3	Principle of operation regarding metastability	237		
		7.2.4	Influence of the $CdIn_2S_4$	245		
	7.3	Further insights, summary and future work		257		
	7.4	The memristor test				
8	Neuromorphic behaviour of the devices 2					
ð	Neu	ıromoı	rphic behaviour of the devices	265		
8	<b>Ne</b> v		rphic behaviour of the devices rical stimulation			
8				266		
8		Electr	rical stimulation	266 266		

#### CONTENTS

		8.2.1	Optical potentiation	274		
		8.2.2	Paired-pulse facilitation	278		
	8.3	Summa	ary	280		
9	The	Final	Conclusions	283		
	9.1	List of	open problems	285		
	9.2	Epilog	ue	287		
Bi	bliog	raphy		289		
Αι	ıthor	's diss	eminations	321		
Ac	cknov	vledgeı	ments	323		
List of Symbols 32						
List of Figures						
Li	List of Tables					
List of Appendices						
$\mathbf{A}_{\mathbf{I}}$	ppen	dices		336		

## Preface

The doctoral dissertation herewith submitted presents a walk-through of a research problem, namely, the realisation of the memristive, and/or neuromorphic devices based on the CdIn<sub>2</sub>S<sub>4</sub> chalcogenide compound, utilising metastable defects. The research was principally conducted in Semiconductors Department of the Faculty of Physics at the Warsaw University of Technology, which has extensive experience and a long tradition of researching metastable defects in semiconductors with an application in photovoltaics, specifically thin-film solar cells. While keeping with the tradition of researching issues related to such defects, this work explores them in a different context. It is, therefore, not a continuation of past research but rather the foundation of a new branch. Nonetheless, this work draws heavily upon the inspiration and experience of prior research.

Neuromorphic devices, which aim to imitate the operation of neurons, can be used wherever computations on neural networks are employed. It is therefore a topic inextricably linked to artificial intelligence. We are currently experiencing a period of immense popularity for AI systems, initiated by OpenAI with the release of ChatGPT in late 2022. This does not mean that this work was created on the wave of the AI boom, as the actual research began over a year earlier, and the concept itself precedes the beginning of work by at least another year.

As befits a starting point, this work addresses a number of different topics and problems that make up the undertaken research problem. As the reader soon would note, the set of matters could be considered rather eclectic. The variety of work performed is a direct consequence of the fact that, from the perspective of our research problem, CdIn<sub>2</sub>S<sub>4</sub> could not be deemed a sufficiently well-understood material, despite the existing literature. It

became evident that a broad-ranging investigation was essential, for without it, the desired results could probably not have been achieved. Consequently, a considerable portion of this dissertation is devoted to solving the CdIn<sub>2</sub>S<sub>4</sub> enigma, id est, a material characterisation, in order to formulate a consistent model describing its properties, with a particular focus on its structural defects in desired application.

The issues addressed in this work can be divided into three groups: solved, open questions, and the cases the author thinks he solved. For this very reason, the present dissertation should also be regarded as a pile of problems; that is to say, it would serve as a starting point for future works addressing the opened cases. This, in fact, already happened: it has to be noted that two of the branches born of this very research, i.e. more detailed analysis of the manufactured neuromorphic devices regarding the optoelectronic and electrical analyses (issues form chapter 7 and 8), have been explored in the two altogether captivating Master's theses authored by Gabriela Szczepanik and Mateusz Andrzejewski. Furthermore, the author hopes that rather than gathering dust upon a shelf, this work will serve as a source of knowledge, just as the author himself used other doctorates. Failing all else, it may still prove useful as an example of what not to do.

The work can be divided into two main parts. The first focuses on the study of the material itself; the second concentrates on the fabrication and analysis of the devices. However, these two parts do not constitute separate entities; one originates directly from the other. Furthermore, the second part would not have been possible in its current form without solving the CdIn<sub>2</sub>S<sub>4</sub> puzzle. Here, it also has to be noted that the second part of this treatise, concerning the synthesis and characterisation of the CdIn<sub>2</sub>S<sub>4</sub> thin-films as well as the complete devices, was done at the University of Nantes, during author's fife-month stay, in close collaboration with the group of Nicolas Barreau, to whom we deserve our most sincere expressions of gratitude.

This dissertation is structured as follows: the first chapter introduces the topics covered in the work. Those are further explored in Chapter 2, which provides the necessary background for the topics raised throughout this thesis, i.e., the concept of memristor – allegedly the fourth fundamental electric element and controversies around it; basic

biological facts about neurons and their operation; and finally, concepts regarding the neuromorphic computing and devices, thus the very topic of this work, including existing technologies and their challenges.

The third chapter addresses physics topics related to this work. It is assumed that the reader is familiar with the basics of semiconductor physics; therefore, certain theoretical matters that were applied in the work but do not require an in-depth analysis or expansion have been omitted, such as photoluminescence or XRD.

The fourth chapter contains a literature review on the CdIn<sub>2</sub>S<sub>4</sub> compound, mainly from the point of view of semiconductor physics.

Fifth chapter presents the results of the material characterisation experiments, conducted in order to construct the  $CdIn_2S_4$  model explaining the material's properties. The section 5.6 is a culmination point of the enquiry. Here, the  $CdIn_2S_4$  model is revealed. In conjunction with the fourth chapter, this chapter provides a complete account of the investigation into  $CdIn_2S_4$  and thus could be considered as a complete thread of the work.

Chapter six reports the issues regarding the growth and characterisation of the CdIn<sub>2</sub>S<sub>4</sub> thin films, which have been used to create complete devices in the further part. In this sense, it forms a bridge between chapters 4 and 5 and the chapters on device characterisation. Some obtained results were used to verify and extend the CdIn<sub>2</sub>S<sub>4</sub> model. All results presented in this chapter were obtained at the University of Nantes.

Chapter seven is devoted to study of the devices produced and analysing their operation in the light of the CdIn<sub>2</sub>S<sub>4</sub> model. Figure 7.2.1a depicts a pinched hysteresis loop, which is a fingerprint of the memristive devices, and can be considered as the culmination point of the entire work. It provides a tangible demonstration of the validity of the concepts developed, which were far from certain at the beginning of the research. The appearance of the pinched hysteresis loop was, in fact, a surprise to the author himself.

Chapter eight demonstrates the operation of the devices we developed as artificial synapses. It includes experiments showing the ability of the devices to mimic biological synapses, typically found in the literature on neuromorphic computing.

Chapter nine summarises the entire work. It gathers the results and open questions

#### Preface

raised in the other chapters. It also addresses the thesis assumptions together with research questions, and outlines avenues for further investigations.

A list of symbols consistently used throughout the work is provided on page 325. At the end of the work, the appendices have been included, containing results that went beyond the narrative of the work but could serve as a valuable supplement to the presented results.

## Chapter 1

## Introduction

We live in a fast-changing world.

It is an undeniable fact that the technological progress in electronics achieved over the past eighty years has been of an exponential character, and has driven us into the Information Age. In 1965, Gordon Moore arrived at the conclusion that the number of transistors in an integrated circuit doubles at regular intervals, all while the production costs remain constant or decline [1]. That observation, known as Moore's Law, has been delineating the semiconductor industry for over half a century. The industry that has changed most aspects of our lives. It is perhaps not too bold to state that the next advancement is unfolding before our very eyes: Artificial Intelligence. The exploding popularity of ChatGPT-3 at the turn of 2022 and 2023 launched an incredibly fast development of the large language models, as well as other models based on artificial neural networks, wildly hailed as AI. Whilst these models do not embody the very essence of AI as conceived by cognitive philosophers (a pursuit, it would appear, is now inherited by the term artificial general intelligence) they are, nonetheless, a close realisation of the visions of science fiction writers, such as Isaac Asimov or Arthur C. Clarke. Visions which were considered distant not so long ago. Despite the apocalyptic perspectives presented by popular culture in the form of various scenarios of machine rebellion, as well as the current, more grounded trend of ambivalent perception of AI development, artificial intelligence, as a powerful tool, has the potential to contribute positively to the development of humanity. As an example

one could give the AlphaFold project, which performs predictions of protein structure – a task that is practically impossible for humans to solve due to its complexity [2]. Awarding the Nobel Prize in Physics to Geoffrey Hinton and John Hopfield in 2024 [3] could also be considered a kind of positive recognition of the merits of the artificial neural networks invention among the scientific community.

When exploring the issues related to artificial neural networks, one quickly finds that the inherent topics are their high demand for computing power and, consequently, high energy consumption. Training neural networks is hard. Modern LLMs require an enormous amount of data and energy to train. ChatGPT-3 includes up to 175 billion parameters to trim [4], and its training was estimated to consume 1287MWh [5]. Training ChatGPT-4 consumed 50GWh, enough to power San Francisco for three days [6]. Moreover, it is estimated that a single ChatGPT-4 query consumes 0.42Wh [5]. Worse still, the demand for AI services is growing, perhaps best exemplified by Microsoft's decision to restart the infamous Three Mile Island nuclear power plant to power their data centres supporting the growing AI services needs [7]. Furthermore, everything indicates that the previously mentioned Moore's law will not come to the rescue. The progress of microelectronics, it is to be observed, will shortly arrive at a barrier raised by the immutable rules of quantum mechanics. It is commonly agreed that in the next 15-25 years, a "Moore's crisis" will develop, thus the continuous improvement in computational power and the decrease in cost will end [8]. Therefore, alternative paths should be sought, trying to bypass the inevitable and prevent the development of computational systems from stagnating during the incoming post-Moore era.

At the same time, the reader viewing this dissertation is far superior in his cognitive abilities to any AI model ever developed. Brain, a remarkable instrument, consumes only ~20W of power, when a supercomputer requires a million times more to face the same challenges [8]. It is simply because the cognition in the brain is done on a *physical* neural network. In contrast, the artificial neural network is in fact a mathematical model emulating the operation of neurons in software, and often running on the von Neumann architecture. As it will be outlined later, the von Neumann architecture has serious

downsides, including a lower speed and higher energy consumption, when applied to the computations, which are essentially inspired by the operation of artificial neural networks – a neuromorphic computing.

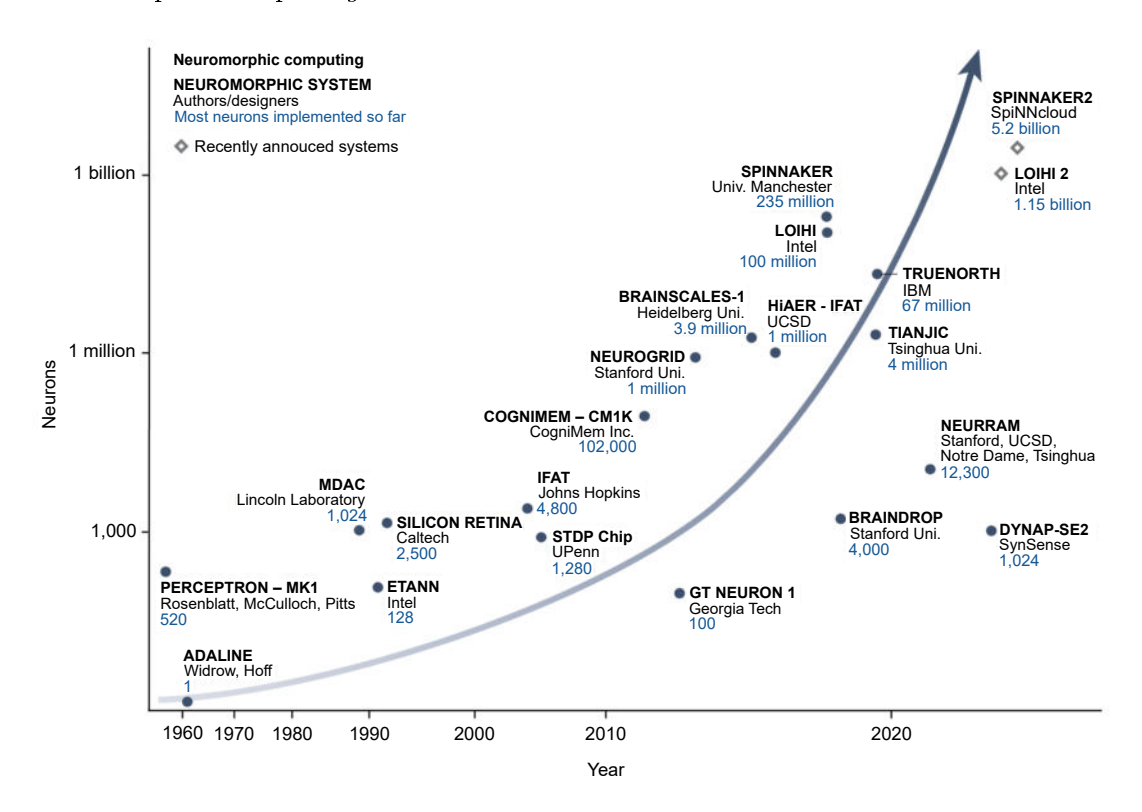


Figure 1.0.1: Progression of neuromorphic computing systems.

Source: Kudithipudi et al. [9]

Various attempts to construct neuromorphic systems, that are not based on von Neumann architecture, but tried to form hardware neural network, have been made for a long time; starting with simple apparatus such as ADALINE or Perceptron in the 1960s and ending with contemporary CMOS-based devices (Fig. 1.0.1). Their drawback, however, is still only the emulation of the neurons. Provided we confine ourselves to electronic implementation, the critical need is for a component that will serve as the electronic counterpart of a neuron, an artificial one – a neuromorphic device.

In recent years, the primacy of the most promising candidate for the artificial synapse (a crucial part of a neuron) has been credited to the memristor, which is sometimes considered as the fourth fundamental electronic element, the resistance of which depends

on past electrical stimulation; to put it simply, a resistor with memory. As the neuron is in fact a cell with learning abilities/memory properties, the memristor became an excellent candidate for becoming the neuromorphic device. Moreover, memristors can take form of compact nanoscale devices with simple structure, which endows them with ease of very-high-density integration and low-cost fabrication. Thus, leading to the possibility of assembling a relatively compact memristor network – an artificial brain. Figure 1.0.2 apposes the successive levels of complexity of the human brain with the corresponding levels of neuromorphic computing devices: the memristor constitutes a single artificial synapse, which can be further assembled into the more intricate network, ultimately building a neuromorphic chip, an analog of the brain.

Extrapolation from the recent rate of progress in neuromorphic systems suggests an enormous potential for future AI applications: the market for neuromorphic computing chips is expected to reach US\$556.6 million by 2026 [9]. Facing incoming difficulties and such extraordinary possibilities, solid-state researchers took off like a shot, searching for materials with memory capabilities that could be used to build a memristor. The present situation may, in certain aspects, be considered analogous to the period of the 1950s, when a rivalry existed between silicon and germanium within the developing semiconductor industry. Similarly, today, several methods of memristor realisation have been devised, each possessing its own advantages and disadvantages, and it remains, as yet, unclear which will prevail in the race.

As is often the way of things, a profound solution may appear from an unforeseen source. Chalcogenides, such as Cu(In,Ga)Se<sub>2</sub> (CIGS), are a promising candidate for an absorber material in thin-film solar cells. However, these chalcogenides had some unexplained properties. One of the issues was an observation that, through various external factors, i.e. illumination or voltage polarisation, the resistivity of the absorber, and thus parameters of the solar cell, such as the fill factor, can be changed; moreover, such an effect is metastable and fully reversible by heating or illumination with different wavelength [11].

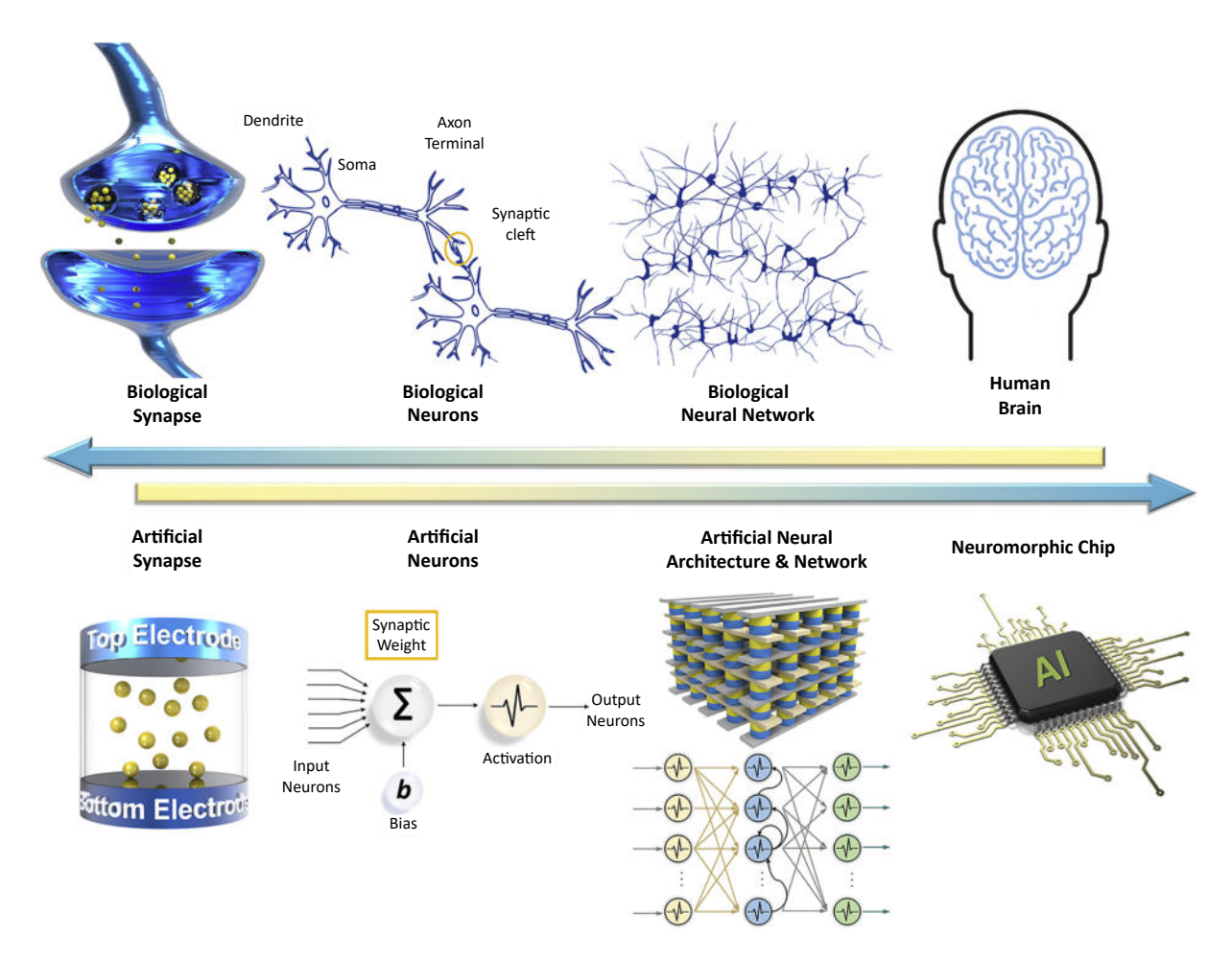


Figure 1.0.2: Levels of complexity of the human nervous system and the corresponding levels of neuromorphic devices architecture.

Source: Kim et al. [10]

The phenomena behind it, revealing itself as the persistent photoconductivity, was a puzzle that took years, multiple dissertations, and collaborations to solve [12–17]. It was eventually found that native metastable defects of the chalcogenides, are responsible for these phenomena. The metastable defects are considered defects in which a change in charge state is accompanied by a large lattice relaxation, resulting in the quasi-stability of the particular charge states. Such defects have been widely described in the literature, as those are present in variety of semiconductors [18, 19]. In CIGS, native metastable defects were described by the Lany-Zunger model [20], which, in essence, resolved the conundrum. Another chalcogenide, cadmium-indium sulphide (CdIn<sub>2</sub>S<sub>4</sub>), came to attention during this preceding research. Whilst it has proven valuable in the thin-film

solar cells research [21], it has, on its own account, posed a further mystery alongside CIGS, not least because it is also rich in metastable defects [22], and one can find observations in the literature that are yet to be explained [23,24], as well as its curious optoelectronic properties [25,26]. Metastable phenomena observed in chalcogenides-based solar cells were generally perceived – as one might reasonably surmise – as a drawback. This is hardly surprising, given that they led to a difficult-to-control operation of the cells, and often to a efficiency decrease. On the other hand, the very thing such cells truly gain is a memory. If one were to look beyond the confines of photovoltaics, such metastable properties do not pose a flaw and could become, in fact, a feature. It would then be a logical step to take advantage of those, and attempt an application of such materials in the role of the memory devices. At this point, we therefore arrive at the very purpose of the research presented in this dissertation: to investigate a particular chalcogenide, cadmium indium sulphide, in its capacity as an active material for memory, particularly neuromorphic devices.

It is a necessary practice in doctoral theses to establish a precisely defined research goal. Therefore, let us define it as the: Application of metastable defects in chalcogenides as a source of memristive behaviour towards building the artificial neuromorphic devices, using the cadmium-indium sulphide. Or, in other words: Is it possible to apply the metastable defects in chalcogenides as a source of memristive behaviour towards building the artificial neuromorphic devices? The presented work constitutes, in fact, a proof of concept of this particular approach, id est, application of such metastable defects in neuromorphic devices. Certainly, we cannot expect here the best results, meaning the results that will allow for implementation of this solution straight into the industry, or even that the neuromorphic devices we construct will match the performance of the devices reported in the literature. We contend, however, that the solution presented herein will be competitive in its performance when measured against the current technologies. The rationale behind our choice of CdIn<sub>2</sub>S<sub>4</sub> over, for instance, CIGS, is to be found in the existing literature, which will be discussed in greater detail in

Chapter 4. Generally speaking, any compound rich in metastable defects would likely prove suitable. Moreover, CdIn<sub>2</sub>S<sub>4</sub> had a considerable role in prior investigations of us and our collaborators; therefore, solely examining its properties would be beneficial. The optoelectronic properties of the material are particularly interesting as they open up the possibility of constructing a light-controlled device – a photomemristor. Following this line of thought, the advantage of CdIn<sub>2</sub>S<sub>4</sub> over CIGS is its much larger energy gap, falling into the visible range. Here, virtually at the beginning of our research, we did not know where our work would take us. We could have tried to predict the outcome with basic theoretical knowledge of metastable defects; however, CdIn<sub>2</sub>S<sub>4</sub> was still an enigma back then, and without solving it, we could not proceed with the device's design that would be more than just a blind shot. Therefore, if we think back to the Figure 1.0.2, matters raised in the presented work go even further to the left side of this diagram, as we first needed to investigate the CdIn<sub>2</sub>S<sub>4</sub> compound before designing the devices. Comparing this to biological archetypes would be equivalent to studying the chemistry of neurotransmitters. Only after that, we were able to move on to the matters related to artificial synapses, and, in fact, the issues described here will stop at this level. The dissertation will therefore also include topics that lie at the very foundations of the physics of semiconductors. After that, starting from the very bottom, through anfractuosity, we shall move gradually to the practical realisation of the neuromorphic devices. This dissertation, then, is a story about this path.

## Chapter 2

## On the neuromorphic devices

In this chapter, we will explore the current state of knowledge on neuromorphic devices. Yet, we will begin with basic concepts from electronics theory and biology, which will lead us to the future of computing. We shall likewise consider currently developed technologies, their limitations, and challenges.

#### 2.1 The Memristor

In the year 1972, Leon O. Chua presented the theoretical basis for the existence of a memristor – a fourth two-terminal circuit element, next to resistor, capacitor and inductor [27]. As posited by Leon Chua, the three basic circuit elements are defined in terms of the relationship between, as he claimed, fundamental variables: electric current I, voltage U, electric charge q and magnetic flux  $\varphi$ .



**Figure 2.1.1:** Memristor symbol, proposed by Chua. Despite hinting its polarity, the asymmetry of the element is not its internal property, but is defined by the technology used (similar to capacitors).

The flux-voltage and charge-current relations are simply given indirectly by the definition of the electric current and the Faraday's law:

$$q(t) = \int_{-\infty}^{t} I(\check{t}) d\check{t}$$
 (2.1.1a)

$$\varphi(t) = \int_{-\infty}^{t} U(\check{t}) d\check{t}$$
 (2.1.1b)

The axiomatic definition of the three circuit elements gives the other relations  $(\frac{\mathrm{d}U}{\mathrm{d}I} = R, \frac{\mathrm{d}q}{\mathrm{d}U} = C, \frac{\mathrm{d}\varphi}{\mathrm{d}I} = L)$  besides one – the relation between magnetic flux and electric charge. As Chua postulated, from the logical point of view and for the sake of completeness and symmetry, a fourth fundamental circuit element, which is characterised by the  $\varphi - q$  relation, is missing.

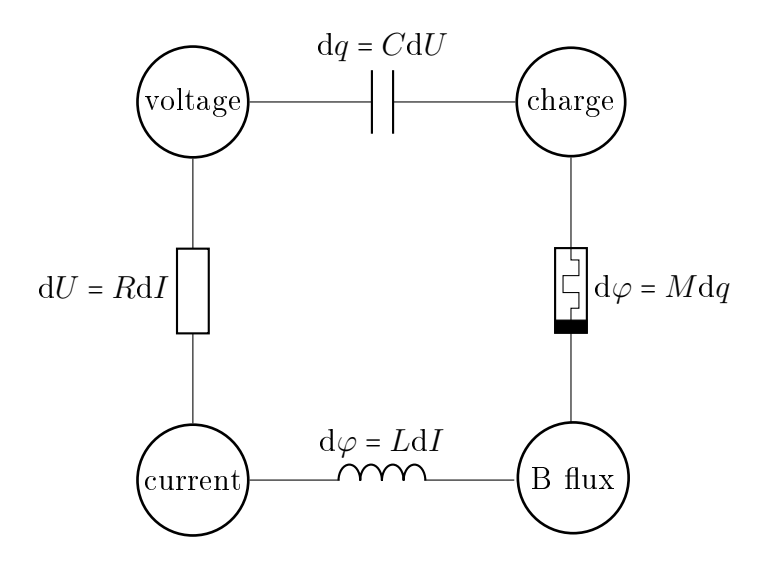


Figure 2.1.2: Four axiomatically-defined electrical circuit elements.

Based on: Chua et al. [28]

In the original paper, Chua defined the *charge-controlled* and *flux-controlled* memristor. For a charge controlled memristor<sup>1</sup>, we have:

$$U(t) = M(q(t))I(t)$$
(2.1.2a)

$$M(q) \equiv \frac{\mathrm{d}\varphi(q)}{\mathrm{d}q}$$
 (2.1.2b)

where M is called *memristance* and has a unit of  $[\Omega]$ . The value of memristance at any time t depends on the time integral of the memristor current from  $t = -\infty$  (or from the arbitrary point marked as a starting point). Therefore, the memristor state depends on its history, i.e., the past current flown through it. The memristor behaves as a resistor, whose resistance, at a given instant t, is a resultant of its past; thus, the memristor is a time-varying resistor. Hence the name of this element: "memristor" = "memory resistor". In a special case, when  $M(q) = const \equiv R$ , the memristor reduces to an ordinary linear time-invariant resistor.

In his seminal paper, Chua proved that memristors are passive elements, i.e. can only dissipate power, unlike the capacitor, which can store energy in an electric field, and the inductor, which can store energy in a magnetic field; do not have such a property, i.e. cannot be a *source*. He also gave a proof that the memristor is indeed a fundamental element, meaning it cannot be constructed from the remaining three basic elements. Lastly, Chua claimed that although the memristor has not been discovered yet, such a device probably exists or existed somewhere, perhaps improperly identified.

Later, Leon Chua extended the idea of the memristor to a much broader class of memristor devices [29]. The extended current-controlled memristor is defined by a state-dependent Ohm's law, as:

Similarly, a flux controlled memristor is defined as:  $I(t) = M^{-1}(\varphi(t))U(t)$  $M^{-1}(\varphi) \equiv \frac{\mathrm{d}q(\varphi)}{\mathrm{d}\varphi}$ 

However, whether a memristor is flux-controlled or charge-controlled does not depend on the properties of the memristor but on its excitation method.

$$U = R(\mathbf{y}, I)I \tag{2.1.3a}$$

$$\frac{\mathrm{d}\mathbf{y}}{\mathrm{d}t} = \mathcal{Y}_M(\mathbf{y}, I) \tag{2.1.3b}$$

The  $\mathbf{y} = (y_1, y_2, ..., y_n)$  is a state vector, having n state variables  $y_1, y_2, ..., y_n$ . Those variables represent internal physical parameters of the device (such as temperature, impurity concentration, etc.) that do not have to depend on external variables, such as current or voltage. Therefore, a charge-controlled "ideal memristor" is a special case of the "memristor class", where n = 1 y = q, thus:

$$U = R(q, I)I \tag{2.1.4a}$$

$$R(q, I) = \frac{\mathrm{d}\mathcal{Y}_M(q)}{\mathrm{d}q} \tag{2.1.4b}$$

One might get the impression that the "extended memristor" covers a vast class of elements. Indeed, according to Chua, a broad class of devices having a nonlinear state-dependent physical properties fall into the class of memristive systems. Devices such as thermistors, Hodgkin-Huxley neurons, or discharge tubes satisfy conditions to be memristors according to Chua [30].

Since  $\frac{dq}{dt} = 0$  when I = 0, and by virtue of (2.1.1a), the memristor can assume a continuous range of equilibrium states  $q = q(t_0), t \ge t_0$  when the power is switched off at any time  $t = t_0$ . Thus, the memristor can be used as a non-volatile analog memory, which is actually a consequence of the state-dependent Ohm's law [28].

Since the state of a memristor is a function of the charge flowing through it, its resistance will dynamically change during the voltage or current sweep. This will result in a hysteresis loop in its voltage-current characteristic. Perhaps the most important

signature of memristors is that the loci (i.e., Lissajous figure) in the U-I plane under any periodic current or voltage stimulation must always be pinched at the origin, meaning that the IV trace must always cross the point (0,0). A clear apprehension of this principle is gained upon recalling that the memristor is a passive element; that is to say, it cannot be neither a current nor a voltage source. This property is claimed by Leon Chua as a definitive fingerprint of the memristor, i.e. a memristor is defined as any two-terminal device exhibiting the pinched hysteresis loop [31]. Moreover, the memristive systems can exhibit two types of pinched hysteresis loop [32]: self-crossing or transversal pinched hysteresis loop, and tangential or non-transversal pinched hysteresis loop. However, it was shown that the pinched hysteresis loop for an ideal memristor must be self-crossing [33].

Another property of the hysteresis loop of real memristors is that the area of the loop is frequency-dependent. Precisely, the area reduces with increasing frequency, and the IV trace tends to a single-valued function as the frequency tends to infinity. The proof can be found e.g. in [34]. This phenomenon, next to the existence of the pinched hysteresis loop itself, is claimed by Chua as two *fingerprints* of the memristor.

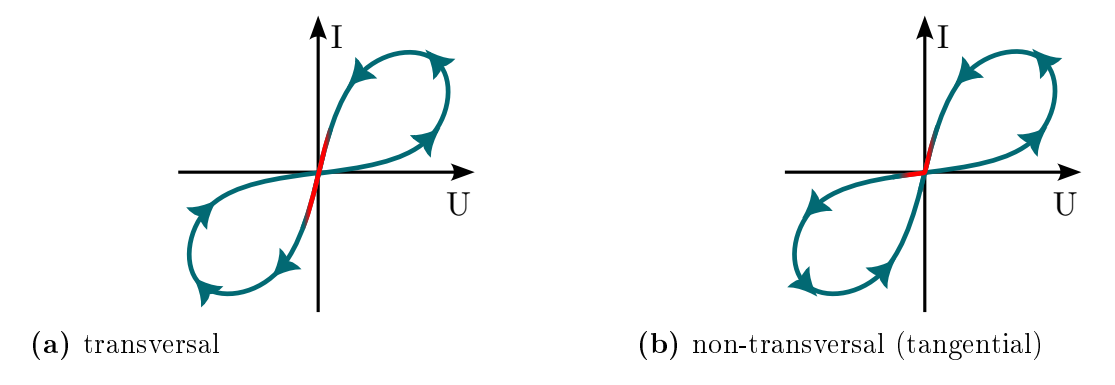


Figure 2.1.3: Two types of the pinched hysteresis loop.

After the Chua's discovery, the memristor was forgotten for over 30 years, until in 2008, researchers from Hewlett-Packard, led by Stanley Williams, announced a successful realisation of a device exhibiting the pinched hysteresis loop predicted by Chua [35]. This discovery (as an aside, described as accidental [36]) attracted global attention and launched strikingly fast development both in solid-state research and technological

matters, as well as in understanding the memristor on a theoretical level. It was then that Chua fully developed the memristor model, formulating, for example, the fingerprints. The HP memristor was based on titanium oxide, and the memory behaviour relied on the diffusion of oxygen vacancies. Although the researchers provided no evidence of the charge-flux relation, the device was agreeably hailed as the wanted memristor. Since then, in the mid-2010s, thousands of papers have been published, expanding the field and outweighing the rare criticisms. Pinched hysteresis loops have started being found in random places, such as: tungsten filament bulbs [37], microtubules [38], rectifying bridges [39], or Josephson junctions [40]. Amid that period, Leon Chua found evidence for his claim that memristors had existed undetected for years by showing that memristive properties were present in carbon arc discharge lamps c.a. 1801 [41], and in coherers<sup>2</sup> [42]. Further development of the memristor theoretical framework led to extending the memristive systems to capacitive and inductive elements. Namely memcapacitor<sup>3</sup> with the hysteretic charge-voltage relation, and meminductor having the hysteretic flux-current relation [43]. Above all else, the memristor's discovery provided a new branch of the theoretical and experimental framework for developing resistive RAM (ReRAM) technology. While ReRAM devices existed before the 2008 HP discovery, they became linked directly to the memristor concept, establishing ReRAM as a practical embodiment of a "memristor". Due to its speed, low power consumption and scalability, ReRAMs are a promising candidate for future data storage, serving as a fast, low power and high-density memory [44].

However, the core idea of a *real memristor* with the flux-charge relation was still waiting to be resolved. An attempt took place in 2019, when Wang et al. proposed the "Φ-Memristor" – a realisation based on the ferrite core apparatus [45], supposedly

 $<sup>^{2}</sup>$ Components used in early radio technology as a demodulators in the days before crystal detectors were invented

<sup>&</sup>lt;sup>3</sup>Similar to equation (2.1.3), the memcapacitor can be defined as:

 $q = C(\mathbf{y}, U)U$ 

 $<sup>\</sup>frac{\mathrm{d}\mathbf{y}}{\mathrm{d}t} = \mathcal{Y}_M(\mathbf{y}, U)$ 

where  $C(\mathbf{y}, U)$  is state-dependent capacitance – memcapacitance. Similarly, the meminductor with meminductance  $L(\mathbf{y}, I)$  is defined as:

 $<sup>\</sup>varphi = L(\mathbf{y}, I)I$ 

 $<sup>\</sup>frac{\mathrm{d}\mathbf{y}}{\mathrm{d}t} = \mathcal{Y}_M(\mathbf{y}, I)$ 

providing an experimental realisation of the direct  $\varphi - q$  interaction. However, due to incorrect interpretation and a misunderstanding of the device behaviour, the paper was retracted [46–48], thus the real memristor remains undiscovered.

#### 2.1.1 Criticism of the memristor

After the supposed memristor "discovery" in 2008 and consecutive elaborations on memristors, the topic elicited a significant volume of criticism. The vast majority of publications dealing with new devices implementing the new memristor realisation (understood as a resistor with memory) used the term memristor quite frivolously without considering the  $\varphi - q$  relationship in any way. With the increase in popularity, the question of the memristor as a missing passive element and whether the  $\varphi$  – q linkage exists at all began to be considered. Several papers have been published in which the existence of the memristor as a passive and fundamental electrical element was questioned [49–52]. One of the leading voices challenging the symmetry lying in the memristor foundation is Isaac Abraham, who argues that memristor is not a fundamental circuit element and proposes an alternative classification without implying four-element symmetry. According to Abraham, it is incorrect to state that current, voltage, charge and magnetic flux are fundamental variables. Instead, he proposes classification based on charge and its time derivatives. Moreover, he accuses HP of cleverly hiding active elements in their model to obtain memristance [51]. The problems of HP memristor do not end here; the authors did not show any magnetism-related properties, which are claimed to be required for real memristors [49] to work. The question of passivity/activity of the theoretical memristor itself is also a matter of discussion, as there are claims that such an element is not passive [50, 53]. Moreover, it was shown that the ideal memristor is unphysical – its assumptions lead to violating the second law of thermodynamics [50]. Ideal memcapacitors and meminductors have been shown to be overunity devices, i.e. there are modes of excitation that allow to extract more energy from the device than is put into [54]; therefore, real memcapacitors and meminductors must be somehow inherently non-ideal, or do not exist at all. Thermodynamics violation and the possibility of a perpetuum mobile are

arguments that, if true, definitely rule out existence of memristors.

Blaise Moulett formulated several severe accusations against Leon Chua and the HP memristor discoverers [55], concluding that the research lacks scientific value. As an aside, memristor-like device exhibiting filamentary switching has been discovered in 1995 [56], but the discoverers do not claim that their devices are real memristors. Moreover, the memory behaviour of certain systems was known before 1971 [57,58]. Yet, Chua and the Williams' group proclaimed themselves discoverers after Chua modified his memristor theory to fit their findings [55].

Through long discussion, some mere agreement among the community arose, that the memristor should be treated instead as an extension of the electrical elements, a resistor in particular [52]. According to Massimiliano Di Ventra, what differs the memelements (memristors, memcapacitors and meminductors) from their classical counterparts is only the presence of memory degrees of freedom (the state variables y) whose time scale is accessible under the appropriate experimental conditions [48]. In other words, the memelements are nonlinear extensions of the classical elements.

The flux-charge linkage in the memristor does not emerge directly from the Maxwells equations, but from the time integral of the voltage drop across the device; therefore, it is put somewhat arbitrarily. In fact, Leon Chua treats the four physical quantities and electronic elements in a sense like Platonic ideas; thus, all of the relations are axiomatic to him.

However compelling, the discussion regarding the existence of the memristor falls well beyond the scope of this dissertation. Whether a memristor exists or not, and whether it is passive or active, in the sense of a resistor with memory, it is a valid electronic component that can be constructed in the lab. Nonetheless, it is then not pointless to at least attempt to search for the device close to an ideal memristor. Nevertheless, after Di Ventra, we will avoid using the term memristor for devices for which the existence of the relation  $\varphi - q$  has not been proven. Instead, in this work, we will use the term memristive device. The memristive device possesses certain features of a memristor, especially a memory, but it is not the Chua's desired memristor.

#### 2.2 Biological archetypes

The neural network in the human brain is a complex system comprising around 80 billion interconnected neuron cells having  $\sim 10^{11}$  connections [59]. They are responsible for all human cognitive functions, including information processing and storage. Those multiple interconnections are responsible for massive parallelism, structural plasticity, and robustness of the brain.

A neuron consists of: the soma, the dendrites, and the axon as schematically shown in Figure 2.2.2a, and is coated with the neuronal membrane, separating inside of the neuron from the outside world (Fig. 2.2.2b). However, the neuron is not an isolated system complex ion interchange processes trough the membrane are controlling its behaviour. The dendrites work as the neuron connectors and receive signals from neighbouring neurons, scaled by the strength of the connections – the synapses, located in the dendrite or axon terminals. The axon receives the information – a nerve spike (that can be either electrical or chemical signal), transfers it over the distance in the nervous system, and then comes in contact with dendrites in downstream neurons and passes information on to them through the axon terminal. One can distinguish the presynaptic and postsynaptic neurons by the direction of information propagation through the neural network. Most of the synapses transmit information signals through particular chemical molecules – neurotransmitters: an action potential – nerve impulse arriving at the axon terminal causes the presynaptic neuron to release neurotransmitters 4; those bind with the receptors in the postsynaptic neuron, generating either excitatory or inhibitory postsynaptic potential (EPSP, IPSP) depending on the transmitting efficiency of the particular synapse. The transmitting efficiency can vary as a consequence of frequent activation of both presynaptic and postsynaptic neurons. This variation is termed as the synaptic plasticity (or in other words, the synaptic weight). The synaptic plasticity constitutes the basis of learning and memorising in the brain.

<sup>&</sup>lt;sup>4</sup>Transmitting the nerve impulses is based on the releasing the K<sup>+</sup> and Na<sup>+</sup> ions. An exemplary action potential time ecolution is shown in Fig. 2.2.2b

The time evolution of the synaptic strength can vary from milliseconds to hours, days or the entire brain lifetime. Thus, the synaptic plasticity can be loosely divided into short-term plasticity (STP) and long-term plasticity (LTP), where STP lasts milliseconds to seconds, and LTP – hours or longer. Conversion from STP to LTP, which lies at the basis of learning, occurs through frequent neuron activation, when the total duration and intensity of the stimulus reach a certain threshold value. The transformation to the long-term memory from the short-term memory is usually equated to converting STP to LTP.

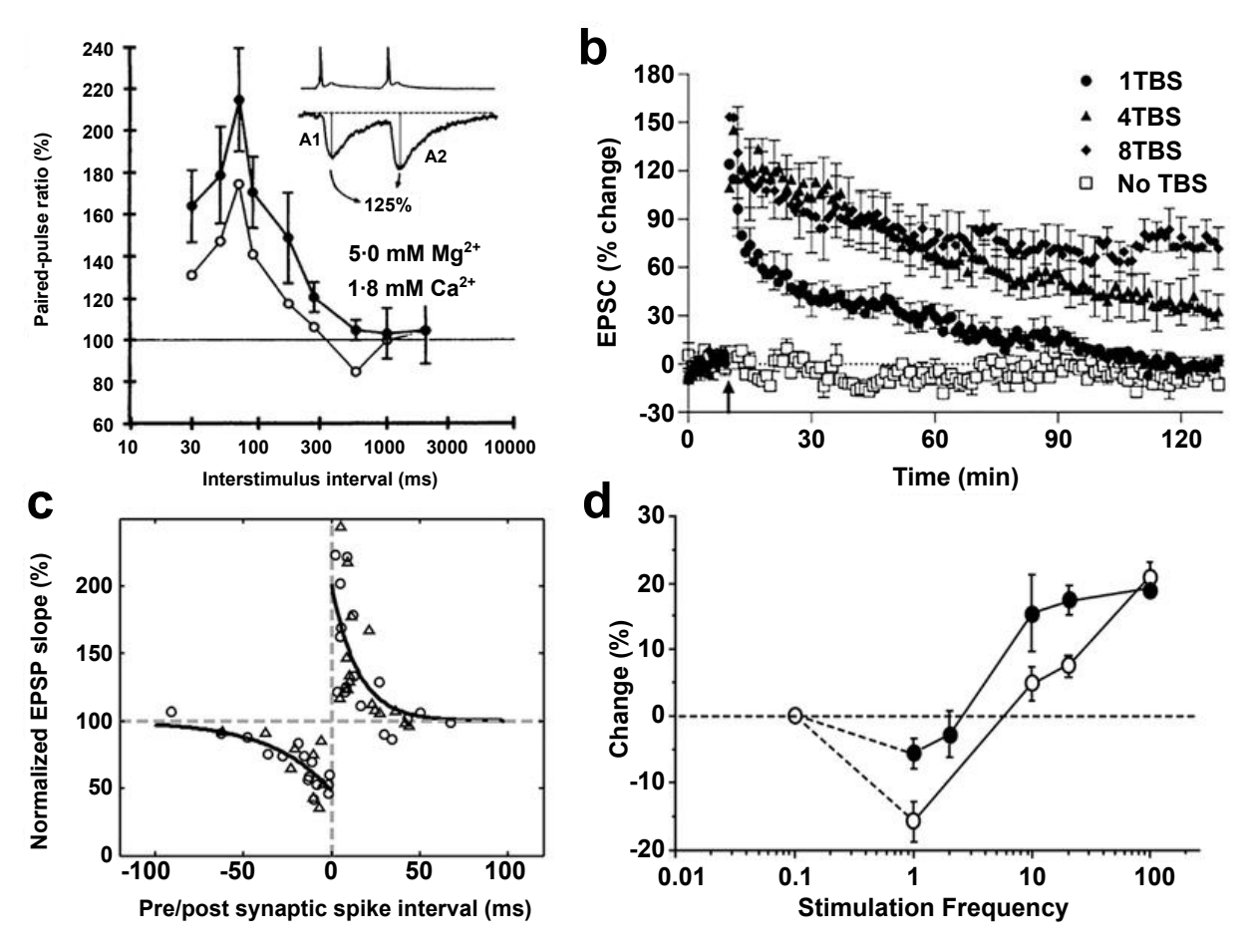


Figure 2.2.1: Typical synaptic plasticity in biology: (a) Paired-pulse facilitation (PPF), (b) Long-term potentiation (LTP) response of the CA1 pyramidal neurons to different stimulus conditions, (c) Spiking time-dependent plasticity (STDP), (d) Bienenstock-Cooper-Munro (BCM) learning rule.

Source: Yang et al. [60]

Various forms of stimulation underlie short-term plasticity, including synaptic potentiation/depression and paired pulse facilitation/depression (PPF/PPD). Synaptic potentiation (or depression) occurs when a brief train of stimuli is applied to the presynaptic (postsynaptic) nerve, in which the amplitude of EPSP progressively increases (decreases). In PPF (and PPD), the EPSP (IPSP) is strengthened (weekend) for a single pair of spikes, when the second spike closely follows the first spike; therefore, the neural response is time-dependent, enhancing high-frequency activity while dampening low-frequency or single-pulse signals (Fig. 2.2.1a). It was found that the PPF and PPD mechanisms occur due to a surplus accumulation (or temporal removal) of neurotransmitters after the second stimulus, before the neurotransmitter concentration introduced by the first spike returns to normal [60].

Unlike STP, in LTP, potentiation or depression lasts hours or days, and is usually triggered by repetitive activity in a similar manner as the short-term potentiation and depression. Although the LTP lasts longer, it still decays over time (Fig. 2.2.1b).

A spike time-dependent plasticity (STDP) is a temporally specific rule describing the synaptic weight change depending on the interval between the presynaptic and postsynaptic spikes (Fig. 2.2.1c): if a presynaptic spike precedes a postsynaptic spike with a short interval, the synaptic weight enhances; whereas, if the postsynaptic spike precedes a presynaptic spike, the synaptic weight decreases, and there is no change of synaptic weight if the time interval between pre- and post-spike is too large. In some sense, it is a PPF behaviour joined with its symmetric counterpart (PPD), which depends on the firing order of the pre- and postsynaptic neurons.

In addition to STDP, a Bienenstock-Cooper-Munro (BCM) rule is another fundamental activity-dependent learning rule. Here, the synaptic weight modulation performs frequency-dependent filtering response (Fig. 2.2.1d): high frequency stimulation leads to potentiation and low-frequency stimulation leads to depression, and there exists a threshold frequency at which the synaptic weight is constant. The threshold frequency is not fixed and can shift according to the neuron activity.

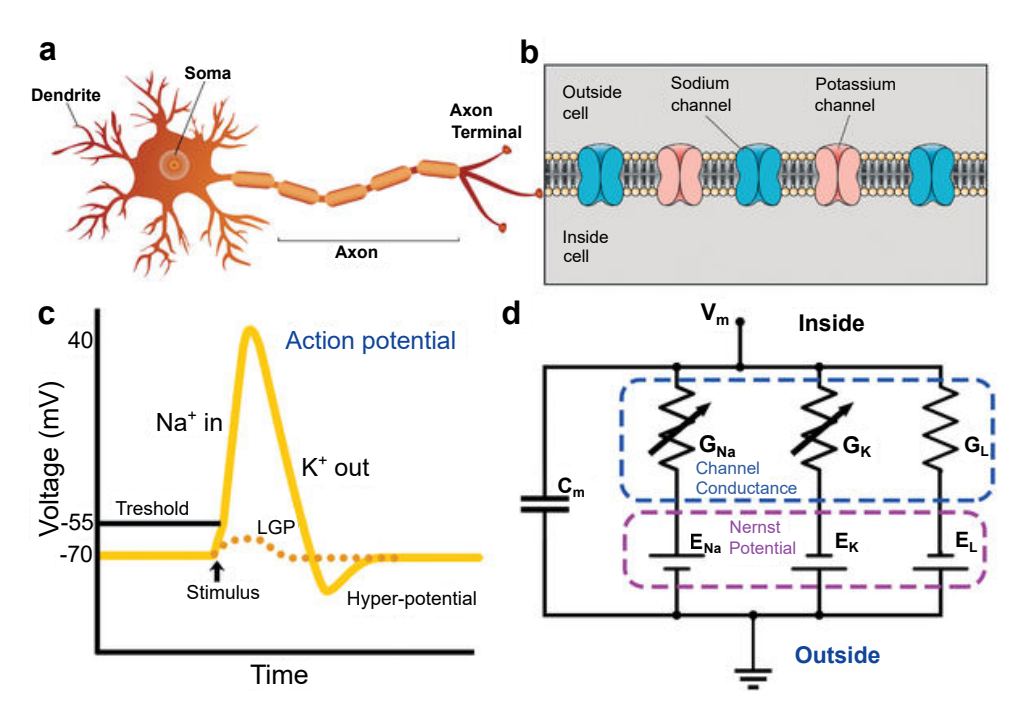


Figure 2.2.2: Biological neurons. (a) structure of a biological neuron; (b) structure of neuronal membrane (c) action potential in a biological neuron. (d) Hodgkin-Huxley neuron model.

Source: Mark F.Bear [61]

Among the physical models describing properties of the neuron, one can mention Leaky integrate-and-fire (LIF) and Hodgkin-Huxley (H-H) models. In the LIF model, the spikes from the presynaptic neuron, scaled by the weights, cause ESPC due to the depolarisation of the neuronal membrane induced by the upcoming spike. Those will be temporally integrated, but concurrently, a leaking process reduces the buildup. The neuron fires when the accumulated depolarisation reaches a threshold point. The H-H model, invented in 1952 by Alan Hodgkin and Andrew Huxley [62], gives a detailed biophysical interpretation, that describes the dynamics of the neuron based on the concentration of Na<sup>+</sup> and K<sup>+</sup> ions being absorbed by the ion channels in the neural membrane (Fig. 2.2.2b). When the concentration of particulate ions reaches a certain threshold, the membrane generates an electric spike – an action potential (Fig. 2.2.2c) being the delineated synaptic pulse. Hodgkin and Huxley managed to encapsulate the biophysical neuron model within an equivalent electrical circuit (Fig. 2.2.2d) describing neuron operation. In the circuit, the ion channels are represented as variable conductances (resistances)  $G_{Na}$  and  $G_{K}$ .

An attentive reader will notice that in the Hodgkin-Huxley model, one of the model elements was variable resistance ion channels, suspiciously resembling memristors; moreover, Leon Chua himself had already shown in 1976 that memristors could have been used to describe some properties of the H-H neurons. Indeed, after the memristors gained their popularity in 2008, it was shown that the simple memristor-based circuits can successfully model the behaviour of the neurons [63] within the H-H model<sup>5</sup>. When followed to its logical conclusion, the trail laid by this research leads indirectly to the present exploration into neuromorphic devices and their emulation of biological synapses.

#### 2.3 Towards neuromorphic devices

Today, the vast majority of computer systems are based on the classic Von-Neumann architecture, in which the computational machine has a separate operation memory and a central processing unit (CPU). Both the data and the execution program are transferred between memory and CPU through the shared data bus during the computation. Consequently, the CPU must sequentially fetch instructions and data from memory in successive cycles and then store the results, significantly slower than performing its internal operations. Thus, the CPU remains idle for a considerable time fraction. The resulting overall system performance is therefore limited by the bus bandwidth, which acts as a bottleneck in the computing speed. Conversely, when analysing the operation of neural networks, it can be discerned that there is no separate space in which information is stored. Unlike the classic von Neumann architecture-based computational systems, the neural networks realise the *in-memory computing* approach. The main advantage here is eliminating the problem of continuous data transfer from the memory to the hypothetical processing unit and vice versa, as done in the von Neumann architecture. Instead, in-memory computing integrates computation directly into memory, allowing operations

<sup>&</sup>lt;sup>5</sup>Intriguingly, it was also demonstrated that adaptive behaviour, observed in some primitive organisms, can be simplified to basic RLC circuits with memristors: an amoebalike cell *Physarum polycephalum* is very clever; when exposed to periodic environmental changes, learns and adapts its behaviour in anticipation of future events. Such behaviour can be modeled by the response of a simple electric circuit consisting of an LC load and a memristor [64].

to be performed where the data already resides, making the approach processing much faster and more energy-efficient.

Artificial neural networks (ANNs) try to realise artificial intelligence (AI) by simulating biological neurons, capturing the advantages of biological neural networks. Some pioneering ideas regarding AI development go back to the thoughts made by John Von Neumann himself, who first pointed out the otherness of human brain operating principles [65]. Truly, the research on ANN is as old as information technology, it dates back to the 1940s, and the McCulloch-Pitts model of the neuron, implementing the weight parameters, parallel to synaptic strengths. Thereafter, mainly in the 1960s and '70s, the field of ANN began to develop<sup>6</sup>. At that time, several algorithms and network implementations were invented, often directly inspired by biology<sup>7</sup>.

As the ANN computations come down to a large number of matrix operations (precisely vector matrix multiplication), which requires continuous transfer of large blocks of data between the processor and memory, the Von Neumann bottleneck, besides other limitations, becomes particularly problematic. Hence, *Neuromorphic computing* tries to implement ANNs in hardware (and partially algorithm design), drawing inspiration from the functioning of the human brain [8].

Recently, many hardware realisations dedicated to AI have appeared. However, many of them are not true neuromorphic processors, but accelerators – specialised hardware approaches designed to efficiently perform computations related to neural networks [68]; they still utilise classic architecture<sup>8</sup>. True neuromorphic computing systems are ASICs

<sup>&</sup>lt;sup>6</sup>However, the development of ANN and AI was not continuous; it was interrupted by periods of stagnation. Such "AI winters" [66] were caused by many hard-to-solve problems and a lack of computational power at that time. In fact, many algorithms currently used in neural networks originate from the sixties and seventies, but it was not until nowadays, when the computing power allowed their practical implementation. Modern neural networks are large systems that go beyond the early-day simple ANNs, and can perform complicated tasks, from reasoning to natural language processing (NLP), image and video processing, etc.

<sup>&</sup>lt;sup>7</sup>Classical ANNs, similarly to modern Transformer-type systems, are still based on weights, the operations on which actually reduce to calculations on large matrices. The algorithmic and hardware approach to neuromorphic computing is a subject of profound intricacy falling beyond the scope of this thesis. One can find more details in the literature [4,67–70].

<sup>&</sup>lt;sup>8</sup>The difference between a neuromorphic system and an AI accelerator is worth noting: AI accelerators

designed from the very basics to work as neurons, whose purpose is not to speed up matrix calculations, but to imitate biological mechanisms. As an example could serve an Intel Loihi chip [73] with 130 million synapses and power consumption under 1.5W; or IBM TrueNorth [74] with 256 million synapses and only 65mW power consumption. Research on such devices has been conducted, as mentioned, since the 1960s. Modern, neuromorphic devices incorporate many billions of neurons (vide Fig. 1.0.1). However, all such devices still rely on standard CMOS technology to simulate single neurons. State of the art solutions use 14-20 transistors to achieve a single LIF-based neuron behaviour [75], and need to consume energy ~900 pJ to simulate a single synaptic event [76].

As in the brain, the basic unit is the neuron and its synapses; similarly, a search was made for an element that could replace complex electrical circuits that could perform as nerve cells, in other words, an electrical equivalent of a neuron, reducing the complex CMOS circuitry to one element.

The memristive resistance change phenomenon (wherever it has the  $\varphi$ -q linkage or not) was found to be an attractive candidate to realise those neuromorphic functionalities in practice. The application of the memristive device can be twofold: on the one hand, the memristive device can serve as a weight-storing element, encoded as its resistance. Unlike existing CMOS-based memory technology, which reads volatile capacitance states, memristive devices stores data using non-volatile resistance states. This approach utilises the resistive switching (RS) effect, which is a change in the resistivity under an application of an electric bias<sup>9</sup>. Besides non-volatile memory, resistance switching also promises high speed, low power consumption (compared to CMOS) [77], and high memory density, promising  $>0.7\text{Tb/cm}^2$  for 2nm technology [78]. Secondly, apart from more

speed up computations on large, dense data arrays to emulate ANNs for AI services using well known architecture. They utilise significant computing power and often have high energy consumption. An example could be Google Tensor Processing Unit (TPU) [71], or Apple Neural Engine [72]. Some companies also pursue the development of Field Programmable Gate Arrays (FPGA), or Graphics Processing Unit (GPU) based accelerators.

<sup>&</sup>lt;sup>9</sup>Traditionally, the pulse that produces the resistance change from high (high resistance state – HRS) to low value (low resistance state – LRS) is the "SET" process, and the one that returns it to HRS is the "RESET" process. The current state of the resistance can be read with a "read" pulse, which is often a small bias current or voltage that should not affect the given resistive state. The elements are arranged in the crossbar arrays, and the setting and reading operations are done by applying voltages between particular vertical and horizontal lines.

typical memory applications, the memristive devices can implement spiking behaviour and emulate the operation of single synapses or whole neurons using various physical phenomena when stimulated by electrical impulses. Therefore, those can be applied in the spiking neural network-oriented architecture (a crossbar array architecture can practically realise the input and the output layer of the neural network, vide Fig. 2.3.1), reducing the complexity of the hardware neurons from CMOS circuits to a single electronic component. Such neuromorphic devices can be further integrated into larger systems, which form neuromorphic chips together with peripheral elements<sup>10</sup>. Cutting-edge realisations of the neuromorphic devices achieve energy consumption <10fJ per single synaptic spike, reaching the human brain's efficiency (1-100fJ) [75,78].

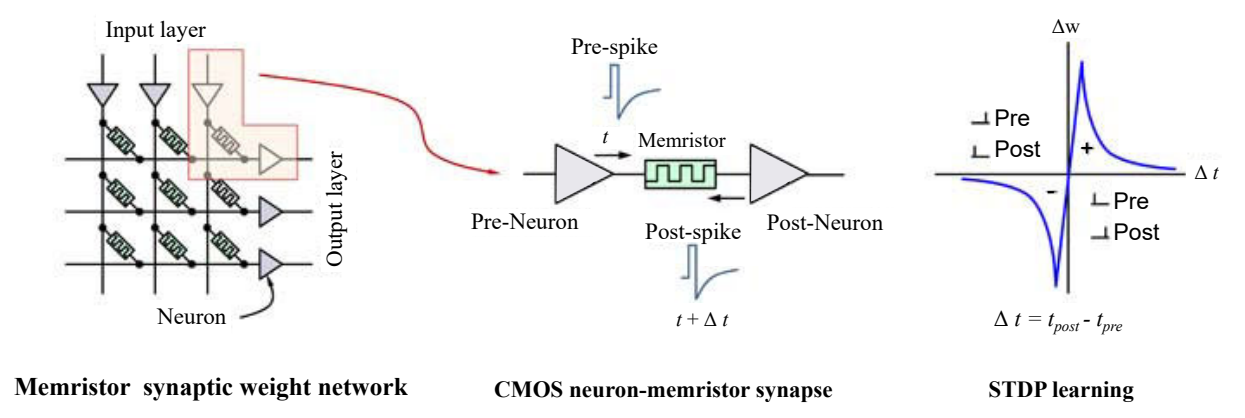


Figure 2.3.1: Crossbar spiking neural network architecture with memristor synapses.

Source: Sung et al. [75]

During the period of dynamic development of neuromorphic devices, i.e. after 2008, the idea of introducing optoelectronics into the world of memristive devices emerged. Adding light control to memristors, creating so-called optoelectronic "memristors" (OEMs), offers several benefits compared to purely electrically controlled memristors: In addition to even greater energy efficiency by minimising electrical joule heating and potentially faster switching speeds, OEMs offer, above all, the possibility of optical programming, adding the third *virtual* electrode to the device – an optical input, which can be stimulated by light impulses, in a similar manner as electrical potentiation pulses. This can enable

<sup>&</sup>lt;sup>10</sup>A diligent reader may find more detailed information on this subject in the following bibliography: [8–10, 44,60, 75, 78, 79].

programming of large arrays by light patterns, masks, facilitating ultrafast setting of the weight parameters on large arrays, when learning a particular ANN is not required. Incorporating broadband wavelength-dependent response could facilitate the usage of the light wavelength in the role of the synaptic weight parameters. An all-optically controlled (AOC) memristive device could be realised, where its resistance is reversibly tunable over a continuous range by varying only the wavelength of the controlling light [80]. Such devices require mechanisms enabling both potentiation and depression using light pulses. Moreover, OEMs can be used to build energy-efficient visual systems, "artificial retinas", which function similarly to the human eye and brain, recognising images and patterns, and simultaneously sensing, storing, and processing information within a single memristive array, thus, taking a step forward in the development of machine vision [10,60,75,80–83]. Finally, OEMs can be integrated into photonic systems [84].

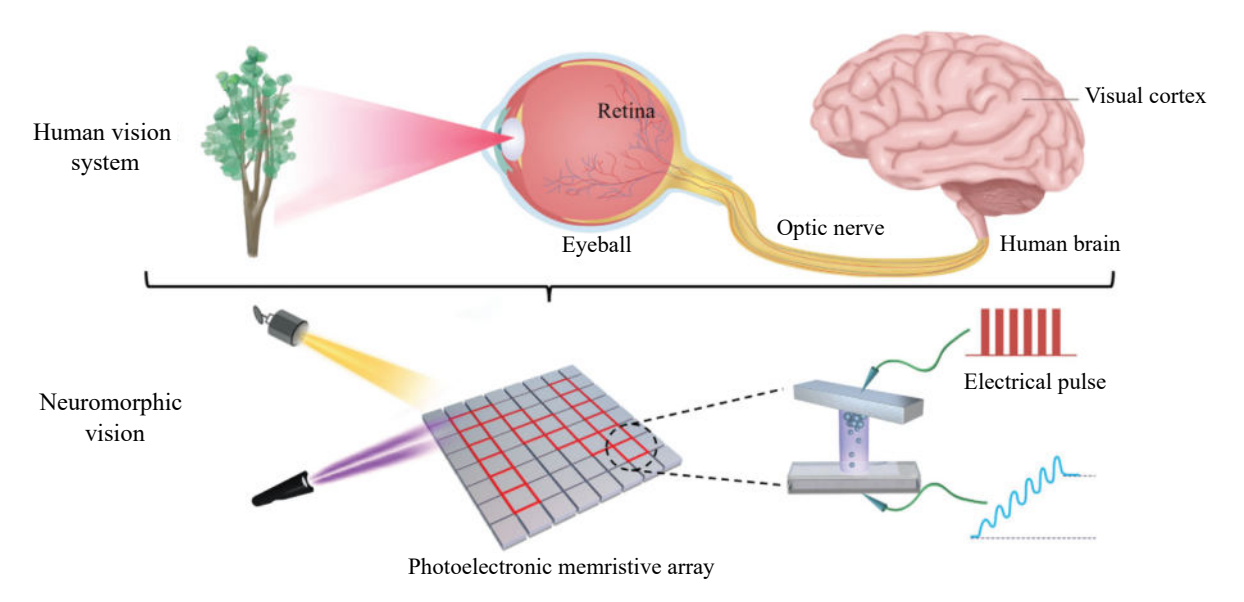


Figure 2.3.2: Idea of neuromorphic vision, based on optoelectronic "memristors".

Source: Shan et al. [85]

## 2.4 Existing technologies

Over the last 17 years, several practical realisations of neuromorphic devices, and/or memristive devices, based on various physical phenomena have been developed. Many phenomena resulting in the appearance of hysteresis loops in the IV curves of manufactured devices, previously ignored or dismissed as faults, have gained a second life as candidate technologies for neuromorphic devices. Solid-state physics attained a new research focus. Researchers worldwide have begun exploring various materials to search for pinched hysteresis loops – the holy grail of memristive devices. Two main research currents have emerged: for non-volatile resistive memories (ReRAMs), where key parameters for memory implementation are crucial: write and read speed, information density, low power consumption, and finally, a wide discrimination window between HRS and LRS states. The second research stream tries to develop devices that can best mimic the functioning of synapses or neurons.

Given the large number of articles devoted to neuromorphic devices, one might venture the assertion that currently each research team has its own way of physically realising a neuromorphic device. Yet, several principal groups may be discerned when considering the physical mechanisms controlling the switching operation. However, it is important to be mindful that none of the practical realisations do not even attempt to elicit the mythological  $\varphi - q$  linkage. Researchers use various processes that produce a pinched hysteresis loop, resulting from the voltage-dependent resistance exhibiting memory, which collectively can be summarised under the term "resistive switching". Thusly, among the switching mechanisms we can distinguish:

1. Ionic migration –it was the basis of the first memristive device presented by HP in 2008, based on TiO<sub>2</sub> [35]. An ionic migration device consists of a solid-state dielectric material (usually an oxide) sandwiched between two (upper and lower) metallic electrodes. The ionic migration is an extensive term. Depending on the migration of the ions we are dealing with, those devices can be further divided by the ion type:

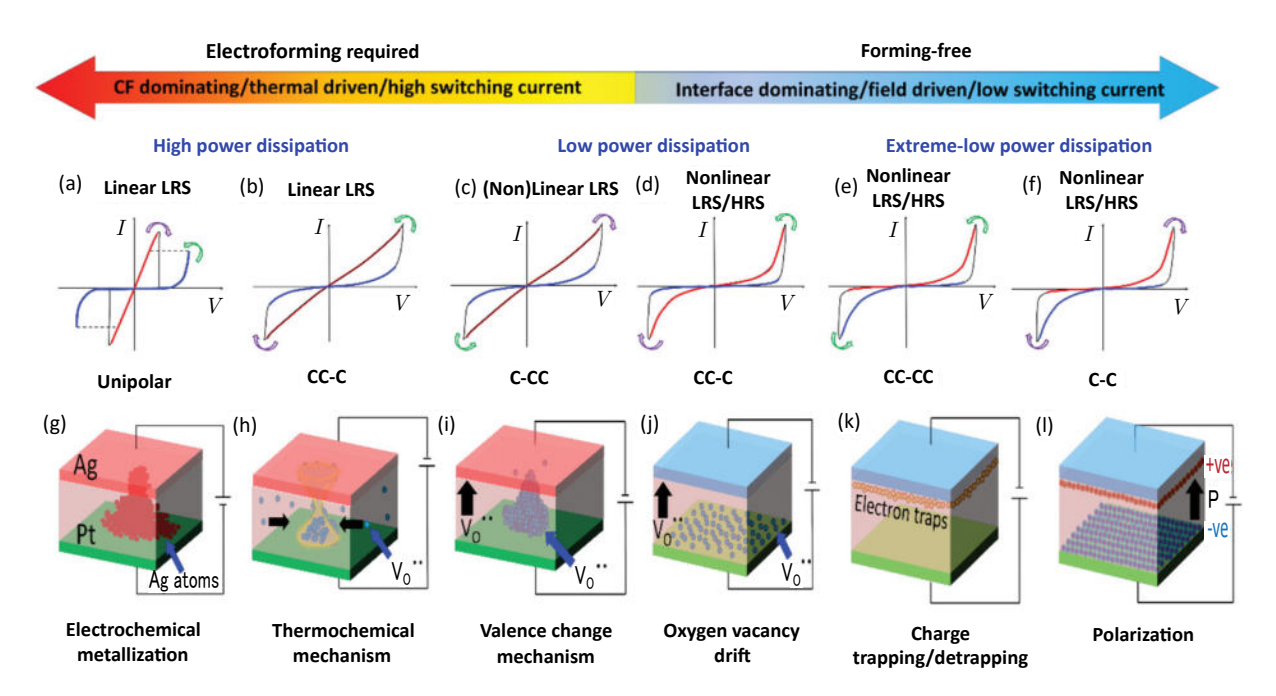


**Figure 2.4.1:** Different types of resistive switching mechanisms observed in memristive devices.

(a)-(f): types of pinched hysteresis loop: C – clockwise, CC - counter-clockwise, as schematically shown on the graphics;

(g)-(l): schematically presented switching mechanisms.

Source: artwork from Roy et al. [86]

(a) Filamentary switching, where metal cations (e.g., Ag or Cu) originating from the metallic electrodes migrate through the insulating layer under external electrical bias, creating a conductive filament across the insulating layer. A potential difference induces the cation migration and leads to an electrochemical reaction within the insulator. When the conducting filament shunts the electrodes, the device switches from HRS to LRS. A reset process can be performed in two ways, hence the consecutive division to unipolar and bipolar switching: in unipolar switching, the filaments are ruptured by the joule heating induced by increasing the current (thermochemical metallisation, TCM); in bipolar switching, a negative bias reverses the diffusion primary impetus, causing the filament rupture (electrochemical metallisation, ECM). The filamentary switching produces a binary hysteresis loop, where the switching occurs abruptly between HRS and LRS (vide Fig. 2.4.1a). The

hysteresis shape and rotation direction depend on the particular type of switching and the conduction mechanism when the filaments are ruptured [87]. It is a simple matter of deduction that the hysteresis loop in the case of bipolar switching is counter-clockwise-clockwise (CC-C), i.e. transversal. It has been shown that it is also possible to facilitate the filaments' rupture using light stimulation [88]. Filamentary switching devices usually require performing a process known as electroforming in which initial filaments are built up under high long-duration bias, thus after, there is only a need to build or rupture a small fragment of the filament at the very end to switch the device. Filamentary switching seems to be currently the most popular and extensively studied technology [77]. Although some researchers are pursuing the application of filamentary switching in neuromorphic systems, the niche this technology occupies turned out to be mostly ReRAMs.

- (b) Valence change memory (VCM) the switching occurs by migration of anions, mostly oxygen, halide, nitride, and sulphur anions. The anion vacancies are utilised to achieve electron equilibrium by changing the valence state of the material. As the anions migrate, the vacancies move in the opposite direction, creating a conductive filament, similar to ECMs. The hysteresis curve is transversal, and the shape depends on a particular transport mechanism through the filaments. Some of the reactions can also be controlled by light [81].
- (c) Oxygen vacancy drift, was the mechanism present in the famous HP device. Here, the external bias causes oxygen vacancies to drift across the oxide layer. The migrating vacancies cause a stoichiometry gradient along the thickness of the oxide, which results in the appearance of high and low resistance areas and, consequently, changes in net resistance. Unlike the filamentary switching-based devices, the vacancy drift is uniform across the sample cross area. The hysteresis loop (counter-clockwise-clockwise) comes from the voltage-dependent vacancy gradient drag following the voltage bias. Here, the electroforming is not

required; the devices also do not have a strictly defined SET and RESET voltage due to the uniform vacancy gradient change constituting the switching process. Binary oxides predominate, such as TiO<sub>2</sub>, CeO<sub>2</sub>, BFO, or Al<sub>2</sub>O<sub>3</sub>.

- 2. Charge trapping/retrapping occurs in the presence of a Schottky barrier on the interface between electrode and a defect-rich active material. Changing resistance is not the result of physical migration of atoms, but electronic modulation of the transport over (or through) the barrier by compensating the space charge region with the charged traps. This modulation is implemented through trapping and releasing charge carriers [89] by applying external bias with alternating polarity. The resulting CC-CC hysteresis derives from modulation of the barrier height, and thus will be compounded from the IV characteristics resulting from the particular transport through the barriers; for the simplest case of Schottky emission – exponential traces. A broad variety of materials can be used to realise this type of switching; virtually any material with charge traps could be utilised to some extent. Those including various oxides, such as BFO [56],  $CeO_2$  [90],  $TiO_2$  [91],  $Nb:SrTiO_3$  [92],  $BiFeO_3$  [93]; sulphides: ReS<sub>2</sub> [94], Bi<sub>2</sub>S<sub>3</sub> [95]; and also 2D materials: HfO<sub>2</sub> [96], MoS<sub>2</sub> [97, 98]. This approach also offers opportunities to construct all optically controlled devices. Such an attempt was made by Yang et al. on ZnO-based devices, where SET and RESET operations can be performed using two different wavelengths [99].
- 3. Polarisation switching mechanism the ferroelectric materials can be switched by applying an electric field with opposite polarity. The polarisation switching modulates the height of the Schottky barrier, which affects the net resistance of the device [10,86]. This particular line of inquiry, however, is a niche concern in comparison to those aforementioned.

In addition to the above-mentioned switching realisations, a number of solutions exist, e.g. switching based on phase change, Mott insulators, intercalation, or spin-based devices.

For the purpose of our further discourse, it shall be instructive to briefly examine one selected realization of modulated Schottky barrier-based switching: Shuang Gao et al.

have shown structures based on ITO and Nb:SrTiO<sub>3</sub>. The device consists of a simple ITO/Nb:SrTiO<sub>3</sub> heterojunction, in which the barrier can be modulated both electrically and optically (Fig. 2.4.2): optical stimulation can excite electrons from the trap states. Unoccupied, now positively charged trap states reduce the space charge region in the Nb:SrTiO<sub>3</sub>, increasing the tunnelling current and thus raising the junction conductivity. As the trap occupation can be changed gradually, and the unoccupied state (which is in fact metastable) persists, the device exhibits a memory effect, facilitating neuromorphic functionality. Figure 2.4.3 shows the neuromorphic behaviour of the devices. The gradual modulation of the Schottky barrier and subsequent slow relaxation due to retrapping enable mimicking synaptic behaviour under electrical or optical pulse stimulation; here, the current value under constant bias (conductance) plays the role of a synaptic strength. Those experiments can serve as a vital example of how the neuromorphic experiments in the devices are performed in general. Fig. 2.4.3 can be compared with the biological counterparts in figures 2.2.1a, and 2.2.1b.

Even though Gao et al. successfully deduced the mechanism of operation of the presented devices and conducted successful neuromorphic experiments, they did not present any in-depth analysis of the defects themselves, which play a key, if not the leading, role in the operation of the devices! Since the defect excited state holds even after the voltage is removed, this means that they are dealing with some persistent effects, and the defects in question must be of a metastable nature. However, it is in vain to look for the detailed physics of these defects, which, after all, underlie the operation of devices and contain clues for further device optimisation. The aforementioned work of Yang et al. [99], which demonstrated ZnO-based devices with optical RESET utilising a principle of operation that is, in fact, fairly similar to Gao et al., also did not elaborate upon the specifics of the defects. Fortunately, there are papers trying to provide models describing switching processes in memristive devices, e.g., the Threshold Adaptive Memristor Model (TEAM) [100], the dopant drift model formulated by HP [35], the Advection-Diffusion Model formulated by Isaac Abraham [101] or descriptions of conductive filaments [77,102],

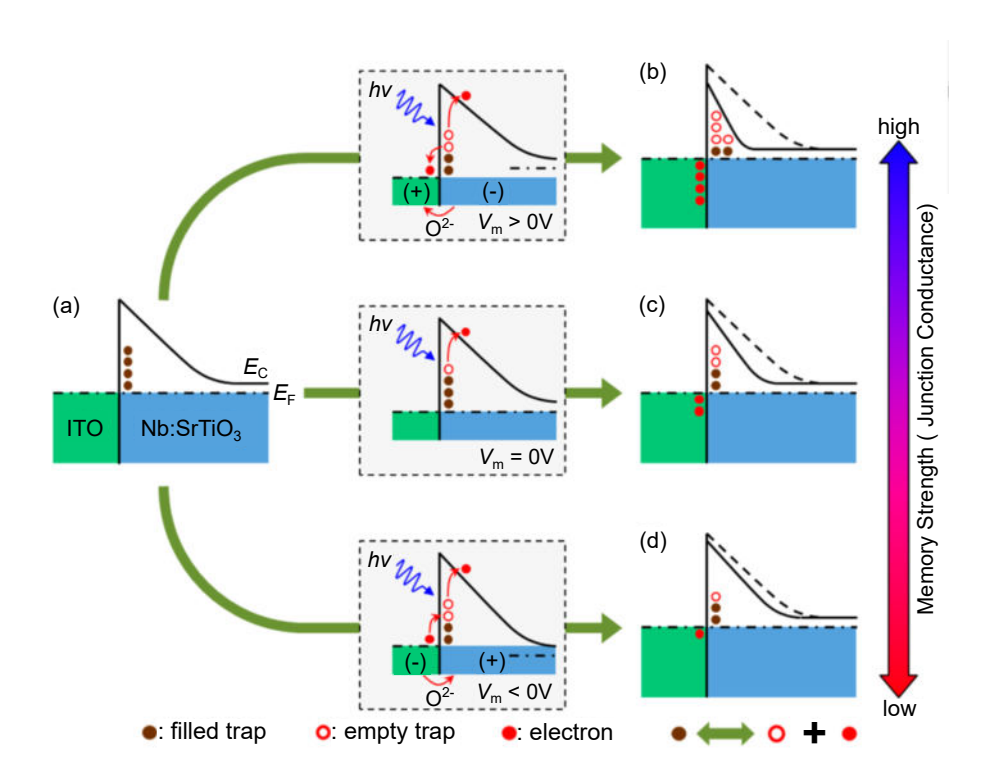


Figure 2.4.2: Schematic operation mechanism of the ITO/Nb:SrTiO3 device presented by Shuang Gao. (a) Initial barrier profile; (b) Barrier profile after light illumination with positive voltage bias; (c) Barrier profile after only light illumination; (d) Barrier profile after light illumination with negative voltage bias. The dashed lines in (b-d) represent the initial energy band profile (before stimulation).

Source: Gao et al. [92]

as well as models that thoroughly scrutinise the mechanisms of transport across the barrier [89, 103], which we shall examine in the next chapter. Such models often return to Chua's definition of the extended memristor (vide equation (2.1.3)), bringing physical meaning to the state variables<sup>11</sup>. Yet, an attempt to tame the physics metastable defects is usually not discussed.

$$U(t) = \left(R_{ON} \frac{\mathbf{w}(t)}{D} + R_{OFF} \left(1 - \frac{\mathbf{w}(t)}{D}\right)\right) I(t)$$

<sup>&</sup>lt;sup>11</sup>For example, in the HP memristor [35], the state variable w characterises the boundary position between the doped and undoped regions along the layer with thickness D, and the following equations are:

 $<sup>\</sup>frac{\mathrm{dw}(t)}{\mathrm{d}t} = \mu_V \frac{R_{ON}}{D} I(t)$  where  $\mu_V$  is the mobility of oxygen vacancies, w is doped region width, and  $R_{ON}$ ,  $R_{OFF}$  are resistances of the doped and the undoped regions. The meaning of the formula, describing the two virtual resistors connected in series, is self-explanatory.

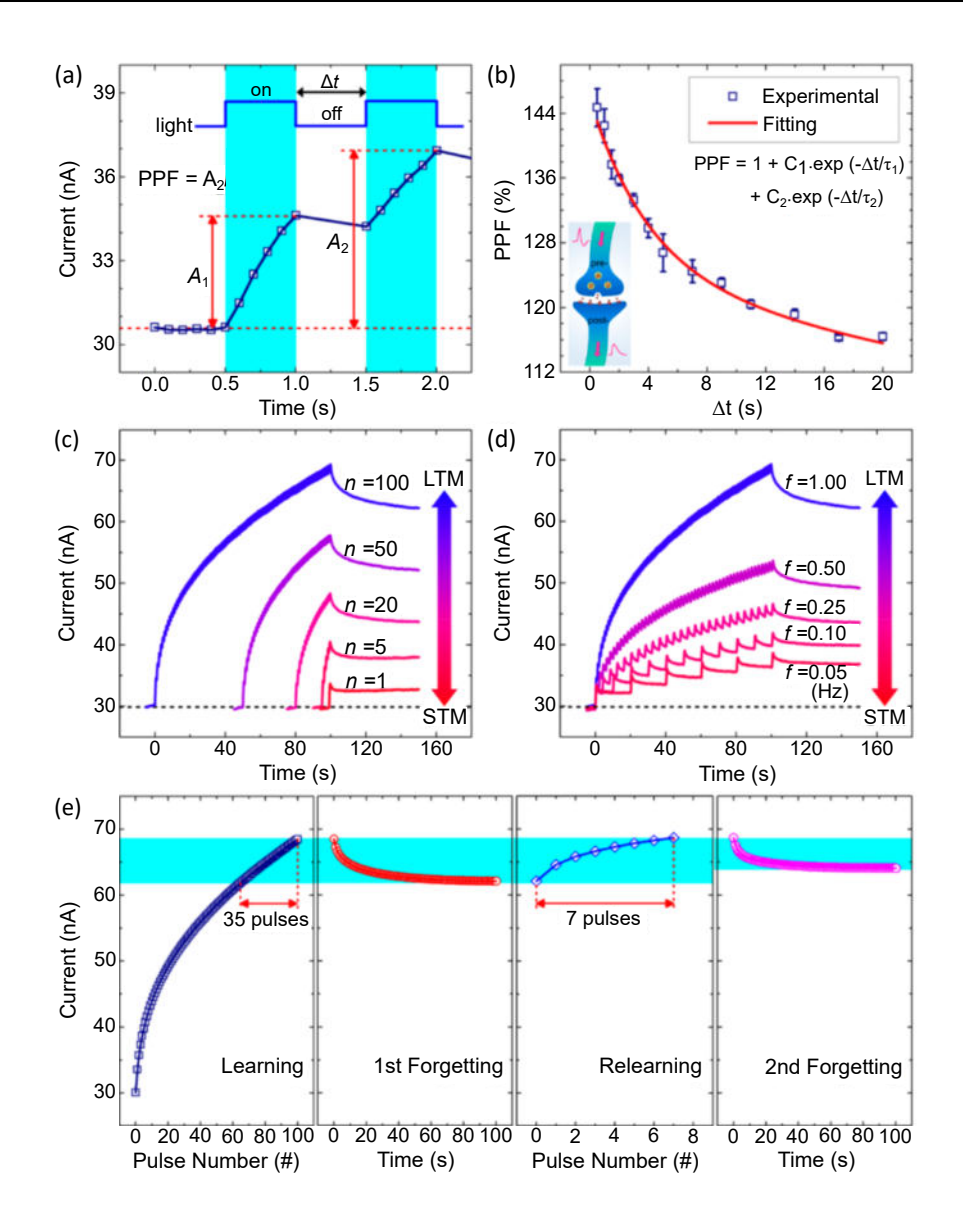


Figure 2.4.3: Photoresponsive characteristics of the device under pulsed light stimuli:

(a) Photoresponsive characteristic of the heterojunction under a light pulse pair; (b-d) PPF and its variation with the interval of light pulse pairs, and transition from short-term (STM) to long-term memory (LTM); (e) The "learning-experience" behaviour under pulsed light stimulation.

Source: Gao et al. [92]

## 2.5 Challenges

Despite the fierce blossoming of the neuromorphic devices after 2008, the technologies being developed still suffer from several conditions that effectively prevent them from breaking through the barrier of leaving the laboratory. Hence, no large-scale neuromorphic computing system based on memristive devices has yet been developed. As of now, the only instances of complete neuromorphic chips that have reached any advanced stage are the TDK "spin-memristor" [104], and the chips sold by KNOWM Inc. [105], which are more of a demonstrator than any complete neuromorphic computer.

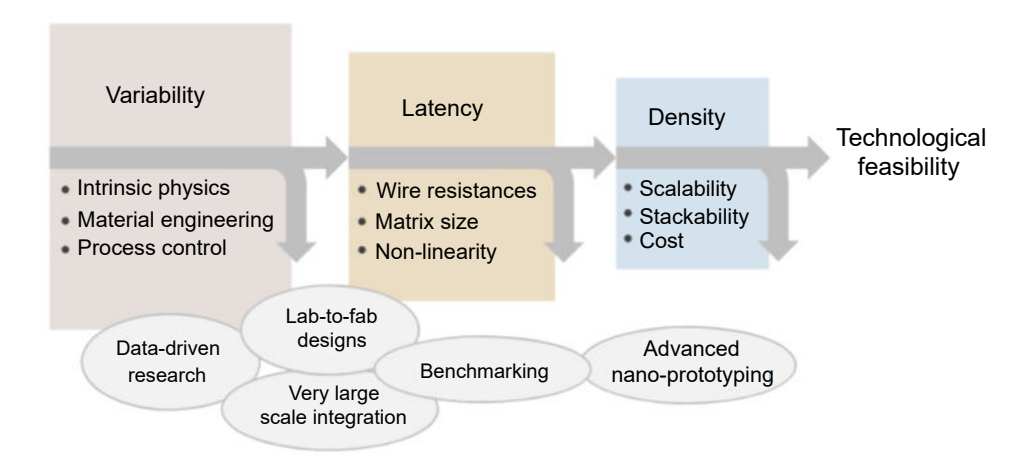


Figure 2.5.1: Roadmap for manufacturing challenges and possible approaches to accelerate progress.

Source: Adam et al. [78]

Thinking back to diagram 1.0.2, one could identify challenges at each level of complexity of neuromorphic computing. Starting with the single devices, synapses, one of the most common and at the same time more serious problems is the variability, resulting in irreproducible performance, and working parameters, e.g. variation in SET and RESET voltage values. The variability can occur between devices (device-to-device variability) and within the same device over multiple switching cycles (cycle-to-cycle variability). For some devices, its capriciousness results from immature technology; for others, it appears during scaling when minor imperfections start to play a significant role; some mechanisms have an intrinsic stochastic nature of the switching itself<sup>12</sup>. Repeatability over time is limited due to the device degradation during switching, and is particularly troublesome for devices based on filamentary switching [75,78]. The material properties of the devices,

<sup>&</sup>lt;sup>12</sup>For example, the number of conducting paths occurring during switching shows Poisson distribution [106].

including the physics involved, are not yet fully mature, and satisfactory candidates for neurons, synapses, and memristive logic have not yet been fully developed [75]. Ultimately, obtaining a repeatable process is essential for implementing the technology into any mass production. It is still unknown which technology will prove to be the leading one.

The other challenging issues in memristive-based synapses are its linearity and multilevel. Many devices suffer from a non-linear current increase as a function of the number of pulses. The linearity of synaptic weight is highly required in deep learning, where vector matrix multiplication is realised on the neural networks. Symmetry between potentiation and depression is also crucial for learning in the neural network. Multilevel operation is, to be sure, a necessary condition for setting analogue weights, yet it presents a considerable difficulty for devices with filamentary switching. Hitherto, no symmetric multilevel switching has been demonstrated for such devices [75].

Most OEM research mainly focuses on blue or UV light. While there are examples of devices in which both the SET and RESET operations can be triggered by light of broader band of wavelengths, these are rare. Optoelectronic memristive devices with broadband continuous wavelength response are in the early stages of research; although studies show that the memristor resistance can be modulated by light pulses of different wavelengths, setting the weights linearly with wavelength is challenging to achieve [83].

We do not expect any dramatic changes in semiconductor technology in the near future; thus, short-term applications of the memristive devices will undoubtedly be integrated with existing technologies such as CMOS. Manufacturing procedures incompatible with existing technologies might be a challenging problem, and some materials might not be suitable. Commonly used electrode materials (especially in filamentary switching devices), such as Pt or Pd, are incompatible with CMOS technology, so other electrodes, such as TiN or Ru, must be used. Materials such as NbO<sub>2</sub>, VO<sub>2</sub>, or V<sub>2</sub>O<sub>3</sub> are grown at high temperatures (~700°C) to obtain optimal device properties. Such high temperatures produce deleterious dopant redistribution in the CMOS transistors [8]; therefore, their use is limited.

At the level of neuromorphic networks, there are problems such as latency or crosstalk.

The practical size of the matrix is limited by the accessibility of individual devices in the matrix. The line resistances can induce a non-negligible voltage drop across the connections, increasing the latency (the time it takes to access a device) and energy consumption [78]. A critical disadvantage of crossbar implementations is the "sneak-path" problem, which is caused by excess leakage current when one of the nodes is in a high-resistance state. When reading such a state, the current can flow through an unintended path, through neighbouring low resistance nodes, giving an incorrect readout [8]. The limitations notwithstanding, the promise of an exceedingly small footprint presents a clear advantage when one compares it with more mature technologies such as flash memory. Various designs may be employed, with the crosspoint, plug-via, and vertical topologies being the most thoroughly investigated. Each, it must be noted, has merits and challenges, necessitating inevitable trade-offs concerning scalability, stackability, and overall cost-effectiveness [78].

The question arises how metastable defects fit into the contemporary landscape of memristive devices<sup>13</sup>. In a way, as we saw, they are already being exploited, albeit somewhat superficially, or even desultorily. From a fundamental physical perspective, metastable defect-based switching, which involves changing the defects' charge state, should be much faster and more energy efficient compared to, for example, filament switching, which utilises Joule heating to reset devices, or devices based on vacancy drift, where ionic conduction is indisputably slower than electronic processes. Secondly, exploiting native defects existing in materials (and these are precisely the sort of defects that are present in our material) is, in a sense, a reversal of the problem of optimising technological processes, which typically aim to eliminate defects that generally degrade devices' performance. The question of what possibilities CdIn<sub>2</sub>S<sub>4</sub> can offer in the field of neuromorphic devices without introducing findings from this work is a matter of conjecture. We will revisit the outlined challenges at the end of this dissertation.

<sup>&</sup>lt;sup>13</sup>From a fundamental physical point of view, almost every switching mechanism, in principle, is based on defects of some sort and, since the device maintains its state, these defects are, in fact, metastable. In this work, however, we mean *metastable defects* in the sense of Anderson negative U centers, which can exist in multiple inequivalent atomic configurations for a particular charge state.

# Chapter 3

# Theoretical matters

In this chapter, we will briefly visit some of the theoretical descriptions of various issues related mainly to the physics of semiconductors and a some more aspects related to memory and neuromorphic devices, as well as crystal growth. The portrayal focuses mainly on its experimental aspects. This is a subjective choice of matters that have been selected because of their significant importance in the research, or those topics will be further developed in the sailent chapters.

### 3.1 Metastable defects

The subject of defects in semiconductors is a broad, extensive matter. Among point defects alone, one can distinguish: antisites, intersitials, substitutionals, and Frenkel pairs, or Schottky pairs. Due to their electric charge, defects in semiconductors can be additionally classified as donors, acceptors or amphoteric. A weighty collection of descriptions has been created for each of these issues.

Unlike crystalline states, defect states are localised in real space. They capture charge carriers if the stabilisation energy overcomes the repulsive coulombic energy. If the stabilisation energy exceeds the repulsion from previously captured charges, defects can capture more than one carrier of the same type. This additional energy is referred to as correlation energy (U) [107]. Mostly, mundane defects have positive correlation energy, i.e.

adding another electron to the singly occupied state requires additional energy, overcoming the repulsion (the double occupied state is higher in the energy diagram). However, a negative-U correlation energy between consecutive charge states is possible. Negative-U means that a double-charged defect is deeper in terms of energy and more stable than an occupied one. It is quite unusual as one expects adding energy with increasing occupancy. This phenomenon is an aftermath of the interaction between the defect and the crystal lattice. As a result of excitation, the change in the charge distribution causes the surrounding atoms to reposition. This leads to the relaxation of the crystal lattice, with the resultant state being more favourable in terms of energy of the whole (electrons + lattice) system. When the new resultant configuration immediately returns to the original state after excitation, it is an unstable configuration; a metastable state persists in the local minimum of the energy landscape, long enough to be observed. Both excitation and return to the equilibrium state require overcoming an energy barrier related to the lattice relaxation. This more intricate defect require now a more detailed description involving phonon-interactions.

The classic method of presenting a defect as a single line (or multiline in case of multiple charges) on a band diagram is now insufficient to contain complete information about the metastable defect, as we now have to include the effects of electron-phonon coupling. To describe such defects, configuration coordinate diagrams (CCD) are used

The configuration diagram shows the dependence of the total energy of a given defect configuration in the function of a specific configuration coordinate (Q). The configuration coordinate is a kind of abstract one-dimensional representation of the entire spatial configuration of the defect and its surroundings<sup>1</sup>. On CCD diagrams, optical transitions can be considered as straight lines (those transitions can be even larger than the bandgap  $E_q$  value). Horizontal transitions require phonon interaction with the lattice.

An exemplary CCD diagram is shown in Figure 3.1.1b. This situation can be considered representative of deep levels in semiconductors (e.g. colour centres): the parabolas

<sup>&</sup>lt;sup>1</sup>In the simplest case, one can suppose that when the defect is located symmetrically between two atoms and the distance between them changes with the change of the defect state, the Q could be assumed as the distance between these atoms.

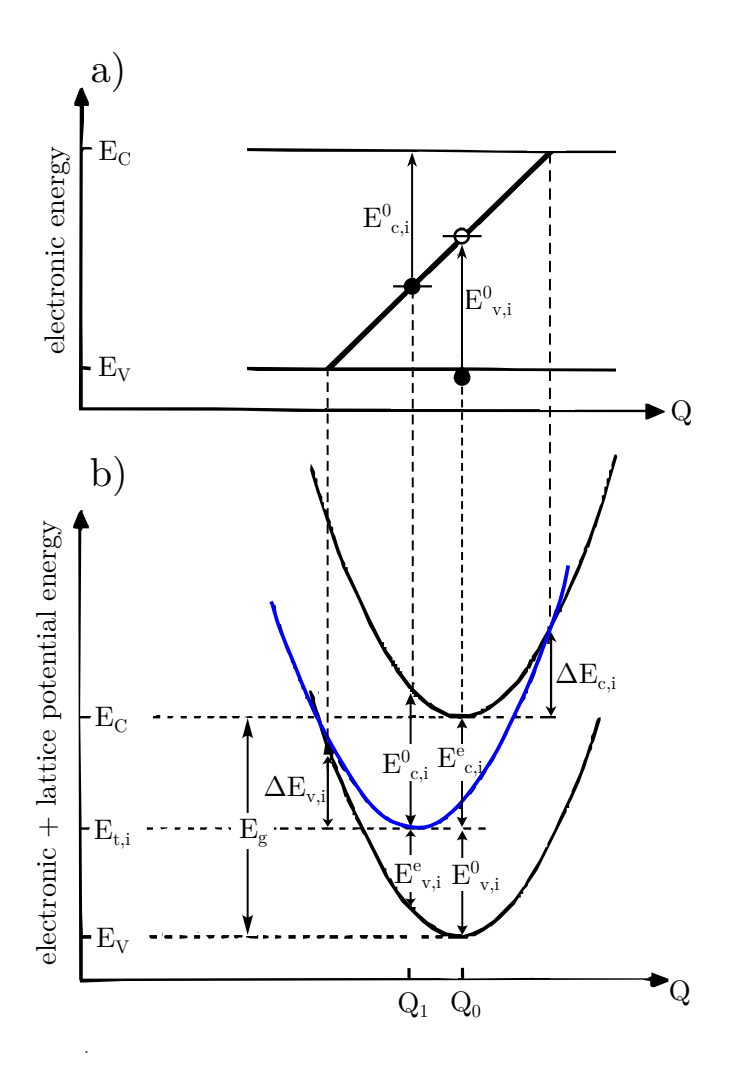
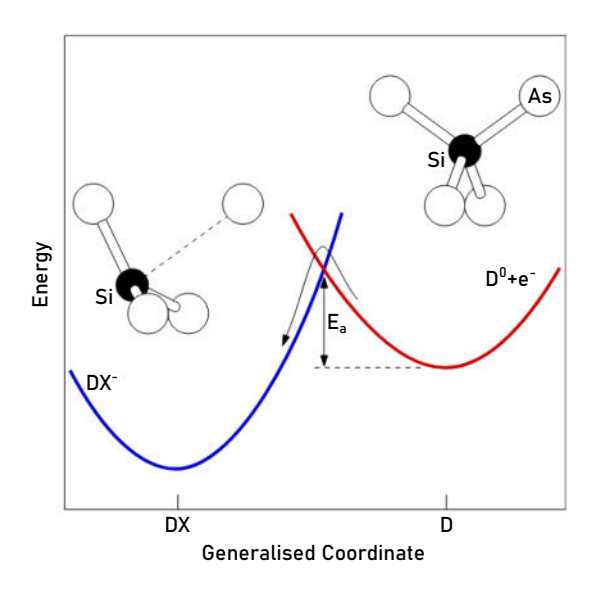


Figure 3.1.1: Schematic diagram of the electronic energy: (a) in configuration-coordinate diagram; (b) as a function of an effective lattice coordinate for trap levels with strong electron-lattice coupling.

Based on: Braünlich et al. [108]

correspond to an empty trap state i; the bottom black parabola represents total defect energy in a ground state; the upper black parabola represents the total energy of the system in the lowest excited state (empty trap plus electron-hole pair); the ground state is denoted by  $Q_0$ ; the blue parabola is the potential energy for an occupied trap, relaxed state for the new configuration with occupied trap is marked by  $Q_1$ . This diagram is valid for both electron and hole capture. The case presented in Fig. 3.1.1 resembles relatively small lattice relaxation. The case of large lattice relaxation is considered if the bottom of the metastable state parabola lays outside the ground state parabola (like in Fig. 3.1.2).



**Figure 3.1.2:** Configuration coordinate diagram of the Si DX center in  $Al_xGa_{1-x}As$ , showing two configurations of the defect.

Source: Coutinho et al. [107]

Thermal electron/hole capture or emission requires crossing the parabolas representing the initial and final state - they occur at the intersections of parabolas. Therefore: for thermal electron capture, the system needs to overcome a barrier  $\Delta E_{c,i}$ , for thermal hole capture:  $\Delta E_{v,i}$ , for thermal electron emission:  $(E_C - E_{t,i}) + \Delta E_{c,i}$ , and for thermal hole emission:  $(E_{t,i} - E_V) + \Delta E_{v,i}$ . Optical transitions can occur between parabolas, and will yield bands marked by the vertical arrows between proper points<sup>2</sup>. Therefore: for optical electron emission:  $E_{c,i}^0$ , optical hole emission:  $E_{v,i}^0$ , optical electron capture:  $E_{c,i}^e$ , and optical hole capture:  $E_{v,i}^e$ . The possible resultant state will then relax to local minimum (minimum in one of the parabolas) by phonon interaction. The barriers associated with thermal transitions are barriers between two defect configurations. At low temperatures (when available phonon energy is insufficient), the metastable configuration will persist because low thermal energy does not allow a return to the ground state. Only at a sufficiently high temperature, when more thermal energy is supplied, the atoms will reconfigure, and the defect will return to the ground state. One can write a general equation for transition rate:

Those transitions are fast compared with the motion of nuclei (the Frank-Condon principle).

$$\tau^{-1} = \nu_{phn}^{-1} \tau_1^{-1} \tau_2^{-1} \exp\left(-\frac{\Delta E}{kT}\right)$$
 (3.1.1)

where  $\nu_{phn}$  is the phonon frequency, and  $\tau_1$ ,  $\tau_2$  are transition rates for capture/emission of one charge (vide [16]).

As said before, a concept of energy levels is insufficient to describe such metastable defects. In a simple diagram, one can only mark the bottoms of the parabolas for the individual states. Drawing the whole CCD diagram would require moving the whole band diagram up to the third dimension.

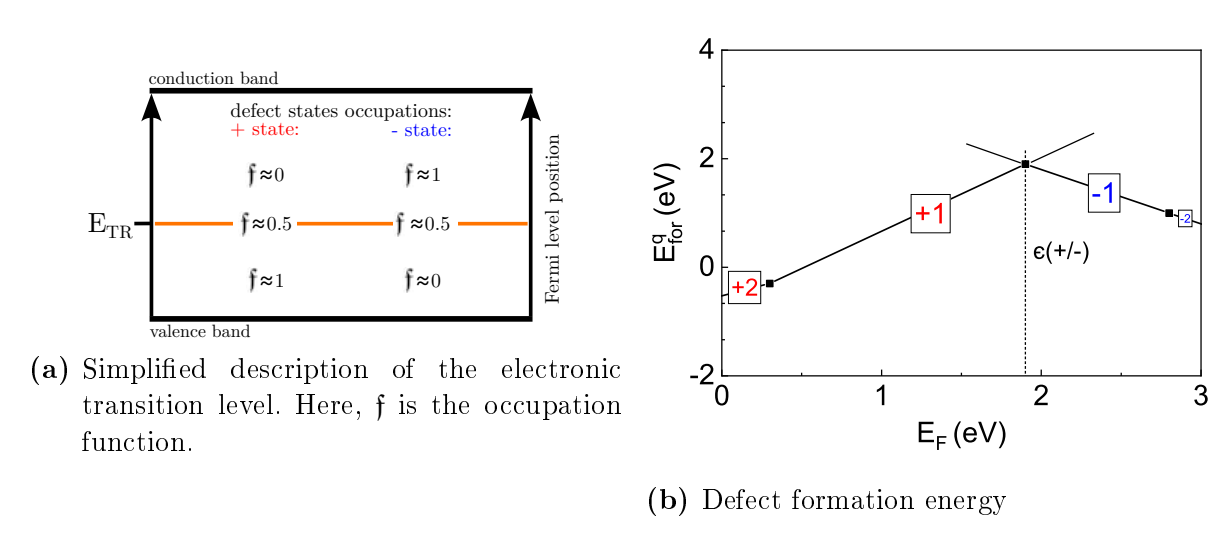


Figure 3.1.3: Illustrations of aspects of metastable defects.

Metastable defects usually have an inherent electronic transition level (denoted by us as  $E_{TR}$  or  $\epsilon$ ). This level corresponds to the Fermi level position above which it becomes energetically favourable to change the configuration from one charge state to another [107]. Such a level is presented by denoting two charge states between which a change occurs. For example, a transition from +1 charge state to -1 is denoted<sup>3</sup> as  $\epsilon(+/-)$ . Analogously, when  $E_F$  drops below an  $E_{TR}$ , the negative state becomes unstable against the positive state. It is important to emphasize here that level is a virtual state resulting from the energy characteristics of the defect, and there is no state at a given energy position associated with it. This idea, in a tremendously simplified way, is presented in Fig. 3.1.3a.

<sup>&</sup>lt;sup>3</sup>The notation and the whole idea of transition levels were formulated by Baraff et al. [18].

The concept of  $E_{TR}$  can link CCD diagrams and the classical energy diagrams, illustrating the position of defect states relative to bands. As with classical defects, we can mark  $E_{TR}$  there, and analyse the Fermi level-dependent occupations of metastable configurations in a manner similar to that used for classical defect states.

Plotting the defect formation energy  $E_{for}^q$  in the function of  $E_F$  is a widely used practice in the defects in semiconductors investigations. Those plots allow for comparing the relative binding energies of electrons to different defects (of variable charge) as a function of the Fermi level. The electronic transition level can be directly determined from the intersection of the formation energy curves representing the two different charge states of the defect in the function of  $E_F$ . At this point, the defect has the same formation energy in both charge states, therefore both configurations are in thermodynamic equilibrium. Again, this idea, in a simplified way, is presented in Fig. 3.1.3b.

### Multiphonon emission

To some extent, all defects in semiconductors are coupled to the lattice. Effects of lattice relaxation can manifest as a Stokes shift of the transition energy for optical ionization or a capture of the carrier in the multiphonon emission (MPE) process. Multiphonon transitions are favoured whenever there is a very strong electron-phonon coupling, which is associated with large changes in the equilibrium lattice coordinates as well as in the energy of the defect state during the capture or emission of the electronic charge carrier. Here, we will capsule the description done by Lang [19] regarding the MPE processes:

The capture cross section in the MPE regime can we written as:

$$\varsigma = \xi (4\pi E_R k T_{eff})^{\frac{1}{2}} \exp\left(-\frac{\Delta E}{k T_{eff}}\right) \tag{3.1.2}$$

The  $E_R$  is the lowering of the energy of the bound state due to lattice relaxation,  $\hbar\omega$  is the average energy of the phonons, and the  $\Delta E$  is (general) barrier height at the crossing of the parabolas on the CCD diagram (vide Fig. 3.1.1). The parameter often associated with the transitions accompanied by lattice relaxation is the Huang-Rhys factor (S), a dimensionless value describing the average number of phonons emitted during the optical transition, id est:

$$E_R = S\hbar\omega \tag{3.1.3}$$

The value of the S coefficient demarcates the weak and strong lattice coupling regimes. S < 1 is considered low latice coupling. For S >> 1 we are dealing with strong coupling. The effective temperature  $T_{eff}$  is defined as:

$$kT_{eff} = \frac{\hbar\omega}{2} \coth\left(\frac{\hbar\omega}{2kT}\right)$$
 (3.1.4)

At high temperatures, the  $T_{eff} \approx T$ , and (3.1.2) becomes classical activation relation for capture cross-section. At low temperatures,  $kT_{eff} \approx \frac{1}{2}\hbar\omega$  and the lattice vibrations play a more significant role in governing the MPE transition than temperature.

By consolidating the above-described equations into one, we can obtain a formula describing the capture cross section in the MPE regime, which allows us to determine the basic parameters of metastable defects from the temperature dependence of  $\varsigma$ :

$$\varsigma = \xi \left[ 2\pi k S(\hbar\omega)^2 \coth\left(\frac{\hbar\omega}{2kT}\right) \right]^{\frac{1}{2}} \exp\left(-\frac{\Delta E}{\frac{1}{2}\hbar\omega \coth\left(\frac{\hbar\omega}{2kT}\right)}\right)$$
(3.1.5)

However, under certain conditions, such as those described above, or in the case of small lattice relaxation, equation (3.1.5) describing the temperature dependence of the capture cross-section can be approximated by the classical activation relation [109]. Indeed, assuming the  $\exp(\Delta E/kT)$  is a dominant factor, equation (3.1.5) reduces to (3.1.6). Depending on the adopted metastable defect system, these considerations are

valid for both electrons and holes:

$$\varsigma_n \sim \exp\left(-\frac{\Delta E_{EC}}{kT}\right)$$
(3.1.6a)

$$\varsigma_p \sim \exp\left(-\frac{\Delta E_{HC}}{kT}\right)$$
(3.1.6b)

### **Implications**

The formulation of negative-U metastable defects was made by Anderson in the 1970s to explain the behaviour of glassy semiconductors doped with n- and p-type impurities [110]. In general, metastable defects were found to exist in many semiconductors, e.g. amorphous silicon [18]; EL2 centers in GaAs [111, 112]; the famous<sup>4</sup> DX centers in AlGaAs [113, 114], and in CdTe [115], and anion vacancies in chalcopyrites [20]. The last was explained by the Lany-Zunger model, significantly advancing research in CIGS solar cells [13, 16, 17].

By far, the most important aspect of metastable defects in the context of this work is its achievement in explaining the persistent photoconductivity (PPC) phenomenon. The PPC is an effect of increased semiconductor conductivity after illuminating the sample. In a material not exhibiting PPC, the conductivity immediately returns to the value before illumination after the light is turned off. In the case of PPC, the increase in conductivity persists after the light is turned off. The duration of the state of increased conductivity is temperature-dependent and at low temperatures, this effect is practically stable. When temperature increases, the metastable state relaxes to the state before

<sup>&</sup>lt;sup>4</sup>The DX centers were primarily considered as composed of donor **D** with unknown **X** atom. There have been conflicting theories on whether the defect is an isolated dopant atom or a complex and whether the lattice relaxation is large or not. In 1988, Chadi and Chang proposed that DX is a highly localized and negatively charged defect that arises from large lattice relaxation and behaves like a negative-U center. The model explained observed persistent photoconductivity and verified the existence of negative-U metastable defects. Solving the DX puzzle demonstrated the power of ab initio (first principles) calculations, such as pseudopotential methods, in predicting and explaining complex properties of defects in semiconductors.

illumination [116], showing slow decay kinetics. In order to explain the PPC effects, it was necessary to expand the standard electronic processes model with the interpretation of carrier capture and emission processes with the introduced lattice relaxation. In the frame of the metastability model, depending on the material (and model), after generating an electron-hole pair by illumination, the metastable defect captures one of the carrier species, abandoning the other one to its fate. Due to the discussed barrier for relaxation, this disequilibria carrier concentrations persists at low temperatures. Not until annealing the metastable system relaxes, and the compound reset to its original state. The exact model explaining PPC varies from material to material, but the general idea remains more or less alike.

For the quantitative description of the metastable phenomena (i.e. a slow relaxation), a Kohlraush - Williams - Watts (KWW) function is usually being used, commonly known as a stretched exponential function [117], having the equation (for electrical current):

$$I = I_0 \exp\left[-\left(\frac{t}{\tau}\right)^{\beta}\right] \tag{3.1.7}$$

where  $\beta$  is the so-called stretching parameter and, by default, takes values—from the range  $0 < \beta < 1$ . The case of  $\beta > 1$  values, results in the compressed exponential function. It is usually neglected, however has certain physical interpretations [118–120]. The (classic) KWW function is widely used to describe relaxation phenomena in various materials. This time dependency be found in, e.g. a-Si:H [117], GaAs [121], AlGaAs [122], or SnO<sub>2</sub> [123]. There are several models explaining the origin of the KWW function in various compounds, e.g. dispersive diffusion of trapped carriers [124], based on continuous-time random-walk model [125]; relaxation barrier distributions [126], or serial relaxation [127]. In fact, the KWW function is an empirical relation with no deep rationale to apply, beyond the a posteriori formulated interpretations.

The problem of metastability in semiconductors can be investigated using various methods applied in general semiconductor research, especially those in which the

influence of sample illumination is usually investigated, i.e. the PPC phenomenon and similar ones [128]. Among the methods used, there are: TSC (conductivity in the function of temperature) [13, 112]; DLTS [12, 14, 114]; photocapacitance [129] and photocurrent [15, 122] kinetics; capacitance-voltage characteristics [13, 14]; and imaginably many others. Nevertheless, the most important instruments to advance the study of metastable defects are numerical methods [20, 107].

In the following sections of this work, when we state *metastability*, we will mean phenomena related to defects exhibiting carrier capture/emission barrier related to the large lattice relaxation.

# 3.2 Methods of semiconductor investigation

Herein, we will disclose fundamental models standing behind chosen methods of semiconductor investigation, which will be utilised in further work.

### 3.2.1 Thermally Stimulated Current (TSC)

Thermally stimulated current (TSC<sup>5</sup>) and thermally stimulated luminescence (TSL) are observed in a broad variety of materials, including semiconductors. Mensuration of those phenomena is perhaps the most direct evidence for the existence of electronic trap levels. The first observations of thermally stimulated luminescence date back to the 17th century, but its application as an experimental technique is credited to Urbach (1930). For historical reasons, a TSL is sometimes referred to as a *glow curve* due to its first observations in luminescence [108].

In the classic interpretation of the TSC curve, when a sample is illuminated at low temperature, the photoexcited carriers fill the trap levels. Thereafter, when heated in dark conditions, the carriers freed from traps contribute to the dark current. As the result, we observe a peak in the I(T) dependency, with the maximum at  $T_m$ , being the sum of dark

<sup>&</sup>lt;sup>5</sup>Which can also be an abbreviation for Thermally Stimulated **Conductivity**, fortunately, usually  $I \sim \sigma$  so the two abbreviations can be used interchangeably.

current and surplus of freed carriers. As one will see,  $T_m$  can provide information about the trap levels. The evaluation of the TSC curve is a nontrivial task, as there are many factors determining the trapping and recombination processes, and the TSC is only an indirect trap-spectroscopy method.

For the simplest case of a single electron trap level  $n_t$ , placed at  $(E_C - E_t)$ , and communicating with the conduction band, one can write the kinetic equation for trap occupation, and free electrons [130]:

$$\frac{\mathrm{d}n_t}{\mathrm{d}t} = -e_n n_t + n_t \varsigma_n v_n (N_t - n_t) \equiv n c_n - n_t e_n \tag{3.2.1a}$$

$$\frac{\mathrm{d}n}{\mathrm{d}t} = e_n n_t - n_t \varsigma_n v_n (N_t - n_t) - \frac{n}{\tau_n} \equiv e_n n_t - c_n p_t - \frac{n}{\tau_n}$$
(3.2.1b)

The analytic solutions to those equations are not easily found. For simplicity, we can assume the case of negligible retrapping. As described before, to free the electrons from the trap, we anneal the sample using constant linear heat rate r, thus. dT = rdt. Therefore, we can write:

$$\frac{\mathrm{d}n_t}{\mathrm{d}t} = r\frac{\mathrm{d}n_t}{\mathrm{d}T} = -e_n n_t \tag{3.2.2a}$$

$$\frac{\mathrm{d}n}{\mathrm{d}t} = r\frac{\mathrm{d}n}{\mathrm{d}T} = e_n n_t - \frac{n}{\tau_n} \tag{3.2.2b}$$

Those equations have solutions:

$$n_t(T) = n_t(T_0) \exp\left(\int_{T_0}^T -\frac{e_n}{r} dT\right)$$
(3.2.3a)

$$n(T) = n_t(T_0)\tau_n e_n \exp\left(\int_{T_0}^T \frac{e_n}{r} dT'\right)$$
(3.2.3b)

For exact derivation, one can look into Look et al. [130]. The emission rate  $e_n = e_n(T)$ , is a function of temperature, and will yield peak-shape n(T) TSC curve. To find the temperature of the maximum  $T_m$ , we will put dn/dT = 0. If we neglect the temperature

dependence of  $\tau_n$ ,  $\varsigma_n$ ,  $v_n$ , and  $N_C$ , we can obtain:

$$E_t = kT_m \ln \left( \frac{N_C \varsigma_n v_n k T_m^2}{r E_A} \right) \tag{3.2.4}$$

which can be rewritten as:

$$E_A = kT_m \ln(N_C \varsigma_n v_n) \left[ 1 + \ln\left(\frac{kT_m^2}{rE_A}\right) \right] \equiv kT_m \ln(\nu_t) \left[ 1 + \ln\left(\frac{kT_m^2}{rE_A}\right) \right]$$
(3.2.5)

where  $\nu_t$  is the attempt to escape frequency (in the particular analysed case). Therefore, after few transformation, one get:

$$\ln\left(\frac{r}{T_m}\right) = \ln\left(\frac{\nu_t}{\frac{E_A}{kT_m} + 2}\right) - \frac{E_A}{kT_m} \tag{3.2.6}$$

As  $\sigma \approx ne\mu$ , we can obtain n(T) by measuring the thermally stimulated current. By varying the heating rate r of the TSC experiment, the Arrhenius plot of  $\ln(r/T_m)$  vs 1/T yields  $E_A$ . It has to be noted that  $E_A$  does not necessarily mean  $E_t$ . It is because of the approximations of temperature independence of  $\tau_n$ ,  $v_n$ , and  $N_C$ , and most importantly,  $\varsigma_n$ . By considering activation dependency of  $\varsigma_n$  i.e.  $\varsigma_n \sim \exp(-E_{\varsigma}/kT)$ , and the fact, that:

$$e_n = gN_C \varsigma_n v_n \exp\left(-\frac{E_t}{kT}\right) \tag{3.2.7}$$

the resulting activation energy of  $e_n$  becomes the sum of  $E_t + E_{\varsigma}$ , and this is the value that the  $E_A$  equals to [108,131]. The capture cross-section temperature dependence can be also a result of the lattice relaxation processes discussed in section 3.1. Consequently, the measured activation energies have a temperature dependence determined by the proper metastability models (cf. eq. 3.1.6).

### 3.2.2 AC conductivity

Here, we will consider an impedance response of the semiconductor, in which a certain hopping transport mechanisms can occur. Originating from work of Debye, one can obtain the formula of (complex) electric susceptibility  $\Upsilon$  for a set of an oscillating dipoles in oscillating electric field  $F(\omega)$ :

$$\Upsilon(\omega) = \frac{\Upsilon(0)}{1 + i\omega\tau} \tag{3.2.8}$$

where  $\tau$  is a relaxation time constant, having a fixed value by default. The physical origin behind electric susceptibility, the *oscillating dipoles* are: 1) rotational motion of molecular dipoles, or 2) translational motion of free electric charges. Those two approaches are credited to two *schools* (after Jonscher [132]), namely: 1) "dielectric", and 2) "semiconductor" school. Those two approaches lead to different interpretations of observed  $\chi(\omega)$ , and then electric permittivity, from which conductivity can be calculated:

$$\sigma^*(\omega) = \sigma'(\omega) + i\sigma''(\omega) = i\omega\varepsilon_0\varepsilon^*(\omega) = \omega\varepsilon_0\varepsilon''(\omega) + i\omega\varepsilon_0\varepsilon'(\omega)$$
(3.2.9)

Hence, the real part of conductivity equals  $\omega \varepsilon_0 \varepsilon''(\omega)$ . For simplicity, we will denote  $\sigma'(\omega) = \text{Re}(\sigma^*(\omega)) = \sigma^*(\omega)$  as  $\sigma(\omega)$ , or as  $\sigma_{AC}$  to distinguish it from DC conductivity.

The relaxation time constant  $\tau$  in eq. (3.2.8) might be a true constant. However, in most cases, a distribution of relaxation times  $\tilde{\tau}(\tau)$  would exist. Especially, in random systems (like, highly disordered or non-crystalline materials), one would expect such distribution [133].

For a given continuous distribition  $\tilde{\tau}(\tau)$ , the real part of AC conductivity can be obtained as:

$$\sigma(\omega) \propto \int_0^\infty \tilde{\tau}(\tau) \frac{\omega^2 \tau}{1 + \omega^2 \tau} d\tau$$
 (3.2.10)

A detailed derivation of the equation (3.2.10) can be found in Jonscher [132], Elliot [133], or elsewhere.

One can also notice, that the frequency dependence will be approximately linear for

$$\tilde{\tau}(\tau) \propto \frac{1}{\tau}$$
:
$$\sigma(\omega) \propto \int \frac{\omega}{1 + \omega^2 \tau^2} d(\omega \tau) \sim \omega$$
(3.2.11)

The final formula yielding  $\sigma(\omega)$  depends on the distribution of the relaxation times, that will vary among different models. Note, that the final  $\sigma(\omega)$  dependence will be a product of the first power of  $\omega$  and  $\tilde{\tau}(\omega)$ , wathever the form of  $\tilde{\tau}(\omega)$  is. Therefore in general, the equation (3.2.10) can be written as:

$$\sigma(\omega) \sim \omega^s$$
 (3.2.12)

where s, index of the power, is a constant value, originating from applying a model, that predicts particular distribution of relaxation time constants  $\tilde{\tau}$ .

Moreover, equation (3.2.12) can be written in a more general form, incorporating DC conductivity  $\sigma_{DC}$ , usually independent of the AC conductivity (as they can originate from different physical phenomena):

$$\sigma_{\text{total}}(\omega) = \sigma_{\text{DC}} + \sigma(\omega)$$
 (3.2.13)

There is a number of models, predicting the value of relaxation constant  $\tau$ , and therefore the value of s. To calculate  $\sigma(\omega)$  one has to give a formula for  $\tilde{\tau}(\tau)$ , that depends on the particular type of microscopic relaxation process under consideration. Here we will enclose some of the them:

1. Carrier hopping between localised states in the bandgap, randomly distributed within the material, introduced by Pollak and Pike [134]. This is the simplest and in a way, the most *obvious* mechanism. The relaxation time can be written as:  $\tau \propto \exp\left(\frac{E_m}{kT}\right)$ , where  $E_m$  is a (culombic) barrier height separating two localised states. The frequency dependence is predicted to be linear, therefore:

$$s = 1$$
 (3.2.14)

2. Correlated barrier hopping (CBH) (introduced by Pike [135]) is the modification of the previous model without the assumption, that the barrier  $E_m$  is independent of the separation distance of two sites and therefore independent of frequency. For neighbouring sites, the potential wells overlap, resulting in lowering of the effective barrier. The power factor s equals:

$$s = 1 - \frac{6kT}{E_m} (3.2.15)$$

3. Electronic tunneling, firstly considered by Pollak [136], as a charge transfer driven by quantum-mechanical tunneling between two sites. The s equals:

$$s = 1 - \frac{4}{\ln(\frac{1}{\omega \tau_c})} \tag{3.2.16}$$

One should note, that s is now frequency-dependent, and should be calculated as  $\frac{d\sigma(\omega)}{d\omega}$ .

4. Debye-like relaxation. For systems with single relaxation time  $\tau$ , one should expect a simple quadratic, or close to quadratic frequency dependence, as it states in the eq. (3.2.10). Therefore:

$$s \cong 2 \tag{3.2.17}$$

As one can notice from the given equations, the vast majority of models predicts, that the value of s is in the range 0 < s < 1 or s = 2, with other overunity values even being unphysical from the equations point of view. Jonscher clearly states, that a dependence with the exponent higher than unity is rather impossible, and even s = 2 should be taken with a grain of salt [132].

The models listed above are formulated under the pair approximation assumption, in which the motion of carriers is contained within a pair of states, and the total frequency response is a product of integration over all pairs. At any given frequency  $\omega$ , the major contribution comes from hopping between pairs for which  $\omega \tau = 1$ . [137]

Throughout time, some modifications of the models for AC conduction have been formulated. In particular, they were trying to determine what conditions must be met for the exponent s to be superlinear. Some of them particularly relates to the chalcogenide glasses (or heavily disordered chalcogenide materials), which naturally caches our interest. Elliott [137,138] have shown, that for  $non-random^6$  distribitions of centers between which relaxation takes place can result in a superlinear frequency dependence – there are some cases in which such non-random distribution can occur e.g. pairing (clustering) of defects: In chalcogenide glasses, the defects responsible for the electronic relaxation are the charged dangling bonds. Those are present in the liquid state in thermal equilibrium, and appreciably mobile in the liquid state implying, that the pairing of opposite charged defects is possible in this state. As the compound is (rapidly) cooled-down, at the glass transition temperature  $T_{gt}$  the system gets frozen, preserving the ordered defect distribution. The resulting non-random distribution can be the incorporated into CBH model, yielding the modified formula for power factor:

$$s = 1 - \frac{6kT}{E_m - kT \ln\left(\frac{1}{\omega \tau_c}\right)} + \frac{T}{8T_{gt}}$$
 (3.2.18)

The frequency dependence becomes superlinear for large values  $E_m/kT$ .

Another source for  $\sigma(\omega)$  superlinearity in chalcogenide glasses is a non random distribution of asymetric barrier heights, proposed by Gilroy and Phillips [139]. They postulate an exponential distribution  $p(E_m) = \frac{1}{E_{gt}} \exp\left(-\frac{E}{E_{gt}}\right)$ , where  $E_{gt}$  is the cut-off energy, related to the glass transition temperature  $T_{gt}$ . The energy distribution has similar origin to non-random spatial distribution. The model leads to:

$$s = 1 + \frac{kT}{E_{at}} = 1 + \frac{T}{T_{at}} \tag{3.2.19}$$

As one can notice, the energy distribution model assumes *only* superlinear frequency dependence.

<sup>&</sup>lt;sup>6</sup>In previous models, it was assumed, that the distribution of hopping sites is random.

When discussing AC conductivity, the analysis of impedance spectra and Nyquist plots is worth mentioning. An Impedance plot (or Nyquist plot) – a plot of Im(Re(Z)) is a powerful tool for interpreting impedance spectra of complex systems. While this approach is practical when analysing systems with one or few well-defined relaxation times, it becomes more complicated when it comes to analysing the Nyquist plot for systems with a distribution of relaxation times, as the ones presented here, especially with s > 1.

A system with a single relaxation time  $\tau$  can be represented as a simple equivalent parallel RC circuit in which  $\tau = RC$  – a semicircle on Nyquist plot with the maximum at  $\frac{R}{2}$  or the frequency corresponding to the relaxation time constant. Such system gives  $\sigma(\omega)$  dependence with s=2. Consecutively, a system with two or three relaxation times will result in two or three semicircles in the Nyquist plot respectively. Successively, a system having a continuous distribution of relaxation times (assuming s<1) is equivalent to an infinite number of RC circuits in series or a constant phase element (CPE) [140]. The question about a nature of CPE corresponding to s>1 extends beyond the scope of this discourse, and the superlinear CPE is rather considered unphysical.

There can be more intricate equivalent circuits proposed for particular cases, resulting in various menagerie of impedance spectra. This method shines particularly in electrochemistry and ionic or mixed conductors research, where equivalent circuit elements could be assigned to particular physical phenomena that make up the system under investigation. A detailed description of impedance spectroscopy in this view can be found in the plentiful literature [140,141].

The application of classical impedance spectroscopy to semiconductor materials or devices seems less explored than the case of ionic or mixed conductors, partly because the field has its own sophisticated techniques, e.g. CV measurements, DLTS, et cetera.

Nevertheless, models describing processes in semiconductors using equivalent electrical circuits have emerged. One of the oldest models was formulated by Ching-Tang Sah [142–144], who developed classical equations governing semiconductor processes in terms of discrete electronic elements. Unlike typical *lumped* models commonly used in IS, Sah represents a bulk semiconductor as a transmission line, having manifold circuit loops. Over

the years, modern approaches to the concept have emerged (e.g. Moia et al. [145] have applied very similar models, but replacing the current sources representing recombination with bipolar transistors). In some cases, the simplification of the transmission line to a simple equivalent circuit with lumped elements representing particular sample parts or physical processes can be done under the assumption of sample uniformity [146] or by integrating over sample geometrical dimensions [145].

The question may arise: What about inductive elements? While the physical interpretation of capacitive or resistive elements seems obvious, an inductive element may remain somewhat mysterious. A negative capacitance (e.g. [147]) is an alternative way to describe the problem. It is a known concept whose physical interpretation usually lies within ionic transport (e.g. [148]) or, in the case of semiconductor devices, can emerge from multiple processes, such as carrier transport, injection, recharging, et cetera [149,150]. Bisquert et al. formulated a concept of *Chemical inductor*, which collects many physical processes that can appear in impedance diagrams as inductance, such as catalytic, electrodeposition, and corrosion reactions (e.g. in fuel cells, corrosion electrodes of metal alloys), but also memristive systems and biological neurons. The chemical inductor is built of a two-dimensional system that couples a fast conduction mode with a slowing down element. It is defined as a set of dynamical equations; it could then be easily rephrased to suit the particular physical mechanism. The element can be modelled as a coil in the equivalent circuit having apparent inductance  $L^* = \frac{\tau_k}{g_u}$ , where  $\tau_k$  is an adaptation current time constant, and  $g_u$  is an adaptation function, defined by some state variable y and the differential equation  $\tau_k \frac{\mathrm{d}I}{\mathrm{d}t} = g_u(y, U)$  in a similar fashion as in memristive elements. In impedance spectra, the chemical inductor appears as a negative (inductive) loop on the imaginary part. It has found vast application in e.g. perovskite solar cells to model the influence of mobile ions [148, 151–153].

The thorough analysis of the peculiarities of the physical origins of the negative or apparent capacitances and chemical inductors exceeds the scope of this dissertation. It is worth adding that this approach can be applied to memristor devices and gives the issue additional depth.

### Interlude: A gyrator circuit

As an aside to the matters related to the apparent inductances, an issue that would be worth mentioning and which would clarify potentially unclear concerns related to the inductance considered here is the so-called gyrator. A gyrator is a passive, linear, electrical network element that can transform a load capacitance into an inductance<sup>7</sup> [154]. Figure 3.2.1a shows an exemplary implementation of the gyrator. It consist of a resistor R and a capacitor C forming an RC circuit (low pass filter), and an NPN transistor.

Let us calculate the input impedance of the transistor (collector branch): first, we will calculate the base voltage defined by the RC voltage divider:

$$U_B = U_{in} \frac{\frac{1}{i\omega C}}{R + \frac{1}{i\omega C}} = U_{in} \frac{1}{i\omega RC + 1}$$

$$(3.2.20)$$

The base current is given by the base voltage and the base-emiter input impedance, given by the  $h_{11}$  hybrid parameter  $[\Omega]$  of the BJT transistor:

$$I_B = \frac{U_B}{h_{11}} = \frac{U_{in}}{h_{11}} \frac{1}{i\omega RC + 1}$$
 (3.2.21)

The collector current is given by the base current and the transistor gain  $h_{21}$ :

$$I_C = h_{21}I_B = U_{in}\frac{h_{21}}{h_{11}}\frac{1}{i\omega RC + 1}$$
(3.2.22)

Therefore, the transistor input impedance equals:

$$Z_C = \frac{U_{in}}{I_C} = \frac{h_{11}}{h_{21}} (i\omega RC + 1) = i\omega \left(\frac{h_{11}}{h_{21}}RC\right) + \frac{h_{11}}{h_{21}} \equiv i\omega L^* + R^*$$
 (3.2.23)

One needs only observe that now the transistor input impedance is equivalent to the impedance of an inductor with series resistance (Fig. 3.2.1c). The term  $\frac{h_{11}}{h_{21}}RC$  has indeed unit of  $[\Omega \cdot \Omega \cdot F] = [H]$ . Thus, for a large transistor input impedance, the transistor will be

<sup>&</sup>lt;sup>7</sup>Its primary use is to replace physical inductors, especially at low frequencies, for example in active filters or equalizers. Application of a gyrator reduces the cost and size of the device by replacing large and expensive inductive components.

seen by an external source as an inductor with inductance  $L^*$ , with series resistance  $R^*$ . For a large resistence R (i.e., if one neglects the base and capacitor current), the gyrator circuit can be approximated as an RL circuit (otherwise, one would have to add parallel resistor with resistance  $h_{11}$  to the capacitor). To eliminate the potentially non-negligible base current, one could replace the BJT transistor with FET transistor and obtain a circuit from Fig. 3.2.1b. The input impedance of the FET transistor, calculated in the same manner equals:

$$Z_D = \frac{1}{G_{GD}}(i\omega RC + 1) = i\omega \left(\frac{1}{G_{GD}}RC\right) + \frac{1}{G_{GD}} \equiv i\omega L^* + R^*$$
 (3.2.24)

where  $G_{GD}$  [1/ $\Omega$ ] is a transistor transimpedance function, defined as  $G_{GD} = \frac{I_D}{U_{GS}}$ . Since no current flows through the gate circuit, this circuit falls closer to the equivalent circuit from Figure 3.2.1c.

The principle of operation of this circuit is simple. The RC circuit shifts the current phase by -90°, and the transistor in the common emitter (or common source) configuration reverses the phase by 180° resulting in +90° shift. Therefore, the current phase resembles an inductor. Considering this circuit as a two-terminal black box device, its frequency response and the impedance seen from external terminals would be the same as for the inductor (under positive bias, assuming ideal elements and the transistor working within its active region).

The key idea here is that one can successfully emulate the inductive behaviour using other passive and active elements without actual coils. Despite the absence of nanoscale magnetic elements, a proper arrangement of equivalent resistances, capacitances, and active elements, videlicet, interdependence of particular physical processes, can give a macroscopic inductive response. Resistances and capacitances are widely acknowledged in solid states, including semiconductors (cf. [142]). The transistor, i.e. a controlled current source, could represent, e.g. recombination process (cf. [145]).

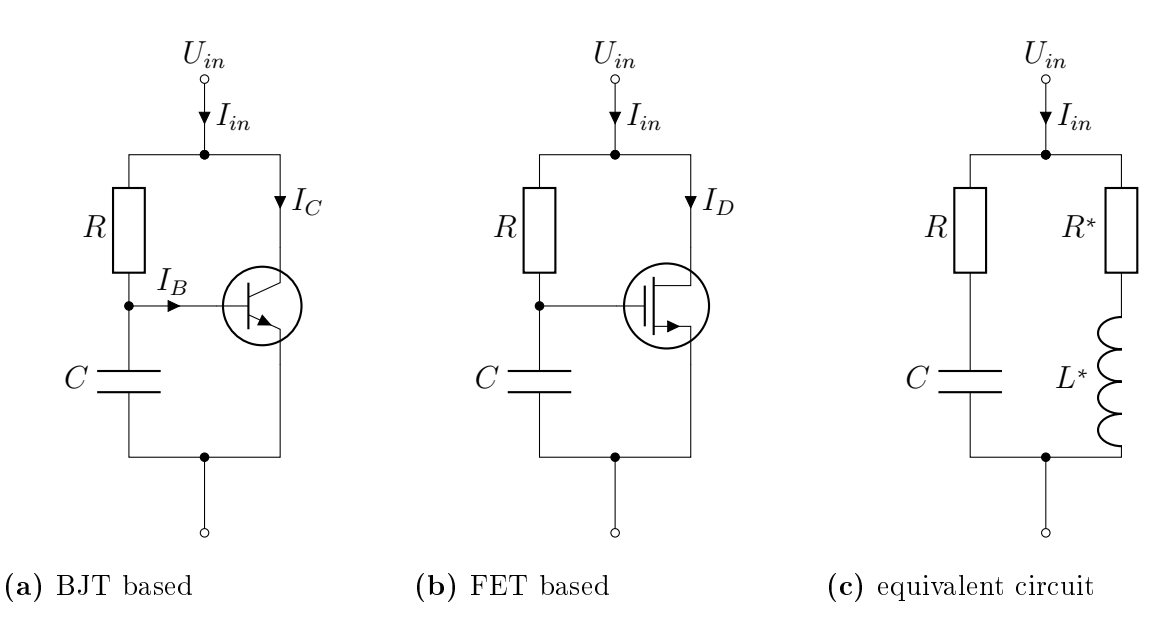


Figure 3.2.1: Gyrator circuit

### 3.2.3 Photoconductivity processes

This section will focus on the relationship between photogeneration, carrier concentration, and the resulting photoconductivity as a function of light intensity and wavelength. We will start with the simplest case of a single defect. Then, we will proceed to consider and describe the illumination-photoconductivity relation in the presence of traps and, further on, in the presence of trap state distributions, gradually gravitating towards more subtle complexities. Lastly, we will briefly describe the experimental method of investigating the analysed illumination dependencies. The derived theoretical description will later help us explain the observed phenomena in our compound, accentuating the densities of trap states.

Photoconductivity in a semiconductor, in terms of the excess increase in photocurrent under the influence of illumination, can be defined as follows:

$$\Delta \sigma = e(\mu_n \Delta n + \mu_n \Delta p) \cong e\mu f\tau \tag{3.2.25}$$

where the total conductivity is plainly  $\sigma = \sigma_0 + \Delta \sigma$ , and  $n = n_0 + \Delta n$ ,  $p = p_0 + \Delta p$ .

#### 3.2. Methods of semiconductor investigation

Herein, we assume a homogenous bulk semiconductor, and the mobility  $\mu$ , whatever it may originate, remaining constant. We can further make simplifying approximations that one type of carrier dominates the photoconductivity, so the contribution by the other can be effectively neglected [155].  $\Delta\sigma$  could be further simplified to  $e\mu f\tau$ , where  $\mu$  and  $\tau$  represent general parameters depicting certain type of carriers or is average value. f is the generation rate of photocarriers [cm<sup>-3</sup>s<sup>-1</sup>], which can be successfully determined knowing the power and spectrum of the exciting light, and the absorption coefficient of the material. Lastly a (free) lifetime  $\tau$  in a sense of time that the charge carrier is free to contribute to the conductivity, is a key-parameter in terms of the photoconductivity, and its bound by the relations:

$$f\tau_n = \Delta n \tag{3.2.26a}$$

$$f\tau_p = \Delta p \tag{3.2.26b}$$

The free lifetime is in general governed by recombination or trapping processes in the semiconductor. For an elementary case of a single set of recombination centers, one can write:

$$\tau_n = (\varsigma_n v_n p_r)^{-1} \tag{3.2.27a}$$

$$\tau_p = (\varsigma_p v_p n_r)^{-1} \tag{3.2.27b}$$

 $p_r$  and  $n_r$  are the density of recombination centers unoccupied by electrons and by holes, respectively;  $\varsigma_n$  and  $\varsigma_p$  are capture cross sections for free electrons and holes;  $v_n$  and  $v_p$  are the electrons' and holes' thermal velocities. For multiple species of recombination centers one would have  $\tau^{-1} = \sum_i \tau_{i,n}^{-1}$ . For band-to-band generation, one can write continuity and

charge neutrality equations:

$$\frac{\partial n}{\partial t} = f + \vartheta - \frac{n}{\tau_n} + \frac{1}{e} \nabla \cdot \vec{j_n}$$
 (3.2.28a)

$$\frac{\partial p}{\partial t} = f + \vartheta - \frac{p}{\tau_p} + \frac{1}{e} \nabla \cdot \vec{j_p}$$
 (3.2.28b)

$$\varepsilon \varepsilon_0 \nabla \cdot \vec{F} = e \left( \Delta p - \Delta n + p_r - n_r \right) \tag{3.2.28c}$$

where  $n = n_0 + \Delta n$ ,  $p = p_0 + \Delta p$ ,  $\vartheta$  is thermal carrier generation, and F is applied electric field. As can be seen, those equations describe the dynamics of electrons and holes in a semiconductor; for heavily doped semiconductors, however, one can neglect the influence of minority carriers and consider only the kinetics of a single type of carrier with a satisfactory approximation. Since the dissertation deals with the n-type semiconductor (which, as it turns out, has also strong self-doping), for clarity, we will limit ourselves only to the description for electrons. The formulations presented will later be used to interpret the illumination dependencies in our experiments.

Neglecting the thermal generation and non-zero current divergence, one can write the simplified state equation incorporating only optical generation and recombination (eq. 3.2.29a). The equation (3.2.28a) can be solved for the generation transient (after turning on) and for relaxation (after turning off the illumination) by taking different initial conditions. For relaxation kinetics, the starting point is the steady state illumination, where  $\frac{\mathrm{d}n}{\mathrm{d}t} = 0$ , thus  $n(0) = n_0 + \Delta n = n_0 + f\tau_n$  (cf. equation (3.2.26a)); for generation kinetics:  $\Delta n(0) = 0$  ( $n(0) = n_0$ ). Therefore, one can obtain two simple solutions: (3.2.29b) and (3.2.29c).

$$\frac{\partial n}{\partial t} = f - \frac{n}{\tau_n} \tag{3.2.29a}$$

$$\Delta n(t) = f \tau_n \left[ 1 - \exp\left(-\frac{t}{\tau_n}\right) \right]$$
 (3.2.29b)

$$\Delta n(t) = f \tau_n \exp\left(-\frac{t}{\tau_n}\right) \tag{3.2.29c}$$

In a steady state, this case gives linear relation between current and photogeneration

rate. Assuming, that optical generation originates from the recombination centers (i.e.  $n_r \equiv n$ ), one will obtain the relation:

$$\Delta n = \left(\frac{f}{v\varsigma_n}\right)^{\frac{1}{2}} \tag{3.2.30}$$

This case is valid also when there is only band-to-band recombination. It gives  $f \sim n^2$ , and will produce sublinear relation  $\sigma \sim f^{\frac{1}{2}}$ , often called bimolecular recombination [156].

The presence of trapping centers will modify potentially observed lifetime, as the generated carriers proportionally occupy trap states, introducing capture and emission time constants. After Rose [157], we can define a response time  $\tau_0$  in the presence of trapping as:

$$\tau_0 = \left(1 + \frac{n_t}{n}\right)\tau_n\tag{3.2.31}$$

where  $n_t$  is a density of occupied traps concentration  $N_t$ . In such case, in the experiment, one will observe growth or decay curve with time constant  $\tau_0$ . In the steady-state condition under illumination, the free electron and trapped electron densities, n and  $n_t$ , are given by:

$$n = N_C \exp\left(-\frac{E_C - E_{Fn}}{kT}\right) \tag{3.2.32a}$$

$$n_t = N_t \exp\left(-\frac{E_t - E_{Fn}}{kT}\right) \tag{3.2.32b}$$

By inserting equations above into (3.2.31) (and neglecting +1), one obtains:

$$\tau_0^{-1} = \frac{N_C}{N_t \tau_n} \exp\left(-\frac{E_C - E_t}{kT}\right)$$
 (3.2.33)

In the case above, when approximately all traps all filled, the lifetime is independent of f, resulting in  $\Delta n \sim f$ , often called the monomolecular recombination.

Whether the defect state will act either as a trap or as a recombination center depends on the relative magnitudes of the probability of thermal emission of the trapped carrier into the band, and the probability of recombination with the carrier of opposite sign before the emission would occur. Both fates are possible for a given defect state, so there is an equilibrium situation where the recombination probability is equal to the emission probability. The energy for a given defect at which these probabilities are equal is the so-called demarcation level. When the electron trap happens to be below the electron demarcation level  $E_{Dn}$  it will act as a recombination center. Similarly for holes demarcation level  $E_{Dp}$ . Therefore defect states located between electron and hole demarcation levels  $(E_{Dp} < E < E_{Dn})$  will act as a recombination centers, and as traps otherwise. It can be shown [155, 157], that demarcation levels are bound with the quasi-Fermi levels  $(E_{Fn}, E_{Fp})$  by the relations:

$$E_{Fn} = E_{Dn} + kT \ln \left( \frac{p\varsigma_p}{n\varsigma_n} \right)$$

$$E_{Fp} = E_{Dp} - kT \ln \left( \frac{p\varsigma_p}{n\varsigma_n} \right)$$
(3.2.34a)
$$(3.2.34b)$$

$$E_{Fp} = E_{Dp} - kT \ln \left( \frac{p\varsigma_p}{n\varsigma_n} \right) \tag{3.2.34b}$$

As one can see, in the first approximation  $E_{Dn} \cong E_{Fn}$  and  $E_{Dp} \cong E_{Fp}$ . In the second approximation, the demarcation levels are displaced form respective quasi-Fermi levels by the same amount. When  $p\varsigma_p = n\varsigma_n$ , the equality holds.

The  $N_t$  does not have to be a single localized energy level, but could be a distribution of states. There are plenty of possible models and combinations of various distributions of traps, often in communication with localized recombination centers [158]. A significant contribution to the development of the description of this type of systems was made by Richard Bube, who developed simple formulation applied to several large signal photoconductivity problems in semiconductors with isolated imperfections with discrete energy levels [159]. He expanded it further by metastable defects, and its impact on recombination dynamics [160]. In fact, the variety of dependencies and relations between

photocurrent, light and lifetime is potentially unlimited. The superlinearity or sublinearity of the concentration-light intensity relationship usually results from the fact that lifetime is a function of photogeneration. The one particular case, to which we would like to pay more attention here, is an exponential distribution of trap (here, electron trap) states, defined by the equation:

$$N_t(E) = \xi \exp\left(-\frac{E_C - E}{kT^*}\right) \tag{3.2.35}$$

where  $\xi$  is a constant. In the analysis of this case, we follow Rose [157], but the derivation can be found in various other sources [155,156]. As one will find later in this dissertation, such traps, having distribution defined by the equation (3.2.35) will play a significant role in our investigated compound.

The temperature denoted here as  $T^*$  is a formal parameter used to quantify the distribution of states ( $kT^*$  has roughly similar sense to Urbach energy). We also assume, that  $T^* > T$ . The case  $T^* \leq T$  reduces the problem to the bimolecular recombination. The  $N_t$  states in dark conditions primarily act as electron traps, particularly active, as the capture cross section is expected to be relatively high for such states. When the light intensity increases, the position of the electron quasi-Fermi level/demarcation level gradually moves upward and eventually pervades the distribution of states. Gradually, a larger fraction of the  $N_t$  is converted from trapping to recombination states. This conversion advances as the  $E_{Fn}$  sweeps through the distribution towards the conduction band. Assuming that  $E_{Dn} \approx E_{Fn}$ , the density of empty states  $p_r$  is given by the number of  $N_t$  states lying between  $E_F$  and  $E_{Fn}$ . Those states have now been brought into the category of recombination centers:

$$p_r = \int_{E_F}^{E_{Fn}} N_t(E) dE = \int_{E_F}^{E_{Fn}} \xi \exp\left(-\frac{E_C - E}{kT^*}\right) dE =$$

$$\approx kT^* N_t(E_{Fn})$$
(3.2.36)

We can now write a basic equation that describes excited electrons concentration as a

function of electron lifetime and photogeneration rate:

$$\Delta n = f \tau_n = \frac{f}{v_n \varsigma_n p_r} = \frac{f}{v_n \varsigma_n k T^* \xi \exp\left(-\frac{E_C - E_{F_n}}{k T^*}\right)}$$
(3.2.37)

By definition, we also have:

$$n = N_c \exp\left(-\frac{E_c - E_{Fn}}{kT}\right) \equiv N_c \exp\left(-\frac{E_c - E_{Fn}}{kT^*}\frac{T^*}{T}\right)$$
(3.2.38)

After inserting  $E_C - E_{Fn}$  calculated from (3.2.38) into (3.2.37), assuming negligible  $n_0$ , and performing few trivial transformations, we obtain:

$$\Delta n = \left(\frac{fN_c^{\frac{T}{T^*}}}{kT^*\xi v_n \varsigma_n}\right)^{\frac{T^*}{T+T^*}}$$
(3.2.39)

Leading to relation:  $\Delta n \sim f^{\gamma}$  where a power factor  $\gamma$  equals:

$$\gamma = \frac{T^*}{T + T^*} \tag{3.2.40}$$

As the light intensity increases, more and more trap states are converted to recombination states. As the density of recombination states for electrons increases, the electron lifetime decreases, resulting in a sublinear relation between  $\Delta n$  and light intensity. According to Rose [157], while the model assumed an exponential distribution of states between  $E_F$  and  $E_C$ , the distribution needs only to extend over the small range of energies. Hence, almost any distribution of states would lead to  $\gamma$  having values between 0.5 and 1. As the distribution approaches nearly uniform one, that is, constant in energy, the characteristic temperature  $T^* \to \infty$ , and n varies nearly linearly with light intensity. The slope of log-log Lux-Ampere characteristics will have two parts:  $\gamma = 1$ , and  $\gamma = \frac{T^*}{T+T^*}$ . The slope inflects, at  $\Delta n = n_0$  [161].

For a given trap distribution, one can calculate electron concentration kinetics. The

density of trapped electrons in (any) continuos trap distribution is given by:

$$n_t = kTN_t(E)\ln\left(\frac{n}{n_0}\right) \tag{3.2.41}$$

The rate equation [116] is:

$$\frac{\mathrm{d}n_t}{\mathrm{d}t} = \frac{\mathrm{d}n_t}{\mathrm{d}n}\frac{\mathrm{d}n}{\mathrm{d}t} = N_t(E)\frac{kT}{n}\frac{\mathrm{d}n}{\mathrm{d}t}$$
(3.2.42)

Therefore, the rate equation for n (without reemission), and its solution (decay transient) are:

$$\frac{\mathrm{d}n}{\mathrm{d}t} = -\frac{n}{\tau_n} - N_t(E) \frac{kT}{n} \frac{\mathrm{d}n}{\mathrm{d}t} = \frac{n}{\tau_n \left(1 + \frac{N_t(E)kT}{n}\right)} \approx -\frac{n^2}{\tau_n N_t(E)kT}$$
(3.2.43a)

$$n = \frac{n(0)\tau_n N_t(E)kT}{\tau_n N_t(E)kT + n(0)t}$$
(3.2.43b)

where n(0) is initial concentration of electrons (during steady-state illumination). For exponential distribution of traps (3.2.35), the decay function is:

$$\frac{n(0)}{n} = \xi \ln \left[ t - \tau_n \ln \left( \frac{n(0)}{n} \right) \right] \tag{3.2.44}$$

The study of response time supplies the experimental basis for the evaluation of the number and distribution of electron traps. A simple expression (after (3.2.31)) relates the response time  $\tau_0$ , to the lifetime  $\tau$ , and to the density of trapped  $(n_t)$  and conduction (n) electrons:

$$\frac{\tau_0}{\tau} = 1 + \frac{n_t}{n} \tag{3.2.45}$$

The position of the quasi-Fermi level for electrons depends on the conduction electron density through the equation:

$$E_{Fn} = kT \ln \frac{N_C}{n} \tag{3.2.46}$$

By varying excitation intensity with the variable light source, the steady state conduction electron density n varies and the Fermi level shifts; the number of traps

governing the recombination kinetics changes and consequently the response time varies.

In the case of a continuous trap distribution we can write:

$$\frac{\tau_0}{\tau_n} = \frac{N_t^*(E_F)}{N_C} \exp\left(\frac{E_F}{kT}\right) = \frac{N_t(E_F)kT}{N_C} \exp\left(\frac{E_F}{kT}\right) \tag{3.2.47}$$

 $N_t^*$  is the trap density in a energy range kT wide at the Fermi level.

Equation (3.2.47) allows the deduction of the trap distribution from experimental values of  $\tau_0$ , if the quasi-Fermi level energy at each excitation intensity and the lifetime  $\tau$  are known. The values of the quasi-Fermi level energy can be obtained through (3.2.46) by evaluating the steady state conduction electron density n from  $\Delta\sigma(\Phi)$  measurements assuming known mobility and neglecting holes contribution. Equation (3.2.47) allows thus the deduction of the trap density  $N_t(E)$  against their energy depth  $E_F$  obtained from (3.2.46).

An extension of the Rose model can be done, with an analogous parallel distribution of states near the valence band acting similarly but as a hole trap. A detailed description was made by Main et al. [161] and applied in some later works [162,163]. In the presence of a distribution of hole traps, for low light intensities, the approximate analysis gives slope  $\gamma = \frac{T}{T_V}$ , where  $kT_V$  is the characteristic energy for the distribution of traps near the valence band. Then, for high excitations, the slope equals approximately:

$$\gamma \cong \frac{T_C}{T_V} \tag{3.2.48}$$

 $T_C$  and  $T_V$  have the same meaning as  $T^*$  for conduction band and valence band distributions of states, respectively. The mechanism stays the same as before, but now we must consider the quasi-Fermi level for holes penetrating hole traps. If those distributions differ, one will expect two changes in the slope. First, when the photoconductivity is governed by the density of hole traps,  $E_{Fp}$  moves downward by a higher shift in energy than  $E_{Fn}$ , and  $\gamma = \frac{T}{T_V}$  – the system is governed by the hole traps. Next, for high light intensities, when the effects of shifting  $E_{Fn}$  and converting more electron traps into

recombination centers start to play a significant role, the exponent equals  $\gamma = \frac{T_C}{T_V}$ . In this regime, the resulting Lux-ampere log-log characteristics will have three consecutive regions with slopes:  $\gamma = 1$ ,  $\gamma = \frac{T}{T_V}$ , and  $\gamma = \frac{T_C}{T_V}$ .

The cases where the  $\gamma$  coefficient value is greater than 1 are worth mentioning. That superlinear Lux-Ampere characteristics are usually explained by sensitizing centers [157] and some more intricate formulae, loosely based on this concept [158, 164–166]. The effects of sensitization occur when the recombination current shifts from states with a high capture cross-section to states with a low capture cross-section for one sign of the charge carriers. Thus, adding recombination centers of the second type increases the lifetime of the particular type of charge carrier. Experimentally, sensitization can be manifested by an increase in the lifetime with increasing light intensity: shifting quasi-Fermi level during the intensification of the illumination through the potential sensitizing centers activates them as recombination centers (similarly as presented in this section before). Due to sensitization, this causes an increase in the lifetime, resulting, among other effects, in superlinear Lux-Ampere characteristics.

Lastly, Shimakawa et al. [124] have shown that in amorphous hydrogenated silicon, the presence of exponential band tails leads to non-exponential photocurrent relation:  $I \propto t^{-\beta}$ , where  $\beta = 1 - T/T^*$ . In the applied extended Rose model, the band tails' electrons recombine with the holes from localised states. This recombination through band tails leads to a dispersive diffusion relation (mentioned in section 3.1). The dispersive reaction (usually associated with disordered materials) is a process in which the reaction rate depends on time. In many cases, the rate is given by [156]:

$$K(t) = \xi t^{\beta - 1} \tag{3.2.49}$$

The nonlinear relaxation kinetics can then be derived from the differential equations:

$$\frac{\mathrm{d}n}{\mathrm{d}t} = -K(t)n\tag{3.2.50a}$$

$$\frac{\mathrm{d}n}{\mathrm{d}t} = -K(t)n^2 \tag{3.2.50b}$$

(3.2.50c)

Where (3.2.50a) is monomolecular type, and (3.2.50b) is bimolecular type equation. The solutions to those equations are respectively:

$$\Delta n = \xi_1 \exp\left[-\left(\frac{t}{\tau}\right)^{\beta}\right] \tag{3.2.51a}$$

$$\Delta n = \frac{\beta}{\xi_2} t^{-\beta} \tag{3.2.51b}$$

where  $\xi_1$ ,  $\xi_2$  are constants. Therefore a distribution of traps alone can lead to KWW function in the relaxation kinetics [125], leaving the question of finding the K(t) function, that has a proper physical interpretation.

#### Photoresponse spectra

Up to now, we have considered photoconductivity assuming band-band excitations. Measuring photoconductivity as a function of wavelength using monochromatic light allows us to obtain elementary knowledge about the energetic structure of the studied compound. The most basic quantity is the bandgap: for a given absorption coefficient  $\alpha$  and reflectance  $\Re$  and assuming  $\alpha d \ll 1$ , the photoconductivity depends on optical constants [156] as:

$$\Delta \sigma \sim e\mu\tau\Phi(1-\Re)\alpha\tag{3.2.52}$$

Therefore  $\Delta \sigma \sim \alpha$ , and one can apply usual analysis of absorption coefficient, i.e. extract direct and indirect bandgap values from plot of  $\alpha^2$  and  $\alpha^{\frac{1}{2}}$  respectively.

Photoconductivity, in general, will be sensitive to any optical excitation that changes free carriers concentration n and p. It will, therefore, be sensitive to other optical

transitions, primarily to excitations from defects to the band. The concentration of excited carriers from the defect will depend on the optical transition probability for a given wavelength of exciting light (i.e. f and  $\tau$  will be  $\lambda$ -dependent). A material with multiple levels within the bandgap will induce a peak-like shape in the photoresponse spectra at the photon energy corresponding to the optical defect-band transition with magnitude related to transition efficiency.

In general, donors in n-type material (or acceptors in p-type) increase conductivity. Donors in p-type material (or acceptors in n-type material) decrease conductivity. Imperfections, which act as efficient recombination centres, reduce the photosensivity. Imperfections that act as trapping centres decrease the speed of response. Imperfections with levels within the bandgap extend the spectral response of the material.

### Measurement setup and transients analysis

Throughout this work, we will apply a particular method of investigating the photoresponse of the materials, sometimes called Phto-induced current transient spectroscopy (PITCS). The method allows for obtaining values of steady-state photoconductivity, together with generation and relaxation transients of the photocurrent. Thus enabling us to get the steady state photoconductivity ( $\Delta \sigma$ ), as well as the evolution of the photocurrent during generation or relaxation, i.e. probing the transients governed by formulas: (3.2.29c), (3.1.7), or (3.2.43b).

Experimentally, a photosensitivity (sometimes denoted as a  $\mu\tau$ -product,  $\mu\tau = \frac{\sigma}{ef}$ ) will be defined by us, simply as:

$$\Delta \sigma = \sigma_{light} - \sigma_0 \tag{3.2.53}$$

where  $\sigma_{light}$  is the conductivity in the illuminated state, and  $\sigma_0$  – in dark conditions.

The setup for measuring  $\Delta \sigma$  in the function of  $\lambda$  (i.e. photoconductivity spectra) is shown in Fig. 3.2.2. The main light source is an incandescent lamp that drives the monochromator (diffraction grating), enabling us to produce monochromatic light in the

range of 350  $\div$  1900nm. Low-pass filters cut off diffraction grating harmonics if necessary. In order to probe sample conductance, we apply  $10V_{DC}$  bias and measure the current. The current measurement is done using a Keithley 485 picoammeter and recorded using a Ni-DAQ card<sup>8</sup>. By opening and closing the mechanical shutter (Thorlabs SC10), we can record the kinetics of photocurrent for generation (after opening the shutter) and relaxation (after closing the shutter). Practically, we apply light pulses long enough to get the sample in its steady state during illumination. The current kinetics are recorded by the National Instruments DAQ card and stored for further data analysis. Note that  $\Delta \sigma$  can be obtained from both the generation and relaxation transients.

We can use the JANIS VPF-100 cryostat to measure at cryogenic temperatures (in the range  $80 \div 320$ K) if necessary. Finally, using equation (3.2.53), we can calculate the  $\Delta G$  by knowing the geometrical dimensions, and  $\Delta \sigma$ . By sweeping the excitation wavelength, we can obtain photoconductivity spectra as shown in Fig. 3.2.3.

We can modify the setup by replacing the monochromator (and lamp) with another auxiliary light source to measure photoconductivity in the function of light intensity (for monochromatic light fixed wavelength). This type of experiment – photocurrent vs light intensity enables us to probe photoexcitation relation, i.e. equation (3.2.30), and most of all (3.2.39). Knowing the light power and spectra, one can easily calculate photon flux  $\Phi$  and photogeneration f. This experiment is sometimes called the Lux-Ampere measurement. It is also possible to replace the filters with appropriate ND filters or change the duration of the light pulse (by varying the opening/close time of the shutter) if necessary.

The kinetics analysis depends on the type of transient observed and the model assumed. For the simple exponential rise or decay, one can extract lifetime by calculating the kinetics' slope in a log-log plot. Similarly, the transient of the type as (3.2.43b) can be analyzed by calculating the reciprocal of the n ( $\Delta \sigma$ ). In the case of the KWW function (stretched exponent), in order to get  $\tau$  and  $\beta$ , one can double log a transient and calculate

<sup>&</sup>lt;sup>8</sup>The picoammeter is set as a transimpedance amplifier. The high resistivity of the Keithley 485 enables us to measure high resistivity samples, up to  $1G\Omega$ .

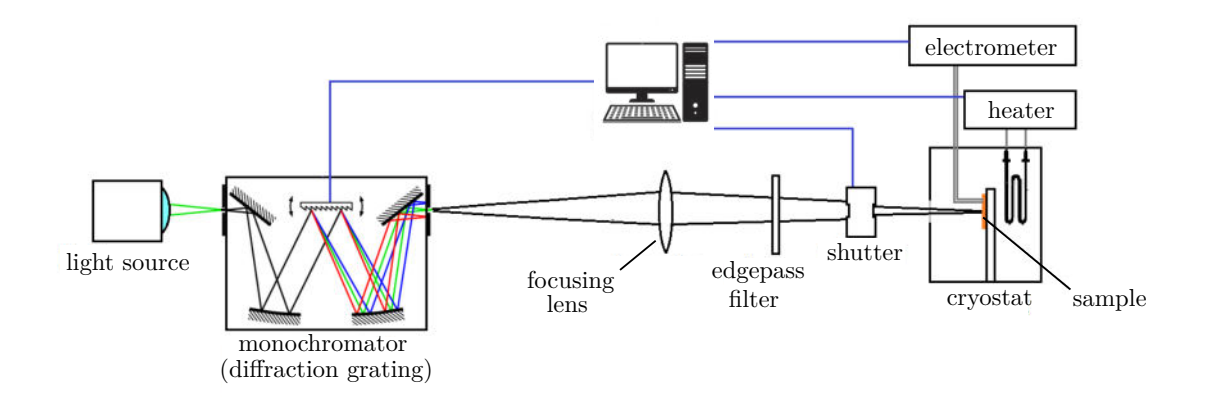


Figure 3.2.2: Setup for photocontuctivity  $(\Delta \sigma)$  spectra measurement

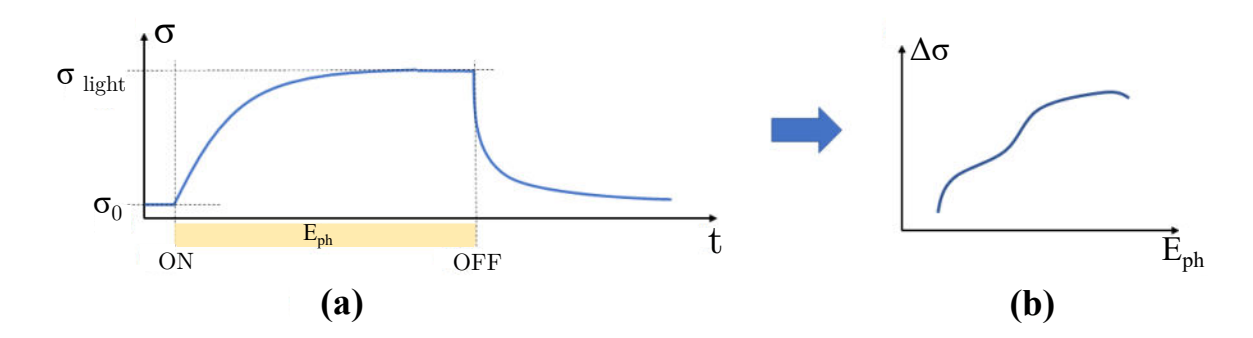


Figure 3.2.3: Idea of photocontuctivity  $(\Delta \sigma)$  spectra measurement.

the parameters by fitting linear functions in the similar manner:

$$\sigma(t) = \sigma_{light} \left\{ 1 - \exp\left[ -\left(\frac{t}{\tau}\right)^{\beta} \right] \right\}$$
 (3.2.54a)

$$\ln\left[\ln(\sigma_{light}) - \ln\left(\sigma_{light} - \sigma(t)\right)\right] = \beta \ln(t) - \beta \ln(\tau)$$
(3.2.54b)

$$\sigma(t) = \sigma_{light} \exp\left[-\left(\frac{t}{\tau}\right)^{\beta}\right]$$
 (3.2.55a)

$$\ln\left[\ln(\sigma_{light}) - \ln(\sigma(t))\right] = \beta \ln(t) - \beta \ln(\tau)$$
(3.2.55b)

For the quantitative analysis of the rise or decay kinetics, it is possible to use a Time analyzed transient spectroscopy (TATS) spectroscopy. It is an isothermal spectroscopy

defined in the time domain, and it is often used to study the relaxation of deep levels in semiconductors by analyzing capacitance or current transients [167]. Unlike analogous temperature-scanning methods such as Deep Level Transient Spectroscopy (DLTS) and Photoinduced Transient Spectroscopy (PITS), which analyze transients at fixed time windows while scanning temperature, in TATS, the kinetics analyzes the transient in a moving window in time at a fixed temperature. This method was applied in multiple cases, e.g. analysis of GaAs [121] or ion-damaged Si [129]. The TATS signal can be constructed from a capacitance or current transient. A common form for the first-order TATS signal from a transient of I(t) is given by:

$$TATS(t) = I(t) - I(t + \iota)$$
(3.2.56)

where  $\iota$  is a selectable constant – a window factor. When plotted against  $\ln(t)$ , the TATS signal exhibits a maximum at  $t_{max}$ , from which (for  $\iota = 1$ ), the time constant  $\tau$  and the KWW stretching factor  $\beta$  can be calculated using formulas:

$$\tau|_{\iota=1} = \frac{t_{max}}{\ln(2)} \tag{3.2.57a}$$

$$\tau|_{\iota=1} = \frac{t_{max}}{\ln(2)}$$

$$\frac{1}{\beta}|_{\iota=1} = \frac{\text{FWHM} + 0.078}{2.417}$$
(3.2.57a)

The formulae (3.2.57) are calculated for  $\iota = 1$ . We have will take advantage of TATS as a guide to nonexponentiality when analyzing the current transients.

#### 3.2.4Metal-semiconductor junctions

When considering metal-semiconductor junctions, it is perhaps most prudent to generally classify them as either injecting or non-injecting. The classification of a junction as injecting (ohmic) or non-injecting (rectifying) hinges on the difference between the metal work function  $W_M$  and the semiconductor work function  $W_S$ , being the sum of electron affinity  $\chi$  and the Fermi level position regarding the conduction band.

An Ohmic contact is a special case of an injecting contact, which is defined as a contact that can supply the carriers demanded by the bulk of the semiconductor [116]. For an **n-type** semiconductor<sup>9</sup>, the ohmic contact is formed when the metal work function is smaller than the semiconductor work function<sup>10</sup>. Provided that the injected electron concentrations do not exceed  $n_0$ , the current flow in the ohmic contact is limited by the conductivity of the bulk semiconductor, i.e. the electron current density  $j_n$  is defined simply by the microscopic Ohm's law:

$$j_n = \sigma F = e\mu_n F N_C \exp\left(-\frac{E_C - E_F}{kT}\right)$$
(3.2.58)

where F is applied electric field.

At sufficiently high electric fields, the injected electron concentration can exceed  $n_0$ , and a net space charge would be developed in the bulk semiconductor. In such a regime, the current will be limited by the created space charge of the injected electrons. For a sample capacitance C and thickness d, the maximum charge on the negative electrode with surface area A would be  $q = CFd = \varepsilon_0 \varepsilon AF$  (assuming the rectangular sample geometry with electrodes on opposite faces). The charge transit time across the sample is  $\tau = \frac{d}{\mu_n F}$  (for electron drift velocity  $v_d^n = \mu_n F$ ). Assuming full charge is injected, a space charge-limited current would be given by the flow rate of charge q [116, 157, 168]:

$$j_n = \frac{q}{A\tau} = \frac{\varepsilon_0 \varepsilon \mu_n}{d} F^2 \tag{3.2.59}$$

which is the Mott-Gurney square law. A more accurate solution, with the right boundary conditions can be obtained by solving Poisson equations. Such solution introduce numerical factor of  $\frac{9}{8}$  [116].

The transition from ohmic to SCLC regime occurs at the crossover voltage  $U_{tr}$ , when

<sup>&</sup>lt;sup>9</sup>For the sake of this exposition, our portrayal will be limited to the n-type semiconductors, for it is this particular type that shall be the subject of the dissertation. For all p-type cases, all the relations and inequalities presented must be reversed in such a manner as to satisfy the conditions for holes.

<sup>&</sup>lt;sup>10</sup>The condition is sufficient if one neglects the interface states.

 $j_{ohmic} = j_{SCLC}$ :

$$U_{tr} = \frac{en_0 d^2}{\varepsilon_0 \varepsilon} \tag{3.2.60}$$

When the trap states present in the bulk semiconductor, they would capture most of the injected electrons. For a single trap level, n and  $n_t$  are described by the equations (3.2.32), and one can write:

$$\frac{n}{n_t} = \frac{N_C}{N_t} \exp\left(-\frac{E_C - E_t}{kT}\right) \tag{3.2.61}$$

The trapped electrons will contribute to the charge  $(q = n + n_t)$  from the derivation above. After [116] we can calculate the  $j_{SCLC}$  reduced by the influence of  $n_t$  by repeating the above derivation, but taking into account the trapping of part of the injected electrons (and assuming  $n \ll n_t$ ):

$$j_n = \frac{q}{A\tau} = \frac{\varepsilon_0 \varepsilon \mu_n}{d} \frac{n}{n_t} F^2 \tag{3.2.62}$$

When the electric field increases, more carriers are injected, and the  $E_{Fn}$  shifts closer to  $E_C$ , eventually reaching  $E_t$  and filling all trap states. The trap-filled limit voltage can be calculated as  $U_{TFL} = \frac{eN_t d^2}{2\varepsilon_0 \varepsilon}$  [116]. The single trap model yields the classical S-shape IV trace typical for the SCLC mechanism, where below  $U_{TFL}$ , for small electric fields, the sample is in the ohmic regime, then after the transition region around  $U_{TFL}$ , the sample experiences the classic SCLC  $F^2$  regime [116,169].

An analogous analysis can be performed for the exponential distribution of traps, defined as (3.2.35) in section 3.2.3. In a similar manner to (3.2.36), we can calculate the density of occupied states  $n_t$ , a fraction of  $N_t(E)$  [168, 170, 171]:

$$n_{t} = \int_{E_{Fn}}^{E_{C}} N_{t}(E) dE = \int_{E_{Fn}}^{E_{C}} \xi \exp\left(-\frac{E_{C} - E}{kT^{*}}\right) dE =$$

$$\approx kT^{*} N_{t}(E_{Fn})$$
(3.2.63)

Which coincidentally gives the same solution as in (3.2.36). Similarly as before, we can insert here the term  $E_C - E_{Fn}$  calculated from (3.2.38). Now, putting the origin of the

space charge to  $n_t$ , i.e.  $q = en = \varepsilon_0 \varepsilon F$ , and inserting  $E_C - E_{Fn}$  calculated from (3.2.63) into (3.2.32a), we obtain:

$$n = N_C \left(\frac{\varepsilon_0 \varepsilon AF}{e\xi kT^*}\right)^{\frac{T^*}{T}} \tag{3.2.64}$$

Further calculation of  $j_n = \frac{\mu_n F}{Ad}n$  leads to superlinear electric field dependence  $j_n \sim F^{l+1}$  (the exact derivation can be found in the cited literature.), and hence to:

$$I \sim U^{l+1}$$
 (3.2.65)

where  $l = \frac{T^*}{T}$ . The model assumes that  $T^* > T$ ; thus, the measured I - U dependency has to be stronger than parabolic. Otherwise, the model does not apply; for  $T^* < T$ , the problem reduces to the case of shallow traps discussed earlier [171].

Curiously, one can notice the similarity to the superlinear photoconductivity (3.2.39) or AC conductivity (3.2.19) analysed before. Experimentally,  $I \sim U^{l+1}$  relation was verified by i.a. Richard Bube [172].

The cases above, i.e. SCLC and ohmic conductivity, were examples of the conductivity limited by the processes in the bulk material. If  $W_M > W_S$  (in the n-type semiconductor), a non-injecting junction will be formed<sup>11</sup>. In this case, when the two materials get in close contact, electrons diffuse from the semiconductor into the metal, leaving exposed positive charge (donor ions). This electron-depleted region results in band bending and in consequence, a built-in voltage  $U_{bi}$  across the depleted, or space-charge region (SCR).  $eU_{bi}$  constitutes the potential barrier against electron diffusion from the bulk region of the semiconductor layer into the metal, and in the basic case is given simply by  $eU_{bi} = W_M - W_S$ . From the other side, electron injection from the metal into the semiconductor is limited by the thermal emission over this barrier. From the metal side, barrier height ( $\Psi_B$ ) is given by:  $\Psi_B = W_M - \chi_S$ , where  $\chi_S$  is the electron affinity of the semiconductor. Under forward bias (negative voltage at the semiconductor layer in case of n-type semiconductor),

<sup>&</sup>lt;sup>11</sup>One must differentiate between a reverse-biased Schottky junction and a blocking contact, although these terms have been used interchangeably [116].

the built-in voltage is being reduced, leading to a large electron diffusion towards the metal surface, hence a large forward current. Applying a reverse bias (negative voltage at the metal) increases the built-in potential and broadens the depleted region in the semiconductor layer. The flowing current is limited by the thermal emission over the barrier  $\Psi_B$ . This current, designated as the saturation current  $I_S$  is given by the equation (3.2.70b)). The pre-exponential current  $I_T$  is then determined by the junction surface area A, and the term  $\frac{4\pi e(kT)^2 m_e^*}{h^3}$ , usually referred to as a Richardson constant [173]. Here, the  $m_e^*$  is the electron effective mass, and  $\varepsilon$  is the electric permitivity of the semiconductor layer.

We can determine the electric field in the SCR region along the distance z from the interface, by solving the one-dimensional Poisson equation:

$$\frac{\mathrm{d}F}{\mathrm{d}z} = \frac{e}{\varepsilon} N_D \tag{3.2.66}$$

Here, we assumed uniform semiconductor doping with donors having density  $N_D$  (and the full depletion approximation). Solving the equation, we obtain:

$$F(z) = \int \frac{e}{\varepsilon} N_D dz = -\frac{e}{\varepsilon} N_D(z_{SCR} - z)$$
 (3.2.67)

where  $z_{SCR}$  is the length of the SCR region. F is a linear function of z with a maximum at the interface. Integral  $-\int F(z)dz$  yields  $U_{bi} = \frac{q}{2\varepsilon}N_Dz_{SCR}^2$ , from which we can calculate  $z_{SCR}$ :

$$z_{SCR} = \left(\frac{2\varepsilon}{eN_D}(U_{bi} - U)\right)^{\frac{1}{2}} \tag{3.2.68}$$

A detailed discussion on the intricacies of the metal-semiconductor junctions and the principle of operation of the Schottky diode can be found in the extensive literature [116, 173,174]. Here, we shall set forth the definitive equation that governs the current-voltage relationship of a Schottky diode:

$$I = A \frac{4\pi e(kT)^2 m_e^*}{h^3} \exp\left(-\frac{e\Psi_B}{kT}\right) \left[\exp\left(\frac{eU}{\eta kT}\right) - 1\right]$$
(3.2.69)

This can be further simplified to:

$$I = I_S \left[ \exp\left(-\frac{eU}{nkT}\right) - 1 \right] \tag{3.2.70a}$$

$$I_S \equiv I_T \exp\left(-\frac{e\Psi_B}{kT}\right) \tag{3.2.70b}$$

$$I_T \equiv A \frac{4\pi e (kT)^2 m_e^*}{h^3}$$
 (3.2.70c)

 $\eta$  is a diode ideality factor, which incorporates all secondary effects that could be considered, making the diode non-ideal [173].

In practice, one does not simply measure diode barriers. In the first approximation, the saturation current can be calculated by extrapolating the semilog I vs U curve to U = 0. Then, from the Arrhenius plot:

$$\ln\left(\frac{I_S}{T^2}\right) = -\frac{\Psi_B}{kT} \tag{3.2.71}$$

one can obtain the barrier height  $\Psi_B$ .

The dependence of  $\Psi_B$  and  $W_M$  is, often weak and, in some instances, entirely absent, a matter which depends entirely on the semiconductor material. The nature of the metal/semiconductor contact is, in reality, dictated by the semiconductor surface states and any interfacial alloy or compound that may have been created<sup>12</sup>. The presence of semiconductor surface states is usually the result of dangling bonds, crystal imperfections (defects), or impurities [116].

Anyone who has delved into the various physics of semiconductor devices now foresees the presentation of p-n junctions. However, these junctions are beyond the scope of this treatise. Instead, herein we will highlight a different type of junction: the isotype n/n++ junctions. Take two n-type semiconductors differing in the doping level, with different

<sup>&</sup>lt;sup>12</sup>A notable example is the junction of molybdenum and CIGS. Whilst it is predicted by theory to be the rectifying junction, it consistently proves to be ohmic, as widely accepted – due to the formation of MoSe<sub>2</sub> [175].

work functions  $W_n$  and  $W_{n++}$ . Here, for the sake of depiction, we set  $\chi_n < \chi_{n++}$ , and  $W_n < W_{n++}$ . When those are brought into contact, a similar electron diffusion as in the Schottky junction occurs, resulting in the discontinuous band bending (Fig. 3.2.4). Thus, it produces the built-in voltage similarly to that in the Schottky junction  $eU_{bi} = W_{n++} - W_n$  in the n side, and an accumulation region on the  $n^{++}$  side<sup>13</sup>. The principle of operation under the forward and reverse bias of the isotype junction is analogous to the Schottky diode, including the formation of the barriers, and its impact on the transport. The detailed examination of the isotype junctions, including electrostatic analysis, can be found in e.g. Oldham et al. [176].

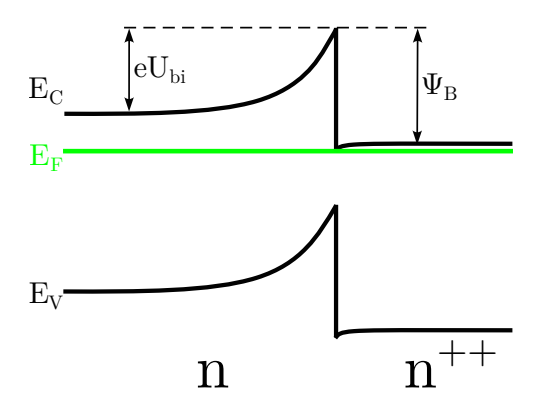


Figure 3.2.4: Schematic of the isotype  $n/n^{++}$  heterojunction.

Schottky emission is not necessarily the only mechanism for charge transport across a potential barrier; several others, including various tunnelling processes, can be distinguished. Since in the realm of neuromorphic devices, metal-insulator-metal (MIM) structures are a prevalent architecture, it is convenient to discuss these processes using such structures as an example. In MIM structures, we deal with an insulator layer (usually an oxide) sandwiched between two metallic layers, resulting in cliff-like band discontinuities (Fig. 3.2.5). We may, therefore, discern the following processes:

1. Schottky (or thermionic) emission, which already was under consideration, is one of the most often observed mechanisms in MIMs, especially at high temperatures. In

<sup>&</sup>lt;sup>13</sup>The accumulation-type contact represents another kind of possible interface situation, one that mercifuly does not introduce further substantial intricacies worth discussing into the description of the transport. A more detailed treatise on this matter can be found in [173].

this case, electrons are thermally activated and injected into the conduction band of the dielectric over a Schottky barrier, having height  $\Psi_B$ , into the conduction band in the insulator. The current density is given by the equation:

$$j_n = \frac{4\pi e m_e^* (kT)^2}{h^3} \exp\left(-e^{\frac{\Psi_B - \sqrt{\frac{eF}{4\pi\varepsilon_0\varepsilon}}}{kT}}\right)$$
(3.2.72)

 $\Psi_B$  is the barrier height. Here, we also accounted for the barrier lowering effect, caused by the image charge located at the mirror image of the electron with respect to the surface of the metal. Hence, the electron approaching the metal surface experiences an attractive force, that substantively reduce the effective barrier height by the term  $\sqrt{\frac{eF}{4\pi\varepsilon_0\varepsilon}}$ . More details can be found in e.g. [174].

2. Direct tunnelling can occur when a high electric fields are applied. Direct tunnelling through the barrier constituted by the insulator layer dominates when the insulator layer is thinner than 3nm [87]. The current density depends on the insulating layer thickness d, and barrier height  $\Psi_B$  [177], and can be approximated by the equation:

$$j_n \approx \exp\left(-\frac{8\pi\varepsilon d\sqrt{2em_e^*}}{3h}\Psi_B^{\frac{1}{2}}\right)$$
 (3.2.73)

3. Fowler-Nordheim (F-N) tunnelling dominates at the thicker insulating layers. In this case, a large electric field causes the bands to tilt significantly and the barrier formed by the insulator to take a triangular shape. Such tunnelling through a triangular barrier is described by the Fowler-Nordheim formulae, giving the current density:

$$j_n = \frac{e^2}{8\pi h \Psi_B} F^2 \exp\left(-\frac{8\pi\sqrt{2em_e^*}}{3hF}\Psi_B^{\frac{3}{2}}\right)$$
(3.2.74)

4. Poole-Frenkel (P-F) emission describes the transport over the barrier (similar to Schottky emission), assisted by the capture and emission by the trap states within the insulating layer [178], effectively lowering the Schottky barrier. The current

density is given by:

$$j_n = e\mu_n N_C F \exp\left(-e\frac{\Psi_T - \sqrt{\frac{eF}{\pi\varepsilon}}}{kT}\right)$$
 (3.2.75)

where  $\Psi_T$  is the distance between the conduction band and the trap energy level, and  $N_C$  is the density of states in the conduction band.

- 5. Trap-assisted hopping was, in fact, already considered in some sense in section 3.2.2 in terms of AC conductivity, starting from the analysis of electronic processes in the time domain, as carrier hopping between states that are close in terms of energy. Crucially, in this particular instance, the current density is a linear dependency on the applied electric field. We can further distinguish Nearest Neighbour Hoping (NNH) and Variable Range Hopping (VRH) [179]:
  - (a) Nearest neighbour hopping (NNH) takes place over trap states simply by direct tunnelling process. The transport is described by the equation:

$$j_n = \sigma_0 F \exp\left(-\frac{E_m}{kT}\right) \tag{3.2.76}$$

where  $E_m$  is the difference between the energies of the two states, and  $\sigma_0$  is the electrical conductivity.

(b) Variable Range Hopping (VRH), developed by Mott, conduction occurs at low temperatures. In the case of VRH, electrons "jump" over longer distances to find a state with a lower activation energy, which is more energetically favourable. The current density is given by the formula:

$$j_n = \sigma_0 F \exp\left(-\frac{\xi_{VRH}}{T^{\frac{1}{4}}}\right) \tag{3.2.77}$$

where  $\xi_{VRH}$  a parameter characterising a given material (dependent on the density of trap states) [179].

6. Trap-Assisted Tunnelling (TAT) is attributed to the tunnelling currents assisted by the defects in the insulator layer. Just as in the case of P-F emission, the trap states

support electron emission; here, the trap states support tunnelling in such a manner that electrons repeatedly tunnel through the barriers between adjacent potential wells. Hence,  $\Psi_T$  has the similar meaning as in the case of P-F.

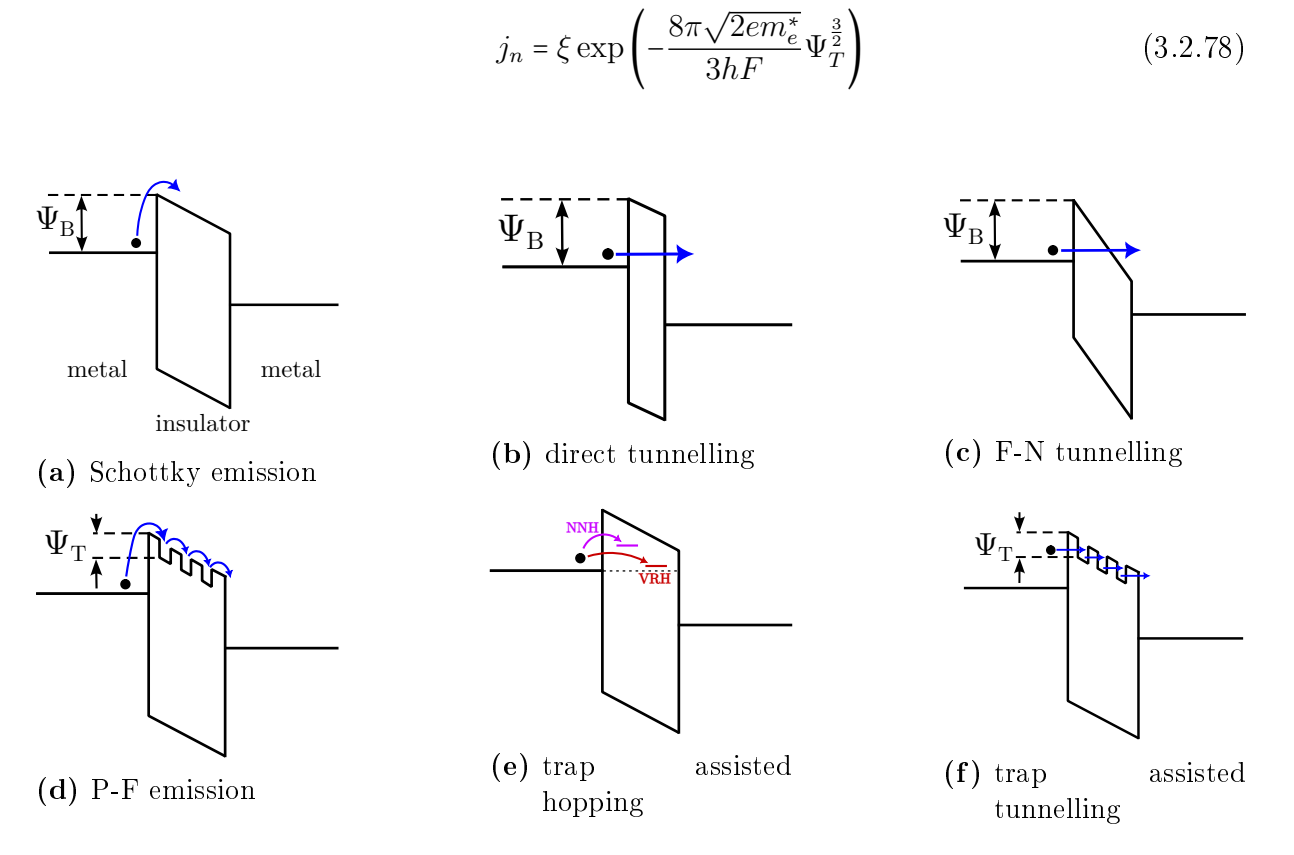


**Figure 3.2.5:** Schematic presentations of transport mechanisms based on the MIM structure.

**Based on:** Thakkar et al. [89]

In practice, the MIM structure is not strictly necessary to conjure the beforenamed transport mechanisms. For example, tunnelling or hopping through states under the conduction band can also occur in the Schottky junction, adding second, parallel, and perhaps dominant, transport path to the system.

From an experimental perspective, identifying the specific transport process across the potential barrier is crucial for investigating the devices. To a first approximation, this is diagnosed by analysing the electrical current dependence on voltage and temperature. It must be borne in mind that the applied voltage is not, at all times, simply proportional to the electric field as U = Fd. The presence of series resistances in the device structure,

which, with the junctions, form voltage dividers, can lead to deceptive misinterpretations in the instance of quasi-linear current-voltage dependencies.

### 3.3 Electrical characterization of memristive devices

The matter, in this instance, is quite elementary. Characterisation of an individual memristor device comes down to measuring its current-voltage (IV) characteristics. A zero-centred periodic excitation is used since one expects to obtain a hysteresis loop; as stated in the chapter 2.1, for memristive devices, a pinched hysteresis loop is expected. The trace and shape of the hysteresis, as well as the overall behaviour of the memristive device, are strictly determined by the physical processes governing the current transport, as well as the processes laying behind the memory behaviour in general. The IV curve shape will then depend on the particular conduction process, yielding the j(F) relation, as just described in the section 3.2.4. Therefore, the particular analysis method depends on the device model adopted. For example, in MIM devices with the filamentary switching, one expects an IV trace close to ohmic for the LRS state, while in the HRS state, the characteristic will depend on the dominant transport process through the oxide layer when the filament is broken. In turn, e.g. devices based on vacancy drift will assume an ionic drift/diffusion model. In fact, due to the vast number of memristor device implementations and the materials used, the number of models describing device operation is too large to be described here. An overview of models can be found in the extensive literature [87, 89, 180, 181].

For the testing of the binary memory retention capability, a train of pulses is usually applied. In this case, the issue to consider is the selection of voltages for read and write pulses. In this case, again, the selection depends primarily on the specific device being tested.

To characterise our manufactured devices, we used the Keithley 2450 SMU. By generating an arbitrary triangular waveform with varying frequency, we are able to explore a possible current-voltage hysteretic behaviour. An appropriate compliance was set to

avoid damage to the devices. The same SMU was used for pulsed stimulation (e.g., memory retention testing). For recording the current transients, next to the SMU, a 1:1 transimpedance amplifier, equipped with the Ni-DAQ card was also used.

### 3.3.1 Neuromorphic behaviour

As outlined in chapter 2, the primary objective in optimising neuromorphic devices is to emulate synaptic behaviour. In order to ascertain the neuromorphic properties of the devices, one needs to emulate the synaptic plasticity observed within biological neurons, but with electrical impulses. To this end, various pulse types and measurement protocols have been utilised in the literature to replicate the shifts in synaptic connection strength, which are the foundation of learning and memory. These measurements, then, reduce to a straightforward examination of the device's response, namely, the change in its resistance (or conductance) to voltage pulses of varying amplitude, duration, and frequency. One then proceeds to analyse the magnitude of these changes, as well as the forgetting – a time required for the device to return to its initial state. This same approach is equally relevant when considering the optical pulse stimulation of photomemristors. A vital example of those experiments is the results of Gao et al. presented before (Fig. 2.4.3).

In fact, no strictly unified neuromorphic tests exist; researchers approach this matter quite creatively, and their methods or models (e.g. fitting functions) are most often dictated by the specific nature of the devices under scrutiny; thus, making this field more akin to the biology itself. Here, we shall outline the most commonly investigated synaptic behaviours:

1. EPSP and IPSP, explained in chapter 2.2, broadly known as potentiation and depression. This is a method of learning by repeatedly applying stimulation (voltage or light) pulses and analysing the changes in current after subsequent pulses, that is, an increase during potentiation and a decrease during depression. Here is where one of the challenges discussed in Chapter 2.5, about linearity of growth, manifests itself – in order to program the weights effectively, both potentiation and depression

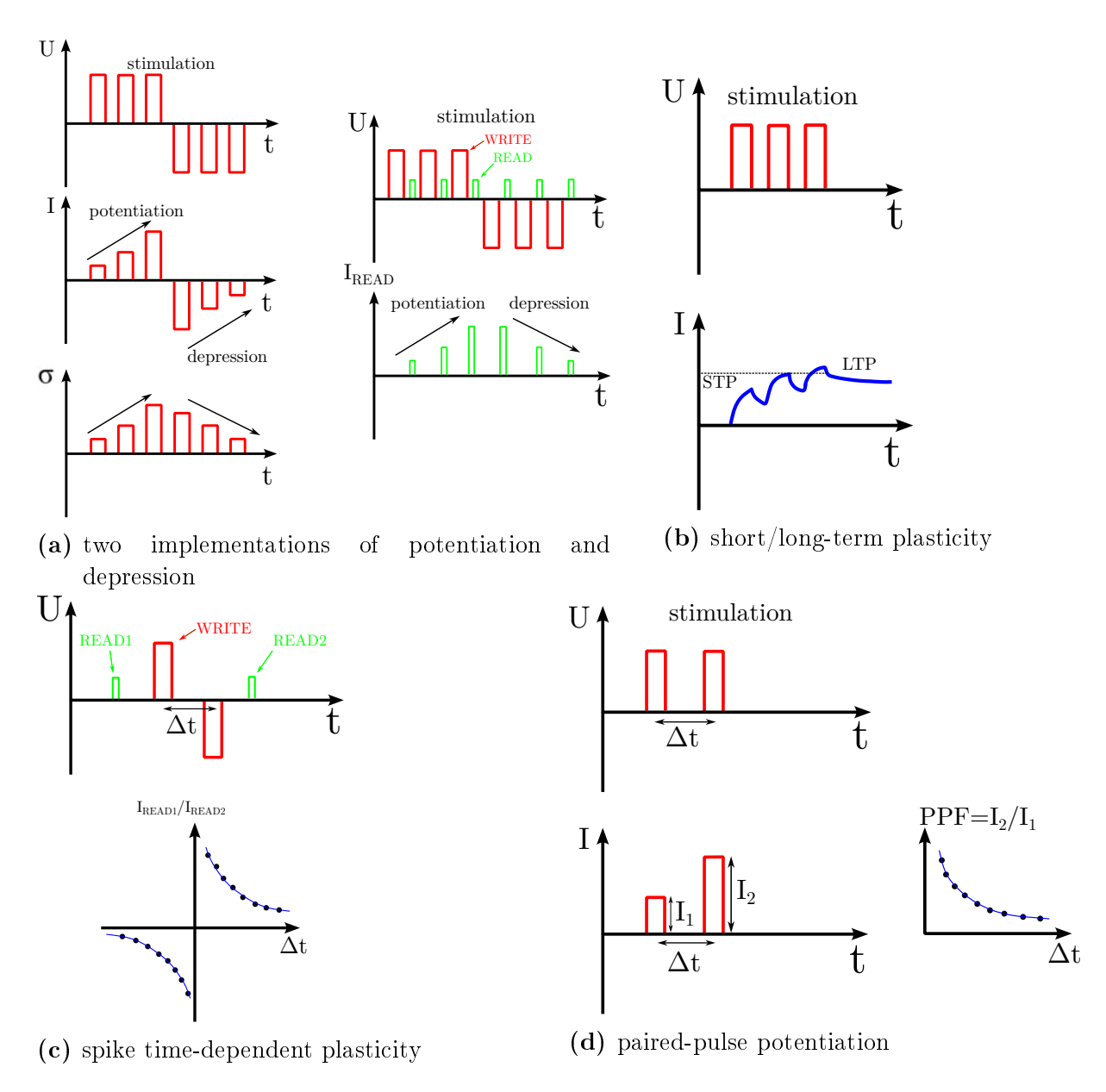


Figure 3.3.1: Various methods of neuromorphic behaviour implementation and testing.

should be linear in a function of the number of pulses. The amplitude of the excitatory pulses ought to remain constant; however, it should be noted that certain studies have employed a gradually increasing pulse amplitude (a method that, in essence, introduces an artificial factor into the results). The synaptic strength readout can also be performed via the "read" pulses with a lower voltage. The presence of potentiation and depression in the device is crucial for any application to

neuromorphic computations – both the gradual SET and gradual RESET processes are required for proper operation. When using light for stimulation, one may find that mechanisms that allow for applying SET and RESET pulses through different wavelengths are a most advantageous development [83].

In general, in this learning method weight change can be simply defined as the current impulses, amplitude ratio; thus the synaptic weight is represented by the conductivity (resistivity) change of the device.

2. Paired-pulse facilitation (PPF), and depression (PPD) – as explained in the chapter 2.2, here, we measure how the postsynaptic response strengthens or weakens after two consecutive stimulations in rapid succession. The increase in the amplitude of the second pulse  $(I_2)$  relative to the first  $(I_1)$  is a measure of facilitation:

PPF 
$$[\%] = \frac{I_2}{I_1} \cdot 100\%$$
 (3.3.1)

The decay of PPF in function of time delay between pulses can be fitted by, e.g., a double-exponential or stretched exponential (KWW) function, and its kinetics are strictly dependent on the mechanism governing the PPF: in biology, it is the neurotransmitter concentration; in memristive devices – the time dependency of the state function y(t) governing the device's resistance [60].

3. Spike time-dependent plasticity (STDP) is a fundamental learning rule in which the synaptic weight change depends on the timing between the firing of the presynaptic (t<sub>pre</sub>) and postsynaptic (t<sub>post</sub>) neurons. It is an extension of the so-called Hebb's rule: "neurons that fire together wire together" [8]. STDP can be realised by carefully designing the electrical pulse waveform. Most STDP demonstrations in memristors rely on overlapping pulses, where information about the pulse timing (Δt) is converted to the waveform of the effective programming pulses that induce a conductance change. However, a closer to reality – bio-realistic implementation of STDP without pulse overlap is possible in some memristive devices [60]. In practice,

for a two-terminal device, a postsynaptic impulse can be applied as an impulse with a negative voltage amplitude, relative to the fixed ground. A weight change can be modelled by two exponential functions [89]:

$$w = \begin{cases} I_{+} \exp(-\Delta t/\tau_{+}) & \text{if } \Delta t \ge 0\\ -I_{-} \exp(-\Delta t/\tau_{-}) & \text{if } \Delta t \le 0 \end{cases}$$
(3.3.2)

where  $\Delta t = t_{post} - t_{pre}$ ;  $I_{+}$  and  $I_{-}$  are constants that scale the potentiation and depression strengths, and  $\tau_{+}$ ,  $\tau_{-}$  are time constants.

4. Short/long-term plasticity (STP, LTP), which represent temporal changes in synaptic strength, that are elicited by repetitive activity. The intensity and duration of the stimuli influence the rate at which these changes decay. Here, the subject of inquiry is the time decay itself – a relaxation of the current/conductivity of the synaptic device that can be fitted by the double-exponential or KWW function, similar to the case of PPF. In the double-exponential function:

$$I(t) = \xi_{STP} \exp\left(-\frac{t}{\tau_{STP}}\right) + \xi_{LTP} \exp\left(-\frac{t}{\tau_{LTP}}\right)$$
(3.3.3)

The two time constants have specific interpretations as the constants related specifically to short-term and long-term memory [182]. The measurement can be performed by acquiring the quiescent current over time, or by applying the "read" pulses over time.

While this foregoing outline does not exhaust the subject, it provides a sufficient grasp of the matter and introduces the general idea behind such experiments. A more comprehensive account can be found in the literature [10,60,89,180,182,183].

### 3.3.2 The memristor test

In order to experimentally determine whether a given device is an ideal memristor or not (vide discussion in chapter 2.1), Di Ventra and Pershin have developed a simple and unambiguous test [48]. Its purpose is to verify if a device satisfies the definition of an ideal memristor, i.e. its state is defined by only charge (vide equations (2.1.4)).

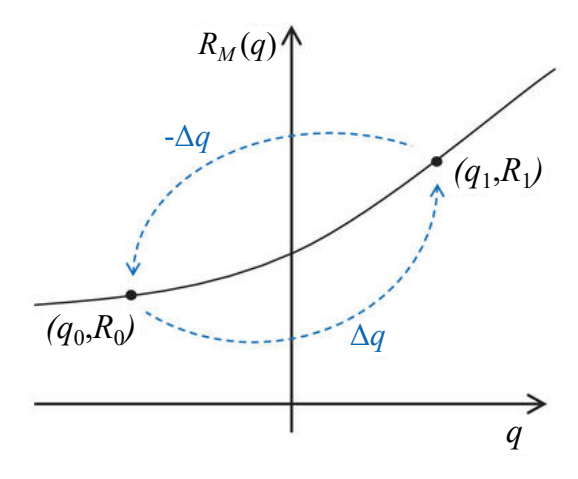


Figure 3.3.2: An example of memristor resistance change upon charge.

Source: Pershin and Di Ventra [48].

The test goes as follows: consider an ideal memristor, which at the initial moment of time  $t_0$  is characterised by charge  $q_0$ , thus  $R_0 = R_M(q_0)$ . By passing (the same amount of) current back and forth through the memristor, we first add a charge  $\Delta q$ , thus  $q_1 = q_0 + \Delta q$ , and then, by passing the same amount of charge in the other direction  $(-\Delta q)$ , we return to  $q_0$ . Therefore, the device's resistance should return to its initial value. Such an experiment can be performed practically by realising the circuit in Figure 3.3.3. Since the charge flowing through the device under test accumulates on the capacitor C, by charging and discharging the series connection of the capacitor and the device under test by switching the voltage U, we can directly implement the aforementioned process – the capacitor serves here as a charge-tracking device. If the tested device is an ideal memristor, its final resistance should always equal its initial value. This test should be performed for a large set of initial states of the memristor and for a large set of stimulation waveforms to ensure a broad spectrum of q(t) time traces. A single negative result is sufficient to infer that

the tested device is not an ideal memristor.

For better comprehending the idea behind the test, one can consider that most electronic components are trivial cases, for which  $R_M(q) = const$ . Such devices will always pass the test because their state does not depend on the passed charge (and such devices do not have resistance memory). Devices with nonlinear resistance, such as diodes, are also trivial, because here  $\frac{\partial R}{\partial U} \neq 0$ , but still  $\frac{\partial R}{\partial q} = 0$ .

As is quite obvious, testing the state of the supposed memristor before and after the trial still comes down to measuring the IV characteristic, which also leads to charge flow; however, if the device fails the test, an identical measurement will give different IV characteristics, as they do not start from the same initial conditions, i.e.  $q_{final} \neq q_0$ .

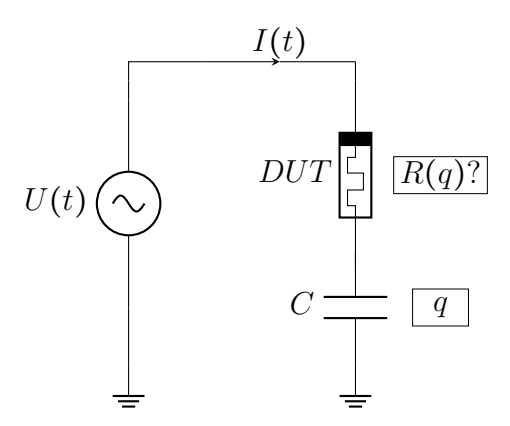


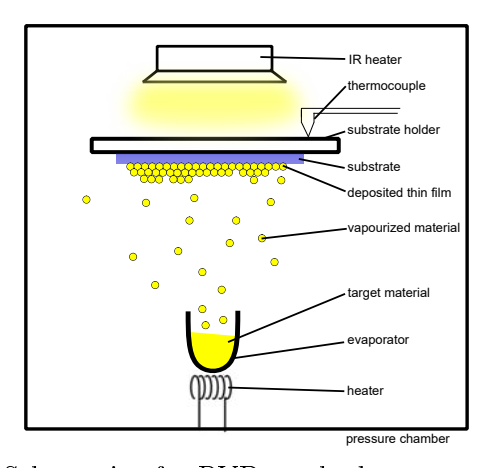
Figure 3.3.3: Schematic of the memristor test circuit.

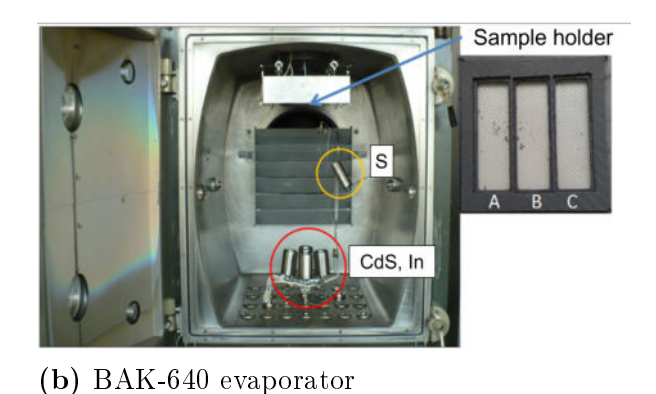
The test has been performed on the Cu-SiO<sub>2</sub> memristive devices fabricated by the authors, and on the commercially available electrochemical metallisation cells [184]; as well as on supposed "Φ-Memristor" (vide chapter 2.1) [185]. None of the devices tested passed the test. No device has been shown to pass the test so far.

## 3.4 Thin-film deposition

During the fabrication of neuromorphic devices, the growth of CdIn<sub>2</sub>S<sub>4</sub> spinel thin-films, which are the core, active layer of the devices, was of primary importance. The polycrystalline CdIn<sub>2</sub>S<sub>4</sub> layers were produced using the vacuum thermal evaporation technique. Here, we will briefly present the basics of this method, which will be a foothold for our further inquiries.

Vacuum evaporation (vacuum deposition) is a physical vacuum deposition process in which the target material is thermally vaporised, and the vaporised atoms (molecules) are deposited on a substrate *physically*, i.e. without any furtherance of the carrier agent or chemical process. The deposited material transits from a condensed phase to a vapour phase and then back to a thin film condensed phase [186]. The deposited compound can be poly- or monocrystalline, and bounds to the substrate due to adhesion. Crystallinity of the deposited film depends on multiple factors, particularly substrate type and temperature. A simplified scheme of a thermal evaporator is shown in Fig. 3.4.1a.





(a) Schematic of a PVD method

Figure 3.4.1: Thermal evaporation method.

The vacuum inside the evaporation chamber should usually be kept better than 10<sup>-</sup>4Torr in order to obtain a long mean free path between collisions.

Thermal evaporation requires a relatively high volume of the source material to be

heated. The resistive heater is a commonly used heating source for a target material<sup>14</sup>. For heating the substrates, an infrared heater coupled with a thermocouple is used.

One of the factors limiting the evaporation rate is the vapour pressure of the material; the free surface vapourisation rate in terms of the vapour pressure relation is given by a Hertz-Knudsen equation [186]. An atomic flux, i.e. the rate of incoming evaporated atoms for the deposition, is controlled by the temperature of the target material. The flux and the thickness of the film being grown are monitored using a quartz crystal micro-balance<sup>15</sup>.

For low vapourisation rates, the material from a point source deposits on a surface with a spatial distribution given by a cosine deposition distribution. Therefore, the fluxes will be also determined by the geometry of the evaporation chamber – different substrate positioning relative to point evaporation sources may result in spatial fluctuations of the resulting stoichiometry. Thusly, a thin film placed closer to, e.g., an indium source, will likely have higher indium content than the thin films placed further away. The same applies to the thickness of the deposited layers. The evaporator being used by us has three evenly spaced slots for target samples, enabling deposition on multiple substrates.

The growth of CdIn<sub>2</sub>S<sub>4</sub> thin films analysed in this dissertation was done in collaboration with the MIOPS group at the Institut des matériaux de Nantes Jean Rouxel (IMN) in Nantes, using the BAK-640 evaporator (Fig. 3.4.1b), on soda lime glass slides, coated with different substrate materials. A co-evaporation was performed using the CdS, In and S sources. The atomic flux ratio of In and CdS was set to achieve desired In/Cd ratio, and the sulphur flux was set to be in excess. The fluxes of CdS and In were set to achieve the desired composition.

The resultant In/Cd atomic ratio was determined by Energy Dispersive X-Ray Spectroscopy (EDX) using a SEM (JEOL JSM 5800LV) equipped with a SAMx SDD energy dispersive spectrometer.

<sup>&</sup>lt;sup>14</sup>The other types of heating sources are inductive RF heating or electron beam. In particular, the e-beam evaporation allows the deposition of materials with a high melting point, such as many metals.

<sup>&</sup>lt;sup>15</sup>which is a commonly used technique.

# Chapter 4

# Introduction to the $CdIn_2S_4$

The following chapter will cover selected pieces of existing literature, and present essential parts of current state of knowledge about  $CdIn_2S_4$ . The review will serve as a starting point for further researching the compound and ultimately developing its application in neuromorphic devices.

### 4.1 Introduction

CdIn<sub>2</sub>S<sub>4</sub>, cadmoindite, cadmium-indium sulphide is an n-type semiconductor with the spinel structure. The compound was extensively researched in the past, mainly from the 1960s to the late 1980s. A large data set was obtained during that period, mostly regarding its optical properties. Soon after, the compound was forgotten for at least 20 years. Then, it regained its interest in photocatalysis as a *novel* compound with promising perspectives [187, 188]. Since then, photocatalytic applications became the main field where the CdIn<sub>2</sub>S<sub>4</sub> is researched [189–201].

Less known but equally important was the impact in the research of CIGS-based thin-film solar cells, having CdIn<sub>2</sub>S<sub>4</sub> as a new, alternative buffer layer replacind the CdS. This approach, researched by the gruop in the Nantes University, enabled obtaining 16.2% efficiency solar cells comparable to standard CdS-based devices using the full-PVD method [21]. An extensive investigation by the nantaise group provided a detailed view of the

influence of  $CdIn_2S_4$  on thin film solar cell performance [202]. Later on, different attempts to incorporate  $CdIn_2S_4$  into solar cells has also been made [203, 204].

However, most importantly for us, there is evidence of some mechanisms within the  $CdIn_2S_4$  that result in the hysteretic behaviour, namely: temperature-resistivity hysteresis observed in  $CdIn_2S_4$  thin films grown in various conditions [24], and classical electrical, memristive pinched hysteresis loop observed in  $CdIn_2S_4$  single crystals [205]. Moreover, this material is suspected of having metastable defects [22]. Those reports and the findings of the nantaise group were an impetus for us to start researching the compound.

### 4.2 Literature review

### 4.2.1 Structural properties

 $CdIn_2S_4$  has a spinel structure formed around a sulphur frame. The sulphur atoms forms tetrahedrals and octahedrals. Inside those, Cd and In cations are located. The spinel space group is  $Fd\bar{3}m$  (227), and the lattice constant is 10.8Å [206].

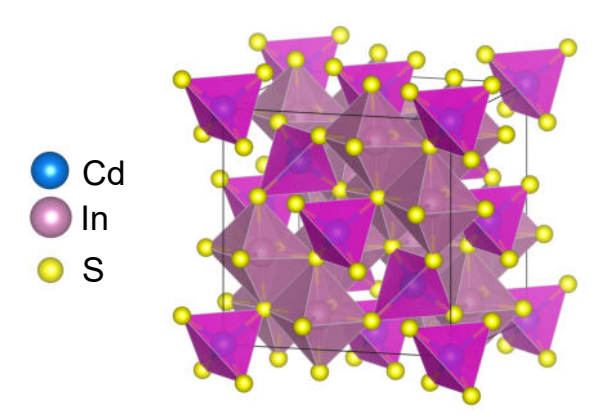


Figure 4.2.1: Visualization of the CdIn<sub>2</sub>S<sub>4</sub> crystal structure.

In a so-called normal spinel structure, all of the Cd cations are located in tetrahedral sites, and the In cations are located in octahedral sites. The deviation from this occupancy is called inversion: In a fully inverted spinel structure, the cations are swapped between

tetrahedral and octahedral sites. A range of partial inversion is possible between those two cases, where only some minor fraction cation pairs exchange their places. In general, one can write the formula:

$$Cd_{1-x}In_x[In_{2-x}Cd_x]S_4$$

where brackets [] represents octahedral sites. x is an inversion degree parameter. x = 0 represents normal spinel and x = 1 – fully inverted spinel.

Investigating the degree of inversion (in other words, the occupation of the cationic sublattice) is not an easy task. Standard diffraction methods will not allow the reveal of the cation occupancies because Cd and In are isoelectronic [207]. However, more sophisticated techniques could be adopted to answer the question [208, 209].

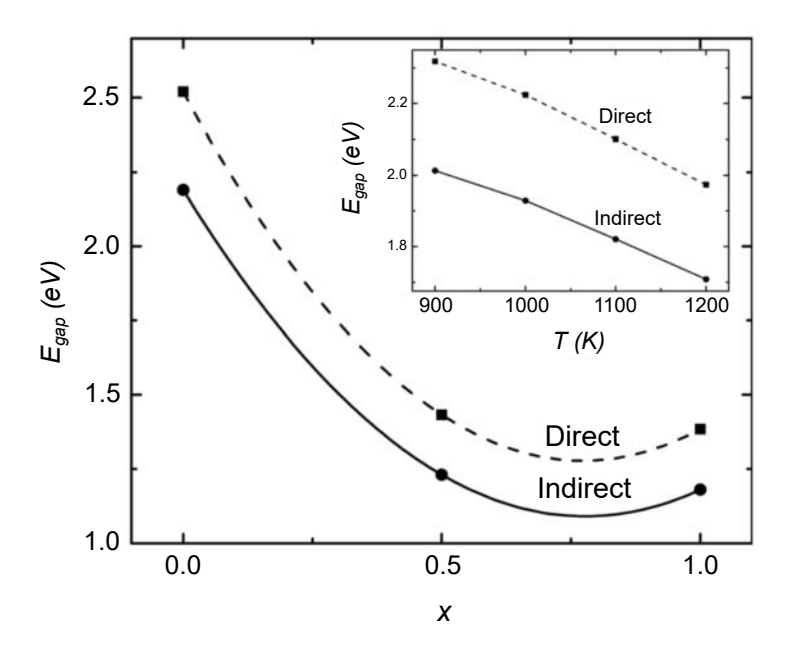


**Figure 4.2.2:** Direct and indirect bandgap as a function of inversion degree in  $CdIn_2S_4$ . Inset: bandgaps as a function of the configurational equilibrium temperature.

Source: Seminóvski et al. [207].

The inversion of the cation sublattice is associated with the existence of the second-order phase transition at 403K ( $\sim$ 130°C), found by Czaja [210] by measuring the specific heat of the CdIn<sub>2</sub>S<sub>4</sub>. Czaja, inferring from general symmetry considerations about crystals with the spinel structure [211], concluded that at 403K an order-disorder

transition of the cationic sublattice takes place. Specifically, above 403K, the Cd and In atoms become distributed randomly over tetrahedral sites.

The CdIn<sub>2</sub>S<sub>4</sub> bandgap falls in the visible band. The literature is, however, not unanimous about its value. For an indirect transition, the value at 300K varies from 2.22eV [212–214] to 2.35eV [204], and for a direct bandgap (300K) from 2.62eV [26] to 2.7eV [215]. Importantly, the difference between a direct and an indirect transition is slight and is, on average, 200meV. Moreover, the bandgap value seems to depend on the synthesis process. It has also been found that the minimum of the conduction band is located at  $\vec{k} = 0$  [216]. Therefore, the indirect transitions originate from dispersion in the valence band (predicted also by Péan et al. [22]). A significant finding regarding the bandgap value was the simulation made by Seminóvski et al. using screened hybrid functional calculations, which show that spinel inversion affects the CdIn<sub>2</sub>S<sub>4</sub> bandgap [207]. Fig. 4.2.2 shows the simulations obtained by Seminóvski. The significance of this result will be shown in the next chapter.

The  $CdIn_2S_4$  can be grown using various techniques. Throughout time, the most popular techniques used were: the iodine transport method [25, 26, 217–221], and the Bridgeman method [214, 222], but also spray pyrolysis [223], or PVD can be used.

By manipulating synthesis parameters (e.g. reagents ratio), the stoichiometry of the compound can be varied, especially in a manner of the transition from  $CdIn_2S_4$  to  $In_2S_3$ . The nantaise group has been studying the  $CdIn_2S_4 \rightarrow Cd_{1-x}In_{2+\frac{2x}{3}}S_4$  system: cationic vacancies in  $In_2S_2$  are ordered and located preferably on one of two tetrahedral sites along one of the cubic axes. The long-range ordering is a source of cubic-to-tetragonal distortion – at stoichiometries close to  $In_2S_3$  another phase is being formed having tetragonal space group  $I4_1/amd$  [224].

Lastly, the electron affinity of the  $CdIn_2S_4$  was found to be ~3.5eV by photoelectrochemical measurement [225] and predicted by DFT calculations [226].

### 4.2.2 Photoluminescence

Photoluminescence is undoubtedly the most studied aspect of CdIn<sub>2</sub>S<sub>4</sub> from the pre-photocatalytic era. The first known photoluminescence research paper dates back to 1963 (Springford et al. [227]). It shows two emission bands, 1.42 and 1.65eV, and attributes their origin to the cationic sublattice. Thermoluminescence was also measured. It consist of a broad band centered at 110K. The glow curve was found to be assiociated with a distribution of trapping levels.

Next, W. Czaja and L. Krausbauer examined CdIn<sub>2</sub>S<sub>4</sub> single crystals, and in addition to the previous two energies, they found a third emission band at 1.31eV [214]. They proposed that the short-wavelength (1.65eV) emission was associated with Cd<sub>In</sub>, and 1.31eV with In<sub>Cd</sub>. This assumption is based on PL measurements (relative intensities, peak wavelengths) of CdIn<sub>2</sub>S<sub>4</sub> and In<sub>2</sub>S<sub>4</sub> mixed crystals. Concerning the structure of the centres, they presumed that only those Cd ions at octahedral sites and those In ions at tetrahedral sites take part in the luminescence emission. Those defects can form a complex with sulphur vacancies next to the respective cations. This sulphur vacancy concentration is then the controlling factor for the luminescence intensity. These authors also stated that PL spectra did not reflect the concentration of antisitial defects but were rather related to the partial inversion of the spinel lattice. Those are considered an *intrinsic property* of the material. Later on, experiments of W.K. Unger and H. Meuth solidified these findings [228].

The work of E. Grilli & M. Guzzi from 1980 [217] is perhaps the most influential work regarding optical and optoelectronic measurements, contemporaneously contradicting or extending previous findings, and bringing more unified understanding of CdIn<sub>2</sub>S<sub>4</sub> PL data. Combining single crystal measurement results with various stoichiometry and excitation energies with photoconductivity measurements, the researchers deduced a band diagram which practically constitutes the current state of knowledge. Authors also introduced the idea of post-deposition treatment, in this case quenching. More importantly, they investigated the temperature dependence of luminescence, pointing to a temperature of

160K at which an essential change in recombination occurs. They found another emission peak at 1.8eV and observed three different excitation maxima at 2.2eV, 2.35eV, and 2.65eV. They also postulated that the  $In_{Cd}$  defects form a quasi-continuous distribution of states below CB (T states). Lastly, the authors postulated the double energy-like behaviour of the E ( $Cd_{In}$ ) acceptor level, which became the revealed truth for most of the future papers. Moreover, this is the group, who gave rise to the denomination of defect states that became used throughout future work, including this dissertation.

H. Nakanishi, H. Miyashita, S. Endo, and T. Irie's work was the first known attempt to wrap up the known PL literature (fig. 4.2.3). They proposed slightly different interpretations of the observed spectra and gave different energy of the acceptor level E. The authors also pointed out that fast-cooled crystals are rather completely disordered.

Table I. Comparison of peak energies of photoluminescence in  $CdIn_2S_4$  obtained by various workers at liquid  $N_2$  temperature. ( $\bigcirc$  observed,  $\times$ unobserved)

P.L. BANDS	PRESENT PAPER	CZAJA and KRAUSBAUER	UNGER et al.	RADAUTSAN	GRILL1 et al.
1.80 eV (689 nm)	0	×	0	×	0
1.60 eV (775 nm)	0	0	0	0	0
1.45 eV (855 nm)	0	×	×	0	×
1.35 eV (920 nm)	0	0	×	×	×

**Figure 4.2.3:** Comparison of peak energies of photoluminescence in CdIn<sub>2</sub>S<sub>4</sub> obtained by various researchers at LNT.

**Source:** H. Nakanishi et al. 1981 [229] ( $\circ$  – observed,  $\times$  – not observed).

The work of A.N. Georgobiani and A.N. Gruzintsev [26, 218] solidified contemporary knowledge. The process of post-deposition treatment (annealing) of the CdIn<sub>2</sub>S<sub>4</sub> was also explored, which causes i.e. cadmium evaporation and creates a high amount of antisite cation defects. Moreover, a different interpretation of emission spectra was presented.

O.V. Kulikova and L.L. Kulyuk's paper (1988) [219] further explores the effects of

PDT (annealing) in a vacuum and sulphur atmosphere. Annealing at temperature 320°C increases the intensity of observed photoluminescence peaks. When the sample is quenched from above >130°C, sulphur evaporates, and the intensity of the whole PL spectrum increases. Further re-annealing restores the spectrum to its initial appearance. The authors propose, however, a completely different interpretation of emission spectra.

Lastly, a paper of Charlebois and Fortin explores a curious case of optical gain observed in  $CdIn_2S_4$  [25]: It is possible to achieve optical gain on defect states within the bandgap by utilising particular excitation and recombination paths between defect states and the conduction band. According to the authors, the E states also have quasi-continuous energy distribution, similar to T states.

Figure 4.3.1 summarizes band diagrams from the presented papers. The extracted information on the location of individual defect states and the data obtained from photoconductivity measurements were consolidated into Fig. 4.3.2.

# 4.2.3 Photoconductivity

Photoconductivity measurements were usually performed together with PL experiments and completed the aforementioned overall picture of defects [26,218,229,230]. Besides band to band transitions, the authors have identified 1.45eV, 2.2eV and 2.35eV excitation peaks that give rise to photoconductivity due to electron transitions from localized levels to the CB. I.A. Damaskin and S.L. Pyshkin have observed multi-photon absorption under monochromatic 1.17eV excitation, which was visible as the superlinear Lux-Ampere dependence [231].

The Lux-Ampere measurement was also used to examine the sub-bandgap quasi-continuous density of T states originating from  $In_{Cd}$  antisites in the work of Anedda et al. [232]. S. Charbonneau, E. Fortin and A. Anedda have calculated the density of E states by measuring the saturation of the PC signal from the excitation from E states into the conduction band. Lastly, a curious case was found by Takizawa et al., who discovered a strong time, intensity, and measuring sequence dependence of the photoconductivity spectra [233]. This case will be revisited later on.

## 4.2.4 Conductivity and electrical properties

The room temperature resistivity values of  $CdIn_2S_4$  single crystals vary between  $10^3\Omega cm$  to  $10^{10}\Omega cm$  depending on the In/Cd ratio [26] and the deposition method. Resistivity values within this range were reported by many researchers [214, 220–222].

Endo et al. have examined transport properties of  $CdIn_2S_4$  single crystals with various compositions (stoichiometries) [222]. From an analysis of the mobility, they found that the high resistivity of the compound is due to compensation of donors by acceptors introduced by excess sulphur. Several compound properties, the carrier scattering mechanisms as well as effects of PDT were determined. The mobility value for  $CdIn_2S_4$  single crystals was found to be in the range of  $10 \div 100$  cm<sup>2</sup>/Vs depending on stoichiometry. The density-of-states effective mass of the conduction band was estimated to be  $0.19m_e$ .

A Lux-Ampere experiment has been performed by Anneda et al. on  $\mathrm{CdIn}_2\mathrm{S}_4$ , in which the T states distribution was closely investigated in the frame of the electron traps model of states [232] (the model is described in more detail in chapter 3.2.3). Anedda determined the trap density of the distribution ( $\approx 10^{20}~\mathrm{cm}^{-3}$ ) and concluded some essential details regarding the cationic sublattice in  $\mathrm{CdIn}_2\mathrm{S}_4$ . Serpi et al. have performed a photoinduced current transient spectroscopy experiment (PICTS) on the compound [234]. According to Seki's interpretation, the observed current decay was non-exponential due to a non-linear multiple-channel recombination mechanism. The T states act as relay centers for the radiative recombination of electrons. They also evidenced an electron trap 0.6eV below CB. Seki reports the existence of memory effects related to the charge transfer processes.

# 4.2.5 Complex defects

One of the most crucial, if not the most important, pieces of information regarding the defects in the  $CdIn_2S_4$  from our point of view, was provided by Péan et al [22]. The aforementioned case of possible buffer substitution for the photovoltaic devices drove their research, and part of their work was the ab initio DFT calculations that resulted in the predictions about the nature of the defects in  $CdIn_2S_4$ . Among the rousing results (i.e.

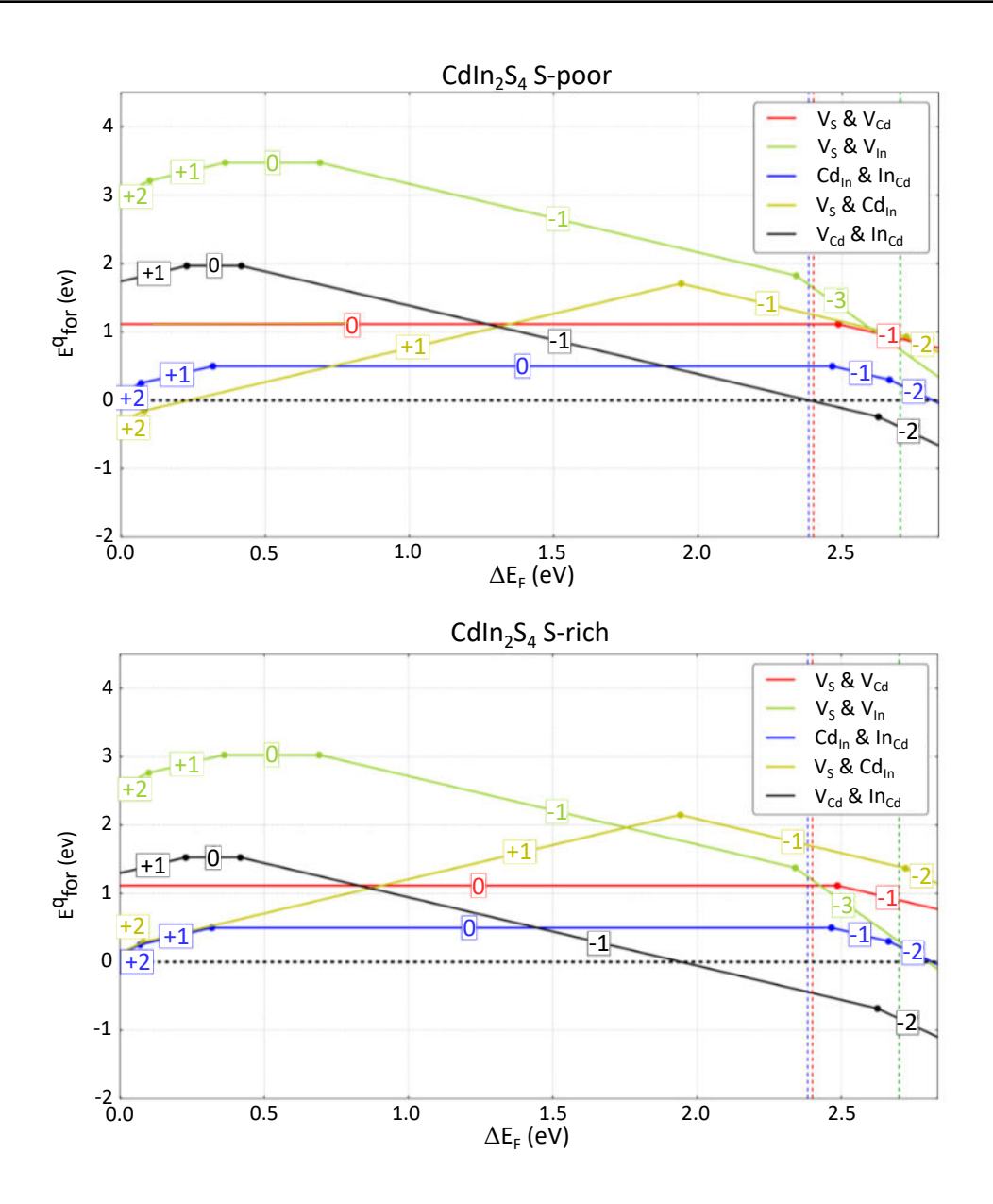


Figure 4.2.4: Defect formation energy of complex defects vs Fermi level in CdIn<sub>2</sub>S<sub>4</sub> prepared in S-poor and S-rich conditions.

Source: Péan et al. [22].

limits of dopability and defect concentrations), the conjectures about defect formation energy of complex defects (presented in Fig. 4.2.4)<sup>1</sup> have the greatest concern. Among the multiple possible complexes, the most probable are:  $V_{S}-V_{Cd}$ ,  $V_{S}-V_{In}$ ,  $Cd_{In}-In_{Cd}$ ,  $V_{S}-Cd_{In}$ , and  $V_{Cd}-In_{Cd}$ . Some of the defects posses negative correlation energy, in particular:  $V_{S}-V_{In}$ ,

<sup>&</sup>lt;sup>1</sup>It has to be noted that complex defects will have different properties than the forming defects alone.

and  $V_s$ -Cd<sub>In</sub>. Besides the formation energies, a piece of vital information for us is the threshold energy ( $E_{TR}$ ) of particular defects or defect complexes and the possible charge states, especially for those having negative U behaviour. It is important to note that the material owes its metastability to native defects. Moreover, as stated before, it is due to these effects that we link our expectations regarding the construction of our neuromorphic devices.

## 4.2.6 Memory effects

Last but not least, there are some instances where multifarious memory phenomena were observed and those should acquire proper recognition: Tarricone et al. observed photomemory effects in Zn<sub>x</sub>Cd<sub>1-x</sub>In<sub>2</sub>S<sub>4</sub>. Seki, Ueno, Endo and Irie al. have observed several memory-related phenomena in CdIn<sub>2</sub>S<sub>4</sub> single crystals: a pinched hysteresis loop driven by hard (filamentary-like) switching [205] (Fig. 4.2.5); low frequency self-sustained photocurrent oscillations at high electric fields [23], negative dynamic resistance [235], and the temperature-resistance hysteresis [24]. The last report is particularly curious, where the authors seem to completely miss the temperature evolution of nonlinear current-voltage characteristics and interpret them as an absolute change of (linear) resistance.

The cases presented above are exotic examples of more intricate electrical properties occurring in the CdIn<sub>2</sub>S<sub>4</sub> compound. Noticeably, those are observed in pure CdIn<sub>2</sub>S<sub>4</sub> single crystals or thin films only, i.e., no additional elements are necessary (besides contacts) to complete an electronic device exhibiting such behaviour. Moreover, the phenomena could be driven by defects-related optoelectronic mechanisms – an approach that is never, or rarely, utilised to implement neuromorphic or memristive behaviour.

Therefore, those reports, especially the pinched hysteresis loop presented in Fig. 4.2.5, were the first indications for investigating the properties of  $CdIn_2S_4$  as a memristive compound.

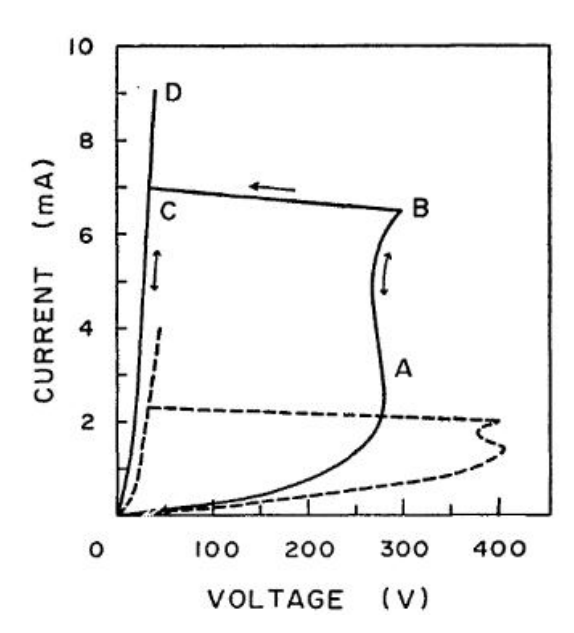


Figure 4.2.5: IV characteristics of CdIn<sub>2</sub>S<sub>4</sub> single crystals reported by Ueno et al. Source: Ueno et al. [205]. Continuous and dotted lines represent two different samples.

# 4.3 Wrapping up the literature

Collecting the literature presented vide supra into a single whole generates a reasonably coherent picture of the compound. The growth methods, structural properties, bandgap, optical and basic electronic properties are generally known material features. It may even seem that all the puzzles related to this material have been solved or only require bringing together all the known results into one whole. Moreover, the compound found its niche in photocatalysis, where it was further explored.

However, as one will see, the final picture is not enough to interpret the results of our experiments, which are going to be presented in the next chapter. Moreover, some open questions remain. Many of them are necessary for the application of the material in neuromorphic devices. Here, we will summarize the knowledge through the prism of optoelectronic transitions and the band diagram:

In Fig. 4.3.1, we collected the band diagrams proposed by various researchers. One can observe how the interpretation evolves throughout time. By synthesising the above

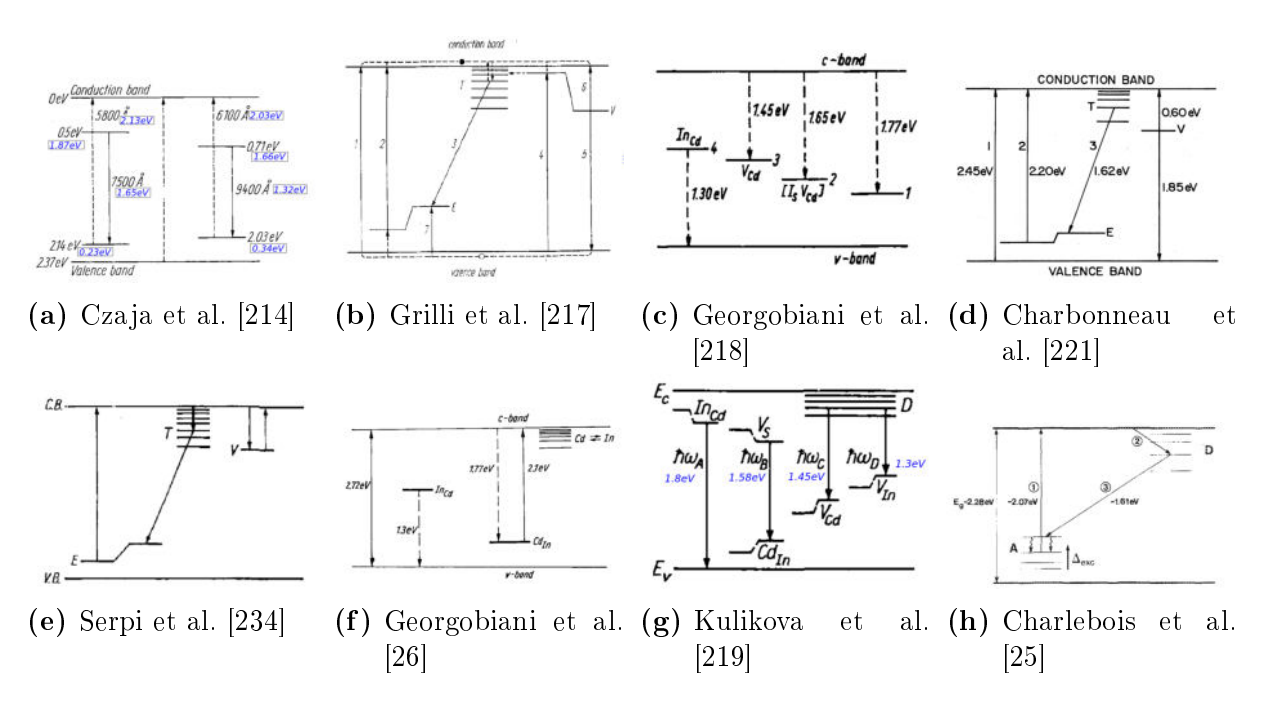


**Figure 4.3.1:** Various band diagrams from the literature. Some of the elements agree with each other, some do not. It is not trivial to reconcile the different results in order to create a coherent model.

images and the authors' interpretation into one whole, we can draw a diagram, shown in Fig 4.3.2. The data about defect levels and transition energies originates mainly from the PL and PC experiments described earlier in this chapter. We distinguish four defect states that contribute the most to the optoelectronic landscape: The shallow donors T – the aforementioned exponential distribution of trapping states below the CB originate from  $In_{Cd}$  antisite defects. Similarly, shallow acceptor E take its origin from  $Cd_{In}$  antisites. The T and E defects are agreeably considered to originate from spinel inversion and were extensively researched [217, 232, 234]. We depicted the E state as a double-level after Grilli et al., who actually did not provide a clear justification for this depiction, though. However, it was blindly reproduced in future papers. The E states could rather also be a distribution of states similar to T, which would maintain some sort of symmetry between T and E as they originate from the same source (E was also considered as the distribution by Charlebois et al. [25]). The shallow donor marked as V is attributed to sulphur vacancy. The double-level depiction of the V state again originates from Grilli et

al. [217], who observed a Stokes shift upon excitation<sup>2</sup> from 2.35eV. Lastly, the level at the 1.45eV, and responsible for the 1.45eV emission band, depicted simply as  $V_{Cd}$  most possibly come from cadmium vacancy and recurs in some papers [229]. We did not draw the level that gives rise to the 1.3eV peak observed throughout the literature because its origin is somewhat unclear.

Electrons from valence band can be excited to V with 2.3eV energy and then recombine by emitting 1.8eV photon or tunnel into T states (and therefore, there are two competing recombination paths for 2.3eV excitation, and possibly any other). Grilli et al. observed a correlation between 2.3eV excitation and 1.6eV and 1.8eV emission peaks – hence, he deduced that there is some communication between those. Tunnelling from T into V (the other way) is also possible. A 2.2eV excitation from E states into the CB can occur<sup>3</sup> – Charbonneau et al. have measured the density of E states using this line. Moreover, the excited electrons from E can recombine through T states back to the E (1.6eV emission), closing the path. This closed loop was reported by Grilli et al. and Charlebois et al. [25], who observed optical gain on those defects. The 2.2eV peak was usually possible to be observed distinctly form the band-band excitation being very close to this transition [218, 221, 230, 232]. The value of 0.25eV (E states above VB) has its source in 1.6eV peak quenching observed by Grilli et al., but similar energies were observed elsewhere (i.e. Nakanishi et al. [229]). Similarly, Grilli et al. observed 0.6eV quenching of 1.8eV peak.

The diagram in Figure 4.3.2 summarises the described transitions. This diagram is, in our opinion, the best synthesis attempt based on literature reports, which optimally collects all elements of the optoelectronic landscape of the  $CdIn_2S_4$ . The vast majority of relatively new works are attached to a fragment of this image. Based on this diagram, we will build our  $CdIn_2S_4$  model (and as we will see in the next chapter, we will find evidence for it being a valid starting point). The diagram will be revisited in the summary of the next chapter, along with the discussion of the formulated  $CdIn_2S_4$  model.

<sup>&</sup>lt;sup>2</sup>Curiously, this excitation energy is smaller than the bandgap value reported by some researchers. Grilli et al. report bandgap values in their monocrystals to be 2.65eV, so this excitation could be intraband indeed (or perhaps indirect transition). However, the converse is more interesting: have other researchers not confused the ~2.3eV excitation to the sulphur vacancy with the band-to-band transition?

 $<sup>^3</sup>$ This could be the same case as with the aforementioned  $\sim 2.3 \text{eV}$  transition.

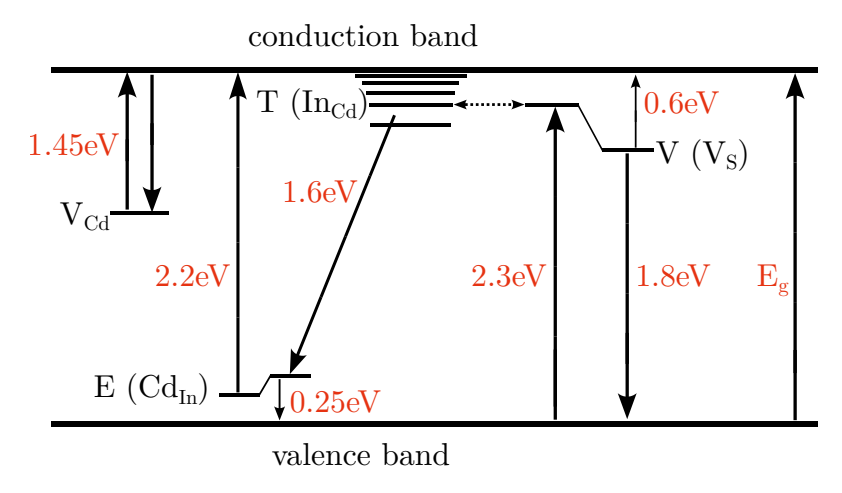


**Figure 4.3.2:** Band diagram created from existing literature on  $CdIn_2S_4$ .

It is self-evident that the spinel inversion governs most of the optoelectronic landscape. We also know general details about growth and effects induced by annealing in vacuum or in sulphur. However, it is unclear how exactly growth parameters or post-deposition treatment relate to spinel inversion and to each other. Why are the early works so different from the later ones? Moreover, it is unknown how to control growth using the PVD method, which was practically unused before. How to relate the literature data to polycrystalline samples? The researchers also do not explain the changes in dark conductivity upon various growth parameters and how they relate to the optoelectronic landscape. Where is the Fermi level?

There is also a case of the relation between Cd/In antisites, spinel inversion and the bandgap: its practical verification, and its implications (Results of Semivóvski et al. suggests, that most of the samples reported in literature have the direct spinel structure). The bandgap values reported by some researchers are smaller than the intraband transitions reported by Grilli et al. Moreover, when do antisite point defects (that result from the disturbance of periodicity) become structural inversion?

Next, the question of the influence of metastable defects predicted by the nantaise group on the outlined energy landscape is also unknown. Do they affect CdIn<sub>2</sub>S<sub>4</sub> optoelectronic properties, and how? We do not know detailed parameters of those defects.

#### 4.3. Wrapping up the literature

Lastly, how can we include the interpretation of observed switching mechanism to the optoelectronic model?

We must extend the model to memory effects and answer some of those questions if we want to use  $CdIn_2S_4$  in neuromorphic devices. In particular, we need to predict how changing the charge state of metastable defects will affect the properties of the compound. Designing the AOC neuromorphic devices will further require us to answer whether and how can we affect the properties of this material using illumination? We will try to answer these questions in the next chapter.

# Chapter 5

# A Study in Spinel – investigation of the $\mathrm{CdIn}_2\mathrm{S}_4$

This chapter presents results of an investigation of the properties of the CdIn<sub>2</sub>S<sub>4</sub>, predominantly related to its intricate defect structure highlighted in the previous chapter. The experiments conducted focus mainly on the investigated compound's electronic and optoelectronic properties. It's paramount goal was to explain the phenomena related to metastable defects, namely persistent photoconductivity (PPC) and persistent photosensitivity (PPS) that will be revealed in this chapter, and eventually could become the core of desired neuromorphic devices. Most of the details about those memory behaviour was unknown at the beginning of the research. However, there was some evidence in the literature suggesting existence of such effects, and we had some clues where to look for them. The main suspect were the metastable defects predicted by Péan et al. [22]. It was then largely exploratory research for the reason, that much information, such as energy barriers of mentioned metastable defects, was simply unknown at the state of knowledge in the beginning of the enquiry. Therefore, a large range of parameters has to be scanned to collect necessary evidence<sup>1</sup>. A lot of details, crucial for the model was also found through the literature review, although some of it was incomplete or contradicted

<sup>&</sup>lt;sup>1</sup>For example, larger than necessary part of optical spectra was scanned, despite not containing any helpful information.

each other. Some of the results obtained by us expand the literature knowledge or show it in a broader picture. The following investigation is based on a set of thin films with different stoichiometry and after various post-deposition treatment. The choice of samples was partially driven by literature.

It has to be noted that experiments performed are considered to be rather simple. It is mainly a result of the fact that more sophisticated experiments require a more complicated model or precise assumptions, which, in this case, due to limited knowledge, were hard to fulfil or the experiments were simply impossible to conduct<sup>2</sup>. However, we do not exclude the possibility of conducting more detailed research based on our current knowledge. The obtained results, presented in subchapters, bring certain parts of information about  $CdIn_2S_4$  and contribute to a coherent body of knowledge, which we will call the model. The  $CdIn_2S_4$  model then enables us to interpret and explain most of the observed behaviour of the compound within a consistent frame of reference. Moreover, the model can further predict the unexplored properties of  $CdIn_2S_4$  to some extent, but most importantly, it will serve as a foundation to create  $CdIn_2S_4$ -based neuromorphic devices. The completion of the model required several experiments and the model could only be formed by taking a holistic view of all the measurements performed, which was probably the most challenging part of the presented research. The model is summarized in section 5.6.

In this chapter we will firstly examine the material-oriented measurement results and its interpretation. Later on, the CdIn<sub>2</sub>S<sub>4</sub> model will be unveiled and in the end, open questions will be discussed.

# 5.1 The object of study

From the literature review evaluated in the previous chapter, we possess fundamental information regarding CdIn<sub>2</sub>S<sub>4</sub>. At this stage, we posses basic knowledge about its crystal structure [208, 210, 211, 224, 230, 236], bandgap [207, 229], and defect states [22, 217]. It is widely understood that the primary source of the optical response is defects originating

<sup>&</sup>lt;sup>2</sup>Like, for example, CV measurements, that require rectifying junction.

from the cationic sublattice [26, 214, 229, 232] and sulphur vacancies [22, 26, 217]. The literature also demonstrates the influence of post-deposition treatment, i.e. annealing, on the material [26, 218, 237].

Facing this state of knowledge, we can then hypothesize, that potential desired neuromorphic properties will arise from metastable defects, particularly sulphur vacancies and their complexes [22]. Based on the presented evidence, an optimal set of samples can be selected, allowing us for performing set of measurements in order to obtain as much information as possible, and build the model.

A set of  $CdIn_2S_4$  thin films was fabricated and deposited onto soda-lime glass (SLG) in collaboration with the University of Nantes. Two series of layers were produced. The first consists of stoichiometric  $CdIn_2S_4$  material. The second series is a cadmium-poor material with twice-reduced cadmium content, namely  $CdIn_4S_8$  (or  $Cd_{\frac{1}{2}}In_2S_4$ ). The thin films were deposited using the co-evaporation method from CdS, In and S sources. The base pressure in the deposition chamber was  $10^{-6}$ mbar. The temperature of the substrates was  $400^{\circ}C$ . During 1h deposition, 350nm thin films were obtained. The substrates were slowly cooled after the deposition. After the deposition, stoichiometry was checked, and satisfactory results of S/(Cd+In) and Cd/In ratios were obtained at 1.35 and 0.5, respectively. XRD measurements were performed as well. All XRD reflexes followed  $CdIn_2S_4$  (00-27-0060) thiospinel, and no secondary phase was detected.

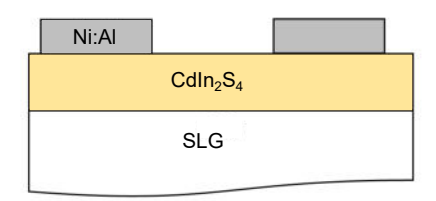
After the growth, films were divided into three groups. First group remained unchanged (as deposited). Second group was annealed in an evacuated tube (in vacuum) at 300°C for 72h. Third group was annealed under the same conditions, but in the sulphur atmosphere. After the annealing, samples were slowly cooled down to room temperature.

Finally, Ni:Al contacts were deposited using electron beam evaporation, allowing for electrical measurements in lateral manner. Picture of the samples is presented in (Fig. 5.1.1).

Herein, the abbreviations for the manufactured set of samples will be introduced. Those abbreviations will be consequently used throughout rest of this work, videlicet:

- C24-AS CdIn<sub>2</sub>S<sub>4</sub> sample, as grown, without any post-deposition treatment;
- C24-R CdIn<sub>2</sub>S<sub>4</sub> sample annealed in vacuum;
- C24-RS CdIn<sub>2</sub>S<sub>4</sub> sample annealed in sulphur atmosphere;
- C48-AS CdIn<sub>4</sub>S<sub>8</sub> sample, as grown, without any post-deposition treatment;
- C48-R CdIn<sub>4</sub>S<sub>8</sub> sample annealed in vacuum;
- C48-RS CdIn<sub>4</sub>S<sub>8</sub> sample annealed in sulphur atmosphere;





(b) Schematical structure of the samples.

(a) Picture of the samples. Up: C24, down: C48 samples.

**Figure 5.1.1:** C24 and C48 samples used in primary CdIn<sub>2</sub>S<sub>4</sub> investigation. Planar structure with Ni:Al contacts for optical measurements and electrical measurements in planar configuration.

Although, in our research, we intend to cover the topic of CdIn<sub>2</sub>S<sub>4</sub> broadly (hence the chosen set of samples), in some parts of the following work, only the C24 set will be covered. It is because of limited experiment time, technical difficulties, or unsolvable problems. It also has to be noted that during the research, the C24-R sample experienced partial damage that prevented further electrical measurements. However, it will be

demonstrated that the core  $CdIn_2S_4$  model-related research questions can be answered based on the data from the three C24 samples. The following sections will take up the individual experiments performed on the presented set of samples, and, in the end, conclude the findings into whole.

# 5.2 Optical measurements

#### 5.2.1 Photoluminescence

Photoluminescence (PL) measurements are probably the most studied aspect of  $CdIn_2S_4$  research in the literature. As shown in Chapter 4, individual luminescence peaks can be assigned to specific defect states present in the material. Thus, the PL can provide basic knowledge about defects in specific samples, making the PL a robust tool for diagnosing the energetic landscape of the compound.

In the experiment, the samples were excited using a 532nm CW laser line at room temperature. Emission photoluminescence spectra were measured at using a monochromator setup equipped with a Si detector. The spectra were corrected (using reflectance spectra) for interference effects, and then fitted out using four Lorentz functions. Figures 5.2.1, and 5.2.2 show the obtained results. The photoluminescence spectra presented in this chapter were measured by Cezariusz Jastrzębski and Marek Pawłowski<sup>3</sup>.

We have severed the spectra into four peaks at energies 1.4 eV, 1.66 eV, 1.76 and 2eV. Those components can satisfactorily reproduce the original spectra. We successfully applied the same energy values for each sample (the same maximum energies) to fit all of the data. Comparing the measured samples, one can see a systematic decrease in the PL response amplitude with annealing in vacuum and in sulphur. Only the C48-R sample breaks out of this regression, in which we observe an increase in the PL amplitude. However, intensity change of the observable order (one order of magnitude) is generally

<sup>&</sup>lt;sup>3</sup>These results are the instance within this chapter where the author has drawn upon the work of other members of the research group. One extends sincere gratitude to Marek Pawłowski and Cezariusz Jastrzębski for their valuable data and the productive discussions which have transpired.

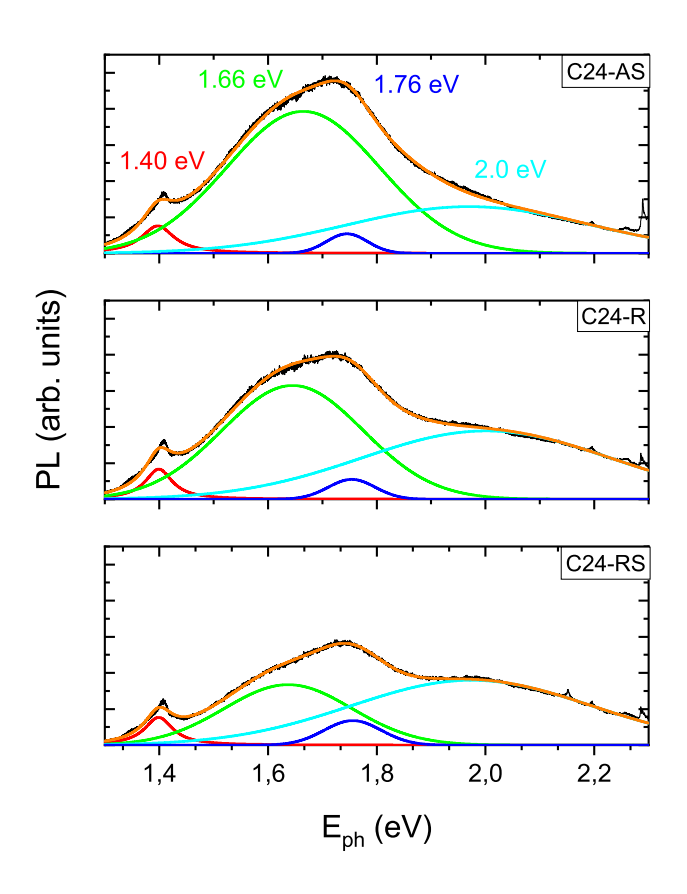


Figure 5.2.1: Photoluminescence spectra of the C24 samples

not considered significant among PL experimentalists.

The literature provides clear grounds for assigning the present peaks, as the commonly accepted values—of the photoluminescence maxima corresponding to the individual defects are very close to ours. Thus: The 1.45eV peak is the transition from the conduction band into the cadmium vacancy ( $V_{Cd}$ ); The 1.6eV peak is the transition from T to E states ( $In_{Cd} - Cd_{In}$ ), and the 1.8eV is the electron emission from the sulphur vacancy (V) to the valence band. The transitions are depicted in the band diagram in chapter 4 (Fig. 4.3.2). The last observed peak – 2eV does not have a literature-based explanation.

The T and E defects are agreeably considered to originate from spinel inversion; precisely, T states arise from  $In_{Cd}$  and E states from  $Cd_{In}$  antisites. As the T and E states directly depend on antisite defects only, the T-E transition can be treated as an

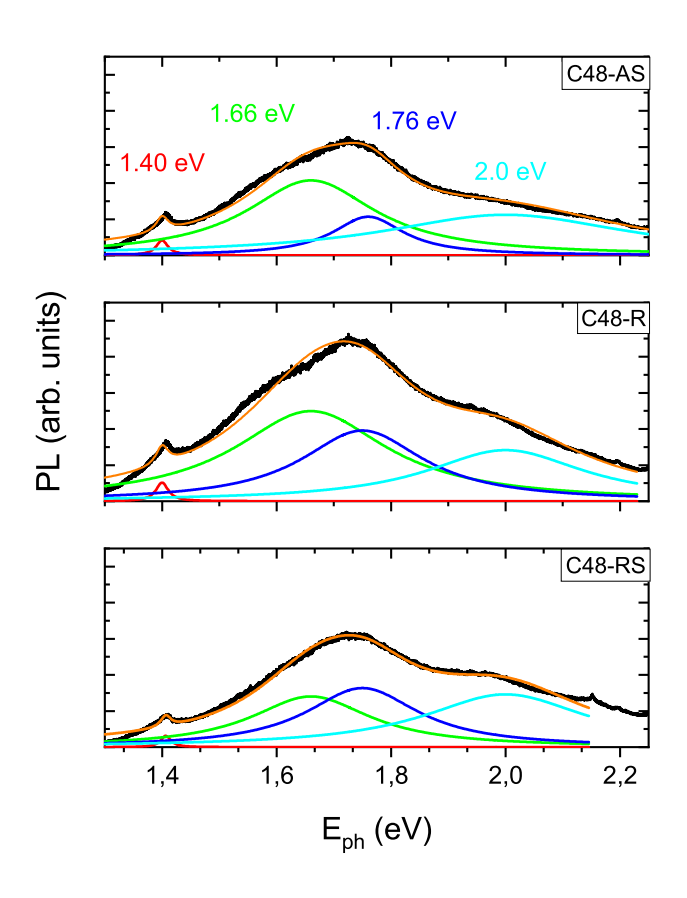


Figure 5.2.2: Photoluminescence spectra of the C48 samples

indicator, a marker of the density of antisites, or in other words, an indicator of disorder in the cation sublattice. To estimate its contribution to the PL spectrum, we calculated the ratio of the area under the 1.6eV component and the total emission spectra (Fig. 5.2.3). This simple analysis shows the annealing causes a general reduction of optical transitions between antisite defects. Therefore, the annealing gradually reduces the concentration of antisite defects in the  $CdIn_2S_4$ . As this 1.6eV transition originates from quasi-continuos density of states, a certain change in its distribution would result in the change of the emission maximum, hence the possible deviation from the literature value.

Further on, 1.6 eV and 1.8 eV transitions are believed to be concurrent processes (due to two-path emission after 2.3 eV excitation) [217]; thus, those peaks' intensities should change the opposite way, which we also observe here, especially in the C48

samples. It is, however, hard to see a clear, unambiguous PL shift from T-E (1.6 eV) transition to sulphur vacancy (1.8eV) after annealing, as one could expect. It is because the charging/discharging process of those defects is more intricate than expected, i.e. there is tunnelling mentioned before (Grilli et al.), the complex defects incorporating sulphur vacancies are likely metastable, and we cannot certify that the concentration of sulphur vacancies does not change upon annealing. For the same reason, there is no significant drop in the 1.8eV peak after annealing in sulphur.

The 1.45 eV peak is most often attributed to  $V_{\rm Cd}$  vacancy (Georgobiani et al.). Its sharp PL band implicates a transition to a well-defined energy level in the bandgap. However, it is hard to infer how the concentration of cadmium vacancies will change upon annealing-induced cation sublattice relaxation. In terms of peaks' maxima shifts, we currently do not have any explanation for the deviation of the values of 1.75eV and 1.4eV peaks from their literature archetypes.

**Table 5.2.1:** Comparison of the fitted PL peaks with the literature values.

peak (eV)	literature value (eV)	origin	
1.4	1.45	$\mathrm{CB}-\mathrm{V}_{\mathrm{Cd}}$	
1.66	1.63	$T - E \left( \operatorname{In}_{\mathrm{Cd}} - \operatorname{Cd}_{\mathrm{In}} \right)$	
1.76	1.85	$VB - V (V_S)$	
2	?	unknown	

Finally, the origin of a 2eV peak in emission spectra is unsettled. We propose two explanations: 1) emission backwards to the E state from CB and 2) radiative indirect recombination from T states. The large width of the 2eV peak supports the second hypothesis as it is a transition from or quasi-continuous density of states, which could have such a broad emission spectrum. Literature usually reports PL spectra at low temperatures, where the probability of this transition is decreased severely due to the low phonon interaction probability, hence the absence of the 2eV emission peak.

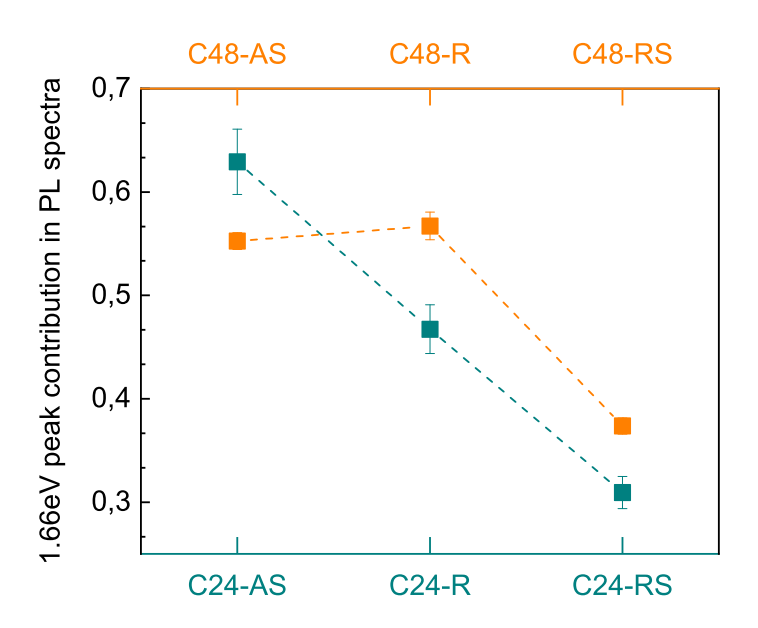


**Figure 5.2.3:** Contribution of the 1.66eV emission to the total photoluminescence spectra.

Lastly, we will focus on the curious case of the observed time dependence of the photoluminescence spectrum. The effect was spotted when we measured the C24-RS sample on a different measurement setup, consisting of the chopped excitation source and a detector with a homodyne amplifier instead of the CW laser. Substitution of the continuous-wave light source with a chopped one (175Hz) resulted in a complete disappearance of the typical CdIn<sub>2</sub>S<sub>4</sub>PL spectra. Instead, a small amplitude 1.32eV peak emerged. Only reducing the chopping frequency to  $10\text{Hz}^4$  resulted in the reappearance of a 1.6eV luminescence component in place of the former spectrum<sup>5</sup>. It seems, that the chopped light acted as a low-pass filter, exposing the frequency response of the PL spectra. It does not mean, that there is no other emission there; it means, that we cannot observe it, because we have filtered it out using the lock-in amplifier. This discovery reveals an extreme time dependence of photoluminescence and, consequently, the time dependence of electronic processes that contribute to radiative emission. The fact that even the 10Hz chopper cannot reproduce the CW photoluminescence spectrum means that the time

<sup>&</sup>lt;sup>4</sup>It was the lowest measurable chopper frequency.

<sup>&</sup>lt;sup>5</sup>Further lowering the chopper frequency to zero would probably gradually restore the original spectre.

constants governing the emission are on the order of at least hundreds of milliseconds. Besides providing an unusual piece of evidence, and uncovering weak 1.32eV emission peak, these findings highlight the need to investigate time-resolved photoluminescence.

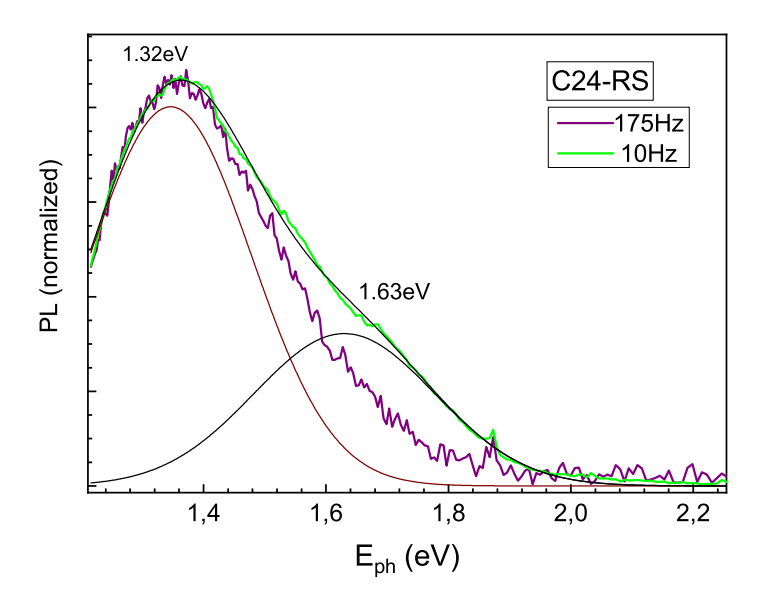


**Figure 5.2.4:** Effects of changing the chopper frequency on the photoluminescence spectrum of the C24-RS sample.

# 5.3 Electrical measurements

Herein, results obtained using electrical methods will be presented. This data are a core element of inference about  $CdIn_2S_4$  and the construction of the model. All electrical measurements in function of temperature were performed using cryogenic setup or its modification, which is presented in section 3.2 unless stated otherwise. However, different experiments were carried on various measurement equipment having different sensitivity. The measurements was performed in lateral configuration, and the conductivity ( $\sigma$ ) values were recalculated concerning the measured geometrical dimensions of the part of the film between the contacts being used. The conductivity was calculated using the simple formula  $\sigma = R\frac{d}{A}$  for the rectangular sample between contacts' edges, i.e. areas excluding parts covered by the contacts. This approximation can be considered valid for a given sample dimensions (e.g. for  $A = 1400\mu m^2$ , d = 1mm). It also can be, in fact, useful when one

attempts to compare samples' conductivity when illuminated and, so simple difference between light and dark conductivity will cut off residual series conductance.

Some doubts may arise regarding the contacts, precisely whether the C24/Ni:Al junction is blocking or not. Theoretical considerations counting  $CdIn_2S_4$  electron affinity<sup>6</sup> predict that the junction should be rectifying. In contrast, we do not observe any nonlinear current-voltage response. On the other hand, with such a high resistance of the tested samples, it can be assumed that bulk resistance will be dominant over voltage drop on barriers; thus, almost all the electrical current change will come from bulk<sup>7</sup>. In the following sections, we will silently settle with the statement (or approximation) that the junctions are ohmic and treat the experiment results as the aspects of the processes occurring in the bulk semiconductor. We will give an argument for this statement in the shape of IV characteristics of chosen samples. This issue will be raised again in section 5.7.2 and chapter 7 devoted to  $CdIn_2S_4$ -based devices.

# 5.3.1 DC conductivity vs temperature

In order to measure the DC conductivity, samples were cooled down, polarized with 10V bias voltage, and direct dark (at state without any illumination) current was measured in function of temperature in the range of  $80K \div 300K$  (LNT  $\div$  RT) in the cryogenic system. Figure 5.3.1 shows results for C24 and C48 samples. Due to the limited operational range of measurement setup, low-temperature parts of some of the samples were immeasurable. In those regions, the samples' resistivity exceeded the sensitivity of the setup, and the signal dropped below the noise floor. Therefore, part of the data was cut off. The cut-off lies at different points (temperatures) in particular samples due to different geometrical dimensions, resulting in total resistance R.

The first thing that can catch one's eye is grouping samples into three distinct groups based on their conductivity values, with a difference in conductivity of three orders of magnitude between each group. First group – samples C24-AS and C48-R: have the

 $<sup>^6\</sup>mathrm{CdIn}_2\mathrm{S}_4$  electron affinity is found to be ~3.5eV. The work function of the metals is above 4eV.

<sup>&</sup>lt;sup>7</sup>In other words, diodes, if any, will behave like diodes with large series resistance and only the change in this resistance will be measurable.

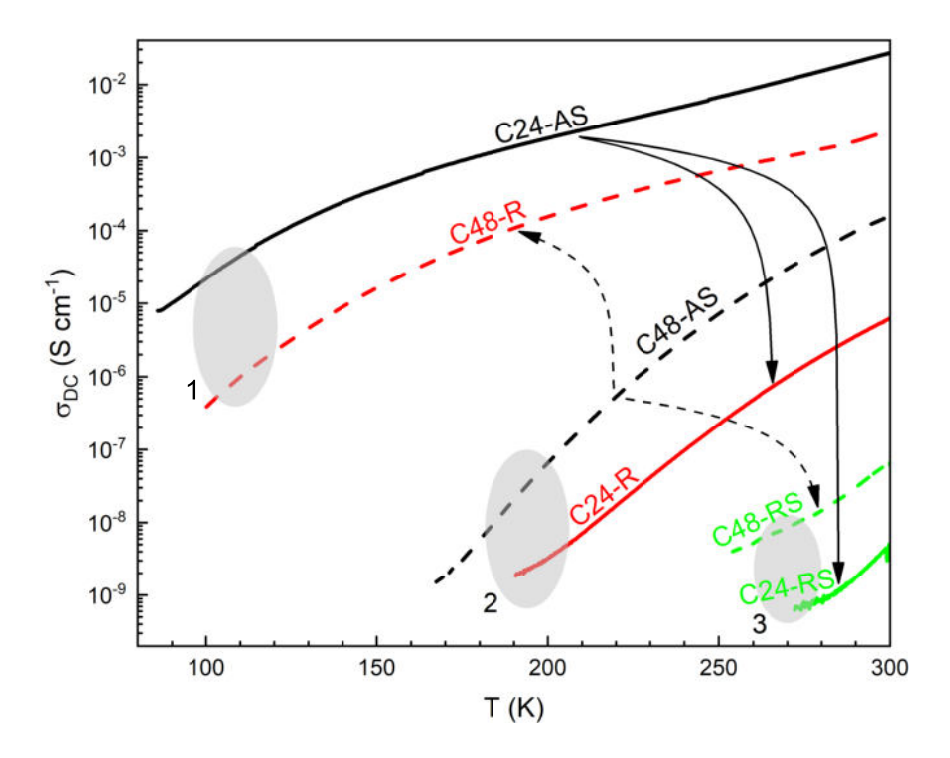


Figure 5.3.1:  $\sigma_{DC}(T)$  relation for C24 and C48 samples. Arrows represents effects of post-deposition treatment on the films i.e. changes of conductivity upon annealing in vacuum or sulphur. Ellipses represent perceptible lumping of the samples into three groups (see text).

highest conductivity, and their temperature dependence is almost the same, i.e.  $\sigma(T)$  is close-to-parallel with one order of magnitude shift. The second group: samples C24-R and C48-AS, with similar parallelisms in temperature function and 10x shift. Third group: samples C24-RS and C48-RS, with the lowest conductivity values. The second remark is that the pairs of samples: C24-AS – C24-R and C48-AS – C48-R, behave in exactly opposite manner, i.e. the impact of annealing in vacuum has exactly opposite effects, and the samples land on opposing sides of the grouping. Sample C48-AS starts from the C24-R conductivity level and becomes similar to C24-AS after annealing and vice-versa. Whatever causes the conductivity to decrease during annealing has the same visible effect as changing the cadmium content. Moreover, the effect is the opposite for Cd-poor CdIn<sub>2</sub>S<sub>4</sub> (CdIn<sub>4</sub>S<sub>8</sub>). The third observation is that both C24 and C48 films annealed in sulphur exhibit the largest conductivity drop and become roughly similar (third group).

We made Arrhenius plot for obtained  $\sigma_{DC}(T)$  data (Fig. 5.3.2). As one can observe, each curve contains at least one linear part indicating the Boltzmann activation relation. We fitted a slope to most significant linear parts for each curve and obtained activation energies (E<sub>A</sub>) having values: 0.1eV, 0.4eV and ~0.7eV for C24-AS, C24-R and C24-RS samples, respectively, as well as 0.4eV, 0.1eV and ~0.5eV for samples C48-AS, C48-R and C48-RS. Values of the activation energies are listed in table 5.3.1.

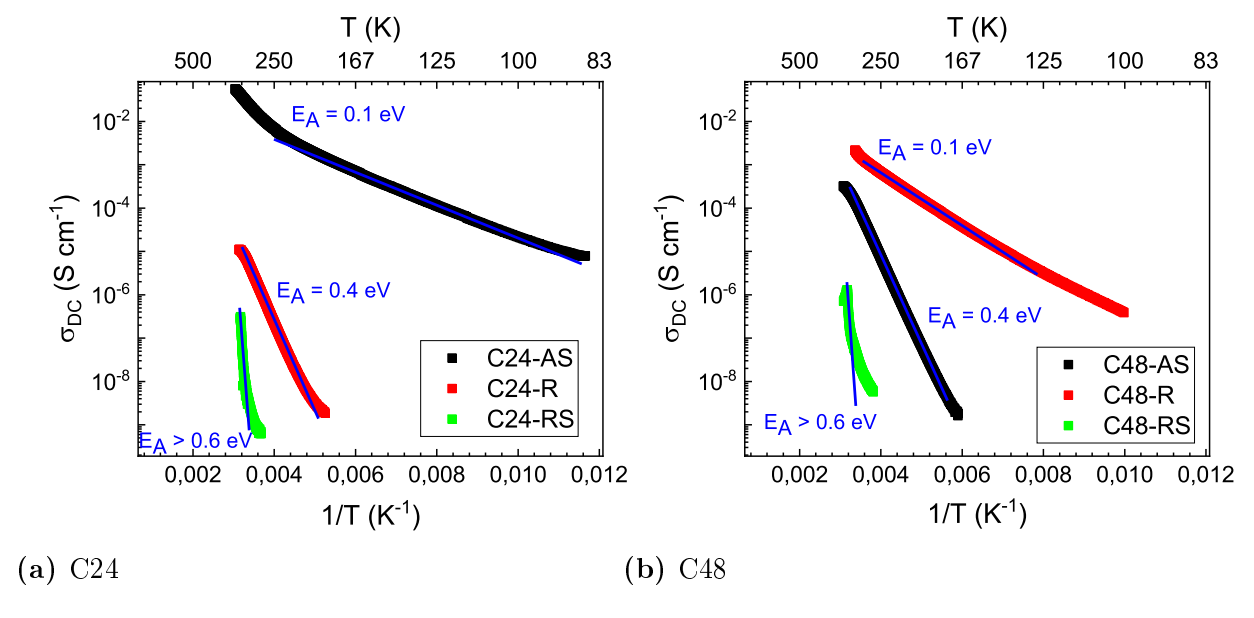


Figure 5.3.2: Arrhenius plot of DC conductivity for C24 and C48 samples.

In the presented case, bulk conductivity activation can be considered a sign of Fermi level-pinning. In the  $CdIn_2S_4$ , electrons are majority carriers; therefore, the activation energy can be written as the position of the Fermi level relative to the conduction band  $E_A = E_C - E_F$ . Knowing that:

$$N_C = n_0 \exp\left(\frac{E_A}{kT}\right) = n_0 \exp\left(\frac{E_C - E_F}{kT}\right) \tag{5.3.1}$$

we can take  $n_0$  from  $\sigma$  at 300K, and assuming  $\mu_n = 1 \text{cm}^2/\text{Vs}$  and disregarding holes, obtain values of  $N_C$ . Then, having  $n_0(T)$  calculated from  $\sigma(T)$  in the same manner, we

can calculate Fermi level position in function of temperature:

$$E_C - E_F = kT \ln \left( \frac{N_C}{n_0(T)} \right) \tag{5.3.2}$$

thus, obtain plots, presented in Fig. 5.3.3 for C24 and C48 samples respectively. Values of  $n_0$  and  $N_C$  for each sample are listed in table 5.3.1 as well.

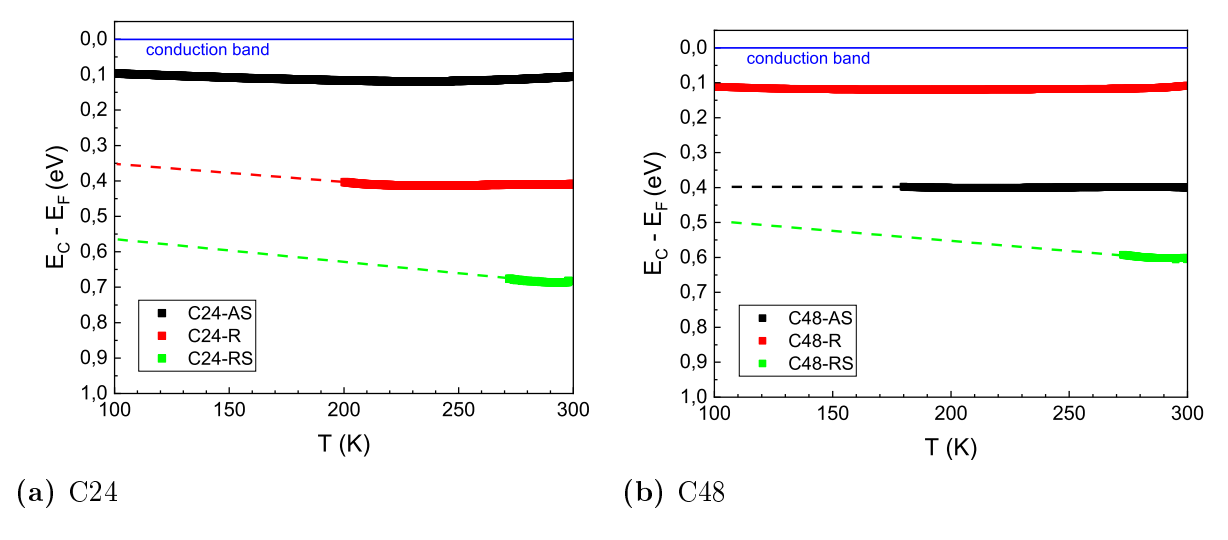


Figure 5.3.3: Fermi level position calculated form  $\sigma_{DC}$  measurement for C24 and C48 set of samples. Dotted lines are the extrapolation of the function in a range, were the measurement was impossible due to limited sensitivity of the measurement setup.

On the presented plots, the Fermi level pinning emerges. In the C24-AS sample,  $E_F$  is pinned around 0.1eV below CB, close to the conduction band. During the annealing in vacuum,  $E_F$  gets repinned at 0.4eV below CB (sample C24-R). In turn, in C48-AS,  $E_F$  is pinned at 0.4eV in as-grown (pristine) conditions, and during annealing, it gets repinned to 0.1eV below CB. Annealing in sulphur depinns the Fermi level in both cases, thus samples C24-RS and C48-RS behave more as quasi-intrinsic material with  $E_F$  located deep below the conduction band, and possibly pinned by some deep stated at 0.5-0.6eV below CB. As stated before, measuring current below a certain temperature was impossible due to limited sensitivity. Hence, we extrapolated  $E_C - E_F$  towards low temperatures (dotted lines).

Towards the derivation of the simplest possible explanation, we can assume that the

defects pinning the Fermi level in samples C24 and C48 are, in fact, the same defects. The annealing then has the opposite effect on defects in the compound depending on its cadmium content: the annealing decreases conductivity in the C24 sample but restores the high conductivity state in C48 (first and second group). Therefore, the 0.1eV and 0.4eV energies are associated with defects related to the difference between C24 and C48 – the cadmium content. In the case of annealing in sulphur, it should be remembered that annealing in sulphur has the same effect as annealing in general, so it should make a similar impact to annealing in a vacuum, plus it introduces the effect of sulphur: Introducing sulphur itself is believed to minimize the concentration of sulphur vacancies (third group).

**Table 5.3.1:** Parameters of the C24 and C48 samples calculated from  $\sigma_{DC}$  measurement, with assumption of constant  $\mu=1cm^2/Vs$ .

sample	$E_A$ (eV)	$\sigma_0$ (at 300K) (S/cm)	$n_0 (at 300 K) (1/cm^3)$	$ m N_C~(1/cm^3)$
C24-AS	0.1	$3\cdot 10^{-2}$	$1.8 \cdot 10^{17}$	$1 \cdot 10^{-19}$
C24-R	0.4	$6.3\cdot 10^{-6}$	$4\cdot 10^{-13}$	$3.5\cdot 10^{-20}$
C24-RS	> 0.5	$5\cdot 10^{-9}$	$3\cdot 10^{-10}$	$1.4 \cdot 10^{19}$
C48-AS	0.4	$1.6\cdot 10^{-4}$	$1\cdot 10^{-15}$	$9 \cdot 10^{21}$
C48-R	0.1	$2.5\cdot 10^{-2}$	$1.5\cdot 10^{-17}$	$8.2 \cdot 10^{-18}$
C48-RS	> 0.5	7 · 10 <sup>-8</sup>	$4.3 \cdot 10^{-11}$	$2 \cdot 10^{-20}$

The general interpretation of the results will be presented at the end of the chapter. Nonetheless, here, we will spoil its outline, which for C24 goes as follows: In as-grown conditions, the most dominant defects are the T states, which originate from relatively high spinel inversion<sup>8</sup>. Annealing in vacuum reduces the inversion, and the Fermi level gets then repinned by the second most dominating agent: sulphur vacancies. When annealed in a sulphur, both sources of pinning are removed, leaving the sample in a quasi-intrinsic state.

In the case of C48, the cadmium deficiency must be included:  $CdIn_4S_8$  without inversion should have a smaller density of E ( $Cd_{In}$ ) states (due to Cd deficiency), therefore, in C24-R sample, T states will be dominating impurity and pin the Fermi level. Especially when Cd

<sup>&</sup>lt;sup>8</sup>The inversion will be discussed in more detail in further sections.

is in deficit, the  $In_{Cd}$  states will be further favoured. In the as-grown sample, the spinel is additionally inverted. Thus, the original balance between Cd-In defects is disturbed in favour of the other states as the distribution between Cd and In atoms in particular positions in the cation sublattice is additionally imbalanced by inversion. In other words, the increased inversion forces the C48-AS to be in an opposite state to C48-R.

The values of  $n_0$  were obtained from the Fermi level position, which then is a resultant of the sum of all specimens present in the compound. The values of  $N_C$  have a deeper connection to the structural intricacies of the  $CdIn_2S_4$ , which extends out of the scope of this work.

In summary, the observed conductivity behaviour among the samples can be explained by native CdIn<sub>2</sub>S<sub>4</sub> defects and spinel inversion. Those two concepts will be discussed more broadly in the next sections.

## 5.3.2 Current-voltage characteristics

The main purpose of this measurement was mainly to check the I-U linearity in search of any possible signs of blocking contacts. We focused on the C24 series, and measured IV characteristics<sup>9</sup> (Fig. 5.3.4) at room temperature, within the range of  $\pm 10$ V (giving the electric field<sup>10</sup> ~100V/cm). We fitted the characteristics with linear functions obtaining conductance values. The fit gives satisfactory results regarding uncertainty, even in the case of the C24-RS sample, experiencing a large signal-to-noise ratio. As observed, there is no doubt about the linearity of the obtained IV characteristics within the  $\pm 10$ V range. Therefore, there is no reason to assume any barriers, peculiar transport mechanisms, space charge limited current (at least not within the measured voltage range) or effects other than occurring in bulk semiconductor with free charge carriers under a (quasi)uniform electric field, and prospectively, illumination.

Nevertheless, the presence of such blocking contacts cannot be ruled out. However, we have neither evidence for their presence nor any data allowing for their characterisation.

<sup>&</sup>lt;sup>9</sup>The measurement was performed using Agilent E4980A (LCR meter) for the best accuracy.

<sup>&</sup>lt;sup>10</sup>In the most extreme case.

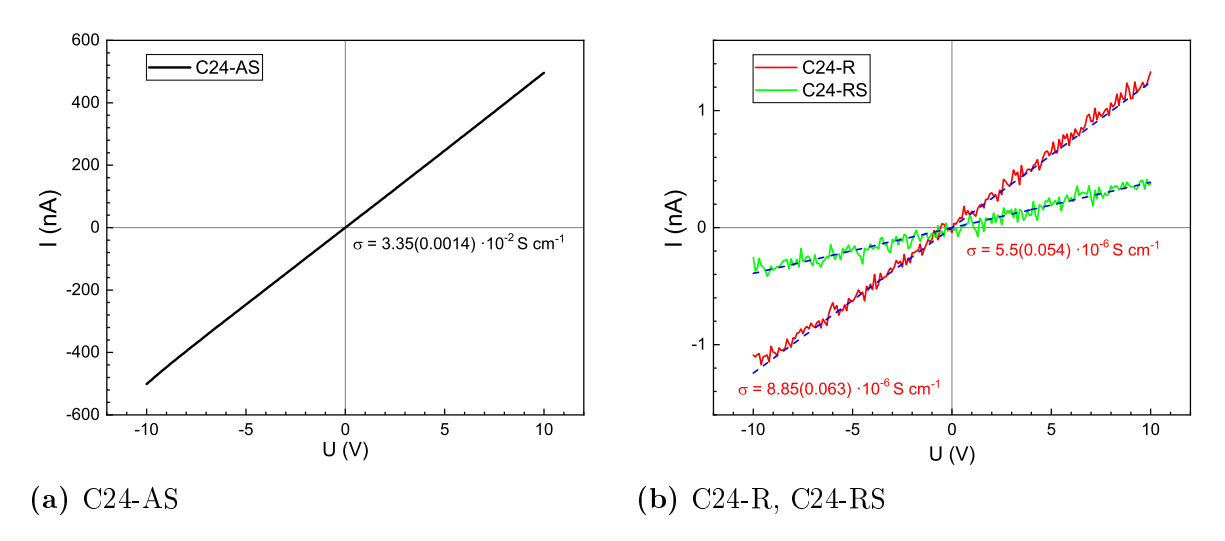


Figure 5.3.4: IV characteristics of C24 samples with linear fit and conductance values.

Table 5.3.2: Conductivity of the C24 samples calculated from IV measurement.

sample	σ (S/cm)
C24-AS	$3.35(0.0014) \cdot 10^{-2}$
C24-R	$8.85(0.063) \cdot 10^{-6}$
C24-RS	$5.5(0.054) \cdot 10^{-6}$

Given the linearity of the IV characteristics, one can, however, with great certainty, accept the stated approximation and interpret the electrical measurements for a case of factual bulk material only. The obtained conductivity values only roughly matches the values from  $\sigma_{\rm DC}(T)$  measurement, although we cannot propose an clear explanation of the difference, beside the influence of sample metastability, which we will discuss in Chapter 5.5.

# 5.3.3 Thermally stimulated current

Here, we continue the conductivity measurements in a function of temperature presented in section 5.3.1, which is a Thermally Stimulated Current (TSC). The experiment comes down to a standard conductivity measurement once more after first exciting the sample by illumination. A more detailed theoretical description has been introduced in section 3.2.1.

Here, and in the consecutive sections in this chapter, we will focus on the C24 series. In

Fig. 5.3.5, we show a summary plot of TSC measurements. The figure compares dark conductivity for the samples in a relaxed state (as in the previous chapter) to dark conductivity for samples after illumination. As a light source, we have used 460nm (2.7eV) power LED. The effective optical power per sample area was  $\sim 100 \mu \text{W}$ , which yields average photogeneration of  $10^{20} \text{cm}^{-3} \text{s}^{-1}$ . The pre-illumination was applied in two manners:

- EWC excitation while cooling. The sample was illuminated the whole time during cooling down from RT (room temperature) to LNT (liquid nitrogen temperature, 77.5K);
- LNT the sample was illuminated in LNT for a given time (15min.).

We will consequently use those designations throughout the rest of the work.

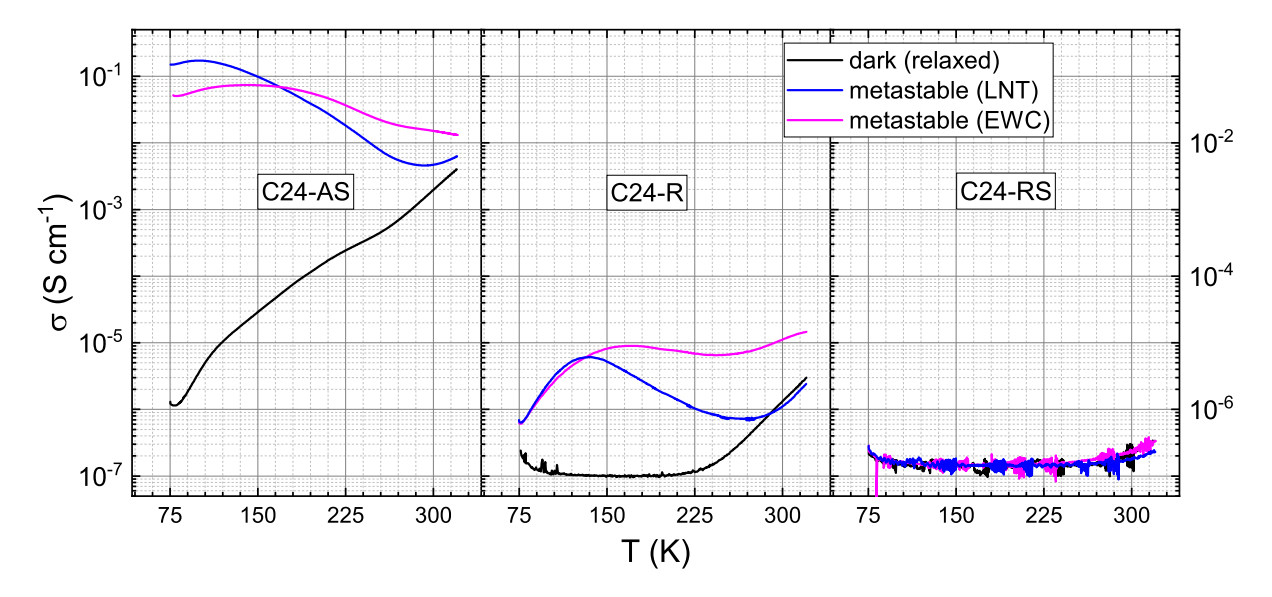


**Figure 5.3.5:** Summary of thermally stimulated current measurement for C24 samples. Heating rate r was 10 K/min.

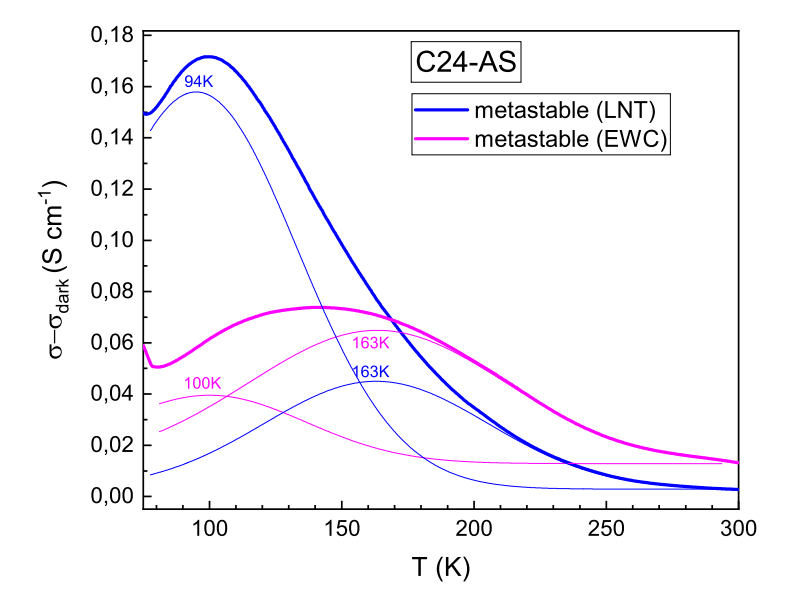
For each measurement, the cooling rate was constant (15K/min.). The samples at LNT were illuminated for 15min. (900s). The time required to cool down the sample from RT to LNT was 15min.; thus, for EWC, the samples happened to be illuminated for the same time interval as in the LNT case. The heating rate (For curves in Fig. 5.3.5 was 10K/min.).

Here, we witness the first manifestation of the memory in CdIn<sub>2</sub>S<sub>4</sub>. For the C24-AS and C24-R samples, we can observe a distinct peak-alike increase in conductivity. The C24-RS sample does not exhibit any increment; there is a slight decrease in conductivity upon illumination.

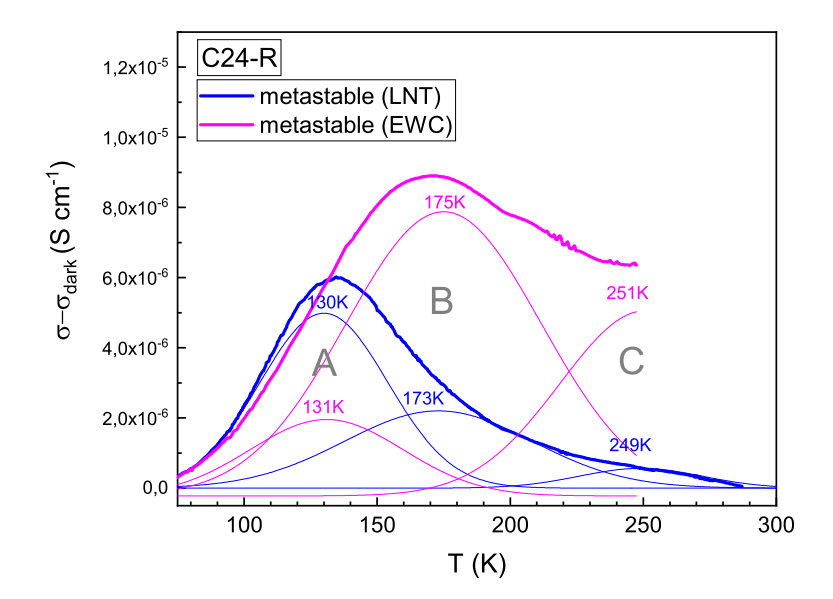
For the C24-AS sample, both EWC and LNT illuminations yield similar temperature dependence with five orders of magnitude conductivity difference at 80K. The illumination effects do not anneal (the sample does not relax) below RT, and the LNT and EWC TSC spectra consist of more than one peak.

In the C24-R sample, we observe a more dramatic difference between EWC and LNT illumination. The LNT TSC curve evinces a large peak around 150K and then anneals out completely below 300K. Contrarily, the effects of EWC persist even at room temperature. The initial current drop visible in Fig. 5.3.5 for all of the samples, is caused by the shallow traps freeze-out, and is a common behaviour for TSC curves [238].

In order to examine the TSC characteristics a bit closer, we subtracted dark conductivity  $\sigma_0$  from TSC curves to extract the excess current. Then, we fitted the curve using two or three Gaussian peaks. The effects of the operation are presented in Fig. 5.3.6. In C24-AS, both LNT and EWC curves can be resolved into two peaks. For LNT: 94K and 163K. For EWC: 100K and 163K. Similarly, in the C24-R sample, we have 130K and 173K for LNT, and for EWC: 131K, 175K and an additional prominent peak at 251K. The last peak is also visible in LNT, but only for 10K/min.; therefore, we will not include it in the analysis. It also has to be noted that the 251K peak in EWC partially overlaps with the activation, i.e. it was very hard to separate this distinct peak successfully. In Fig. 5.3.6, we have shown the peak fitting results for C24-AS and C24-R for r = 10 K/min. It will probably not be too much of a disgrace if we consider that in sample C24-R, we see the same peaks in both LNT and EWC. Thus, we will mark the lower 130-131K peak as A, the medium 173-175K peak as B, and the 250K as C. Comparing the A and B peaks (similarly in sample C24-AS: ~100K and ~163K) for LNT and EWC illumination, both peaks contribute significantly to the TSC curve. Nonetheless, when we excite the sample at low temperatures, the A peak dominates, and when cooling, the B peak dominates,



# (a) C24-AS



**(b)** C24-R

**Figure 5.3.6:** Results of TSC measurements for C24-AS and C24-R samples with the heating rate r = 10 K/min.

hence the difference between the LNT and EWC curves.

The TSC experiment shows the general precepts governing the metastable phenomena observed in  $CdIn_2S_4$ . In order to induce the metastable state, one has to illuminate the

sample with sufficient power and time, using light from (as it will be revealed later on) visible range. After removing the illumination, a long conductivity tail will be observed over a certain time until the sample conductivity decays towards a relaxed value. The effects of illumination would then emerge as TSC peaks. To reset the sample, one has to increase the temperature above 150-160K, preferably to room temperature. Annealing restores the relaxed state. It should also be added that it is hard to induce the metastable state at room temperature (and generally at high temperatures) – the sample will swiftly relax to its original state.

Now, we will focus on the C24-R sample, as its TSC spectre is the most resourceful case and potentially carries the most explicit situation regarding the observed phenomena. We have repeated the TSC experiment, both LNT and EWC, for multiple heating rates r (2K/min., 5K/min. and 10K/min), performed the fitting procedure scarcely demonstrated, and obtained a series of peaks' maxima  $T_m$  in the fashion shown in Fig. 5.3.6. We are obligated to mention here that we can interpret the TSC experiment in at least two ways. The first interpretation, which one could call *classical*, assumes the ordinary emission from trap states, as described in chapter 3.2.1. The second explanation involves the direct intervention of metastable defects. It will be discussed in more detail later, in section 5.5, until we learn more about the metastability phenomena in the studied samples. Here, we will follow the classical interpretation.

At this point, it is safe to accept that we deal only with the majority carriers here. As we have the n-type semiconductor, we assume all states to be electron traps. Based on the theory specified in chapter 3.2.1, we applied equation 3.2.6 to calculate activation energy, here, having the meaning of a depth of potential electron trap. Figure 5.3.7 shows that the obtained points fall into three lines corresponding to the energies: A: 150meV, B: 100meV and C: 350meV. One can see that the energy level responsible for peak A is deeper than the level generating peak B while being more favourable to trap electrons at LNT than peak B, and the B peak is being populated more efficiently at high temperatures while cooling than peak A, which is inconsequent at first glance. The conundrum can be

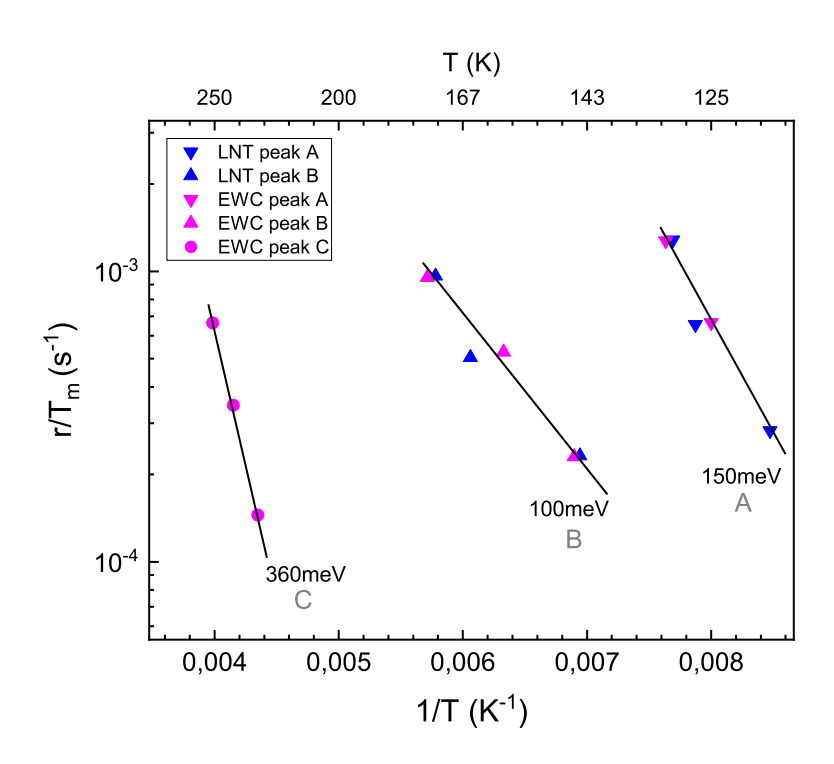


Figure 5.3.7: TSC peaks analysis for C24-R sample.

resolved, however, if we assume that these two levels have different capture cross-sections and emission coefficients that define their  $T_m$  values. The following reasoning unveils that A must have a higher capture/emission probability than B. Indeed, calculating an attempt to escape frequency using the formula 3.2.6 gives  $\nu_0 \approx 10^3 \text{s}^{-1}$  for A, and  $\nu_0 \approx 10^1 \text{s}^{-1}$  for B. For C:  $\nu_0 \approx 10^6 \text{s}^{-1}$ . The question of what defects should be assigned to the found peaks now arises. 360meV falls close to the energy at which the Fermi level in relaxed C24-R sample is pinned, although there is probably no real level there. The 100meV is sometimes appointed to the T states – those are believed to pin the Fermi level in C24-AS sample. Lastly, we currently do not have any candidate for 150meV energy level.

In the C24-AS sample, the situation is somewhat simpler, as the lower peak dominates in LNT and the higher peak at EWC. Except that, in the C24-AS, the bearing is roughly the same. In the C24-RS sample, we observe conductivity reduction instead of the typical *glow curve*, as mentioned before. The explanation of this phenomenon requires metastability. We will return to this issue and the mentioned alternative interpretation in section 5.5.

# 5.3.4 $\sigma(\omega)$ measurements

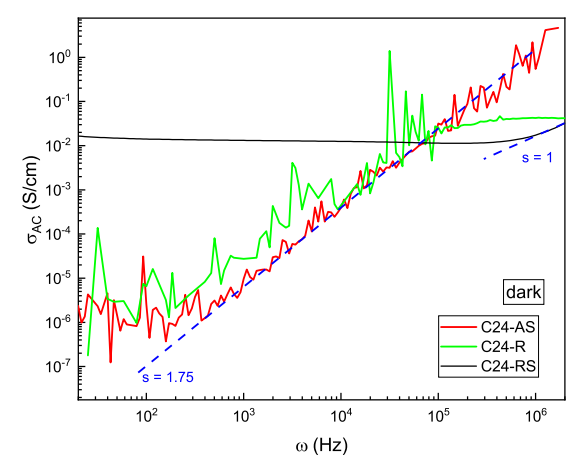
An AC conductivity measurement gives a deeper insight into peculiar transport mechanism, or multiple mechanisms standing behind the samples' conductivity performance. We have measured the complex impedance in range 20Hz–2MHz with amplitude of 50mV and 0V bias using Agilent E4980A (LCR meter)<sup>11</sup> at room temperature<sup>12</sup>. The results are shown in Fig. 5.3.8.

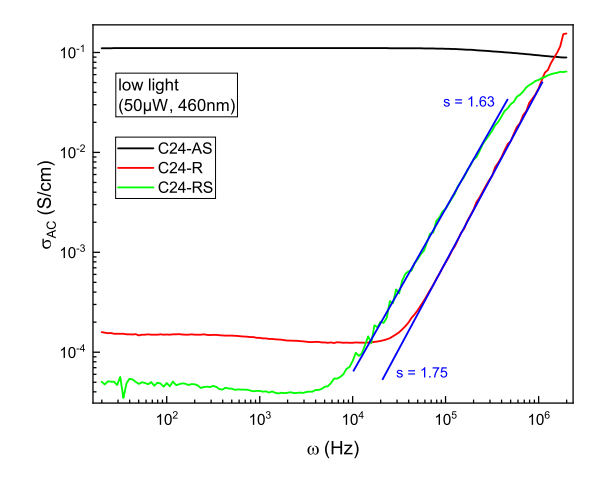
Let us start with dark (relaxed state, no illumination)  $\sigma_{AC}$  dependence, shown in Fig. 5.3.8a. The measured conductivity follows a general shape of  $\sigma(\omega)$  introduced by equation (3.2.13): we can observe two parts within the measured frequency range which are:

- 1.  $\sigma_{DC}$  part with the frequency plateau the DC conductivity is the dominant part (in C24-R and C24-RS samples this part is very narrow); Closer inspection of the  $\sigma_{DC}$  reveals, that this part actually evince slightly decreasing frequency dependence. The decreasing AC conductivity is, in general, an indication of an inductive behaviour from the electrical point of view.
- 2.  $\sigma_{AC}$  part where we start to observe the  $A\omega^s$  relation, completely dominating the DC conductivity. The power dependency plainly indicates a certain relaxation process governing conductivity, which was discussed in chapter 3.2.2. For the C24-AS and C24-R samples, the  $A\omega^s$  propagates throughout the entire frequency band; for the C24-RS sample, one can observe saturation at ~ 10<sup>6</sup>Hz. For C24-AS, the power factor s=1, and for C24-R and C24-RS, s=1.75. As the transition region between the DC and AC regime in C24-R and C24-RS samples is rather gradual, one should infer, by inspecting the C24-AS curve, that we might do not see a fully developed  $A\omega^s$  dependency here. Therefore, s=1 with great probability could be an artefact. In two remaining samples: C24-R and C24-RS, the  $\sigma(\omega)$  dependency is superlinear. Therefore, it is necessary to provide an adequate model, extending beyond classical, Jonscher interpretation, as briefly presented in chapter 3.2.2.

 $<sup>^{11}</sup>$ Appropriate corrections for parasitic reactance are applied in the measuring system.

<sup>&</sup>lt;sup>12</sup>It was impossible to scan the temperature range due to insuperable noise induced by the cryogenic setup.





- (a) without illumination (dark conditions).
- (b) at low light conditions  $-460 \,\mathrm{nm}$  (2.7eV),  $50 \,\mathrm{nW}$ .

Figure 5.3.8:  $\sigma(\omega)$  conductivity at room temperature for set of C24 samples. As the C24-R and C24-RS samples exhibit high resistivity, there is significant noise in the data. Small illumination increases SNR while keeping similar behaviour of  $\sigma_{AC}$  frequency dependence.

We can go deeper into the analysis of frequency dependence of conductivity by measuring  $\sigma(\omega)$  in the function of light intensity. The illuminated  $\sigma(\omega)$  characteristics are shown in Fig. 5.3.9. After the illumination with 460nm monochromatic wavelength (fig. 5.3.8b), the DC conductivity increases severely, shifting the transition point between  $\sigma_{DC}$  and  $\sigma_{AC}$  domination towards higher frequencies. The shift progresses along with increasing illumination intensity. For the C24-AS sample, the  $\sigma_{DC}$  completely overwhelms the conductivity dependence, fully covering  $\sigma_{AC}$  in the observed frequency range. For comparison, we have shown  $\sigma_{AC}$  for low light illumination (Fig. 5.3.8b) next to the dark characteristics (Fig. 5.3.8a). Even relatively small illumination increases the  $\sigma_{DC}$  by two orders of magnitude, increasing signal-to-noise ratio. The slope s does not change, but we observe slightly vertical decrease of the  $A\omega^s$  part. Besides, only the  $\sigma_{DC}$  and the inductive behaviour seems to be readily illumination dependent. One should note, that in C24-AS sample even relatively small illumination is enough for DC conductivity to cover almost entirely AC conductivity part.

Having thorough literature knowledge on the AC conductivity and the  $CdIn_2S_4$ , we will attempt to deduce the mechanism governing  $\sigma(\omega)$  here:

A textbook case of  $\sigma(\omega)$  dependency obtained here indicates hopping conductivity. Increasing illumination intensity does not affect the hopping but affects DC conductivity simply by increasing free electron concentration  $n_0$  by  $\Delta n$  photogenerated carriers. Consequently, frequency-independent conduction band transport gradually overwhelms hopping transport. Therefore, in the C24-AS sample, where the Fermi level is closely below the conduction band (see table 5.3.1), thus  $n_0$  is the highest. Hence, the hopping conductivity dominates until above  $10^5$  Hz. Furthermore, even a small illumination intensity is enough to completely saturate the C24-AS transport with conduction band electrons. In C24-R and C24-RS samples, where the  $E_F$  is deeper below  $E_C$ , and  $n_0 + \Delta n$  cannot fully cover the hopping transport.

To unravel the origin of the slope s, we will bring the Gilroy-Phillips model of electron hopping incorporating asymmetric potential wells<sup>13</sup> [139]. Applying the s parameters to the formula (3.2.19), assuming the T = 300K, we obtain:  $E_{gt}$  equals 33.3meV for C24-R and 39.7meV for C24-RS. It is then unforeseen outcome, that the s=1.75 gives  $T_{gt}=400\mathrm{K}$  – surprisingly, it is almost the exact (!) temperature of the order-disorder transition measured by Czaja [210]. To decipher the results let us firstly recall the physical interpretation of the Gilroy-Phillips superlinear frequency dependence. A defect pairing occurs in chalcogenide glass or heavily disordered materials, especially above the melting point. The consequent order can be preserved during the fast cool-down, thus vitrification of the defects, resulting in the non-random distribution of defect states, both in space and allegedly in energy [133]. Superlinearity is then a direct outcome of the distribution of the relaxation times related to hopping over asymmetric double-well potentials with exponential distribution of barrier heights, as postulated by Gilroy and Phillips.

The fact that those analyses are inherently related to chalcogenides gives some apparent credibility to the results obtained. The question is, which states are responsible for the hopping transport? Considering the possible defects in  $CdIn_2S_4$  and the literature-based energy diagram (4.3.2), T states seem to be a good candidate. Those defects are a source of quasi-continuous Urbach-like distribution of energy states below  $E_C$ . Thus, it is not

<sup>&</sup>lt;sup>13</sup>Analysis with Pollak model did not give any satisfactory results.

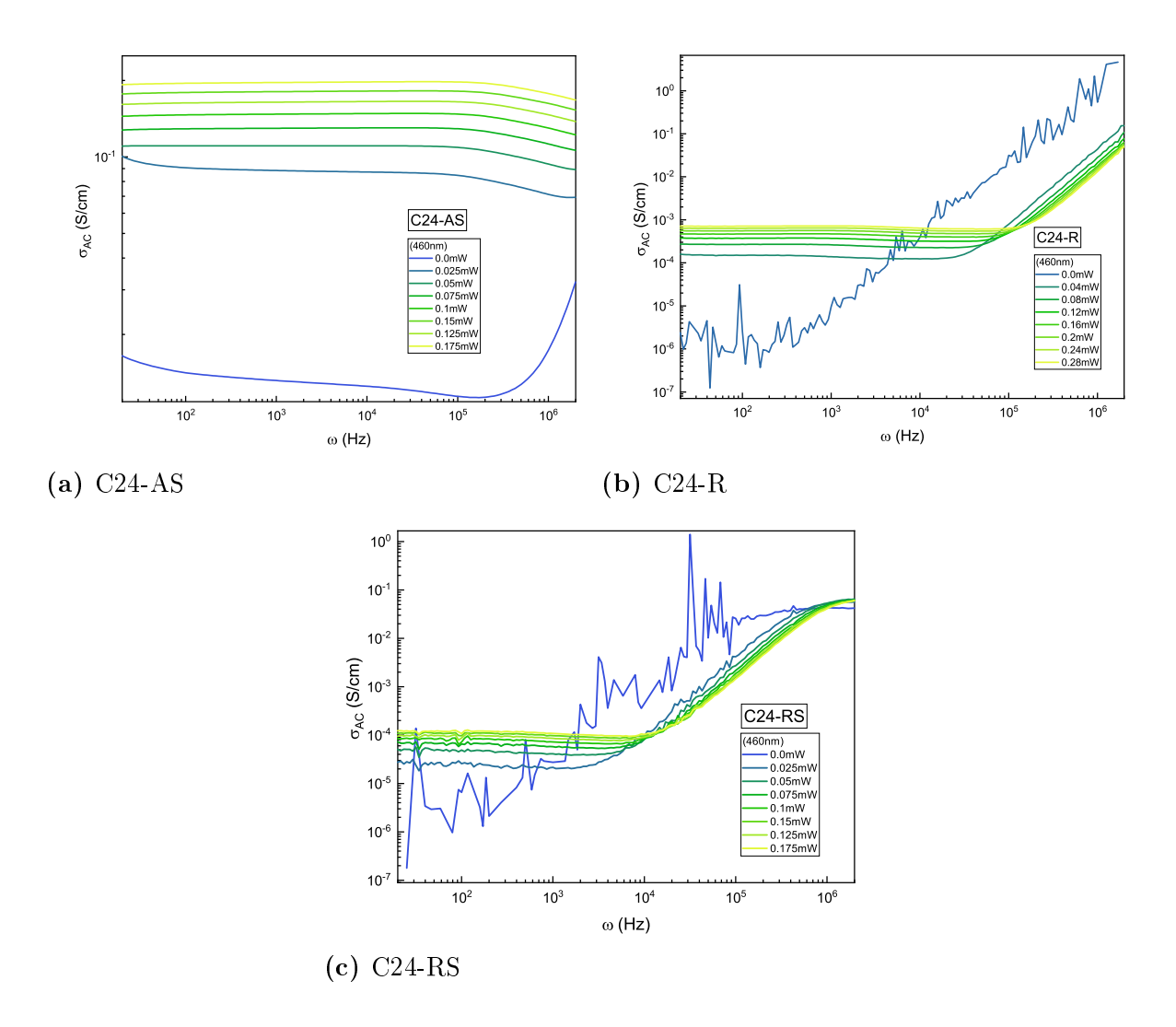


Figure 5.3.9: Room temperature  $\sigma_{AC}$  conductivity measurement for set of C24 samples in function of illumination intensity.

unreasonable to attribute exponential barrier height relation to those<sup>14</sup>. However, most importantly, the T states originate from the inversion of the spinel, which is a primary source of disorder in the crystal structure, and the 403K temperature measured by Czaja is the temperature where the order-disorder transition of the cation sublattice takes place (vide chapter 4.2.1).

On the contrary, it is bold to assume that the compound in the form we examined is a disordered semiconductor, not to mention calling it glass. The melting point of  $CdIn_2S_4$  is

<sup>&</sup>lt;sup>14</sup>Then, we would be able to pinpoint a specific measured value characterizing those states.

far above deposition temperature, and it is highly questionable whether there is room for the forming of, in fact, an ordered defect compound<sup>15</sup>. Yet, it has been shown that it could be done using PVD [224]. Moreover, the glass transition is an entirely different entity than the order-disorder transition, and there is no reason to equate them here besides some alleged similarity in model derivation. The energy value in the Gilroy-Phillips model could be, however an entirely unrelated parameter, that only characterizes barrier energy distribution, leaving the surprising connection with the phase transition temperature completely coincidental.

The slope obtained for the C24-RS sample equals 1.63, giving  $T_{gt} = 476$ K. The possible deviation from the *tentatively correct* value might be that sulphur vacancy mediates in the hopping transport or reducing the sulphur vacancy concentration relaxes the lattice, thus modifying the energy distribution of the barriers.

Lastly, only one source of literature was found that deals with  $\sigma(\omega)$  of  $CdIn_2S_4$ . Single crystals were tested, and the coefficient s = 0.8 was obtained [239]. It is then a question of whether the grain boundaries are responsible for the observed abnormal s value in our polycrystalline samples or whether a specific property of the compound, controlled by the technological process, determines the observed abominable hopping.

An additional depth of  $\sigma(\omega)$  conductivity measurement can be added by analysing the complex impedance of the samples in the form of impedance spectra (Nyquist plots). In Fig. 5.3.10, we have presented the impedance spectra that have the exact origin as  $\sigma(\omega)$  characteristics presented in Fig. 5.3.8b. The big semicircle is usually associated with an RC circuit, as described in chapter 3.2.2. As has already been shown, a particular distribution of relaxation time constants is present here. Therefore, this apparent semicircular shape is, in fact, a sum of an infinite number of perfect semicircles. For all that, we can get approximately the averaged relaxation constant from the half of the semicircle to obtain at least its order of magnitude. For the C24-R sample  $\tau \approx 23 \mu s$ , and for the C24-RS sample  $\tau \approx 117 \mu s$ .

 $<sup>\</sup>overline{^{15}}$ The cooling rate after deposition process is around  $5 \mathrm{K/min.}$ , far too slow to achieve any glass transition.

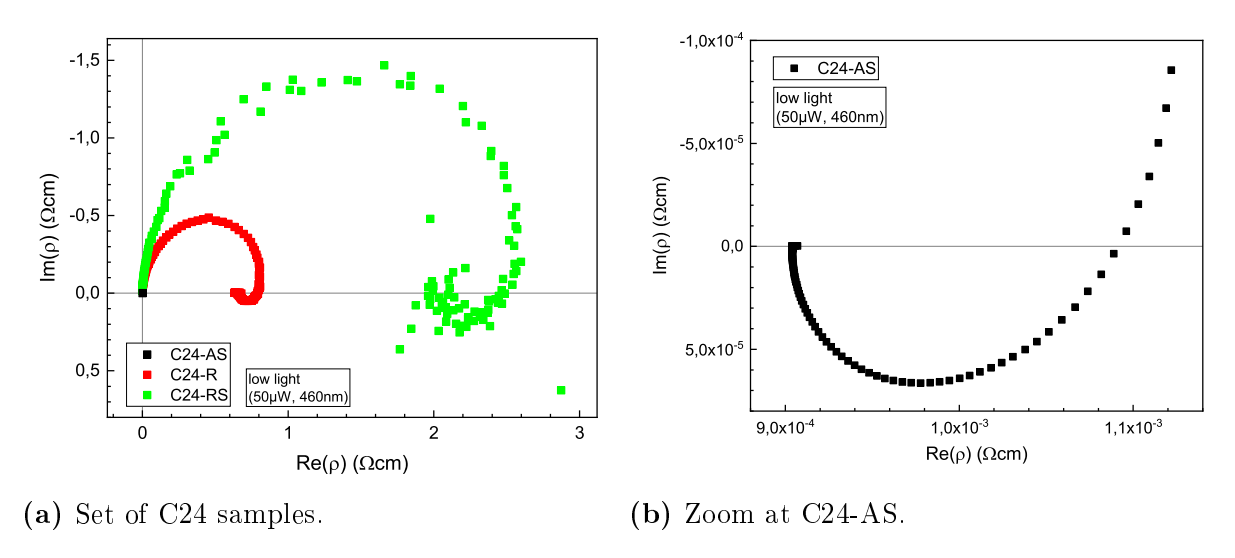


**Figure 5.3.10:** Nyquist plots obtained form  $\sigma_{AC}$  measurement (Fig. 5.3.8) at low irradiation (460nm (2.7eV), 50  $\mu$ W).

Nevertheless, the most conspicuous and perhaps crucial feature of those spectra is the low-frequency part, where the reactance (imaginary part) is positive. Those positive reactances are, in general, associated with inductive behaviour. The first and most obvious solution would be the influence of the measuring system, particularly the electrical connections, *electrodes*. It is not an uncommon problem for spectroscopy measurement, and it can lead to such inductive behaviour [240]. However, the measured inductance value for these frequency ranges would imply that there is a massive iron core transformer hidden somewhere in the measurement setup or that the setup is heavily uncompensated.

This inductive branch in the Nyquist plot originates from the negative slope in the DC part of the  $\sigma(\omega)$  dependency (manual artificial flattening removes the inductive loop completely). It is hard to conclude any physical interpretation of the phenomena at this point. It is non-trivial to bring an analysis within the frame of the chemical inductor (briefly presented in chapter 3.2.2) when we do not have a strong candidate for a physical process that can produce inductive behaviour. Moreover, a chemical inductor model implies the IV curve's nonlinear and/or hysteretic behaviour, which is not observed here (cf. Fig. 5.3.4). Linear IVs also exclude interfacial processes that could bring inductive loops. An ion displacement current could explain this phenomenon, but it is a broad implication to consider that  $CdIn_2S_4$  is a mixed conductor now. However, the

literature knows cases where the results of the  $CdIn_2S_4$  study were interpreted in terms of mobile ions: Ueno et al. ascribe the observed pinched hysteresis loop to the formation of conductive filaments [235], and Seki et al. credits his negative resistance observations to In ion displacement [205].

The last aspect worth mentioning is the illumination dependence of the inductive part. The Nyquist plots in the function of the illumination (from which Fig. 5.3.9 is also calculated) are shown in the appendix on page 336. The evolution of impedance spectra under illumination could both serve as an argument for bad measurement<sup>16</sup> and for light-dependent inductance-generating mechanism. This curious case, however, extends beyond the scope of this chapter, but we will revisit the issue in part 5.6.

### 5.4 Photocurrent measurements

In this branch of our inquiry, we will focus on the experiments regarding the photoexcitation kinetics that were described in chapter 3.2.3. The assumptions regarding the samples' geometry still apply. The quantities relating to photon flux  $(\Phi)$  and thus the photogeneration (f) were obtained by measuring the optical power using calibrated instruments and recalculated taking into account the sample area, thickness and absorption coefficient.

## 5.4.1 Lux-Ampere/PITCS measurement

We have performed PITCS experiments in a function of light intensity and temperature for the C24 set of samples using a modified setup from Fig. 3.2.2. We have used a 3W variable intensity LED illumination source with a wavelength of 460nm (2.7eV)<sup>17</sup>. It is the band-to-band transition for all of the samples at 300K. For each temperature we ran the measurement series (sweeped the light power) twice. After each temperature point, the sample was annealed to 320K, and only then cooled to the next temperature. The

 $<sup>^{16}</sup>$ as the light increases, the sample resistance changes, modifying the resultant RLC circuit.

 $<sup>^{17}</sup>$ The FWHM of the 460nm peak was <10nm; thus, we can consider the source as acceptably monochromatic

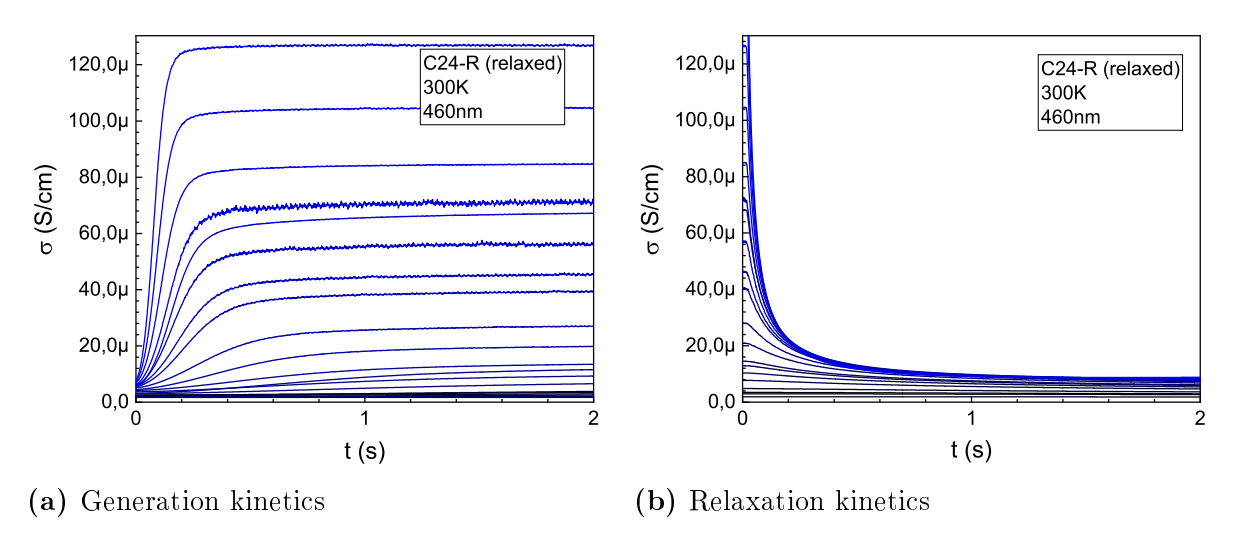


**Figure 5.4.1:** Illumination kinetics at various light intensities in range of  $10^{16} \div 10^{19}$   $1/\text{cm}^3$  at 300K for C24-R sample. dark stands for the state without the pre-illumination.

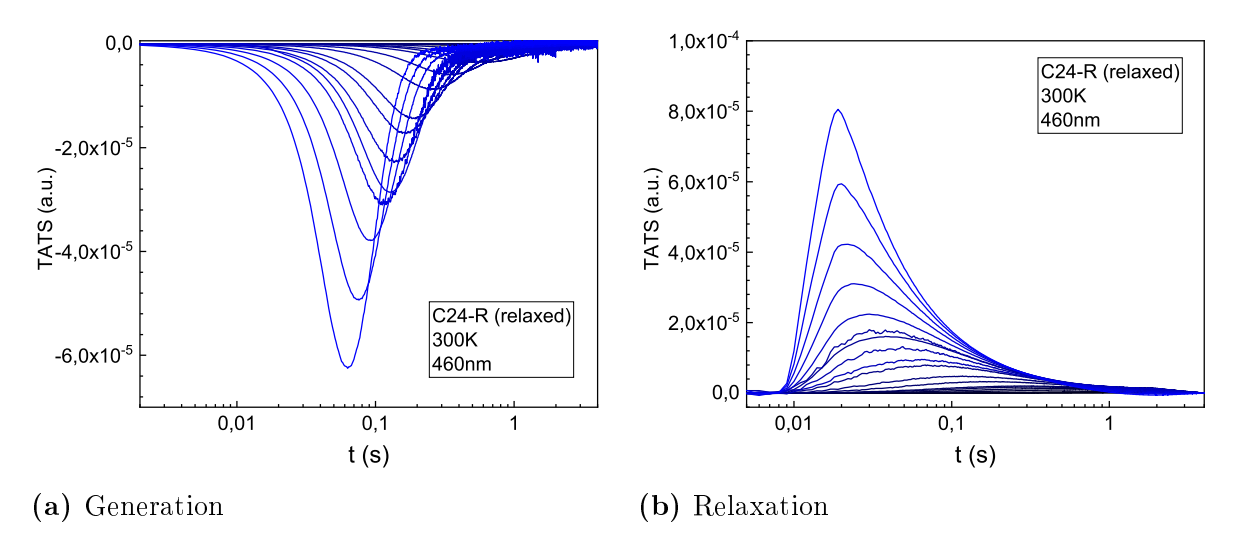


Figure 5.4.2: TATS analysis for various light intensity at 300K for C24-R sample.

measured light intensity was recalculated into a photon flux and then into the total incident generation rate (incorporating the volume of the sample and its absorption coefficient at this particular wavelength). We obtained a photocurrent kinetics series for various illumination intensities and recalculated it into photoconductivity. At room temperature, the amplitudes and transient times obtained from generation had the same values (or at least similar in the range of uncertainty) as those obtained from relaxation. In Fig. 5.4.1, we have shown the exemplary generation and relaxation kinetics for the

C24-R sample at 300K, that represent a typical set of kinetics. Using TATS analysis, we calculated processes' transient time constant  $\tau_0$ . The result of the TATS analysis we have shown in Fig. 5.4.2.

Herein, we will focus on the steady-state photoconductivity as a function of light intensity (Lux-Ampere measurement) in order to inquire about the formulations from chapter 3.2.3, that considers the n-f linkage. Fig. 5.4.3 shows the  $\Delta\sigma(f)$  relation of the measured samples at room temperature. Since the  $\Delta\sigma \sim \Delta n$  here, we can directly analyse  $\Delta\sigma$ , omitting the case of mobility values.

The  $\Delta\sigma(f)$  dependency in the C24-AS sample consists of three linear regions, starting with the linear part (slope  $\gamma=1$ ) for low light intensities, followed by two sublinear parts with  $\gamma=0.63$  and  $\gamma=0.4$ , respectively. Similarly, in the C24-R sample, the linear part is followed by two sublinear regions with slopes of 0.75 and 0.63. Lastly, in the C24-RS sample, only a singular sublinear part is visible, probably due to the limited range and resolution of the photocurrent measurement setup – it was impossible to obtain clear photocurrent transients at low light intensities due to the low signal-to-noise ratio. We would then expect to see a linear part for the sample annealed in sulphur at photon flux lower than  $10^{16}~1/\mathrm{cm}^3\mathrm{s}$ .

For the sublinearity analysis, we avail of the extended Rose model, presented in the chapter 3.2.3. As fundamental concepts expound, a defect level can act as a trap or as a recombination center depending on its position relative to the demarcation levels, either for holes  $(E_{Dp})$  or for electrons  $(E_{Dn})$ . Taking proper approximations, one is free to assume that  $E_{Dp} \approx E_{Fp}$  and  $E_{Dn} \approx E_{Fn}$ . Herein, we will straightforwardly move to our proposed interpretation in the Rose-Main model frame, that goes as follows: We posit the existence of trap distributions below the conduction band and above the valence band, having the characteristic temperatures  $T_C$  and  $T_V$  respectively. Those are type of distributions defined by formula (3.2.35). At low illumination, without additional recombination from filled traps (more precisely, when electron lifetime is constant) one will expect linear photoconductivity-intensity dependence – it is the case of equation (3.2.33). Increasing

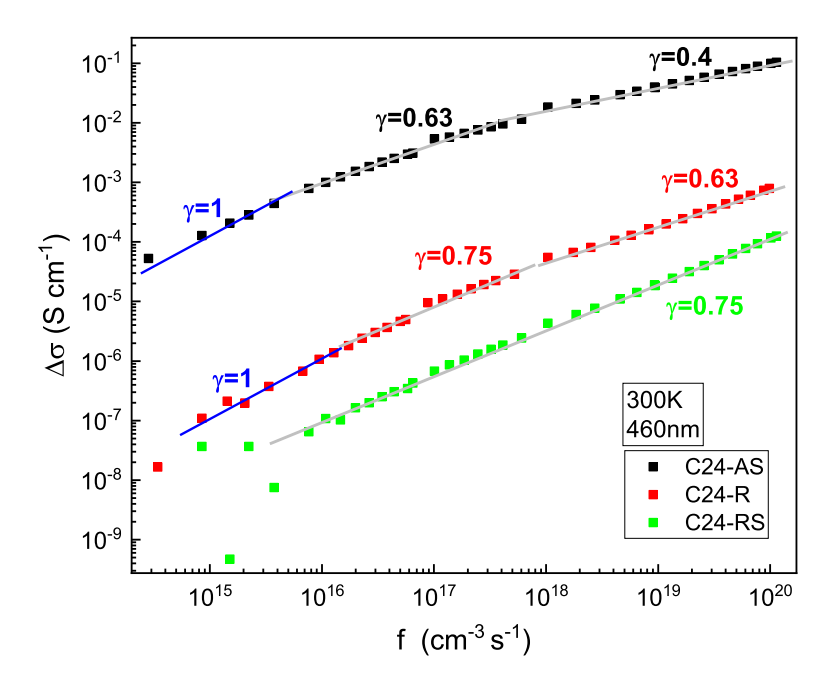


Figure 5.4.3: Photoconductivity in function of photogeneration rate at 300K.

the illumination causes the quasi-Fermi levels to sweep trough the traps distributions, increasing recombination at the expense of trapping and re-emission.

In the C24-AS sample, we observe a linear PC relation under low light conditions. As the light intensity increases,  $E_{Fp}$  enters the sub-VB band distribution  $T_V$ . Thus the photogeneration is governed by those states converting into recombination centers, and  $\gamma = \frac{T}{T_V}$ . Hence, we can calculate the characteristic energy of the distribution of the near-valence band states equal to 40meV. By further increasing the light intensity, states below EC begin to play a significant role, and  $\gamma = \frac{T_C}{T_V}$ . Knowing the value of  $T_V$  obtained from the intermediate slope, we calculated  $T_C = 16$ meV. Note that  $\frac{T}{T_V}$  regime starts to dominate first, as the quasi-Fermi level of the minority carriers will experience a much larger shift at the beginning of the light intensity increase. Sample C24-R behaves in the exact same way as C24-AS with slightly deviated characteristic energies:  $T_V = 30$ meV,  $T_C = 18$ meV. In the C24-RS sample, we can observe only one linear fragment, which we assign to the  $\frac{T}{T_V}$  regime. In the C24-RS sample, we expect that extending the light intensities, we would expect to observe a linear part. The  $E_{Fn}$  would shift enough for large light intensities to reach

sub-CB states, and the third sublinear part would be visible. Table 5.4.1 summarizes values obtained from Lux-Ampere characteristics and appoints the regimes governing particular regions of the photogeneration. As the values of  $T_V$  and  $T_C$  show, the distribution of sub-VB states is much broader in terms of energy. Nonetheless, we cannot infer the total concentration of states from those values alone. It only provides the basic information about the evolution of the distribution of states during annealing.

**Table 5.4.1:** Slopes obtained from the Lux-Ampere measurements with corresponding energies and relevant dominant regimes at 300K.

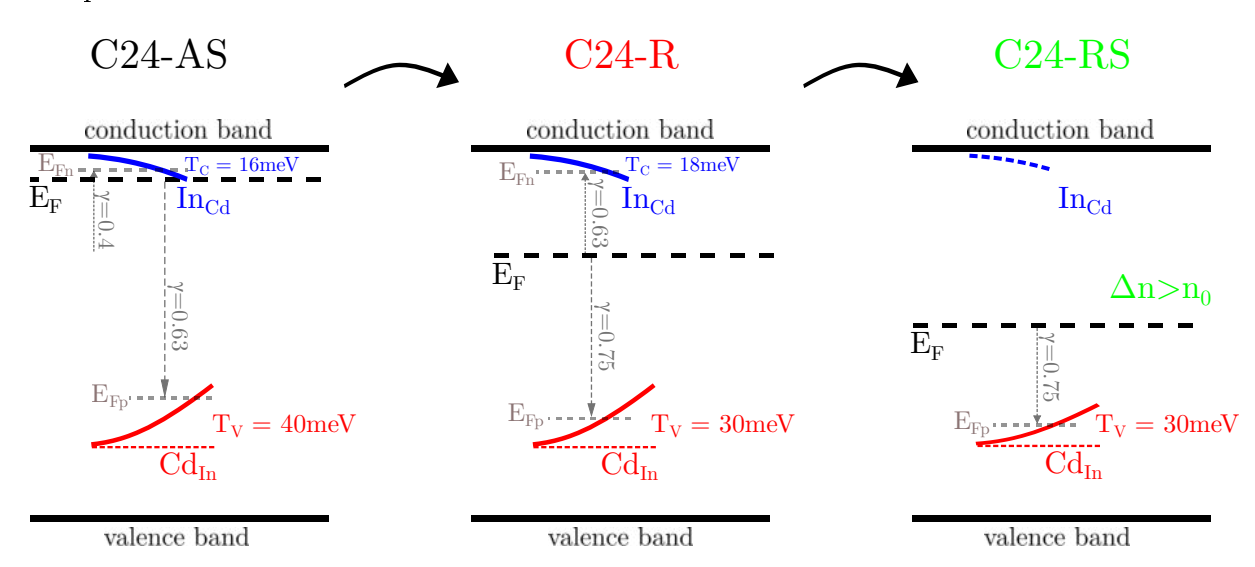
Sample	$\gamma$ (slope)	States involved	Regime
	1	-	band-to-band
C24-AS	0.63	$kT_V = 40 \text{meV}$	$rac{T}{T_V}$
	0.4	$kT_V = 40 \mathrm{meV}$	$rac{T}{T_V}, rac{T_C}{T_V}$
	0.1	$kT_C = 16 \text{meV}$	$T_V$ , $T_V$
	1	-	band-to-band
C24-R	0.75	$kT_V = 30 \text{meV}$	$rac{T}{T_V}$
	0.63	$kT_V = 30 \text{meV}$	$rac{T}{T_V}, rac{T_C}{T_V}$
	0.00	$kT_C = 18 \text{meV}$	$T_V$ ' $T_V$
C24-RS	0.75	$kT_V = 30 \text{meV}$	$rac{T}{T_V}$

It would now be desirable to assign the origin of the revealed trap distributions to the particular defects in  $CdIn_2S_4$ . Firstly, it seems more than evident that the sub-CB  $(T_C)$  states are the well-recognised T states - the defects originating from spinel inversion,  $In_{Cd}$  in particular. It is widely acknowledged in the literature that those antisites form a quasi-continuous density of states below the conduction band [25, 26, 217, 219, 229]. In fact, such distribution of defects below the conduction band was investigated by Anedda et al. [232] using the same methods as in this work, and similar value of  $T^*$  (39meV) was obtained. The sub-VB  $(T_V)$  states would be presumably the E states  $(Cd_{In})$ . The E defect seems to be the best candidate for this distribution, as it is located near the valence band and has a similar origin to  $T^*$ . Assuming this is true, a consistent picture emerges from evaluating the results. As the Fermi level differs between the samples, we observe different contributions from valence and conduction band distributions of states because quasi-Fermi levels' starting point moves toward the middle of the bandgap. Thus,

having the same light intensity range, we can scan only part of the distribution, which differs between samples. Simultaneously, with the annealing, the density of antisite In-Cd defects changes, further influencing the states' distributions. The general evolution of densities of states towards a clearer system during annealing implies a simple decrease of the concentration of T and E states induced by inversion, which stays in agreement with the findings from DC conductivity experiment (section 5.3.1). However, perhaps the most importantly, the three-part Lux-Ampere characteristics in C24-AS and C24-R samples imply that the suspected E states are indeed a distribution of states close to the valence band instead of a single defect state, as it was proposed by Charlebois et al. [25].

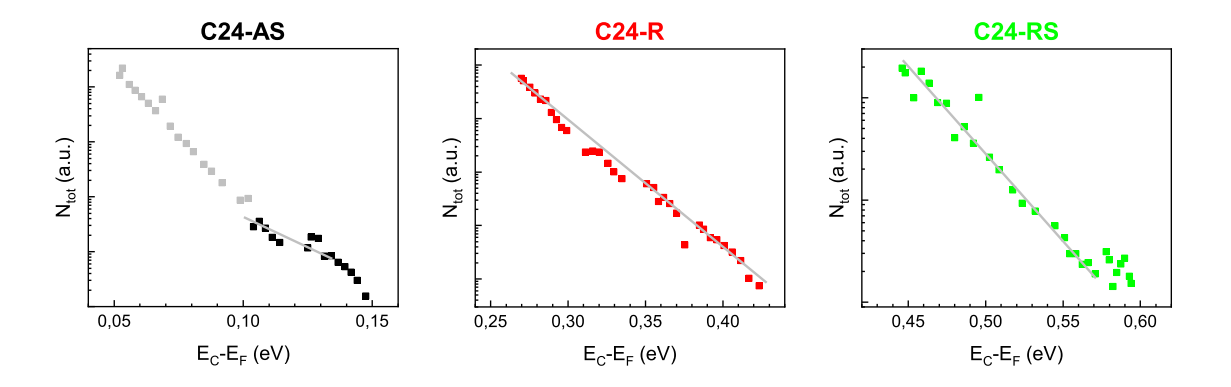
Lastly, it has to be pointed out that in the C24-RS sample, we are not able to infer the distribution of T states as we cannot reach sufficient light intensity level, or T states are non-existent in the material after annealing in sulphur. The latter would imply that the annealing in sulphur reduces  $In_{Cd}$  antisites more efficiently than the  $Cd_{In}$ .

Figure 5.4.4 shows schematically described mechanisms and differences between the samples.



**Figure 5.4.4:** Schematic representation of exponential densities of sub-bandgap states with respect to dark Fermi levels for the analysed samples, which we assign to  $Cd_{In}$  and  $In_{Cd}$  defects. As the Fermi level position changes between the samples, we can observe different parts of the distributions. From Lux-Ampere characteristics, we can obtain characteristic energies of particular distributions.

Having values of  $\sigma_{light}$ , parameters from 5.3.1, and transient times  $\tau_0$  (from the kinetics), we get carrier concentrations at steady state illumination. Then, we can attempt to calculate the distribution of states with the method shown by Bube et al. [238], and later applied by Anneda et al. [232] in the  $CdIn_2S_4$ , using the formulae (3.2.46) and (3.2.47). The free electron lifetime can be calculated from equation (3.2.26b). Thus, we can plot the profile of the distribution of sub-bandgap states  $N_t(E_{Fn})$  (Fig. 5.4.5). One should note that we cannot infer by any way which distribution we scan during the experiment. Therefore, if both exist, the resulting profile is a conglomerate of T and E distribution. The effective range of the distribution we can scan is again limited to the position of Fermi level – starting point, the range of light intensities used, and the total densities of states participating in the trapping-retrapping process. At the end of the profiles, the starting point should point to the dark Fermi level of the particular sample. In the C24-AS sample, the grey-coloured points are artefacts created by very short transient times  $\tau_0$ , impossible to measure in our current experiment setup. In general, the linearity of profiles in the semilog scale indicates that the densities are indeed exponential, as in equation (3.2.35). Since we are dealing with two distributions of states and are unsure about the exact concentration values (mobility issues, transients' nonexponentiality), we will refrain from further speculations on the concentration profiles.



**Figure 5.4.5:** Density of states profiles, calculated from equations (3.2.46) and (3.2.47) for set of C24 samples.

An additional element of the presented picture is the examination of the Lux-Ampere characteristics as a function of temperature. The equations (3.2.40) and (3.2.48) allow us to predict the temperature dependence of the  $\gamma$  parameter, assuming the rightness of the adopted model: The extended Rose-Main model predicts constant slope (when  $\gamma = \frac{T_C}{T_V}$ ) or linear temperature dependence. In the classic Rose model, the  $\gamma$  parameter depends approximately as  $\propto \frac{1}{T}$ , and  $\gamma$  is only in the  $0.5 < \gamma < 1$  range.

At all temperatures, our  $\Delta\sigma(f)$  dependencies are analogical to those obtained at 300K, shown in Fig. 5.4.3. We will, therefore, limit ourselves to presenting only the slopes at the highest photogeneration range. The  $\gamma$  coefficients are shown in Fig. 5.4.6. It can be observed that the  $\gamma$  increases significantly with temperature and reaches superlinear values—around 200K for samples C24-R and C24-RS. Only the classical Rose model predicts a decrease of  $\gamma$  as a function of temperature. We will then take the  $\gamma$  at 300K at face value, and determine the theoretical temperature dependence by the formula 3.2.40 (lines at Fig. 5.4.6). Here we observe a significant deviation from the Rose model (and from its extensions). Although classical models generally do not predict superlinear values of the  $\gamma$  coefficient, superlinear Lux-Ampere relations have been studied in the past, among others, by Richard Bube [159, 160, 166]. The source of superlinearity are usually sensitizing centers. Thus, we need an extended model that will describe the induction of the superlinear Lux-Ampere characteristics by sensitization in light of the defect states present in CdIn<sub>2</sub>S<sub>4</sub> and our findings.

Another approach is the analysis of  $\gamma$  in direct relation to the theoretical predictions of the Rose model. In other words, the analysis of the deviation of the measured coefficient from the theoretically predicted one. An excess or deficiency in the slope could be interpreted as an inflow or outflow of carriers relative to the theoretical, pure recombination as per the Rose model. A negative deviation would thus mean we open an additional illumination-dependent recombination channel that causes a dynamic decrease in the free electron concentration. Such a situation is approximately the Rose-Main expansion, which yields  $\gamma = const$  in its extreme version. A classic parallel recombination channel after the fashion of SRH recombination would also fit. In turn, a positive

deviation would imply, that we witness an additional influx of charge carriers from parallel sources. This situation occurs in the C24-AS sample – in the temperature range from 160K to room temperature. In some exceptional cases, it could be an increased generation, but it also could be a horizontal transmission from another defect. This is reminiscent of the tunnelling from the sulphur vacancy to the T states postulated by Grilli et al. [217]. This tunnelling is marked on the band diagram as the dotted arrow between T and V (Fig. 4.3.2). Therefore, in C24-AS sample in range  $160 \div 300 \text{K}$  the mutual arrangement of defects and the Fermi level position would cause the charging of T states from the sulphur vacancy. In fact, appropriate equations have to be made to support such a bold statement; however, as we believe, by deduction, a proper external charging of sub-bandgap states would have to result in a superlinear Lux-Ampere dependence.

From the measurements in section 5.3.3, we found that the illumination induces metastable transition, increasing the conductivity of the sample. Let us then take advantage of the fact that we performed the Lux-Ampere measurements twice, so we can observe the possible change of the  $\gamma$  values—after the sample has been partially turned into metastable state by illumination<sup>18</sup>. As can be seen (Fig. 5.4.6), exposure to light causes a general decrease<sup>19</sup> in the  $\gamma$  coefficient. Moreover, at 300K,  $\gamma$  does not change its value after illumination—and that is why we (as it turns out, reasonably) assumed that the determined values—of  $T_C$  and  $T_V$  at 300K are closest to the real values, i.e. undisrupted by the metastability.

The illumination-induced change clearly implies that mestability must somehow control the superlinear response of the sample. As we suspect sulphur vacancy as the culprit for the metastable effects, the hypothesis of charging by tunnelling still holds; however, in the face of this finding, one should consider the influence of the experiment

<sup>&</sup>lt;sup>18</sup>The illumination intensity and exposure were high enough to consider the sample as being in the saturated metastable state. It will be shown that the applied exposure was probably insufficient to saturate the sample completely. To remove any unwanted artefacts, we annealed the samples after each temperature measurement, as the annealing is currently the only known method to reset the sample.

 $<sup>^{19}</sup> But$  in the C24-RS sample  $\gamma$  slightly increases. This is an important fact, which we will use later.

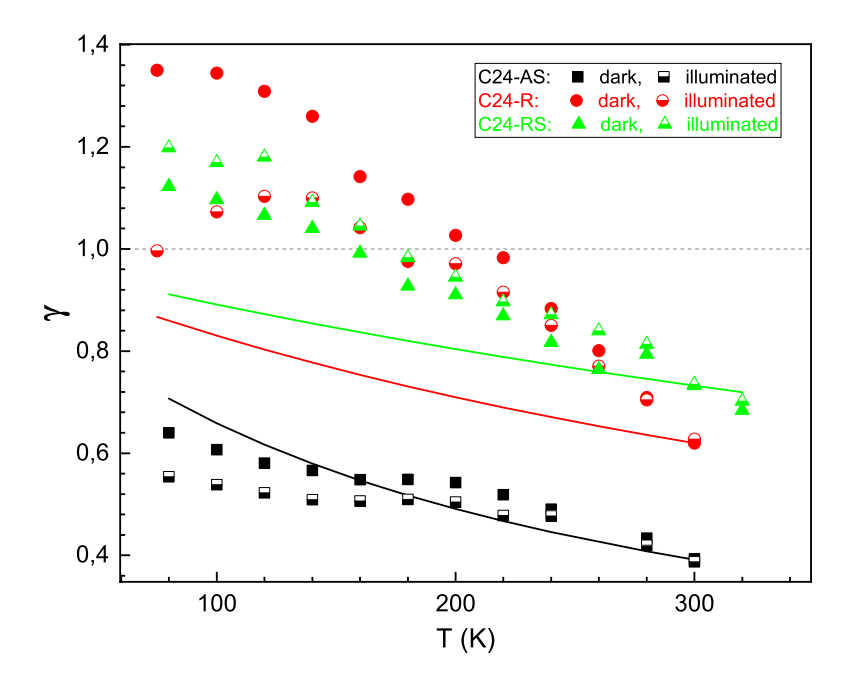


Figure 5.4.6: Slope of the Lux-Ampere characteristics in function of temperature. Semi-filled symbols represent measurements done after illumination at given temperature. Lines show theoretical value of  $\gamma$ , predicted by equation (3.2.40).

itself on the sample: illumination, probably at any intensity, affects the metastable state of the sample. Thus, the subsequent measurement in the series of illumination intensities will always face the sample in a slightly changed state. So, if we assume that illumination somehow changes the resultant value of  $\gamma$  (and it does), the resulting superlinearity will be an artefact originating from the measurement method itself. This does not mean that its value carries no information –  $\gamma$  can still be analysed by the reasoning presented earlier, as a relative deviation from the theoretical slope coefficient<sup>20</sup>. Except that, we now know its cause, which is metastable effects. Again, the construction of appropriate equations, this time extended to include the dynamic recharging of metastable defects, should be able to predict the superlinear Lux-Ampere coefficients. Finally, the observations presented bring one more piece of evidence: charging metastable defects causes an overall reduction in recombination. We will return to this case in section 5.5.

<sup>&</sup>lt;sup>20</sup>Or as a time-dependent parameter analysed within a fixed time window.

Lastly, we are obliged to address one key issue, which has been unaddressed so far: the non-exponentiality of photoconductivity kinetics. A cursory look at the kinetics shown in Fig. 5.4.1 shows a serious deviation from the exponential dependence. Indeed, TATS analysis gives  $\beta > 1$  (in some part of the photogeneration range), i.e. the transient function is a compressed exponential (calculated  $\tau_0$  and  $\beta$  values for 300K are shown in the appendix on page 338). This fact puts kinetics-based analysis into question, as the calculated response time might also be affected. Also, none of the models described in chapter 3.2.3 cannot be applied, as those assume stretched exponentials or power dependencies. None of those satisfactorily fit our photocurrent kinetics. The model of Nelson-Shimakawa [125] (vide page 71) assuming dispersive transport based on the continuous-time random walk, could explain the non-exponential kinetics in the frame of the distributions of T and E sub-bandgap states found here, but it assumes  $\beta < 1$ , thus it does not apply.

However, suppose we accept the hypothesis of a decreased recombination current induced by metastable defects. In that case, the presence of compressed exponent kinetics becomes logical: the sample should show a dynamically increasing photocurrent value for the same reason as it shows an increasing photocurrent in the steady state, i.e. superlinearity – no matter the time period. The photocurrent transient would be accelerated as the opposing force decreases during time – by gradually charging the metastable defects. Again, solving this problem requires finding an applicable model and relation of the form  $\frac{\mathrm{d}n}{\mathrm{d}t} = f - R(n, f, t)$ , where R represents alleged time-photogeneration-dependent recombination function.

## 5.4.2 PITCS-wavelength measurement

The  $\Delta\sigma$  measurement in the function of wavelength and temperature is perhaps the most influential experiment in our material investigation. It provides essential evidence and greatly influences the CdIn<sub>2</sub>S<sub>4</sub> model.

The method of measuring  $\Delta\sigma(\lambda)$  is described in chapter 3.2.3. Similarly, as in TSC experiments (cf. section 5.3.3), next to dark (relaxed) measurements we applied two types of pre-illumination (in the basic set of experiments) – the illumination was applied while cooling down (EWC) or at low temperature (LNT) and then, a series of measurements in a temperature range was made afterwards. The illumination source was the 460nm power LED used before.

In appendix on page 339 we have shown the photoconductivity transients for C24-R sample at in the relaxed state: in function of wavelength at single temperature 300K and in function of temperature for single wavelength respectively. Those kinetics can serve an an exemplary result of the experiments. Similarly to the Lux-Ampere transients, the TATS analysis (figure on page 340) was preformed in the way described in chapter 3.2.3.

A typical set of  $\Delta\sigma(\lambda)$  spectra (obtained from generation kinetics) is shown in Fig. 5.4.7. It shows the type of spectra evolution common for all samples, temperature scans and wavelength sweeps. In other words, the characteristic elements of the spectra, which will be presented shortly, appear in most cases in all samples and instances of the experiment.

The spectra can be divided into three main parts regarding the temperature dependence of the photoconductivity: the part where  $\Delta \sigma$  is a steadily increasing function of temperature, up to roughly 2.6eV, followed by the second part, where the  $\Delta \sigma$  gets quenched above a specific temperature value (later, it will be shown, that the cut-off photon energy is the value of the direct bandgap). The temperature, where an inflexion of  $\Delta \sigma$  above 2.6eV is observed, is found to be 160K. The third part is the drop in photoconductivity above 3eV.

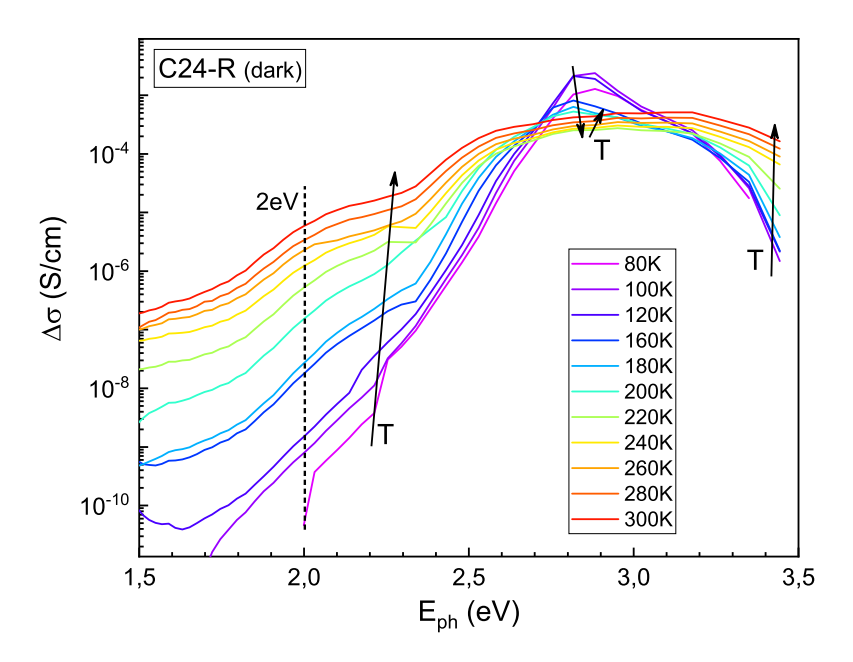


Figure 5.4.7: Photoconductivity in function of wavelength. An example for C24-R dark (relaxed). An exemplary case for the  $\Delta\sigma$  spectra observed in all of the samples. The temperature evolution is highlighted by the arrows. Multiple processes are visible there: increase in amplitude with rising temperature in the excitation range below  $\sim 2.6eV$ , the quenching above the bandgap, and the de Vore effect above 3eV.

The first part – energies below 2.6eV can be definitively considered as a sub-bandgap. According to the literature revised in chapter 4, we should expect at least three transitions from defects states into CB (1.45eV, 2.2eV and 2.3eV). Instead, we observe a rather blended continuous increase in photoconductivity over excitation energy. The only peak mentioned in the literature that could be tentatively recognised here is the  $2.1\sim2.2eV$  peak, an excitation from E states into CB. It is hard to infer why we do not see the other peaks. A possible explanation could be the polycrystallinity of the examined films (as opposed to the single crystals studied in the literature), the excitation peaks are broad enough to overlap, creating such continuos increase. The high disorder present in the compound might be a natural cause, and a reason why we observe such a broad photoconductivity response below the bandgap in the first place.

The second part – in which we observe a more peculiar temperature dependence, is

the direct outcome – as we deem – of the effects explained in the section 5.4.1. When the photon energy approaches bandgap energy – absorption rises dramatically, resulting in  $\Delta \sigma$  increase, causing the effects, described more broadly in 5.4.1.

The third part – the drop in photoconductivity above 3eV – is the most probably caused by the de Vore effect [241]. Such peak-like photoconductivity shape is widely observed in semiconductors, including  $\text{CdIn}_2\text{S}_4$  [26, 218, 229, 232, 242].

Here, we should revisit the band diagram (Fig. 4.3.2), presented in chapter 4. As the photoconductivity is sensitive to every excitation that ends with a change in free electron or hole concentration, we should observe (next to bandgap) any generation from or to conduction or valence band. Next, the signal amplitude would be proportional to generation efficiency (transition probability) and recombination currents or lifetime (according to equation 3.2.25). In  $CdIn_2S_4$ , we should observe those three mentioned transitions: 1.45 eV – excitation from  $V_{\text{Cd}}$ ; 2.2 eV – excitation from E state and potentially 2.35 eV – excitation from valence band to V, followed by tunnelling to T states and emission to CB. The last path is particularly non-trivial as it involves a rather complicated electrons journey, with each transition potentially having a certain emission efficiency. Given the knowledge from section 5.4.1, we should take into account the conclusions that follow from it, namely, the presence of a given distribution of states should give a diffused excitation spectrum, which is a resultant of the presence of the density of states (and the position of the Fermi level). Thusly, the literature's peak of states E should now be broad in energy. Further, a similar broadening of the excitation spectrum should result from other potential transitions that can occur here: an excitation from the density of E states to the density of T states and further from the valence band to the T states, resulting in a complete blurring of any expected peak-like dependence in the ~ 2eV excitation band.

Moving on to temperature dependence of  $\Delta \sigma$ , one must ask oneself why we observe temperature dependence on photoconductivity in the first place. The  $\Delta \sigma$  should be weakly temperature dependent [155]. A  $\Delta \sigma$  change in temperature observed below the bandgap is the most probably due to temperature-dependent  $\mu\tau$  product. As no significant difference in mobility is expected, the main contribution to the observed change is the difference in carrier lifetime, according to the eq. (3.2.25), that directly controls the amplitude of the photoconductivity [155]. It is then the recombination that mainly controls the photoconductivity in this range (and the second range, as described in the section 5.4.1).

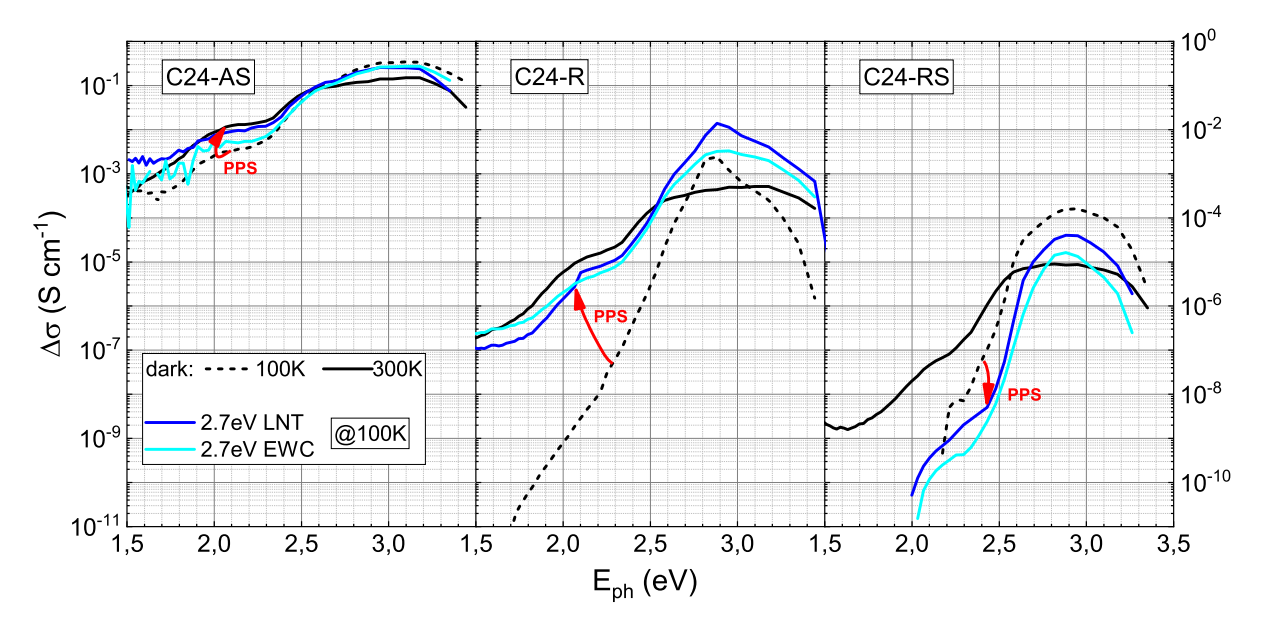


Figure 5.4.8: Photoconductivity in function of wavelength for C24 samples, calculated from generation kinetics. Black lines – dark (relaxed) photoconductivity spectra at 100K (dotted lines) and 300K (continuos lines). Blue lines – metastable state at 100K.

The mentioned gradual degradation of the photoresponse after annealing in vacuum and in sulphur, respectively, can be observed here. Note, that the illuminated C24-R sample at 100K from being more similar to C24-RS starts to resemble C24-AS sample.

The difference in photoconductivity between C24 samples is similar to that of DC conductivity. The C24-AS sample shows the highest amplitude of  $\Delta\sigma$ , C24-R – intermediate, and C24-RS – the smallest photoresponse. As stated before, the temperature and photon energy evolution are similar among the samples. The comparison of the samples is shown in Fig. 5.4.8. Again, the  $\Delta\sigma$  amplitude limiting factor is the recombination. Hence, its domination is the strongest in the C24-RS sample and the weakest in C24-AS.

The effects of pre-illumination on photoconductivity are second, after TSC, case of metastable photomemory observed in the samples. Herein, we witness persistent photosensitivity (PPS) – an increase in photoconductivity amplitude upon illumination. In Fig. 5.4.8, besides the comparison between C24 samples, we show the effects on illumination at 75K (LNT) and while cooling (EWC). In the C24-AS sample, although hardly visible in Fig. 5.4.8, the PPS is the strongest among the samples. A similar situation occurs in the C24-R sample. In both samples, pre-illumination increases the low-temperature photoconductivity up to the values present at high temperatures. In other words, the metastable state removes the mentioned conspicuous activation of photoconductivity below the bandgap. The bandgap quenching also disappears<sup>21</sup>. In the C24-RS sample, we do not observe any increase in photocurrent; on the contrary – PPS is slightly negative. However, in all cases, illumination produces identical effects, regardless of whether it is EWC or LNT. It is worth noting a certain regularity in the C24-R sample: In the relaxed state, it behaves like C24-RS, having only an order of magnitude greater photoconductivity. In the metastable state, by contrast, it more resembles the C24-AS sample.

To investigate the sub-bandgap generation spectra, we will analyse its activation dependence at one particular excitation energy. For samples C24-AS and C24-R, an energy of 2eV was chosen, while for C24-RS: 2.3eV – for the C24-RS, energies below 2.2eV were not measurable at low temperatures. We are aware that we might be comparing different entities, but we are interested in the overall behaviour of the samples, not a response from a particular energy. Second, the activation energies have close values—for a wide range of excitation energies (which has been verified). Fig. 5.4.9 shows an Arrhenius plot of  $\Delta \sigma$  for chosen excitation energies. The plot illustrates the effects of PPS in more detail: Starting from the C24-R sample, in a relaxed (dark) state, the  $\Delta \sigma$  exhibits a temperature activation with  $E_A \approx 100$ meV (red line in Fig. 5.4.9). When the sample is in a metastable state, the photoconductivity becomes very weakly activated ( $\approx 15$ meV, orange dotted line

<sup>&</sup>lt;sup>21</sup>Although, in the relaxed state is not present as well.

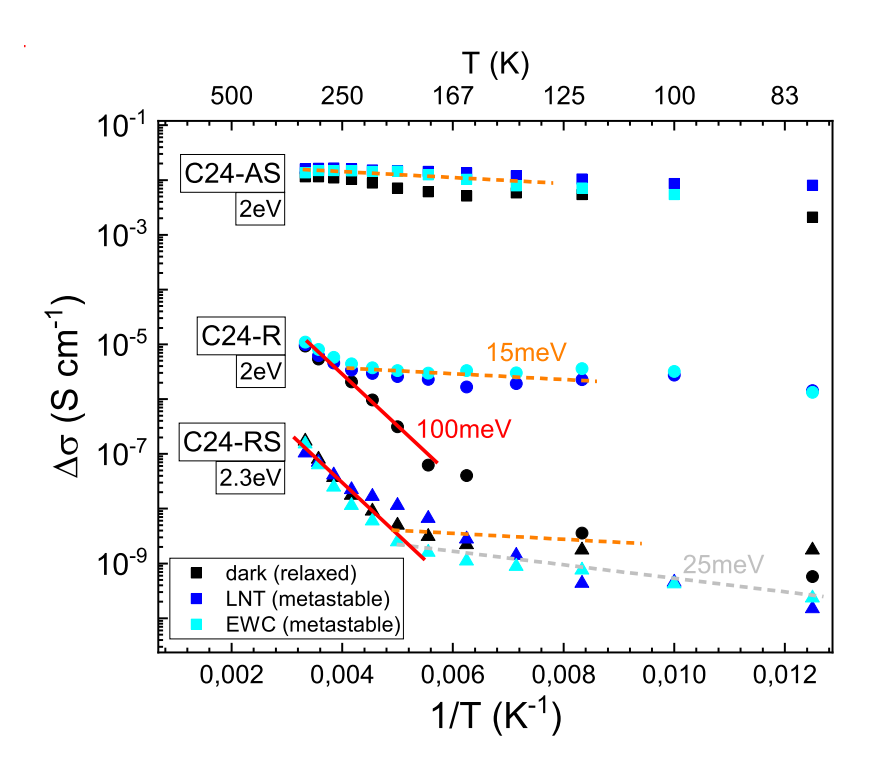


Figure 5.4.9: Arrhenius plot for  $\Delta \sigma$ . The lines highlight the regime the sample falls into and roughly mark the linear parts of the temperature dependence, indicating particular activation energy. Both the red lines and all three orange lines are parallel to each other.

in Fig. 5.4.9), keeping a value close to the dark  $\Delta \sigma$  at 260K. This is the visible (Fig. 5.4.8) low temperature  $\Delta \sigma$  increase close to room temperature value. Above this point, the metastability anneals out and the  $\Delta \sigma$  and follows the dark photoconductivity. This plot also shows that inducing the C24-R sample into a metastable state causes the sample to switch from the C24-RS-like state to the C24-AS-like state, only with a difference in the photocurrent value.

The C24-AS sample (in relaxed conditions) is already in a state that resembles a metastable state of C24-R – the illumination introduces only a relatively minimal increase, bringing up the activation dependence to  $E_A \approx 15 \text{meV}$ .

In the C24-RS sample, the metastability behaves in an opposite way: the dark (relaxed) conditions keep 15meV, and illumination decreases the photoconductivity, increasing the activation energy, but only up to 25meV. The C24-RS samples experience a negative PPS. Slight, nonetheless visible on the Arrhenius plot and excitation spectra (Fig. 5.4.8).

Before we move on to the interpretation of the PPS and further matters, there are a few issues necessary to consider:

The first issue is the case of the nonexponentiality of the photocurrent kinetics, which are, in this case, compressed exponential kinetics, similar to the circumstance of the Lux-Ampere characteristics. Appendices (page 340) show parameters obtained by TATS analysis of photocurrent kinetics for the C24-R sample (exemplary case). The questions and problems mentioned in section 5.4.1 still hold here.

The second is the influence of the preceding kinetics on the measurement based on them. One can point at an increasing value of  $\sigma_0$  with each kinetic in the figure on page 339 as confirmation of these suspicions. It is actually the exact same problem as in Lux-Ampere measurements and similarly puts the facticity of the obtained results in question. It probably means that the dark (relaxed) photoconductivity spectrum is not entirely relaxed but carries certain memories of previous excitations. Therefore, the activation energies obtained are probably not entirely correct. Nevertheless, the effect is not significant enough to discard the measurements' results completely.

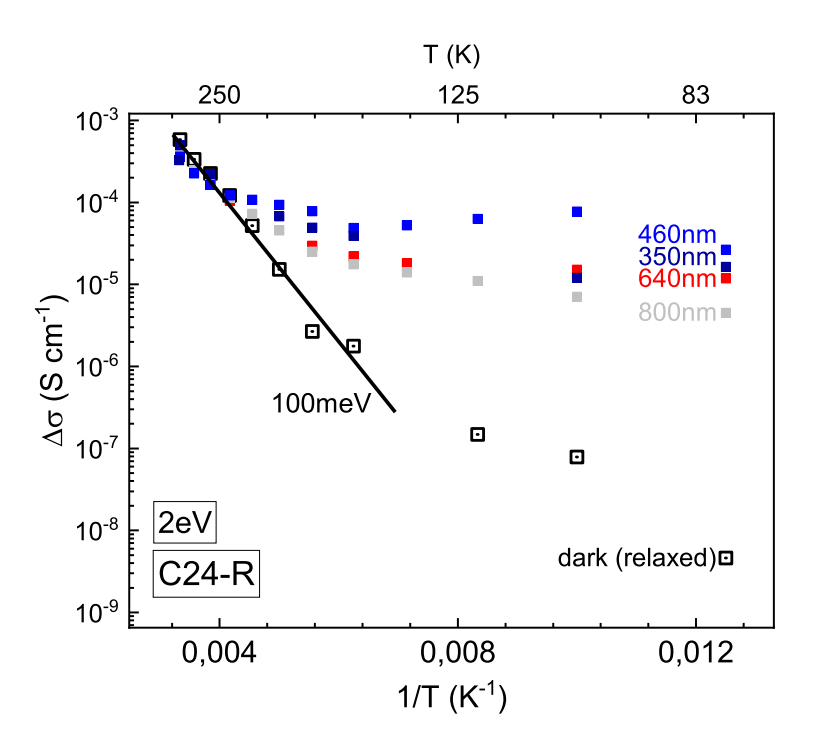


Figure 5.4.10: Arrhenius plot for  $\Delta \sigma$  for 2eV for C24-R with various pre-illumination sources applied at LNT.

The third issue is the determination of the excitation energies that can induce the metastable state. Such knowledge might be crucial to unveiling the mechanism that governs metastable phenomena. To explore the problem, we repeated the experiment on the C24-R sample in the LNT pre-illumination variant multiple times, using multiple high-power sources, having the energies (wavelengths): 1.5eV (800nm), 2eV (640nm), 2.7eV (360nm) and 3.5eV (350nm). The procedure was the same in each reiteration. As the figure 5.4.10 unveils, every applied source caused the C24-R sample to turn into a metastable state. Moreover, we have found that the amplitude of the PPS strictly varies with the illumination intensity; furthermore, each source used, caused photocurrent generation. Upon that, we postulate that any illumination, that contributes to photoconductivity will also contribute to metastability.

## 5.4.3 Bandgap determination

From the photoconductivity spectra, we can obtain bandgap values by calculating the  $(\Delta\sigma)^2$ , and  $(\Delta\sigma)^{1/2}$ , as it was described in chapter 3.2.3. Assuming  $\Delta\sigma \sim \alpha$  (absorption coefficient), bandgap values can be obtained using the same method as for the absorption coefficient. The intersection of a line fitted to the linear part of  $(\Delta\sigma)^2$  slope gives a direct bandgap value. Plot of  $(\Delta\sigma)^{1/2}$  yields two linear parts. Fitting the slopes in the same manner as previously yields values of  $E_{indir} - E_{phonon}$  and  $E_{indir} + E_{phonon}$ . Due to the transition at 2÷2.35eV, present in the samples, that significantly contributes to photoconductivity spectra, it is practically impossible to find the real value of  $E_{indir}$ , as the linear part corresponding to  $E_{indir} - E_{phonon}$  is usually partially or fully covered by  $E \to CB$  transition. Albeit, expected phonon energy should be low enough to neglect, therefore:

$$E_{indir} = \frac{(E_{indir} - E_{phonon}) + (E_{indir} + E_{phonon})}{2} \approx E_{indir} + E_{phonon}$$
 (5.4.1)

The fits – a source of the bandgap values in a function of temperature are given in the appendix on page 341. In Fig. 5.4.11, we have shown the obtained results.

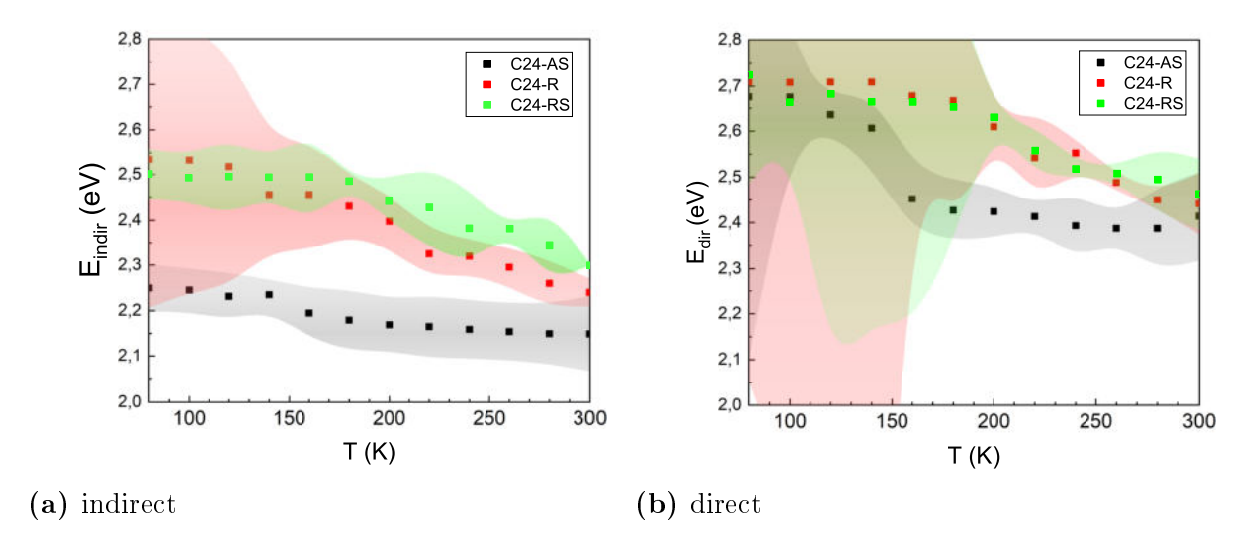


Figure 5.4.11: Temperature-bandgap dependence for C24 samples. Left: indirect bandgap; Right: direct bandgap. Annealing process causes increasing the bandgap. Values of C24-R and C24-RS locates closely to each other in the scope of uncertainty.

In the 150÷300K temperature range, one can see a clear distinction between the C24-AS sample and the C24-R and C24-RS samples. The second two samples have distinguishably higher bandgap values than C24-AS, and the difference extends beyond the uncertainty bands. Uncertainty overlaps for the second two samples (C24-R and C24-RS), thus the difference is not statistically significant. Nevertheless, we can observe the difference between the as grown sample and the other two. The indirect bandgap values in C24-AS however, are smaller, than the values found in the literature. In the 150÷300K temperature range, one can see a clear distinction between the C24-AS sample and the C24-R and C24-RS samples. The second two samples have distinguishable higher bandgap values than C24-AS, and the difference extends beyond the error bars. Uncertainty overlaps for the second two samples (C24-R and C24-RS). Thus, the difference is not statistically significant. Nevertheless, we can observe the difference between the C24-AS sample and the other two.

A sudden leap at 150K in  $E_{dir}$  for the C24-AS sample might be the mentioned 2.35eV transition, which appears to start to cover the direct bandgap. It is then possible that the values of direct bandgap above 150K are invalid, and we could have made the same

blunder as the authors mentioned in chapter 4.2.1. It would then mean that the 2.35eV transition activates as an optical excitation line above 150K, similar as in the paper of Grilli et al. [217]. Nevertheless, the indirect bandgap is not affected by that suspicious event, and its decrease in temperature does not indicate any discontinuities.

Considering the source of bandgap increase upon the annealing, we bring the aforementioned paper of Seminóvski et al. [207], in which simulations were performed showing how the degree of spinel inversion affects the value of the bandgap. Hence, we postulate that the decreased bandgap values in C24-AS samples directly result from increased spinel inversion in as grown CdIn<sub>2</sub>S<sub>4</sub> thin-films. It means that CdIn<sub>2</sub>S<sub>4</sub> is grown already with a significant degree of inversion in the deposition (PVD) process. In other words, the CdIn<sub>2</sub>S<sub>4</sub> is being synthesized in nonequilibrium conditions, resulting in an increased concentration of antisite Cd-In defects. Only annealing leads to the relaxation of the cationic sublattice and a reduction of the spinel inversion by ordering the indium and cadmium atoms. Adding sulphur during annealing obviously does not contribute to the sublattice ordering process. Hence, there is no difference in the bandgap between the C24-R and C24-RS samples. According to Seminóvski et al. calculations, a spinel with such bandgap values has the inversion degree at relatively small range 0 < x < 0.1 (vide Fig. 4.2.2). The decrease of inversion degree and resulting antisite defect concentration upon annealing generally agrees with findings from photoluminescence and DC conductivity experiments.

# 5.5 Investigation of metastable phenomena

This section will finally address the issues regarding sample metastability, which has been notoriously recurring throughout this chapter: PPC and PPS phenomena. Our initial suspicions regarding metastability were due to the influence of sulphur: As the effects of metastability change dramatically after annealing in sulphur (in the sample C24-RS), we infer that it is the sulphur, precisely sulphur vacancy, responsible for the observed metastability. Next, after carefully analyzing the paper of Péan et al. [22], we have

pinpointed one particular defect complex:  $V_S$ -Cd<sub>In</sub>, that has  $\epsilon(+/-) = 1.94eV$  regarding the valence band. After normalizing the Fermi level positions (Fig. 5.3.3) with respect to the valence level – by taking into account the measured bandgap values from section 5.4.3, we found that the pinned Fermi level for C24-R falls almost precisely at the level of  $\epsilon(+/-)$  for this complex. That is why we assumed in chapter 5.3.1, that  $V_S$ -Cd<sub>In</sub> pins the Fermi level in C24-R. We have divided the metastability analysis into PPC and PPS parts, although, as the reader will see, those two phenomena originate from one source.

#### 5.5.1 Persistent photoconductivity

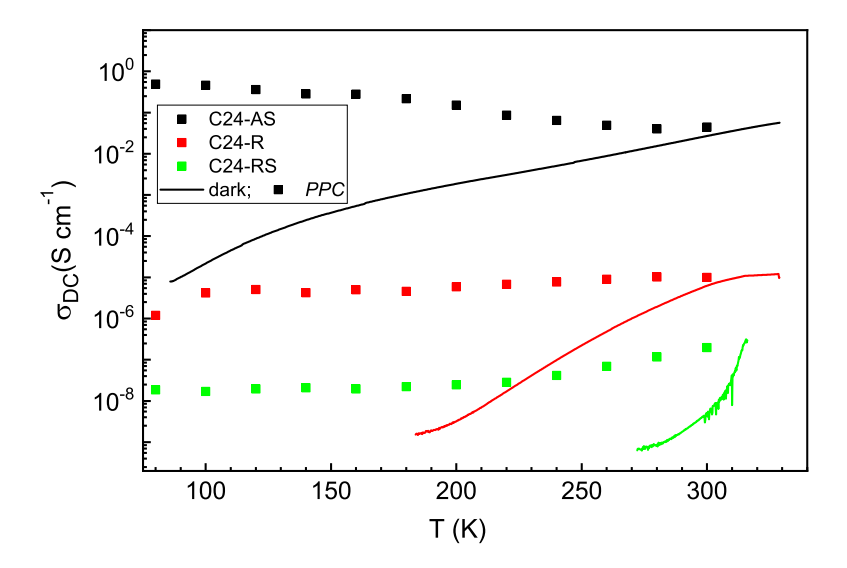


**Figure 5.5.1:** Alleged PPC in C24 samples. Comparison with the DC conductivity measurements from section 5.3.1.

The PPC is probably the most elusive phenomenon mentioned by us, as we do not yet present any direct evidence for its existence. Its presence can be spotted in Fig. 5.4.1 in which the relaxation kinetics do not decay into the initial  $\sigma_0$  value. This effect is more prominent in kinetics in the function of photon energy from the appendix on page 339. However, it is not a persistent effect that lasts *forever* at low temperatures (as in the case of more typical PPC examples), but a very long relaxation that can be empirically described by the formula (3.1.7). The PPC persists for several minutes – it allows, after

turning off the illumination and waiting for a while, to measure the TSC curve that starts from the conductivity level close to relaxed  $\sigma_0$  (at least for C24-R sample) – vide Figure 5.3.6<sup>22</sup>. Let us then determine the values of  $\sigma_{PPC}$  from the relaxation kinetics right after taking down the light excitation, precisely 4 seconds after the illumination was removed. The Figure 5.5.1 shows, that we are dealing with the PPC indeed. The  $\sigma_{PPC}$  keeps the room temperature conductivity level and anneals out near 300K. It should be noted again, however, that these are values—from one specific moment in time during photocurrent relaxation. More importantly, it turns out that PPC is also present in a similar magnitude in the C24-RS sample, which seems to contradict our initial assumption that annealing in sulphur removes (or radically modifies) metastability.

Nonetheless, having the current knowledge about samples, metastable defect complexes, and PPC behaviour, we can attempt to construct a model for PPC:

In the C24-AS sample, the Fermi level is pinned at  $\approx 0.1 eV$  below the conduction band. It means that the Fermi level is above  $\epsilon(+/-)$  of the V<sub>S</sub>-Cd<sub>In</sub>; thus, the complex is in a negative state, occupied by two electrons. Similarly, in C24-R, where E<sub>TR</sub> pins the Fermi level, the V<sub>S</sub>-Cd<sub>In</sub> defects stay in 50:50 occupation. Suppose we generate two electron-hole pairs by illumination. Those two holes in the valence band now have a certain probability of being captured by the V<sub>S</sub>-Cd<sub>In</sub> (having a hole capture energy barrier  $\Delta E_{HC}$ ), according to the formula:

$$(V_{\rm S} - {\rm Cd}_{\rm In})^- + 2h + 2e \rightarrow (V_{\rm S} - {\rm Cd}_{\rm In})^+ + 2e$$

By the hole capture, the defect converts to the positive charge state, two surplus electrons remain, and the Fermi level move up; the whole system persists in this state, as there is a barrier for hole emission (or electron capture) caused by the lattice coupling. Returning to the previous charge state requires the activation of a  $\Delta E_{HE}$  ( $\Delta E_{EC}$ ) barrier for hole emission (electron capture). Thus, above a certain temperature, where this

<sup>&</sup>lt;sup>22</sup>On the other hand, it could be argued that the real PPC is the difference visible in the Figure 5.3.5 – significant for the C24-AS sample, but below one order of magnitude for the C24-R sample

transition becomes more favourable, a relaxation occurs:

$$(V_{\rm S} - {\rm Cd}_{\rm In})^+ + 2e \rightarrow (V_{\rm S} - {\rm Cd}_{\rm In})^-$$

This mechanism will take place in the C24-AS sample and the C24-R sample (but in smaller magnitude, as there are at least 2x fewer defects in the negative state), generating two additional free electrons.

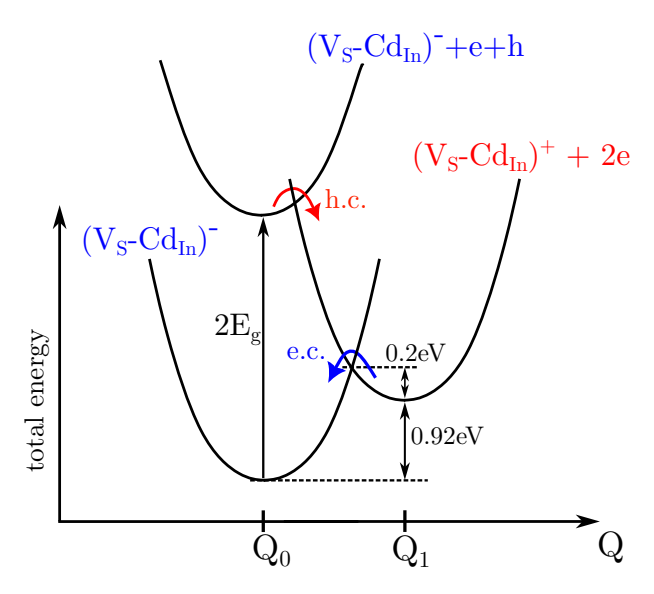


Figure 5.5.2: Coonfiguration-coordinate diagram proposition for V<sub>S</sub>-Cd<sub>In</sub> complex. We plotted the approximate value of electron capture barrier, that will be revealed in the next section.

The V<sub>S</sub>-Cd<sub>In</sub> is a negative-U defect. Thus, the negative state is deeper and more stable than the positive state due to large lattice relaxation. The  $\Delta E_{HC}$  needs to be low enough so the hole capture is efficient at 75K, and  $\Delta E_{HC} < \Delta E_{EC}$ , that the metastable positive state can persist in a temperature range. At this point, we can propose a configuration-coordinate diagram for the V<sub>S</sub>-Cd<sub>In</sub> system (Fig. 5.5.2) (we simplified the energy dependencies to parabolas, however, the parabolic dependence does not have to to be satisfied). As drawn, we assume large lattice relaxation. Next, we can calculate the difference between the parabola's nodes as  $2E_g - 2\epsilon$ . If we accept the literature data, i.e. assuming the values provided by Péan et al., and  $E_g \approx 2.4eV$ , the  $2E_g - 2\epsilon \approx 0.92eV$ . If we take the raw data for the C24-R sample, that is, the  $E_{indir}$  and the pinning of the Fermi

level, the resulting value is  $\approx 0.7 \text{eV}$ . The open question is what bandgap value should be adopted, since it changes with temperature. The crossover between excited negative and positive state parabolas is deliberately drawn to ensure it is close to the bottom of the upper parabola to emphasise a low barrier for hole capture; ergo, we assumed a case of high self-trapping.

Having the coined metastability model in mind, we will move to the aforementioned alternative interpretation of the TSC curve from the section 5.3.3: based on the framework from the work of Maciaszek et al. [16], we can formulate the relaxation kinetic equation for our metastable complex. From [16] (cf. chapter 3.1), we shall write electron capture time constant:

$$\tau_{EC}^{-1} = \nu_{phn}^{-1} (\varsigma_n v_n n)^2 \exp\left(-\frac{\Delta E_{EC}}{kT}\right) \equiv (c_n n)^2 \exp\left(-\frac{\Delta E_{EC}}{kT}\right)$$
 (5.5.1)

where we denoted  $\nu_{phn}^{-1} \varsigma_n v_n$  as the electron capture coefficient  $c_n$ .

Therefore, a electron kinetic equation with the thermal decay of trapped electrons is given by:

$$r\frac{\mathrm{d}n}{\mathrm{d}T} = e_n n_t - \frac{n}{\tau_n} - (c_n n)^2 \exp\left(-\frac{\Delta E_{EC}}{kT}\right)$$
 (5.5.2)

where  $e_n$  is the electron emission coefficient from trap states.

Besides the electron capture, this equation incorporates band-to-band recombination and retrapping, and is too complicated to solve analytically. Let us simplify the problem to the electron capture only:

$$r\frac{\mathrm{d}n}{\mathrm{d}T} = -(c_n n)^2 \exp\left(-\frac{\Delta E_{EC}}{kT}\right)$$
 (5.5.3)

this simplified equation has a solution:

$$n(T) = \frac{rk \exp\left(\frac{\Delta E_{EC}}{kT}\right)}{\xi rk \exp\left(\frac{\Delta E_{EC}}{kT}\right) - c_n^2 \left[\Delta E_{EC} \exp\left(\frac{\Delta E_{EC}}{kT}\right) \int_{-\infty}^{\frac{\Delta E_{EC}}{kT}} \frac{-kT}{\Delta E_{EC}} \exp\left(-\frac{\Delta E_{EC}}{kT}\right) d\left(\frac{\Delta E_{EC}}{kT}\right) + kT\right]}$$
(5.5.4)

Needless to say, this solution is practically similar to the solution obtained by Maciaszek

et al., and the n(T) dependency would follow his results [16], thus not yield a peak-shaped TSC. To obtain the TSC curve observed in the experiment, one has to add one more process – a carrier freeze-out. From this point of view, the observed TSC curve is not a peak but a sum of freeze-out-induced depletion on shallow defects at low temperatures (below the apparent peak), and the concentration of bonus electrons, governed by the occupation function of positively charged metastable complexes, as in Fig. 2 in Maciaszek et al. The real value of  $\sigma_{PPC}$  is then a value at the measured TSC peak maximum. In other words, the  $\sigma_{PPC}$  in the function of temperature firstly perceives a negative peak caused by the additional freeze-out below 160K. Assuming the same metastable complex governs C24-AS and C24-R samples, this interpretation explains the difference between those as simply the difference between its trap densities responsible for the freeze-out. As one can surmise, we suspect the T states in the role of these, whose concentration changes rightly between those samples. In the C24-RS sample, the Fermi level is located below  $\epsilon(+/-)$  of the considered complex. In consequence, the V-E (V<sub>S</sub>-Cd<sub>In</sub>) defect is initially in a positive charge state and, after illumination, undergoes an opposite processes than in the case of the first two samples: the complex captures electrons, effectively decreasing free electron concentration, recharging into a negative state and, during annealing, relaxing back into a positive charge state by releasing electrons. Hence, we observe negative PPC in the TSC curve in the C24-RS sample (Fig. 5.3.5). The magnitude of negative PPC is proportionally weaker as the complexes' concentration decreases upon annealing in sulphur. Of course, in this case, freeze-out does not play a role.

The difference between LNT and EWC illumination for C24-AS and C24-R samples is simply a result of different times of illuminating samples at particular temperatures (and partially due to different concentration profiles of T states).

Persistent photoconductivity could also explain discrepancies in DC conductivity, i.e., the difference between  $\sigma_{DC}(T)$  measurements (vide section 5.3.1), and conductivity values obtained from IV characteristics (section 5.3.2) The resultant metastable state is, in a sense, the sum of the sample's history, i.e. previous heating, cooling and illumination cycles. Some residual metastable state may still be present in the sample even after thermal

resetting, which may account for such discrepancies<sup>23</sup>. The cooling procedure can also significantly affect the metastable state [16].

Lastly, why is then a positive PPC in Fig. 5.5.1 for the C24-RS sample? It is because those values are taken from the long decay tail, which is governed by the T states, also present in the C24-RS sample. The real PPC conductivity, within this interpretation, is the maximum conductivity value at the apparent TSC peak. In C24-RS, we decreased the total value of  $n_0 + n_t$ , whereas, in C24-AS and C24-R, we increased it, after which the new equilibrium between  $n_0$  and  $n_t$  was reached.

#### 5.5.2 Persistent photosensitivity

The persistent photosensitivity is a domain of mainly photoconductivity spectra measurement (Fig. 5.4.8), but also visible in the photoconductivity as a function of light intensity. For the latter, we have further examined the saturation of the effect for the case of C24-R (Fig. 5.5.3). At LNT, the PPS saturates after 900s of full (standard) illumination<sup>24</sup>. Further, the PPS can be saturated up to 160K, above which the saturation time becomes lingering<sup>25</sup>.

Yet the most explicit manifestation of the PPS is the change in photoconductivity activation from section 5.4.2 (Fig. 5.4.9). Herein, we repeat the same plot for a dark (relaxed) state and two illumination variants (Fig. 5.5.4).

Our interpretation of PPS will be based on the mechanism presented as the explanation of PPC. Having access to the temperature evolution of metastability here, we will first perform a naive interpretation: We will extend it with the D.V. Lang multiphonon emission model [19] described in the chapter 3.1. Assuming that the photoconductivity amplitude is governed by the metastable carrier capture processes and the dependence is linear, i.e. assuming the  $\tau_n \sim \zeta_n$ , and then  $\Delta \sigma \sim \tau_n$ , we can directly apply equation (3.1.5) to the photoconductivity, burying all the proportionality factors in the scaling

<sup>&</sup>lt;sup>23</sup>A fairly common belief among experimentalists dealing with metastable defects is that samples lead a life of their own.

<sup>&</sup>lt;sup>24</sup>That is why, we were applying 15 minutes illumination when examining the samples' metastability

<sup>&</sup>lt;sup>25</sup>Saturation time approximation, assumed from the extrapolation of the linear part at log-log scale at the room temperature gives ~56 000 years.

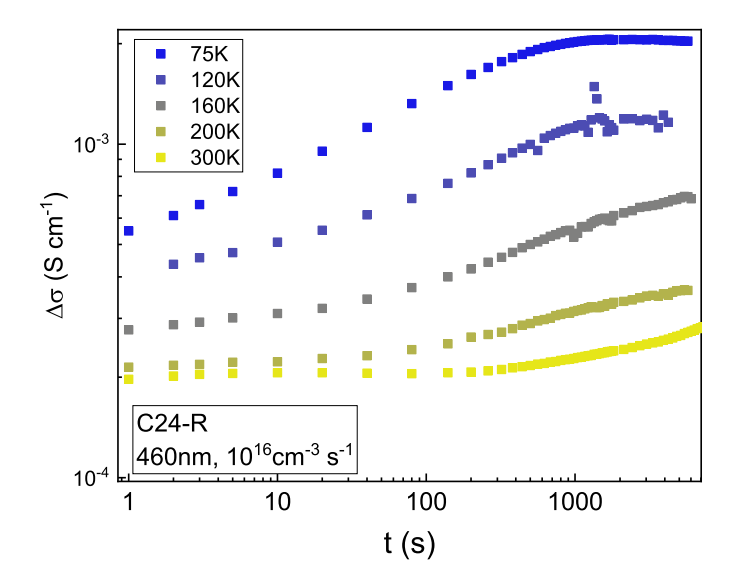


Figure 5.5.3: Saturation of metastable photosensitivity in sample C24-R. The photoconductivity amplitude (measured in the exact same manner as in section 5.4.1) for  $f \approx 10^{16} \text{cm}^{-3} \text{s}^{-1}$  in a function of illumination time (using the same light source with  $f = 10^{20} \text{cm}^{-3} \text{s}^{-1}$ ). At LNT, the sample saturates after ~900s (~15min.). At 160K and above, the saturation becomes impossible in reasonable time frame.

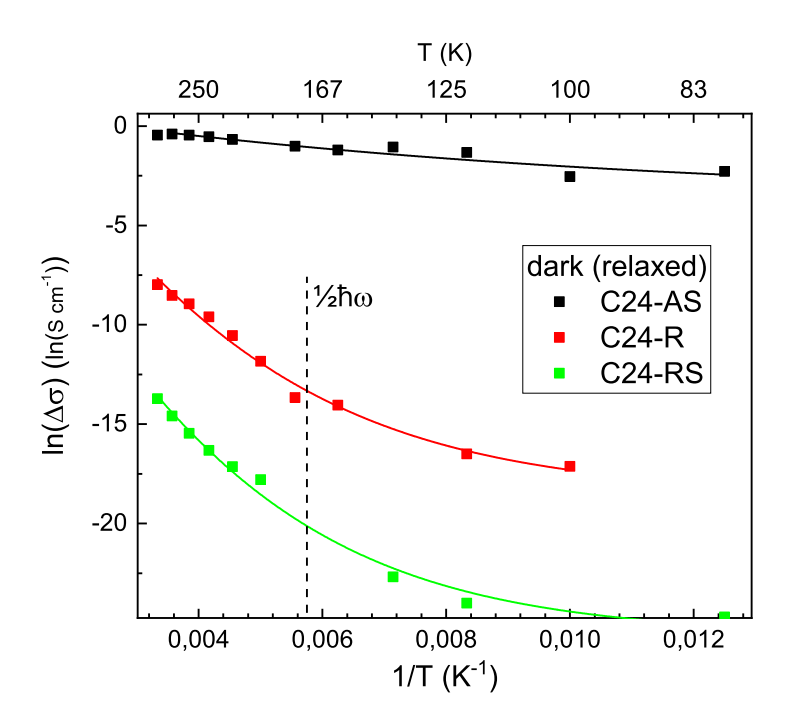


Figure 5.5.4: Arrhenius plot for  $\Delta \sigma$  (for 2eV excitation energy) with the performed fit.

parameter  $\xi$ . Before proceeding, the question is whether the dark (relaxed)  $\Delta \sigma$  activation is indeed relaxed or influences the photoconductivity by measuring the photoconductivity (unintentionally exciting the sample into a metastable state by illumination during measurement). Here, we will assume that the MPE is present in any state.

Table 5.5.1: Fitted parameters for the MPE model.

	S	$\hbar\omega \; ({\rm meV})$	$\Delta E \text{ (meV)}$
C24-AS	11(6)	12(10)	20(14)
C24-R	10(3)	30(3)	300(70)
C24-RS	20(5)	30(4)	500(100)

By fitting the Lang model, we have obtained the values listed in table 5.5.1. The Huang-Rhys parameter keeps the values  $\sim 10$  hinting the strong coupling regime. The  $\hbar\omega$  for the C24-R and C24-RS samples was estimated to be  $\sim 15$  meV, which gives  $\frac{\hbar\omega}{2}$ , roughly corresponding to the found transition temperature of 160K. The  $\Delta E$  is the barrier for electron capture. This is to be compared with the apparent asymptotic slope obtained before from the activation of  $\Delta\sigma$ . Upon the annealing, the whole system seems to increase in terms of energy. We can perform a series of fits specially for the C24-R sample in different states (Fig. 5.5.5). Upon the different illumination procedures, the fitted parameters change, although we do not have coherent interpretation for the obtained values. The effect of illumination by the 640nm (2eV) light can be interpreted as an intermediate state between dark (relaxed) and mostly converted metastable state. Conversely, the overall shape of the series hints at the optical capture process dominating at low temperatures after illumination. Furthermore, there is a question remaining, of how annealing affects the complexes themselves and whether it would affect the barrier values.

At this point, we must stop the analysis within the MPE model due to our insufficient knowledge. Instead, we will propose a coherent phenomenological explanation based on the processes described in the context of PPC:

The electrons from the conduction band will likely end in T states, as such distribution presumably has a large capture cross-section. After being captured in T states, they

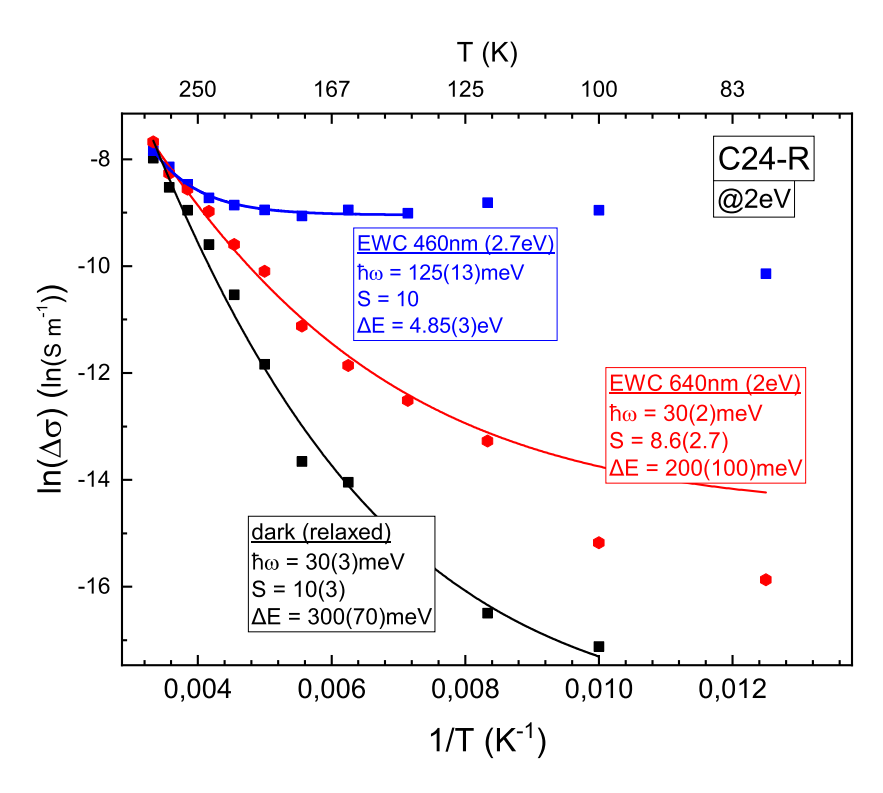


**Figure 5.5.5:** Arrhenius plot for  $\Delta \sigma$  for 2eV excitation energy for C24-R. We fitted the equation (3.1.5), to dark (relaxed) temperature dependency, after 640nm illumination, and after 460nm illumination.

will recombine with holes in E states giving the 1.6eV transition. Hence, we observe high emission from T states to E states (see. Fig. 5.2.1). Due to this fact, those defects are likely in complex. Now, the question is how the sulphur vacancy complex impacts the cation sublattice complexes – through electrostatic interaction. If the V-E is in a negative charge state, it induces coulombic attraction of the positively charged cations. This causes the wave functions of the cations to overlap, increasing the probability for this transition. This results in the appearance of an effective recombination path (observed as the 1.6eV emission). Suppose the V-E is now in a positive state. In that case, it causes coulomb repel of the cations, a decrease in overlap of its wave functions, and, as a result, a decrease in the probability/recombination efficiency of the T-E transition. Thus, the electrons trapped in T states will be more likely re-emitted back to the conduction band instead of recombining. Electrically, this process will be observed as an effective increase in electron lifetime – the PPS. Therefore, the Arrhenius plots of  $\Delta\sigma$  would consist of two

parts representing the mentioned regimes:

- ≥ 100meV part is the activation of the T-E recombination the process dominates in the relaxed state trough full temperature range (e.g. the black curve in Fig. 5.5.5), and above 160K after illumination;
- 2. flat ~ 10meV process is the activation of retrapping electrons back to the conduction band dominating below 200K (annealing the metastability) after illumination (e.g. the blue curve in Fig. 5.5.5).

By applying an illumination, we are switching between the attracting and repelling behaviour of the V-E complex, effectively opening or closing the dominant 1.6eV recombination path. The resulting lifetime change determines the ultimate amplitude of the  $\Delta\sigma$ . Therefore, PPS is governed by (again) the antisite defects by a specific sensitization mechanism. Sulphur complexes are an *éminence grise* of the system, covering behind other electron processes.

The temperature behaviour of V - E complex controls the recombination efficiency, imaginably according to equation (5.5.2). Anyhow, one can not expect a clear, undisrupted recombination temperature dependence.

The change in recombination following the hole capture occurs dynamically during the act of photogeneration; therefore, the photocurrent transient will experience a time-dependent boost during the process, as explained in section 5.4.1.

In the C24-RS sample, the situation is the opposite, precisely the same as in the case of PPC. As the initially positive complex captures electrons, the initially repelling coulombic interaction becomes attractive, causing the negative PPS as a result. Indeed, in the C24-RS sample, we observe an opposite effect of illumination (Fig. 5.4.9), as well as a small increase in  $\gamma$  parameter after illumination (vide Fig. 5.4.6), as the reducing recombination acts as a decelerating force here.

The mechanism of metastable control of the electron concentration and recombination was the last missing element to solve the  $CdIn_2S_4$  conundrum.

## 5.6 The full picture

At this point, after showing all the results of the experiments, we have all the elements that allow us to complete the  $CdIn_2S_4$  model.

All of the problems start with growing the crystal. During the PVD deposition, the CdIn<sub>2</sub>S<sub>4</sub> grows in the non-equilibrium state – the deposition conditions induce a disorder of the cation sublattice, in other words – a spinel inversion of  $x \approx 0.1$  (vide Fig. 4.2.2). The inversion then causes the bandgap lowering in as grown samples (Fig. 5.4.11) and introduces a high concentration of two antisite species: In<sub>Cd</sub> donors and Cd<sub>In</sub> acceptors, known as T and E. Those defects form exponential distributions of states below the conduction band (T) and above the valence band (E) – those emerging in the sublinear Lux-Ampere characteristics (Fig. 5.4.3). Transitions between those distributions and conduction or valence band contribute to the broad photoexcitation below the bandgap (Fig. 5.4.8). The emission from T states to the valence band is visible in photoluminescence spectra (Fig. 5.2.1, 5.2.2) as 2eV peak, and the emission from T and E states as 1.6eV peak. The 1.6eV emission can then be treated as a marker of inversion (or cationic antisites concentration) present in the samples (Fig. 5.2.3). The long relaxation times observed in the kinetics are primarily due to trapping by T states. Similarly, the frequency response of photoluminescence (Fig. 5.2.4) is also due to T states. Further on, the hopping transport trough T states can be observed (Fig. 5.3.9). The superlinear hopping parameter s can be explained by the inversion-derived origin of the distribution of T states, as described in section 5.3.4. Moreover, the obtained from  $T_{gt}$  energy falls close to the  $kT_V$  value (vide Tab. 5.4.1)<sup>26</sup>. Next, the concentration of T states is high enough to pin the Fermi level in the C24-AS sample. Finally, the T-E transition is the main recombination path (because the 1.6eV peak dominates the photoluminescence spectra). Thus, the T and E are likely in the complex. As the T-E recombination dominates, this complex controls the effective

<sup>&</sup>lt;sup>26</sup>With the note that this is the value assigned to the E, not the T states. Although this may mean that we see hopping transport of holes through the E states, and not electrons through the T states as we have thought so far.

lifetime of the electrons and, therefore, the  $\Delta\sigma$  amplitude. The observed long  $\tau_0$  response times are the outcomes of high electron trap densities – T states that, in fact, pull the strings of the optoelectronic response of the CdIn<sub>2</sub>S<sub>4</sub>. Those long response times can be correlated with the frequency dependence of the photoluminescence, reported at the end of the section 5.2.1.

A second agent introduced during the deposition is the sulphur vacancy – the V defect caused by sulphur deficit during growth. V to VB radiative transition gives 1.8eV peak in PL spectra (Fig. 5.2.1, 5.2.2). But, most importantly, according to Péan et al., [22], the sulphur vacancy forms a negative-U metastable complex defect with  $E(V_{S}-Cd_{In})$ , which has  $\epsilon(+/-) = 1.94 eV$ . This is the  $E_{TR}$  that pins the Fermi level in the C24-R sample (V<sub>S</sub> itself is also metastable, according to Péan et al.). When the sample is illuminated, the negatively charged V-E complex can capture two holes and convert to a positive state. (as described in section 5.5), leaving two free electrons. This causes positive PPC (Fig. 5.5.1), which persists up to 160K, where electron capture starts to effectively relax the defect. An opposite transition can occur if the V-E complex starts from the positive state (as in the C24-RS sample, where Fermi level is below  $E_{TR}$ ). Then, by capturing two electrons, the complex becomes negatively charged, and the electron removal causes negative PPC. The negative PPC can be observed in TSC in the C24-RS sample as the TSC curve decrease (Fig. 5.3.5). Moreover, changing the V-E charge state reduces or amplifies the T-E recombination efficiency by attractive or repulsive Coulomb interaction between positively charged cations: positively charged V-E repels Cd and In cations, reducing the T-E recombination efficiency, as more electrons from T states are emitted back to the conduction band instead of recombining (the small 15meV activation energy in Fig. 5.4.9), therefore  $\tau_n$  increases,  $\Delta \sigma$  increases, and we do not observe large photoconductivity activation caused by the metastability-controlled recombination – this is the PPS (Fig. 5.4.8, 5.5.3). The recombination reduction is also visible in the dynamical evolution of the photocurrent kinetics – as the superlinear Lux-Ampere dependency (explained at the end of section 5.4.1). Negatively charged V-E (in the C24-RS sample) causes an opposite effect - increases the recombination efficiency and reduces the  $\Delta \sigma$ , causing the negative PPS.

That is why we observe reversed behaviour in sub-bandgap photoconductivity activation (Fig. 5.4.9). That is also why we observe increase of the superlinear  $\gamma$  parameter in C24-RS sample after illumination – Fig. 5.4.6. Lastly, the  $E_{TR}$  of the V-E complex pins the Fermi level in the C24-R sample.

Now, let us consider the particular effects of PDT: The annealing (in general) modifies the samples by removing the dominating agent. In the C24-AS sample, a high concentration of inversion-induced species dominates, and the Fermi level is pinned by the T states at 0.1eV below CB (Fig. 5.3.2). The value of  $E_F$  causes high  $n_0$  concentration giving high conductivity that dominates the hopping transport trough T states – that is why we do not observe  $\omega^s$  dependency in  $\sigma_{AC}$  (Fig. 5.3.8). The concentration of all of the defects is the highest in C24-AS. Therefore, the PL spectra, PPC and PPS effects have the strongest (absolute) magnitude. The photoconductivity spectra are the broadest due to the lowest bandgap caused by the high inversion and the highest concentration and diversity of possible excitations from and into the defect states. Photoconductivity also has the highest amplitude despite theoretically the most efficient recombination.

Annealing the CdIn<sub>2</sub>S<sub>4</sub> in a vacuum causes relaxation of the cation sublattice, ergo reducing the concentration of the antisite defects. Thus, the inversion degree decreases and bandgap increases, the distribution of T and E states changes (vide tab. 5.4.1), sub-bandgap photoconductivity decreases, 1.6eV transition becomes less dominant (and overall PL amplitude decreases – other peaks also partially derive from inversion). The Fermi level gets repinned by the second dominant force – the V-E complex, on the  $E_{TR}$ , 0.4eV below CB. Therefore,  $n_0$  falls down, allowing the hopping transport to breathe. Due to lower  $n_0$ , the PPC and PPS can also fully shine – its influence becomes more prominent, although, due to less concentration of E defects, the concentration of V-E complexes is also reduced. Therefore, in the C24-R sample, we can fully perceive the effects of PPS and PPC on TSC curves and  $\Delta \sigma$ . The C24-R sample is somewhat in between C24-AS and C24-RS: in a metastable state, it gets some properties of C24-AS, mainly enhanced electron concentration; in a relaxed state, it behaves more like C24-RS.

Annealing the sample in sulphur finally eliminates the positive effects of metastable sulphur vacancy complexes. The Fermi level is repinned by some other unknown species deep below the conduction band. Therefore, the  $n_0$  is the lowest among all three samples. Similarly to annealing in a vacuum, after annealing in sulphur, the cationic structure is relaxed, whereby the T and E defects are diminished, causing the same effects as in sample C24-R. What is left of the defects eliminated by annealing is the source of negative metastability. Remnants of the previous concentration of V - E complexes are now positively charged as the  $E_F < E_{TR}$ , causing minuscule negative PPS and PPC.

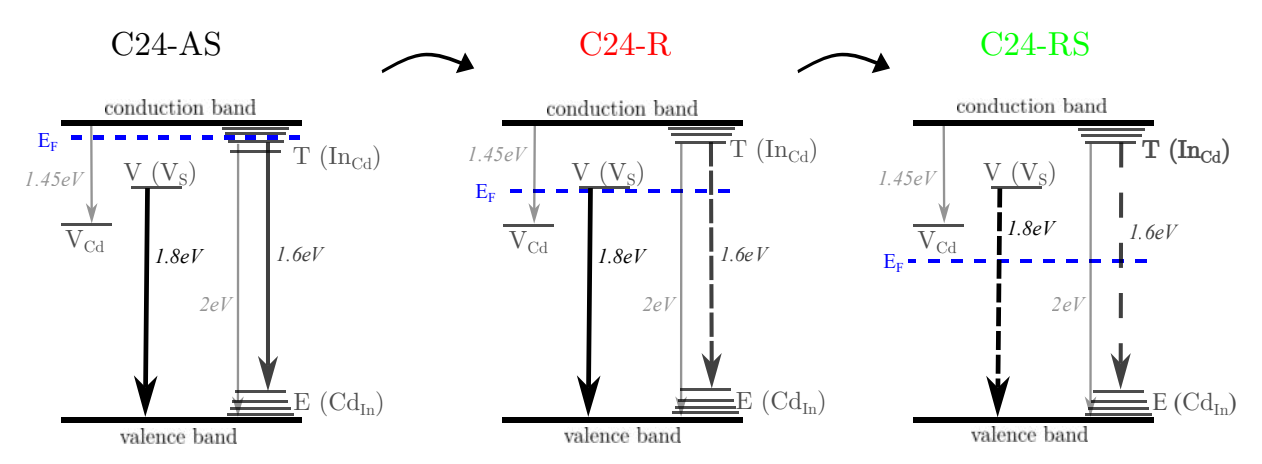


Figure 5.6.1: Radiative recombinations with respect to Fermi level position. Arrow thickness and colour schematically represents the most dominant transitions in each sample. Change from solid to dashed lines represents main impacts of annealing – changing from C24-AS regime to C24-R and C24-RS.

Let us now consider optoelectronic transitions in more detail: Before we begin, it should be noted that lowering the bandgap can change the measured transition values. This may explain why, for example, the peak 1.8 eV (emission from sulphur vacancy) has a value of 1.75 eV in our case, similar to the other peaks. Based on the bandgap values—reported in the literature, it can be assumed that the researchers studied non-inverted spinels, so their emission lines may be enlarged by the differences in the bandgap (see 4.2.1). The emission lines correspond to the literature data, and their evolution during annealing is consistent with the model. The influence of the PDT is schematically shown in Fig. 5.6.1.

Here, we will bring again the band diagram from Fig. 5.6.2. Facing the findings from the photoluminescence and photoconductivity spectra, we can extend the diagram with additional optical transitions:

- 1. the renowned 1.6eV emission occurring the other way, i.e. excitation from E to T states, contributing to the photoconductivity;
- 2. 2eV emission found in photoluminescence. The best fitting place is the transition from the bottom of the T states tail to the valence band;
- 3. the analogous 2eV excitation in the other way, that contribute to the broad sub-bandgap photoconductivity from section;
- 4. the 2.2eV excitation, notoriously reported in the literature is in our case, much broader than the literature-based excitation from localized E level.

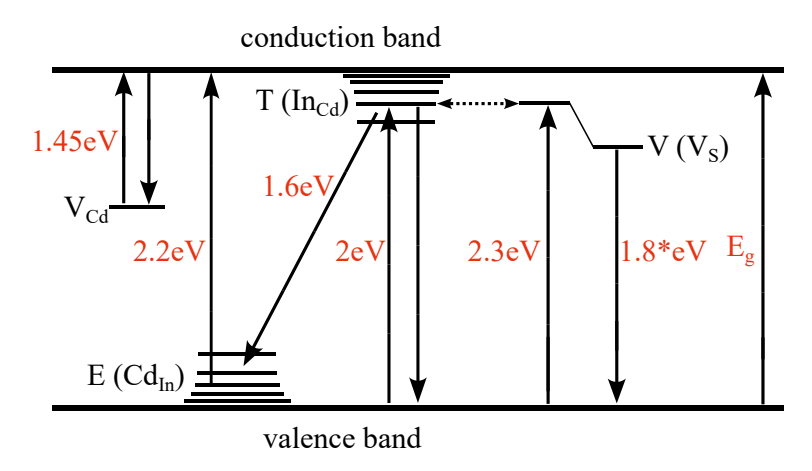


Figure 5.6.2: Extension of the CdIn<sub>2</sub>S<sub>4</sub> band diagram, based on diagram from Fig. 4.3.2.

We acclaim into the model all the optical peculiarities reported in the literature<sup>27</sup>.

The compounds made by other researchers in the past most likely had varying degrees of inversion, resulting from the particular synthesis method. Hence, the researchers, having  $CdIn_2S_4$  with random inversion, reported differing bandgap values or photoluminescence

<sup>&</sup>lt;sup>27</sup>e.g. the stoichiometry dependence of photoluminescence (the effect of antisite defects concentration); the optical gain, based on the 2.2eV excitation and 1.6eV emission, reported by Charlebois et al. [25].

spectra. It is not easy to compare 1:1 the findings from the literature, as we do not know the samples' details. Nonetheless, the general consistency is conserved.

Mentioned in the chapter 4 analysis done by Grilli et al. [217] is particularly curious, as it contains the temperature evolution of photoluminescence and shows the substantial change in the 1.8eV emission occurring at 160K. Now, we know that this temperature corresponds to the value of  $\frac{\hbar\omega}{2}$  and is inherently connected to the V-E metastable system. The defect V, drawn by Grilli et al. as double-level, is metastable, and is in complex. We do not have any detailed knowledge about the potential Stokes shift of our defect, nor do we know the exact positions of the individual metastable states in the band diagram; however, for clarity, we will keep drawing it as a double-level to indicate that it is a metastable defect. Similarly, the E defect was often drawn as a double level [217,221], but for no deeper reason. It is somewhat satisfying that we have found premises to draw it this way, as it participates in the V-E complex. Nevertheless, knowing that it is a complementary density of states, we will draw it similarly to the T defects.

The tunnelling from V to T (from Grilli et al.) can still take place and, more importantly, can occur equally in both directions. Moreover, the tunnelling from T states can assist in changing the charge state of the V-E complex by effectively lowering the electron emission barrier. This tunnelling path also evinces itself as the deviation of the  $\gamma$  parameter, discussed in section 5.4.1, where we hypothesized possible channel of charging/discharging the distribution of T states. It also participates in effective contribution of the 2.35eV excitation in photoconductivity.

In the end, we will conclude the optoelectronic aspects of the CdIn<sub>2</sub>S<sub>4</sub> model with the fact, that similar parameters (Fermi level, concentrations) to ours, was found elsewhere [223]. Regarding the photoconductivity, there are cases where the literature has given an incorrect interpretation. An example is a paper by Takizawa et al. [233], in which the authors tried to interpret a change in photoconductivity spectra in function of time, light intensity and direction of measurement. They did not know that the spinel was governed by metastable defects, the real source of the observed phenomena, and proposed a different explanation.

Although we have not studied the C48 series optoelectronically, the measurements that have been done fit into the model. First, the analysis performed for the DC conductivity in the function of temperature comprehensively addresses the issues related to cadmium deficiency (section 5.3.1), and the intensity of the 1.6eV peak fits into this description (vide Fig. 5.2.3). Moreover, using our freshly minted CdIn<sub>2</sub>S<sub>4</sub> model, we can predict the properties of the C48 samples: For C48-AS, we expect a lower concentration of E states; therefore,  $kT_V$  will be between 30–40meV, and  $kT_C$  will remain unchanged. The amplitude of Lux-Ampere characteristics will fall between the C24-AS and C24-R. Similarly, the amplitude of the photoconductivity spectra will fall between the C24-AS and C24-R spectra. The C48-R sample will be roughly similar to the C24-AS sample. Both C48-AS and C48-R samples will exhibit PPC and PPS effects. The C48-RS sample will be similar to C24-RS, with even lower  $\Delta \sigma$  amplitudes on the edge of measurability. The bandgap values will follow the C24-like dependence.

One last element that needs addressing is the issue of the alleged inductance observed in the AC conductivity (section 5.3.4). Inspired by the work of Moia et al. [145] and the derivations made by Sah [144], let us make an attempt to create a simplified equivalent circuit<sup>28</sup> describing the recombination between T and E defects, controlled by the charge state of sulphur vacancy complex  $V_S$ -Cd<sub>In</sub> – Figure 5.6.3. Herein, we denoted the charge storage capacitance of the conduction and valence band as  $C_n$  and  $C_p$  respectively, and  $C_t$  is charge storage capacitance at the V defect.  $v_n$ ,  $v_p$ , and  $v_t$  represent  $E_{Fn}$ ,  $E_{Fp}$ , and the V-E defect generalised energy level, respectively. Resistors represent the capture conductance for the electrons and holes to the metastable complex  $(R_{HC}, R_{HE})$  and the conductance trough T and E defects  $(R_E, R_T)$ . The transistors represent the recombination conductance between T and E states<sup>29</sup>.

<sup>&</sup>lt;sup>28</sup>This equivalent circuit has to represent only *the idea* of the process and is missing *a lot* of elements, whose Chih-Tang Sah would surely draw.

<sup>&</sup>lt;sup>29</sup>The polarity of the transistors is only a matter of convention here.

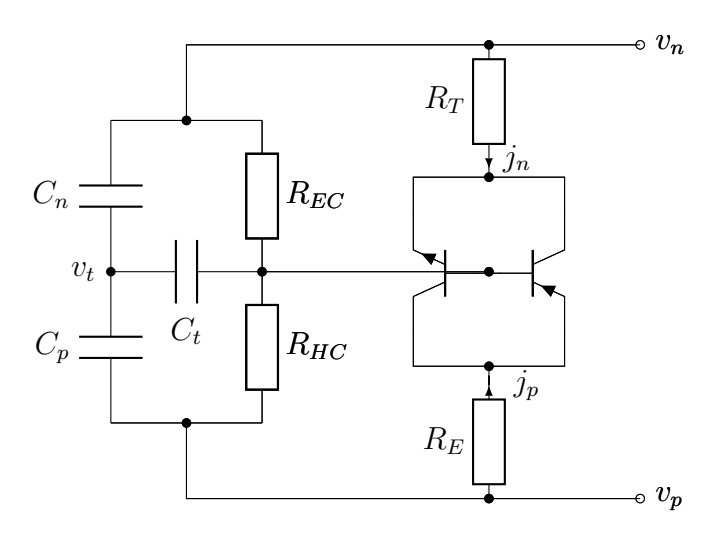


Figure 5.6.3: Equivalent circuit proposition for the V-T-E (V<sub>S</sub>-In<sub>Cd</sub>-Cd<sub>In</sub>) system.

Here, we will not even attempt to analyse this equivalent circuit and try to fit its parameters to the obtained impedance data, but we will point out its striking resemblance to the gyrator circuit from Figure 3.2.1. Indeed, the general principle of operation of the V-T-E defects system, where the coulombic interaction between the metastable complex and the cations controls the recombination current, resembles the field effect transistor in some way. Thus, if the system meets certain assumptions, i.e. signal integration in an resulting RC circuit and the 180° phase shift in transconductance, it could successfully emulate the inductive behaviour observed in the samples (Fig. 5.3.10). This quantum gyrator would then serve as an alternative interpretation of the apparent inductances to the chemical inductor but rooted in the metastable defects in semiconductors. Nevertheless, this bold idea requires further development.

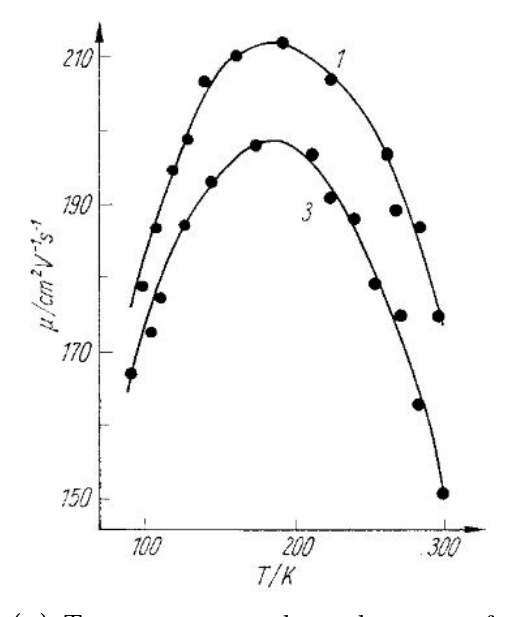
# 5.7 Open questions

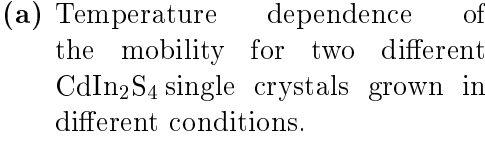
In the preceding chapter, we have shown the result of the CdIn<sub>2</sub>S<sub>4</sub> investigation. Combined, those can consistently explain most of the observed properties of the compound. However, a set of unanswered questions and, especially, open problems remain. Some problems were addressed in previous paragraphs, but some - more importantly - weigh on practically all of the conclusions at this state of work. Those problems originate primarily from the uncertainty of the data, and thus the assumptions and interpretations made while unveiling the model's elements. Rejecting some assumptions and conclusions, for example, in the face of new experimental results, may diminish the model's consistency and thus necessitate its further extension. Here, we will briefly consider or revisit some of them.

### 5.7.1 Real values of mobility

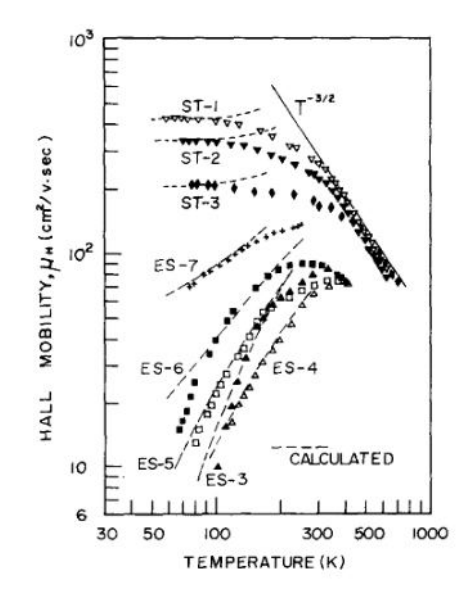
All values of concentration were calculated with the assumption of mobility  $\mu=1$  cm<sup>2</sup>Vs<sup>-1</sup>. This assumption does not have to be entirely true. And probably it is not. Unfortunately, currently we do not have any setup for mobility measurement at our disposal. Thus, true µvalues of our layers are unknown. One can find values in the literature [222, 237], although those values characterise single crystals, which in general have larger mobilities than polycrystalline materials. In polycrystallines, such as our investigated films, it is sensible to assume  $\mu=1$  cm<sup>2</sup>Vs<sup>-1</sup>. Within classical assumptions, mobility depends on temperature as  $\mu \sim T^{-\frac{3}{2}}$  [155], which is a weaker temperature dependency, than the Boltzmann exponential activation, therefore,  $\mu$  could be assumed as constant.

It should be clearly understood, however, that a significant change in mobility as a function of temperature would mean additional complication in our  $CdIn_2S_4$  model.





Source: Neumann et al. [237]



(b) Hall mobility as a function of temperature for eight  $CdIn_2S_4$  single crystals with different stoichiometry.

Source: Endo et al. [222]

Figure 5.7.1: What literature says about the mobility in  $CdIn_2S_4$ .

### 5.7.2 Blocking contacts

All analyses related to semiconductor transport have been carried out, assuming all phenomena are related to bulk. In other words, no consideration about contacts, especially blocking contacts, has not been taken. In fact, the influence of contacts can be neglected when the bulk resistance is so large that it completely covers the influence of barriers on carrier transport. Empirically (on IV characteristics), this is manifested by the covering of the nonlinear shape coming from the carrier emission over barrier by a large series resistance. Bulk transport dominates over transport through barriers.

Truth is, from theoretical point of view, the contacts *should* be blocking. The work function of Al is around 4.2eV [243], and electron affinity of  $CdIn_2S_4$  has been found<sup>30</sup> to have value of  $\approx 3.5eV$  [225, 226].

It is self-evident that if the barrier transport were dominant over the bulk resistivity,

<sup>&</sup>lt;sup>30</sup>Based on XPS and DFT calculations found in literature.

practically all of the elements of the model, which is solely based on the assumption, that we deal only with bulk conductivity, concluded from the electrical experiment, would be invalid. Therefore, in fact, majority of the interpretation would have to be started over again, resulting in an even more complex model.

In spite of this, there is a one solid premise, that the contact are ohmic, or at least the bulk resistance is dominant: linear IV characteristics within the voltage range where all the measurements were carried.

### 5.7.3 Facticity of the $\sigma_{AC}$ measurement

Although the overall appearance of the obtained  $\sigma(\omega)$  measurement is in some way conceivable, the fact that the measured quantities were close to the sensitivity limit of the measurement equipment, casts some doubt on the reliability of the obtained results<sup>31</sup>. Let us not be fooled by apparent regularities in the measurement data. Solely the fact that mysterious inductors appear may be sufficient evidence of incorrect electrical measurements: the presence of uncompensated parasitic reactances or incorrectly selected correction factors. One should also remember that superlinear values of power factor s are generally considered incorrect. It has to be also mentioned, that s > 1 or  $s \approx 2$  can sometimes be an experimental artefact related to electrode resistance [244] or compound/contact interfaces [245].

Nevertheless, we managed to find a model that can explain superlinear frequency dependence, connect it with the structural properties of the compound and obtain uncanny agreement with the literature. Then, we managed to explain the inductance effect with a somewhat dubious hypothesis.

In order to procure quantitatively reliable results, one would require a superior measurement apparatus. However, at a qualitative level, that which has been presented, the data is deemed satisfactory. We can also prepare a new set of samples (with the exact same compound) that are more suitable for this type of experiment. Until then, one ought

<sup>&</sup>lt;sup>31</sup>It should be reminded here that the measurements in a cryogenic system were impossible due to the presence of parasitic reactances, which were enormous relative to the samples' conductivity value.

to approach these findings with a certain measure of caution. Those should be treated as a possibility of compelling physics yet to be explored.

### 5.7.4 Case of non-exponential current transients

The nonexponentiality of photocurrent transients, although seemingly avoided throughout this chapter, serves as crucial evidence for the case of metastable defects. Currently, the only working fit we find is the compressed exponential, which does not yet have a formal description but is well explained by the  $CdIn_2S_4$  model.

The generation and recombination processes should control the photocurrent transients. In the face of the presence of disorder, i.e. the presence of T and E distributions, we expect the kinetics to be well predicted by the Nelson description [125], or the simple trapping model from chapter 3.2.3. Unfortunately, PPS is a distorting factor in this image; in the ascent, we get superlinearities.

One could argue that the TATS peaks are not single but multiple peaks, which could be fitted. We do not have any argument against the fine peaks structure; moreover, we are aware of the fact that we have multiple-processes mechanisms involved in generation-recombination that could produce such kinetics. The continuous kinetics we obtained, would allow for the fitting of a virtually infinite number of peaks. Moreover, we could not force the kinetics recordings to yield separate peaks.

None of the current transients observed by us in any of the experiments current transients do not have distinct features (like, for example, kinetics shown in figure 9.3-1(b) on page 285 in Bube et al. [155]). Therefore, we remain of the opinion that current kinetic is a homogeneous process.

# 5.7.5 Uncertainty of the bandgap values

Despite the high uncertainty values of the obtained  $E_g$  values, we acclaim those as valid evidence for the existence of spinel inversion. That result confirms the theoretical predictions of Seminóvski et al., withal is not a critical element of the  $CdIn_2S_4$  model since

the  $Cd_{In}$ , and  $In_{Cd}$  defects alone are sufficient to explain all the observed phenomena. In further work, carrying out more accurate measurements of the bandgap will allow us to resolve the issue of the alleged inversion $\rightarrow$ bandgap causality.

# 5.8 Model predictions and further work

Having the CdIn<sub>2</sub>S<sub>4</sub> model resolved, we can make some predictions and blaze a way of further research. Here, we will list the possible directions to follow:

The first and most pressing problem is the lack of mobility measurement.

As the metastability controls the T-E recombination, we expect to observe the temperature evolution of the 1.6eV peak that follows the  $\Delta\sigma$  dependence. Therefore, the photoluminescence at low temperatures will exhibit severe memory effects: firstly, we will observe a gradual decrease of the 1.6eV emission while conducting an experiment (assuming the CW illumination), similar to photoconductivity saturation (Fig. 5.5.3) – the evolution of PL spectra in a function of time at LNT. Secondly, after converting the sample to the metastable state by measuring it, we expect to observe the evolution of PL spectra in the function of temperature, namely progressive amplitude increase of 1.6eV peak above 160K (similar as in Grilli et al. [217]). It is also pertinent to note that as the 1.6eV and 1.8eV emissions excited from the 2.35eV source are concurrent processes, we should expect an increase of 1.8eV PL peak parallel to the 1.6eV decrease.

If we assume the classical interpretation of the TSC peaks (section 5.3.3), we would observe a glow curve at energy (likely) 1.6eV. Therefore, a thermally stimulated photoluminescence (TSL) experiment is worth performing, for it would settle the TSC divagations.

Lastly, regarding the luminescence, we need to indagate the chopping effect mentioned in section 5.2.1. Therefore, a time-resolved photoluminescence experiment is required. We expect to observe similar values of response times as in the photocurrent kinetics.

Another experiment from which the CdIn<sub>2</sub>S<sub>4</sub> model could benefit is Raman

spectroscopy, as it provides information about phonon coupling of our defects and potentially could serve as an inversion probing tool.

More sophisticated electrical experiments, focused on probing the defects, e.g. capacitance-voltage spectroscopy, could benefit the model with more quantitative content regarding the defects.

From a technological point of view, it can be checked whether it is possible to synthesise  $CdIn_2S_4$  having a large degree of inversion, e.g. x = 0.5. Since the work of Seminóvski et al. shows that this is impossible by classical synthesis, we propose to try after-deposition quenching (or quenching after PDT), i.e. a process akin to vitrification [246]. It is then worth correlating this with the temperature of 403K and the work of Czaja et al., perhaps by trying to synthesise the  $CdIn_2S_4$  below 130°C.

Because of the high concentrations of defect states pinning the Fermi level, we expect the pinning to be binary, i.e.  $E_F$  will be pinned by T states or  $E_{TR}$ , without any intermediate states. As the Fermi level gets repinned after annealing C24-AS due to removing the T states, and this arrangement is reversed for the C48-AS sample, we could perhaps look for a critical stoichiometry between  $CdIn_2S_4$  and  $CdIn_4S_8$ , where the Fermi level gets repinned. It could be done by manipulating the deposition parameters to obtain the desired In/Cd ratio.

The last, probably the most significant aspect missing in the  $CdIn_2S_4$  model is the lack of a precise theoretical formalism, which incorporates the mechanisms we deduced throughout the experiments. Moreover, a rarely discussed issue is translating the phenomenological description – a set of ideas – into the magnitudes of measured physical quantities. In particular, what is the concentration of defects, especially sulphur vacancies, and how does it translate into the value of the metastable increase in conductivity? Regretfully, the experiments do not provide enough information to determine the missing values.

In the work of Shimakawa [124], similarly to our CdIn<sub>2</sub>S<sub>4</sub> model, the trapped electrons

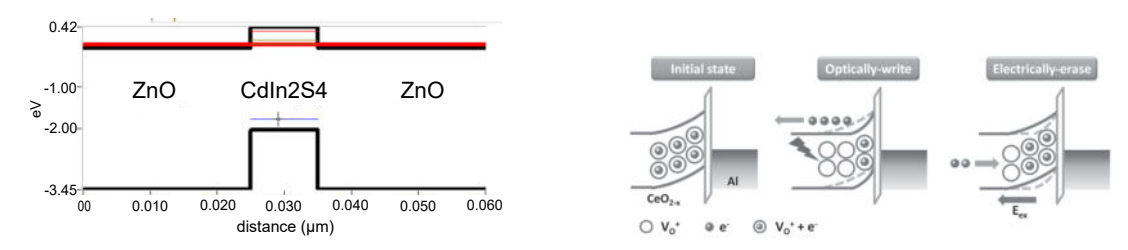
are assumed to be thermally released from the conduction band to the conduction band states and then disappear by recombination with localized hole. Electrons could diffuse dispersively in tail states; thus, the change of defect occupation is described by the dispersion relation (3.2.50b), and yields non-exponential relaxation (vide chapter 3.2.3). An extension of the model incorporating the hole band tail states and the communication with the  $V_S$ -Cd<sub>In</sub> could lead us to the formal description predicting observed superlinear phenomena.

Summarizing all the matters discussed throughout this chapter, we need a formal description that will produce the following:

- 1. peak-like  $\frac{\mathrm{d}n}{\mathrm{d}T}$  curve;
- 2. quantum gyrator, and the inductive behaviour in  $\sigma(\omega)$ ;
- 3. compressed exponential current transients;
- 4. superlinear Lux-Ampere characteristics.

We believe all of these elements would naturally emerge from one well-done theoretical model. Besides the Shimakawa model, a seeding of such a description was also made in (5.5.2). After completion of the model, the task will be for the numerical simulation experts to use, e.g. DFT, to calculate our spinel.

Finally, we can devise the possible architecture of the neuromorphic or memory devices based on the metastable defects in the  $CdIn_2S_4$ . Two alternative implementations come to mind:



(a) ZnO/CdIn<sub>2</sub>S<sub>4</sub>/ZnO tunnelling switch. A (b) ITO/CeO<sub>2-x</sub>/AlO<sub>y</sub>/Al junction structure. simulation of the band diagram. Source: Tan et al. [90]

**Figure 5.8.1:** Two propositions of CdIn<sub>2</sub>S<sub>4</sub>-based devices.

The first proposition is making use of moving the Fermi level position by changing the complex level charge state. This would change the occupation of defects (e.g. T states), the conductivity of the whole  $CdIn_2S_4$  layer, and, most importantly, will turn on or off the hopping transport on those defect states. Suppose we wrap the  $CdIn_2S_4$  thin-film between, e.g. ZnO (to form a symmetrical device having transparent electrodes), ensuring the cliff-type interfaces, and that the  $CdIn_2S_4$  layer is thin enough (Fig. 5.8.1a). In that case, we will effectively create a switch, based on the trap-assisted hopping on the defects within the  $CdIn_2S_4$ , controllable by the illumination (cf. chapter 3.2.4 and paper [103]).

The second proposition is inspired by the devices found in the literature [90,92]. We can manufacture a CdIn<sub>2</sub>S<sub>4</sub>-based Schottky junction (Fig. 5.8.1b). Charging/recharging the metastable complexes would cause compensation of the space charge region, effectively increasing or decreasing its width, in turn modifying the junction resistance. This could also be done through illumination and, possibly, electrically.

Due to the technological difficulties, option  $\mathbf{b}$  is probably easier to implement because of the excellent control over the interface required. Furthermore, if we can technologically reach the ability of implementation the option  $\mathbf{a}$  – we can easily implement option  $\mathbf{b}$ .

# Chapter 6

# Towards the devices – growth and analysis of $CdIn_2S_4$ thin films

The previous chapter finalised with formulating a comprehensive model describing the properties of CdIn<sub>2</sub>S<sub>4</sub>. We believe, the model coherently explains the complexities of how native defects affect the observed optoelectronic properties of a material. In a sense, it is unusual that the model was developed based on the analysis of only three<sup>1</sup> (!) different layers of the compound under study. After all, these three layers are just a narrow slice, a cross-section along one of the axes of the multidimensional space of the growth parameters of the CdIn<sub>2</sub>S<sub>4</sub> polycrystal. Yet, on the basis of only this slice, we have devised a model that we believe satisfactory predicts the CdIn<sub>2</sub>S<sub>4</sub> optoelectronic properties. Those predictions can be experimentally verified and point out further material research paths. These also concern the possibility of realising neuromorphic devices based on CdIn<sub>2</sub>S<sub>4</sub>.

Armed with the CdIn<sub>2</sub>S<sub>4</sub> model, we could begin growing successive CdIn<sub>2</sub>S<sub>4</sub> layers with the desired properties, pushing our research forward. We grew our thin films in collaboration with the University of Nantes using thermal evaporation. This narrows our scope to the technologically possible area to cover using this method<sup>2</sup> by varying the deposition parameters. In addition, we had to repurpose part of the manufacturing

<sup>&</sup>lt;sup>1</sup>six, if we count C48 set.

<sup>&</sup>lt;sup>2</sup>There are other methods existing, that have been used to grow CdIn<sub>2</sub>S<sub>4</sub> thin films, e.g. DC sputtering [24]; vide chapter 4.

process (substrates, electrodes, masks) used by the Nantes group for the production of thin-film solar cells. Hence, we mostly grew thin films intended to be used in a stacked configuration (multilayer device structure).

This chapter serves as an interlude between the material characterisation conducted in chapter 5 and the further part devoted to neuromorphic devices. Herein we will briefly present the results of the basic characterisation of the grown CdIn<sub>2</sub>S<sub>4</sub> thin-films we fabricated with future devices in mind. The grown films will also allow us to verify some of the model concepts and predictions described in the previous chapter.

Again, limited by time and measurement capabilities, we are forced to explore only selected areas of the technological parameters space of  $CdIn_2S_4$  synthesis. By the educated guess, and guided by an attempt to answer the questions from the previous chapter, we undertake to select the most valuable directions of thin-film growth exploration. Notwithstanding this, we tried to arrange these *slices* in such a way that in the future, using more measurement techniques than those presented in this chapter, we could map the largest possible area of the parameters space, deducing the missing squares.

# 6.1 Objectives

Since our primary goal is to implement defect-based switching in  $CdIn_2S_4$ , our technological agenda will orient towards this aspect. By considering what mechanisms could be the basis for the switching behaviour in our compound, on this basis we will set our line of enquiry. Among the possible mechanisms – principles of operation, portrayed in more detail in the chapter 2.4, that could eventually lay behind the neuromorphic or memory behaviour, we can select:

- 1. tunneling-based switching,
- 2. interface switching,
- 3. filamentary and ionic drift switching;

The realisation of the first two was actually presented at the end of chapter 5. As our

agile research problem is the application of metastable defects, that is, utilising a fact, we can change the charge state of the defects to control the electrical conductivity of the devices – the implementation of the first two mechanisms will be our primary goal. One could notice that the most obvious application of the metastable defects would be to create simply a resistor with memory – a device based solely on the phenomenon of metastable change in conductivity of the bulk material. It is feasible, but (as it will be explained later) more difficult from a technological point of view. Secondly, a RESET or the depression mechanism would be missing here, as the currently only known method to relax the metastable defects is annealing<sup>3</sup>. Enclosing the metastability within the higher-level physical mechanism that governs the electrical conductivity of the device is currently considered as a more robust method. The ideas behind the two switching mechanisms were outlined at the end of chapter 5.

The third method does not rely on metastability, nor are there any experimental traces for the ionic conductivity in our investigated  $CdIn_2S_4$  thin films. However, there is some literature evidence that is weighted in favour of mobile ions in  $CdIn_2S_4$  (vide chapter 4.2.6), therefore we cannot exclude the possibility for the apperance of such behaviour. Lastly, the light should not be forgotten as the main factor controlling switching. Both the first and second allow for the construction of light-controlled devices.

Starting from these premises, we will therefore aim at pursuing the amplification of the metastable phenomena of  $CdIn_2S_4$  to maximise its magnitude and control ability.

In search for the metastability amplification among  $CdIn_2S_4$  model predictions, perhaps the most noteworthy is the criticality of the Fermi level pinning regimes: One of the results of the material studies was the Fermi level repinning during annealing due to reducing the spinel inversion degree; additionally, when the stoichiometry was changed to  $CdIn_4S_8$ (reducing Cd content), a similar change was observed (cf. 5.3.1). The final result was a variation in electrical conductivity. On this basis, in addition to the deductions about the influence of defects on  $E_F$ , it was concluded that somewhere in the  $C24\rightarrow C48$  range there

<sup>&</sup>lt;sup>3</sup>Creating a CdIn<sub>2</sub>S<sub>4</sub>-based junction gives expectancy (as it will turn out - rightly) to reset the device using voltage pulses.

must be a transition between the regime, where the Fermi level is pinned by sub-bandgap states (C24-AS, C48-R) – let us call it the T regime; and a V regime – where the Fermi level is pinned by the  $E_{TR}$  of the V – E metastable complex (C24-R, C48-AS). Moreover, on a point of metastability, a general observation was that inducing the metastable state in the C24-R sample was turning it to more resemble the C24-AS (cf. figures 5.3.5, 5.4.8) in the overall behaviour.

The question is, what does the possibly thin film growth on the verge of two regimes mean for the overall behaviour of the hypothetical devices? On the one hand, instability and chaotic behaviour can be expected; on the other, setting the  $CdIn_2S_4$  on a razor's edge between T and V regimes could conceivably yield, generally speaking, a more easily achievable switching process.

In order to find the edge conditions in our new thin-films, we can infer three searching paths that can yield the transition between T and V regimes: inversion degree, stoichiometry, and (virtually) illumination. Hence, based on the  $CdIn_2S_4$  model, we could propose to explore:

- 1. stoichiometry perhaps the most reachable method, as it falls into the basic conditioning of the deposition process. We can grow thin fims with varying In/Cd ratio, i.e.  $Cd_{1-x}In_{2+\frac{2x}{3}}S_4$  with 0 < x < 1, reaching  $CdIn_4S_{6.8}$  at x = 0.42. This has already been the subject of research [224];
- 2. PDT (annealing) it is possible, but technologically infeasible, as it requires long annealing times and employs additional technological steps compared to the stoichiometry manipulation. Moreover, the PDT process can damage the substrate layers, e.g. ZnO films could be degraded during annealing, resulting in its decreased conductivity;
- 3. defect engineering in case of controlling the native defects, the problem reduces to varying the stoichiometry (and deposition temperature and pressure), or employing further passivation processes [247];
- 4. inversion degree Actually, this is an aspect of defect engineering, presented in a

different form. Controlling the inversion degree is de facto controlling the T and E states. It is expected that increasing the growth temperature will change the inversion degree [207].

In fact, the search for this transition is beneficial for both researching the memory devices and investigating the  $CdIn_2S_4$  itself, as examining the effects of growth parameters could provide additional information regarding the  $CdIn_2S_4$  model. Of the above-mentioned methods, we will explore the idea of the first approach, although in a less straightforward manner. Besides searching for the transition edge, we will also try to investigate the effects of deposition above and below Czaja's 403K temperature and the effects of quenching, both mentioned in chapter 5. Our investigation will also include the role of defects, inversion degree and the annealing of the devices. Details of the grown layers and their use are described in the following section.

# 6.2 Thin films' growth

Thin film deposition was performed in collaboration with the MIOPS group at the Jean Rouxel Institute of Materials in Nantes. Thermal evaporation was utilised using a BAK 640 evaporator. The process is described in more detail in Chapter 3.4. The sources were: CdS, In and S. The atomic fluxes of In and CdS were set to achieve In/Cd=2. The sulphur flux was set in excess to keep S-rich conditions. After the first successful run yielding deposited  $CdIn_2S_4$  with acceptable stoichiometry and crystal structure, the fluxes (source temperatures) were kept the same value and constant for all of the runs mentioned in this work. The only  $CdIn_2S_4$  deposition variables being changed were: film thickness (controlled by deposition time), substrate temperature and the substrates themselves. Throughout the work, we have utilised multiple substrates:

- bare 1mm soda lime glass (SLG),
- 1mm SLG with 400nm DC-sputtered molybdenum (SLG/Mo),
- 1mm SLG with 350nm RF-sputtered ZnO:Al (SLG/AZO),

- 1mm SLG coated with ITO (SLG/ITO),
- Si with 100nm SiO<sub>2</sub> (for future use);

The BAK-640 evaporator has three slots for samples, enabling layer deposition on a variation of multiple substrates in one run, ensuring that we grow the films under the same evaporation conditions.

Here we will briefly list the individual CdIn<sub>2</sub>S<sub>4</sub> deposition runs and their purpose:

- 231213 the first film was made to test the growth conditions of the CdIn<sub>2</sub>S<sub>4</sub>. It was grown explicitly on soda lime glass substrates at a temperature of 300°C. An EDX, SEM and XRD experiments were performed to ensure the CdIn<sub>2</sub>S<sub>4</sub> layer quality. The SEM image was performed (see appendix on page 342), from which the layer thickness was estimated to be ~ 400nm. The In/Cd ratio measured by the EDX was 1.9. The 231213 sample can be considered as C24 as grown reference sample, as it is closest to C24-AS from chapter 5. The quenching experiment was performed on samples from this run.
- 240104 the 100nm CdIn<sub>2</sub>S<sub>4</sub> thin films grown at 400°C were made with tunnelling-based switching devices in mind. Deposited on SLG, SLG/Mo and SLG/AZO. Part of the deposited films (for each substrate) was subjected to PDT in the same fashion as C24-R and C24-RS from chapter 5 (annealing in vacuum and in sulphur).
- 240105 a twin run to the 240104, but with the substrates at 130°C. The purpose of this run was to explore the 403K conundrum. Obtained films were 130nm thick. Those layers were grown in a non-usual manner during cooling the substrates from preheat temperatures, the shutter was opened for 15 min. right after the substrate temperature went below 130°C. This method had to be applied because the PID controller of the heater cannot operate stably below 200°C<sup>4</sup>.

<sup>&</sup>lt;sup>4</sup>An alternative approach to achieve low temperatures was used during deposition of the samples from the mainline series.

- 240130, 240208, 240311A, 240311B series of runs, referred later as the mainline series. Those 400nm films were grown explicitly on SLG/Mo substrates at various temperatures. Their purpose (besides creating the devices) was to explore the transition between the T and V regimes.
- 240312 Attempt to grow CdIn<sub>2</sub>S<sub>4</sub> layer twice as thick as in the mainline series (~800nm). Originally for optical measurement purposes. The substrates were: SLG, SLG/Mo and SLG/ITO.
- 240321, 240322 runs intended to grow  $CdIn_2S_4$  on  $SiO_2$  substrates for future use.

We have applied an additional substrate temperature control method in the mainline series and the 240321 and 240322 runs: In addition to different substrate temperatures among the separate processes, the temperature was regulated between individual samples (slots in the evaporator) as well, by using glass covers that effectively blocked part of the infrared radiation that was the substrates' heating source. Precisely: the middle slot remained uncovered, and this slot was probed by the thermocouple controlling substrate temperature; the second slot was covered by 1mm SLG coated with molybdenum, decreasing the substrate temperature by some amount; similarly, the third slot was covered by 3mm SLG coated with Mo, decreasing the temperature to the value lower than in the second slot. Therefore, we obtain three CdIn<sub>2</sub>S<sub>4</sub> thin films grown at three different substrate temperatures in each run. This somewhat crude method enabled us to scan a broader range of temperatures in fewer runs. Moreover, it decreases the problem of reproducibility among runs to some extent. A drawback of this method is that we know only one temperature out of three – the one probed by the thermocouple<sup>5</sup>. Hence, we will use the terms hot, medium and cold for the particular samples to mark the relative temperatures of the substrates, whereby cold had the lowest temperature (covered by 3mm SLG/Mo), and hot is the sample with known substrate temperature. A detailed list of runs can be found in the appendix on page 350.

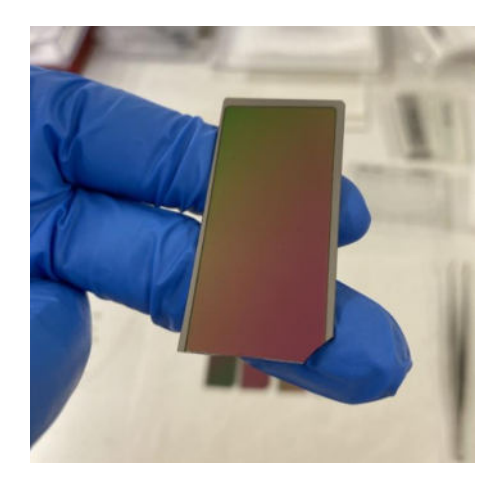
<sup>&</sup>lt;sup>5</sup>This problem, however, can be mitigated by measuring samples' composition, as will be shown in section 6.3.1.

Although controlling the substrate temperature may seem unrelated to the assumptions presented at the beginning of this chapter, as will become clear, it is a practical method for controlling the In/Cd ratio in deposited CdIn<sub>2</sub>S<sub>4</sub> films. In general, stoichiometry should be controlled by manipulating the atomic flux of individual elemental sources. However, this exposes us to the risk of going beyond the CdIn<sub>2</sub>S<sub>4</sub> phase growth region in favour of CdS or In<sub>2</sub>S<sub>3</sub>. We are also aware that by changing the substrate temperature, we likely control both the stoichiometry and the degree of spinel inversion. These two parameters are therefore strongly correlated and may be challenging to separate deductively from a series of samples.

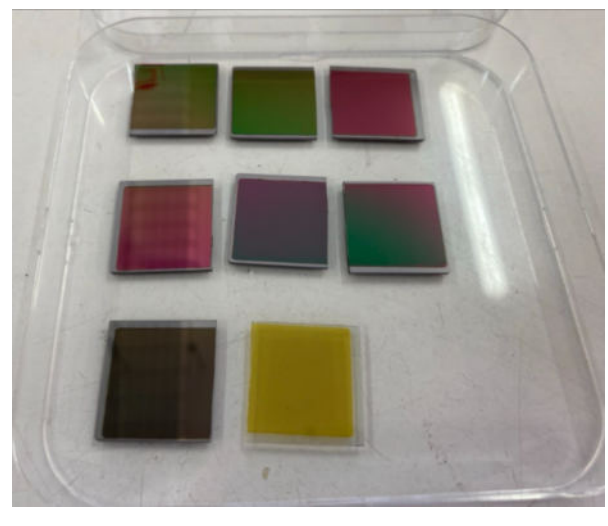
Some of the films we have made will be subjected to post-deposition treatment (annealing in vacuum and sulphur), similar to the samples analysed in chapter 5, keeping the same parameters used. The PDT was performed on as-grown samples in closed, evacuated quartz glass ampules with or without a sulphur grain inside. The annealing temperature was  $300^{\circ}$ C and the duration was 72h. For clarity, we will retain the sample name suffixes from the chapter 5: -R for samples annealed in vacuum and -RS for samples annealed in sulphur. We have annealed samples from runs: 240104, 240105, 240130 and 240208. In order to investigate the effect of quenching, we repeated the annealing processes with identical parameters, adding a rapid cooling (of the order of seconds) at the end. Regretfully, we did not have the technical capabilities to perform quenching after the original deposition process. Therefore, we were forced to perform quenching after PDT (being aware that these two processes may not be identical). We have performed quenching on samples from runs: 231213 (SLG), 240130 (SLG/Mo), and 240208 (SLG/Mo). The quenched samples have suffixes: -RQ for samples quenched after annealing in vacuum, and -RSQ for samples quenched after annealing in sulphur.

Lastly, it has to be noted that the deposited CdIn<sub>2</sub>S<sub>4</sub> thin films are not uniform on the entire surface of the substrate. The non-uniformity can be seen with the naked eye as a variation of colour (see Fig. 6.2.1a). It is a technological issue – the thickness fluctuations

result from the substrate position relative to evaporation sources inside the chamber [243]. The question is, therefore, what effect will such thickness variation have on the performance of the final devices, and will the same composition fluctuations occur?



(a) 240208-hot deposited film. Visible colour gradient results from variation in CdIn<sub>2</sub>S<sub>4</sub> layer thickness [243].



(b) Series: 240311A, 240311B, and 240312 on Mo and ITO.

Figure 6.2.1: Deposited  $CdIn_2S_4$  thin films.

# 6.3 Thin films' analysis

In this part, we will focus on the characterisation of the deposited thin films. At the outset, it should be noted that the presented results could be treated rather as an introduction to the complete characterisation of the samples, which will be performed in the future.

# 6.3.1 Composition

We have performed EDX scanning, mainly on the samples from the mainline series, and got the elemental composition of the samples. Figure 6.3.1 shows the calculated In/Cd atomic ratio. For the film grown on molybdenum, obtaining information on the sulphur content was significantly difficult due to the overlap of the sulphur and molybdenum peaks on EDX spectra. In the plot, we also hint the presumed temperature range, where

 $CdIn_2S_4$  grows amorphous. The In/Cd ratio uncertainty values were calculated from the standard deviations of the Cd and In atomic fractions measured at multiple points on the sample<sup>6</sup>. The most important conclusion from the EDX measurements is the increase in the indium to cadmium ratio with increasing temperature. It is caused by a partial re-evaporation of CdS from the deposited layer. This CdS loss increases with substrate temperature. At temperatures below 250°C, we obtain an In/Cd ratio close to 2 corresponding to the  $CdIn_2S_4$ . Increasing the substrate temperature to 400°C allows for getting In/Cd  $\sim 4$  corresponding to the  $CdIn_4S_8$ . The effect of re-evaporation is a commonly known phenomenon, present during the growth of chalcogenides [248].

Let us now try to solve the issue of the unknown difference in the deposition temperatures of samples where covers were used. Firstly, we can safely take that  $T_{hot}$  >  $T_{medium} > T_{cold}$  in all of the series. Secondly, we will suppose that the temperature differences between those are the same in all series. Since we know the substrate temperature of the samples hot, those will be marked fixed<sup>7</sup>. Thirdly, we will also assume that In/Cd is a monotonous function of temperature. Now, the key to deducing the missing temperatures is finding samples whose compositions overlap. Assuming monotonic temperature dependence, we can then back-propagate temperature changes introduced by the covers. Such a hint is brought by the 240311B series having  $T_{hot}=320$ °C. marked by red circles (●). The In/Cd of 240311B-medium falls close to 240311A-hot and 240130-cold, and the composition of those samples is interlaced with the rest of the series. Thus, we can guess that the difference between hot and medium samples is  $\sim 100^{\circ}$ C, and between hot and  $cold \sim 190$ °C. After applying the deduced differences to the rest of the samples, we get a rearranged composition temperature relation (Fig. 6.3.1). We assumed a 40°C tolerance for the temperature uncertainties for the guessed values. After rearranging, one can observe that the measurements fall into a general trend of decreasing Cd content.

<sup>&</sup>lt;sup>6</sup>Despite taking the measurements from a small fraction of the layer surface (~0.25cm<sup>2</sup>), the composition can still significantly vary among multiple points having size of the focused electron beam. In the absence of better measurements, we must extrapolate these values to the entire sample surface.

<sup>&</sup>lt;sup>7</sup>Those are the points marked with the black contour.

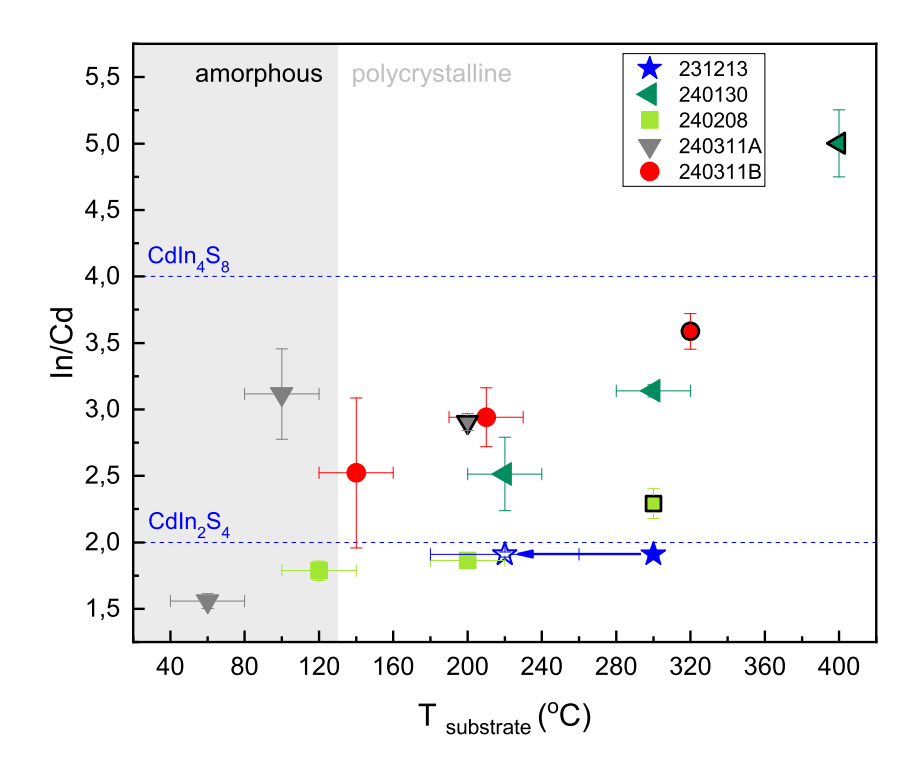


Figure 6.3.1: Substrate temperature – composition (In/Cd) relation, measured using EDX. Black-framed points have non-guessed temperature values.

In the temperature-composition dependency plot, we also marked the In/Cd ratio for the sample 231213 (reference C24-AS) grown on SLG at 300°C (denoted by the symbol  $\bigstar$ )<sup>8</sup>. In the case of the 231213 run, the thermocouple was taking the temperature directly from the SLG substrate. The measured In/Cd ratio falls close to 240208-hot (with a 0.5 difference), having the same deposition temperature. However, if we move this point to the left by the same amount as in the case of the substrate covers, the point falls almost precisely at the 240208-medium – covered by 1mm SLG. The question arises here: how does the measured temperature really relate to the actual substrate temperature experienced by the growing CdIn<sub>2</sub>S<sub>4</sub> layer at the first place? Thermal conductivity of SLG is ~1W/mK [249]; it can be assumed with great certainty that the thermal conductivity of Mo thin

The atomic fraction of sulphur was 58.96(0.19)%, giving  $\frac{S}{Cd+In} = 1.436(0.008)$ , which is larger than theoretical 1.33, thus sulphur is in excess in 231213 series.

films is at least one order of magnitude higher, so the Mo-coated substrate probably only ensures a more uniform growth temperature. The bare SLG substrate, however, could have the same temperature-decreasing properties as the covers applied; therefore, the real substrate temperature perceived by the growing CdIn<sub>2</sub>S<sub>4</sub> is lower than any measured temperature.

On the other hand, SLG has lower absorbance in the infrared range than molybdenum [250] (lower than 100%), so we will heat molybdenum substrates more efficiently. Combining IR absorbance and the low thermal conductivity of the SLG, one could infer that only Mo-coated substrates would achieve the desired temperature. Consequently, all samples grown on SLG would have lower deposition temperatures than expected, including the samples from chapter 5. Therefore, we should shift the 231213 point as shown in Fig. 6.3.1.

From another perspective, the decrease in cadmium content in sample 241213 may be due not to temperature but to a substrate change. Thus, all of the temperatures (without the covers) despite the substrate material are possibly factual. We will return to this issue in subsequent sections.

### 6.3.2 X-ray diffraction spectra

We have measured X-ray diffractograms of a chosen set of  $CdIn_2S_4$  samples. The measurements were taken on a standard Bragg-Brentano X-ray diffractometer. All measured XRD diffractograms (apart from amorphous phases) generally followed the reflections corresponding to  $CdIn_2S_4$  having  $Fd\bar{3}m$  (227) space group. Herein, we will briefly survey selected results:

Figure 6.3.2 shows diffractograms of reference C24-AS (231213-AS) and the 240105 series. By the grey lines we marked reflection positions corresponding to the calculated powder diffraction pattern of the  $CdIn_2S_4Fd\bar{3}m$  spinel phase having lattice constant a=10.97Å. We signed the crystallographic planes corresponding to the individual reflections. Due to the low layer thickness, we do not observe high-angle reflections, and the overall signal is low compared to the noise floor. All observed peaks are shifted relative to their

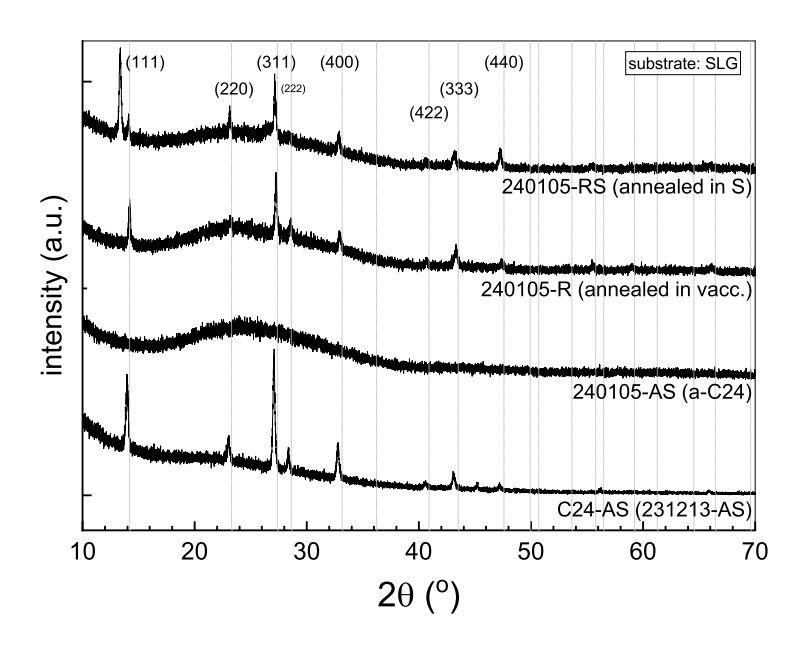


Figure 6.3.2: X-ray diffractogram of the 231213 and 240105 samples (in as grown state and after annealing). Grey lines mark expected peak positions for  $Fd\bar{3}m$ .

calculated positions, possibly due to lattice strain. The amorphous halo, centred at 25°, present in all of the diffractograms of the samples grown on SLG, originates from the soda lime glass substrate [251].

The absence of any reflections in 240105-AS film indicates that the CdIn<sub>2</sub>S<sub>4</sub> indeed grows amorphous below 130°C (a-C24). Annealing, as expected, leads to recrystallisation of the compound, thus the return of the diffraction peaks (samples 240105-R and 240105-RS). The reflections reappear at roughly the same positions as in 231213-AS. In 240105-RS, we also observe the emergence of a strong peak at 13.37°. We did not manage to assign this reflection to the expectable phases, i.e. CdIn<sub>2</sub>S<sub>4</sub> ( $Fd\bar{3}m$ ),  $\alpha$ -CdS (P63m),  $\beta$ -CdS ( $F\bar{4}3m$ ),  $\beta$ -In<sub>2</sub>S<sub>3</sub> (I4/amd). The only observable cause of this peak is the presence of sulphur during annealing: this peak is present in 241014-RS and 231213-RSQ samples<sup>9</sup> (vide appendix on page 343).

As the 240311A-medium and 240311A-cold films fall into the temperature range where we obtain a-C24 layer (cf. Fig. 6.3.1), one could expect it to be confirmed in XRD

<sup>&</sup>lt;sup>9</sup>Parenthetically, quenching during annealing changes the crystal structure to a negligible extent.

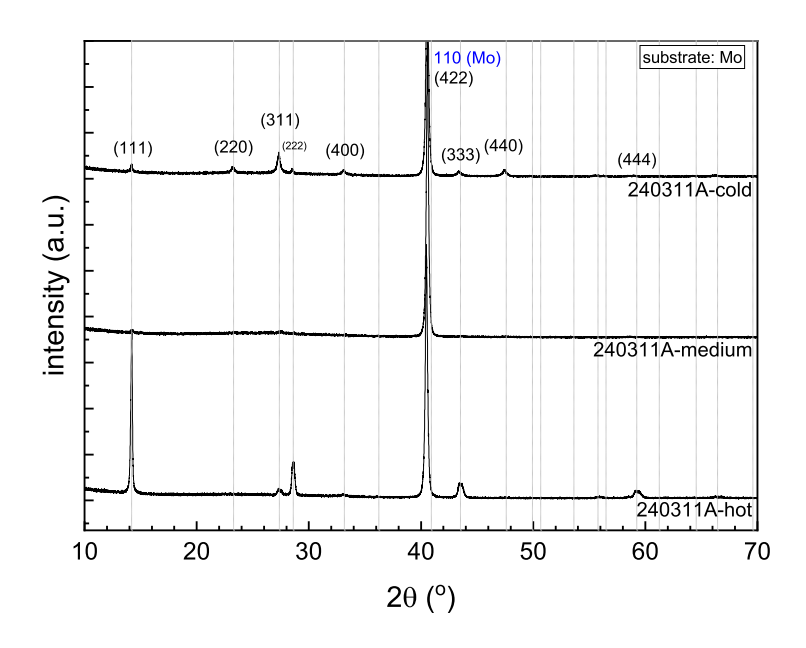


**Figure 6.3.3:** X-ray diffractogram of the 240311A samples. In 240311A-medium we observe only molybdenum (110) reflection. Grey lines mark expected peak positions for  $Fd\bar{3}m$ .

patterns. Indeed, for 240311A-medium, we do not observe any reflections corresponding to  $CdIn_2S_4$  (Fig. 6.3.3). However, in 240311A-cold sample, the reflections reappeared at the same positions, still falling into the  $Fd\bar{3}m$  crystal structure, for which we currently do not have any interpretation.

In the XRD patterns for samples grown on molybdenum, one will also observe reflections at 40.5° and 58.62°, corresponding to (110) and (200) crystalline planes of molybdenum, respectively [252]. The Mo (200) peak overlaps with CdIn<sub>2</sub>S<sub>4</sub> (444) peak. In 240311A-hot sample, we observe a severe increase in the (111) peak amplitude compared to 231213-AS, possibly indicating preferential orientation of this plane, caused by the growth on the Mo substrate. Preferential orientation or texture can occur due to minimising the surface energy during deposition, thus forcing optimal crystalline orientation in relation to the substrate crystal structure [253]. Texture can also be caused by anisotropic growth rates from grains with different orientations.

We can explore the possible substrate impact on preferred orientation by comparing similar samples grown on Mo and SLG. In Fig. 6.3.4 we apposed 231213-AS, sisterly

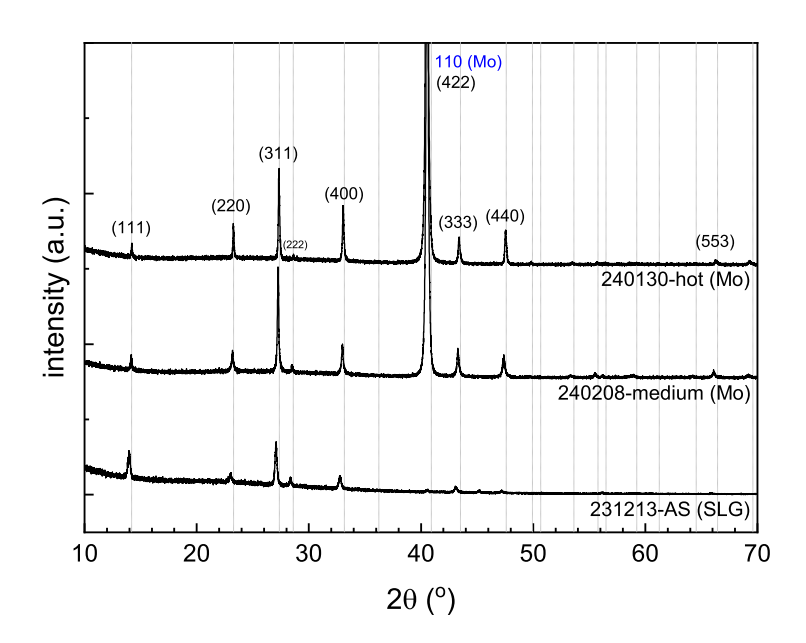


**Figure 6.3.4:** X-ray diffractogram of the 231213 and 240208-hot samples – comparison between samples grown at SLG and Mo. Grey lines mark expected peak positions for  $Fd\bar{3}m$ .

240208-medium (cf. Fig. 6.3.1), and 240130-hot. It can be noticed that the suspected preferred orientation (111) is not the general rule – for these samples, we observe only a significant increase in higher-order peaks.

On account of the fact that the obtained diffraction peaks, especially for samples grown on SLG, have low intensity and a high signal-to-noise ratio, it was difficult to apply any intricate refinement method, such as Le Bail or Rietveld refinement, to the data. Attempts at refinement often produced unphysical results, e.g. grain sizes many times larger than the layer thickness or overunity site occupations. Therefore, we will refrain from giving detailed refined sample parameters<sup>10</sup>. We have obtained only lattice constants for the samples calculated from the reflection positions (table 6.3.1). As one can see, there are no overt regularities, besides, perhaps values closer to 11Å for samples annealed in sulphur. We observe systematic deviation from the theoretical unit cell size for all samples, possibly indicating strain introduced by growth on a particular substrate.

Since we lack the requisite refined structural parameters, any attempt to deduce

<sup>&</sup>lt;sup>10</sup>Besides that, Le Bail and Rietveld refinement methods have limited use for thin film analysis.

**Table 6.3.1:** Lattice constant values, calculated from XRD diffractograms.

sample	substrate	a (Å)
231213	SLG	10.888(0.001)
231213-RQ	SLG	10.8760(0.0006)
231213-RSQ	SLG	10.923(0.001)
240104-AS	SLG	10.88(0.01)
240104-R	SLG	10.90(0.01)
240104-RS	SLG	10.88(0.07)
240105-R	SLG	10.815(0.001)
240105-RS	SLG	10.898(0.001)
240130-hot	Мо	10.8300(0.0004)
240208-medium	Мо	10.8629(0.0004)
240311A-hot	Мо	10.85(0.08)
240311A-cold	Мо	10.860(0.001)

conclusive insights from the diffractograms remains, at best, speculative. The observed variations in peak amplitude can originate from both texture (preferred orientation) and fractional occupations of particular atom sites in the lattice. In C48-type films (e.g. 240130 series), the latter should be peculiarly amplified, as the structure principally lacks half of the cadmium atoms while remaining unchanged. In light of the collected measurements, it is impossible to clearly indicate a causal relation between the reflection intensities and the cadmium content. It is probably due to the fact that a parallel factor determining the occupation of atomic sites is the spinel inversion. However, not in the sense of replacing atoms in the crystal lattice, as it should not be forgotten that Cd and In are isoelectronic, thus their replacement will not be visible in XRD. Cd and In atoms will collectively share tetrahedral and octahedral positions put together, ergo particular sites occupations would be a convoluted function of Cd content and inversion.

The preferred crystallographic orientation may be more important in determining the observed diffraction patterns. The orientation of the substrate crystallites will most likely determine the orientation of the first growing seed. This orientation can be assumed to be random on glass, but not in molybdenum. Subsequent grains may readily adopt the orientation of the original grain, resulting in the texture of the film (e,g. that could be observed on TEM image, in [21]). Moreover, thin films deposited using our method tend

to grow in columnar patterns, which may result in layer texture, grain size anisotropy, and crystal lattice strain.

In summary, perhaps the most crucial conclusion from the XRD measurements is the potential influence of the substrate, which may prove to be more important than initially anticipated. Furthermore, more detailed studies, for example, using a more suitable method for thin films analysis, e.g. a grazing incidence XRD (GIXRD) [254] to examine the structural properties of CdIn<sub>2</sub>S<sub>4</sub>, should be conducted.

#### 6.3.3 Photoluminescence

Here, we will focus on analysing the photoluminescence spectra of the produced thin films. The measurements presented in this section were performed exclusively in Nantes using a system available there, equipped with an 460nm (2.7 eV) excitation laser at room temperature. Regretfully, it is not the same wavelength as in the measurements in chapter 5.2.1, where the 514nm line was used. Therefore, we cannot take the most straightforward approach, which would be a direct comparison of the obtained data with the spectra from chapter 5.2.1 (Fig. 5.2.1, 5.2.2).

Let us start with the reference C24-AS sample (231213-AS). Its PL spectrum is shown in Fig. 6.3.5, as well as in the appendix on page 344. As one can see, in this case, a 1.45eV peak, originating (as we believe) from cadmium vacancies, dominates the spectra. To relate the result to the spectra from chapter 5, the potential effect of changing the wavelength of the excitation laser should be considered. Previously, we did not consider the possible influence of different wavelengths on the photoluminescence spectrum, and which transitions the 514nm line really induces. 514nm, corresponding to 2.4eV, should still fall within the indirect band-band transition's ambit. Therefore, 460nm excitation could be considered as inducing similar emission spectra. From an alternative perspective, suppose we assume that the 514nm induces not band-to-band excitation, but pumps mainly the VB-T transition (directly to the T states – vide 5.6.2), then 1.6eV, 1.8eV and 2eV emissions would indeed dominate over 1.45eV – which requires carriers in the conduction band. Band-band excitation would increase 1.45eV emission, concurrently

decreasing 1.8eV emission as it would have need more complicated recombination traffic, moving the spectrum maximum towards 1.45eV<sup>11</sup>.

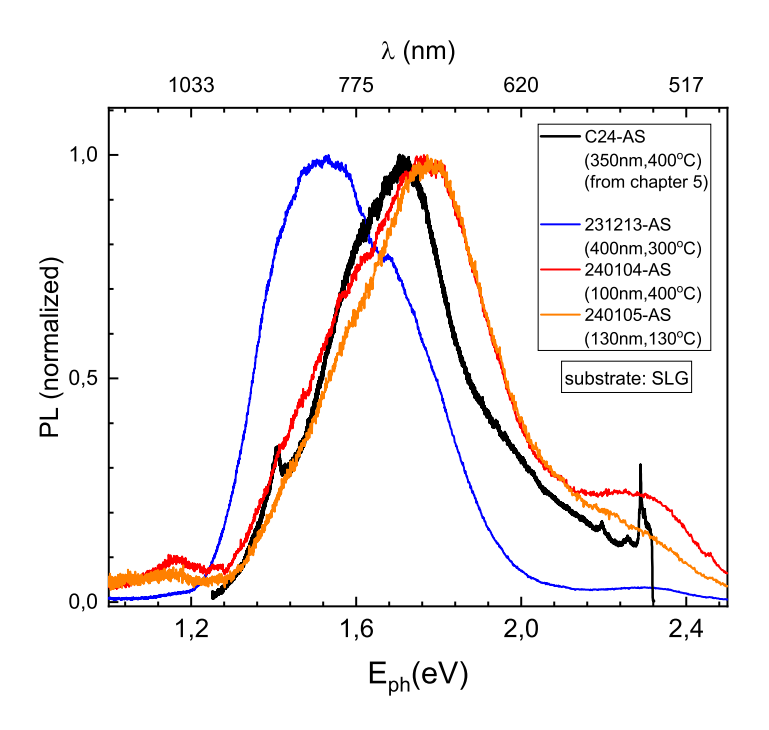


**Figure 6.3.5:** Photoluminescence spectra of the C24-AS from chapter 5 and for as grown samples from 231213, 240104 and 240105 runs.

In Figure 6.3.5, we gathered normalized<sup>12</sup> PL spectra of the C24-AS sample from chapter 5.2.1, and the spectra of 231213, 240104 and 240105 as-grown samples, all deposited on SLG. Those entries differ in three aspects: layer thickness, deposition temperature (and thus composition), and excitation line wavelength. Sample 231213-AS indeed gravitates towards 1.45eV as we reasoned. However, samples 240104-AS and 240105-AS (under 460nm excitation) follow the original C24-AS spectrum. This implies more intricate nature of 1.45eV emission: either its contribution in the PL is a non-monotonous function of deposition temperature (sample 240105-AS vs 240104-AS), it depends on layer thickness, or on stoichiometry. Unfortunately, we do not have composition data for the 240104 and 240105 series; thus, we cannot process the potential third option.

<sup>&</sup>lt;sup>11</sup>Ergo, if we measure PL of 231213-AS using a 514nm laser, we would get a spectrum similar to C24-AS. <sup>12</sup>As the samples have different thickness, we cannot directly compare the amplitude of the spectra.

Lastly, emissions above 2eV for the samples excited with 460nm have a larger amplitude than in C24-AS, mainly for the same reason as discussed in the case of 1.45eV emission – carriers recombining from CB have more emission paths possible, e.g., indirect emission to VB. Presence of those transitions under a 460nm excitation line may indicate the validity of the assumption of potential differences between excitation by the lines 514nm and 460nm.

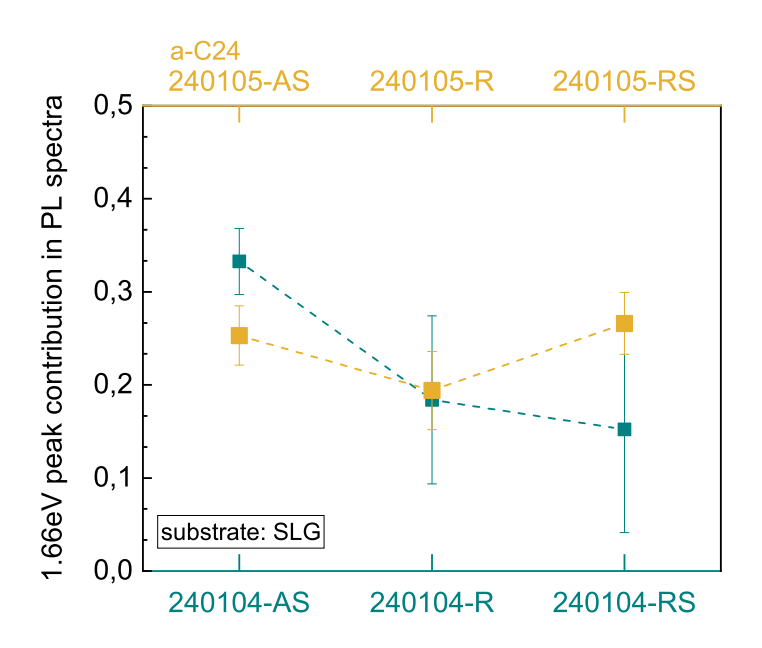


**Figure 6.3.6:** Contribution of the 1.66eV emission to the total photoluminescence spectra for 240104 and 240105 series.

For the series 240104 and 240105, the annealing of the samples induces roughly similar effects on PL as for the old C24 and C48 samples, as discussed in chapter 5.2.1, (the 240104, and 240105 PL spectra can be found in the appendix on page 344), although the total 1.66eV peak contribution (performed akin to the analysis from mentioned chapter 5.2.1 – see Fig. 5.2.3) in total PL spectra is two times smaller compared to original C24 samples, possibly due to discussed enhanced 1.45eV contribution (Fig. 6.3.6). Notwithstanding this, we would infer that the inversion degree in 240104 samples decreases in the same manner as in the old C24 samples. Parenthetically, if we assume that 240104-AS fall closer to C48, as it was deposited at a temperature 100°C higher than

231213-AS (where  $In/Cd \approx 2$ ) – it contradicts our previous findings, in which the 1.66eV peak ratio in C48 samples was disturbed by the cadmium deficiency (cf. Fig. 5.2.3). However, reversing this reasoning, we can conclude that sample 240104-AS is actually closer to C24 ( $In/Cd \approx$ ) 2, because it has the 1.66eV peak ratio dependency more similar to C24, not C48. Ergo, deposition on SLG still produce composition close to C24, unlike deposition on molybdenum.

The fact that 240105-AS is amorphous does not seem to influence the PL spectra in a significant manner, except that we do not observe a clear decreasing dependence, although the actual causation of this fact is, regrettably, still obscured. It is unclear whether the amorphous phase directly relates to the order-disorder transition at 403K. However, from the point of view of condensed matter physics, these are two completely unrelated entities; even if one insists on associating disorder with the amorphous phase, according to Czaja, disordered spinel forms above this temperature, not below.

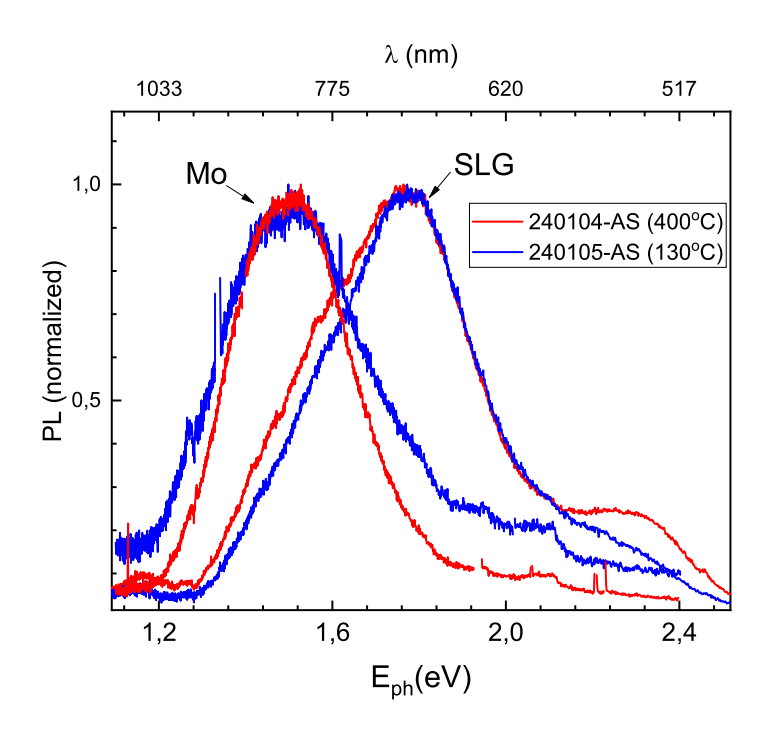


**Figure 6.3.7:** Comparison of PL spectra of samples grown on SLG and Mo. It is evident, that the effects of substrate temperature are minuscule, compared to substrate type.

Just as in the chapter on XRD, where we compared layers grown on SLG and molybdenum, revealing the differences lurking there, we will repeat the same here for photoluminescence. In Figure 6.3.7 we have drawn PL spectra for samples from the 240104 and 240105 series. In this comparison, unlike Figure 6.3.5, we eliminate most variables that obscure the analysis, leaving a clearer picture. It is now readily apparent that there is an essential difference introduced by the substrate, significantly greater than the potential effect of temperature, especially since we are comparing samples 240104 and 240105 – deposited at two extreme temperatures. The observed change is mainly due to the magnitude increase of the 1.45eV peak, which we associate with cadmium vacancies, that shifts the overall observed spectrum towards a lower energy range.

Measuring the PL spectra for the samples from the mainline series (grown exclusively on molybdenum) reveals this effect to be a general behaviour for Mo-deposited samples (Fig. 6.3.9). This, combined with the fact that we do not observe such a shift in any layer deposited on SLG, strongly suggests that the temperature-dependent cadmium re-evaporation might be specific for Mo substrates only. Moreover, if global cadmium deficiency is directly responsible for the  $V_{Cd}$  formation, we should observe a strong correlation between the intensity of the 1.45eV peak and the cadmium content. To search for this correlation, we can analyse the contribution of the 1.45eV peak to the measured luminescence spectrum (Fig. 6.3.9). Alas, no significant correlation is observed here, perhaps due to more intricate relations governing the photoluminescence spectra (e.g., correlation with the inversion degree), or simply the fact, that we try to compare compositional effect with the point defect response.

In chapter 5, we concluded that the luminescence – the 1.66eV peak could be treated as a marker of the inversion degree. We can therefore perform the analysis of the 1.66eV peak ratio for the mainline series, and obtain temperature or composition 1.66eV ratio dependency – possibly unveiling temperature dependence of the inverted cation sublattice formation. Figure 6.3.10 presents the 1.66eV ratio dependency as the function of stoichiometry and temperature. Although plotting the ratio as a function of the In/Cd does not reveal any correlation, it is readily apparent that, in a function of temperature,

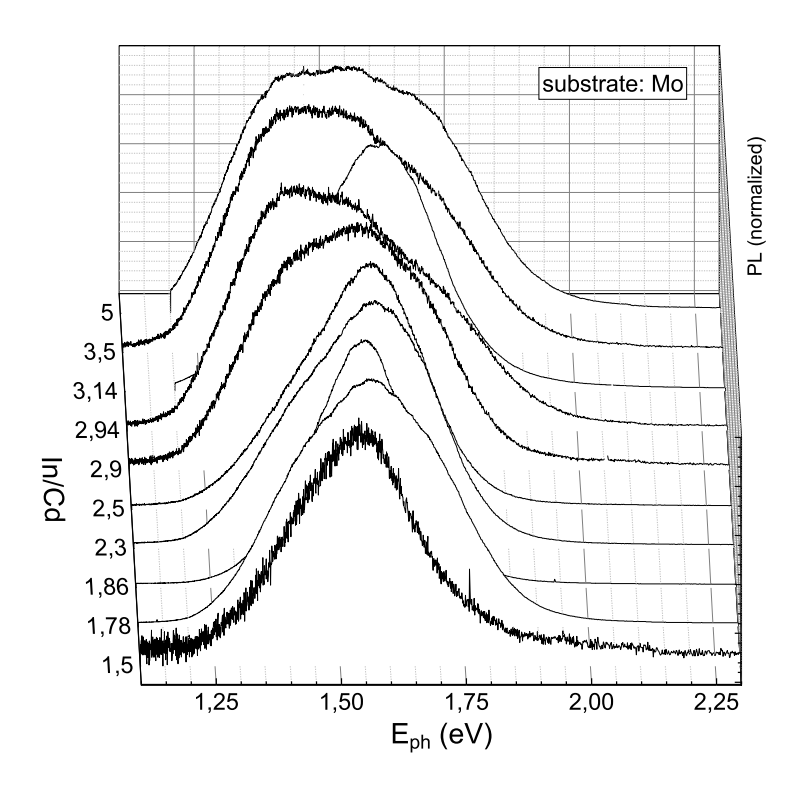


Figure 6.3.8: Photoluminescence spectra for the samples from mainline series, deposited on molybdenum. All of the spectra are shifted towards 1.45eV.

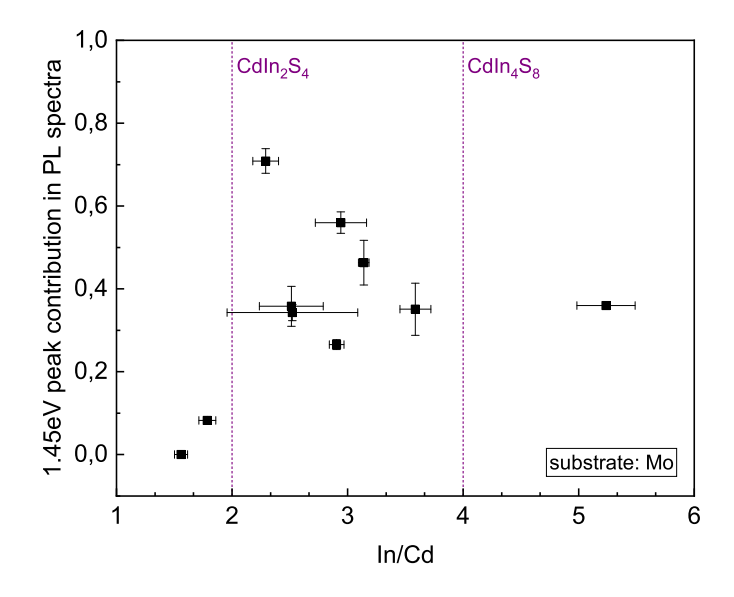
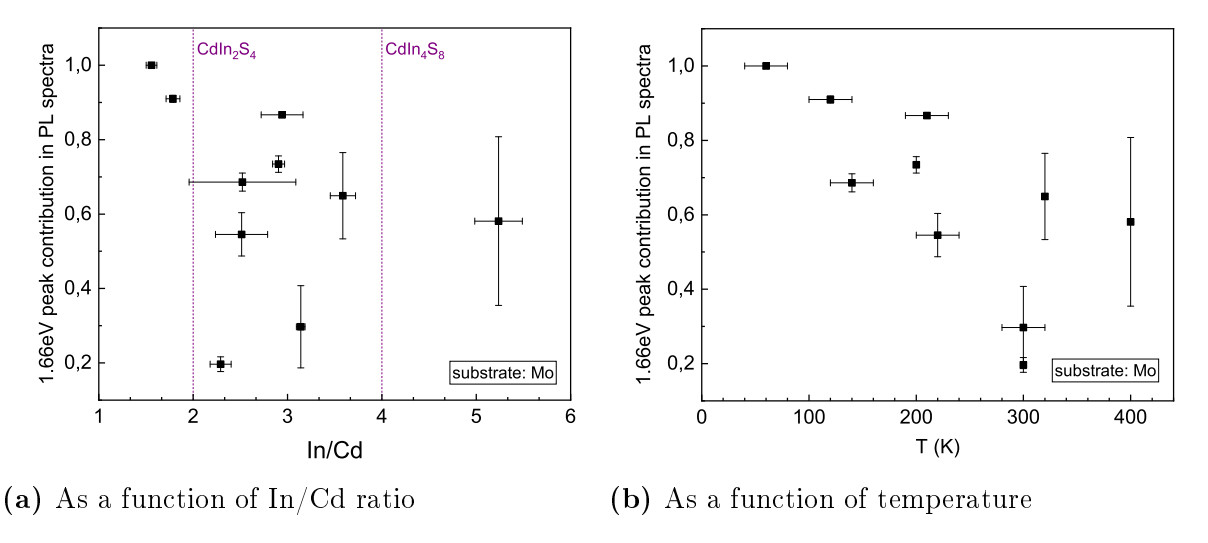


Figure 6.3.9: Contribution of the 1.45eV emission to the total photoluminescence spectra in the function of In/Cd ratio for mainline series.

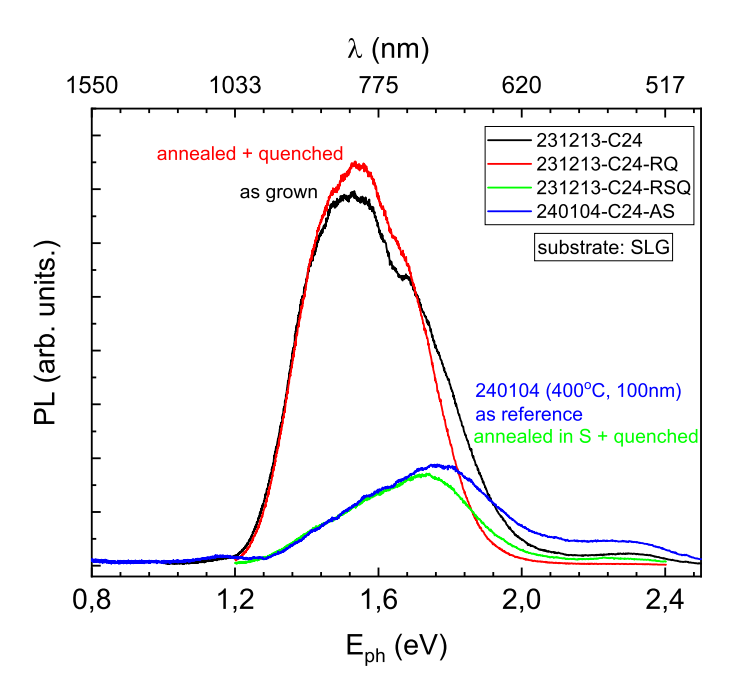
a faint trend can be seen (Fig. 6.3.10), hinting the demanded temperature-inversion dependency. Yet, it is probably too early to announce 1.66eV photoluminescence measurement as a practicable indirect method of estimating the inversion degree before comparison with bandgap analysis or other methods, which can give more credible information about cation sublattice. Even if so, these results cannot be directly compared to the results from 5.2.1 without accounting for the influence of the Cd deficiency; put another way, accounting for the difference between C24-AS and C48-AS as in Fig. 5.2.3. Nevertheless, we may attempt this execution: ratio being equal to 0.6 would represent  $x \approx 0.1$  (samples grown at 200-300°C), and  $0.3 \rightarrow x \approx 0$  (above 300°C). Samples with a higher 1.66eV ratio are therefore expected to have larger spinel inversion.



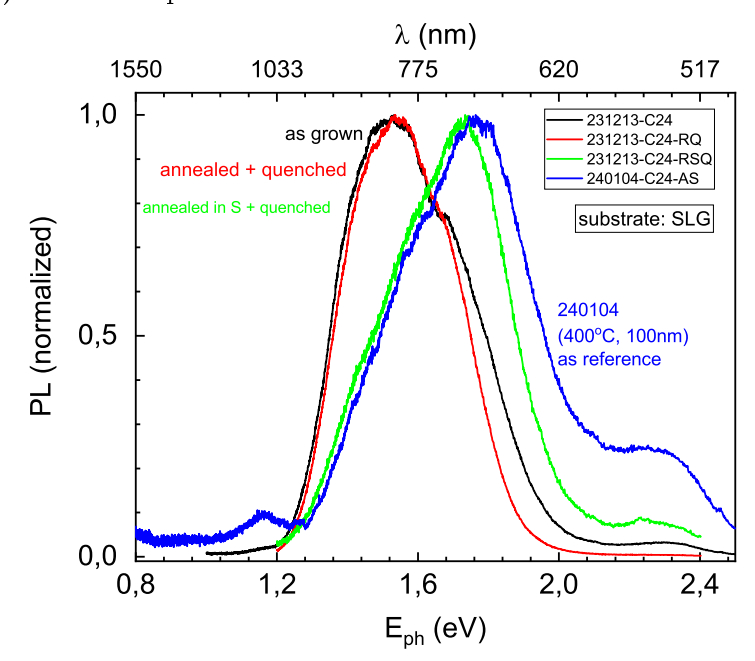
**Figure 6.3.10:** Contribution of the 1.66eV emission to the total photoluminescence spectra for the mainline series.

One more aspect worth considering, are the PL spectra of the samples subjected to quenching (Fig. 6.3.11). As the quenching after annealing in vacuum does not seem to introduce any difference to the PL response, the quenching after annealing in sulphur causes a massive collapse of the 1.45eV and 1.66eV part of the spectrum, i.e. leaving mainly the response of the sulphur vacancies. In the normalised spectra, one needs only observe that the quenching in vacuum makes the 231213 sample resemble the 240104 sample – it reproduces the exact difference from the Figure 6.3.5, deliberated at the beginning of the photoluminescence discussion, or the difference between SLG and Mo

substrates (Fig. 6.3.7). A comprehensive elucidation of this phenomenon – revealing the true action of quenching process, however, necessitates further inquiry.



(a) measured spectra



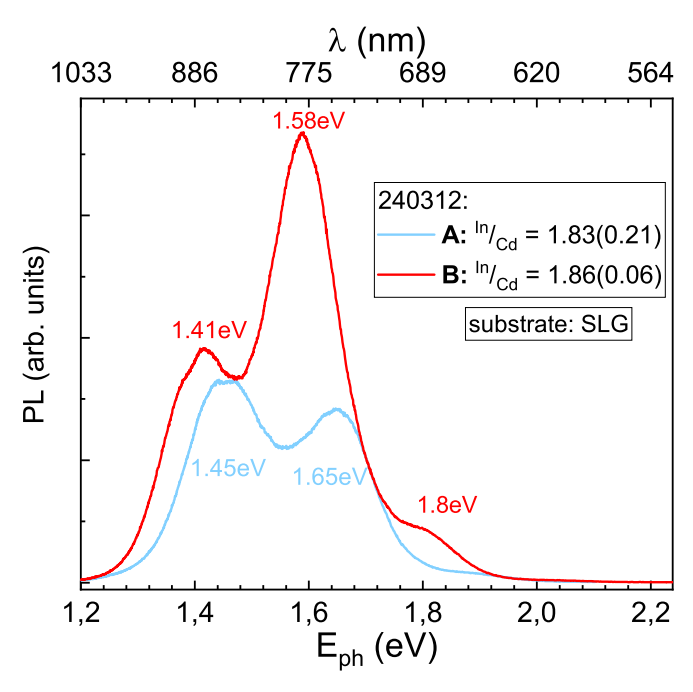
(b) normalized spectra

Figure 6.3.11: Effects of quenching on photoluminescence spectra.

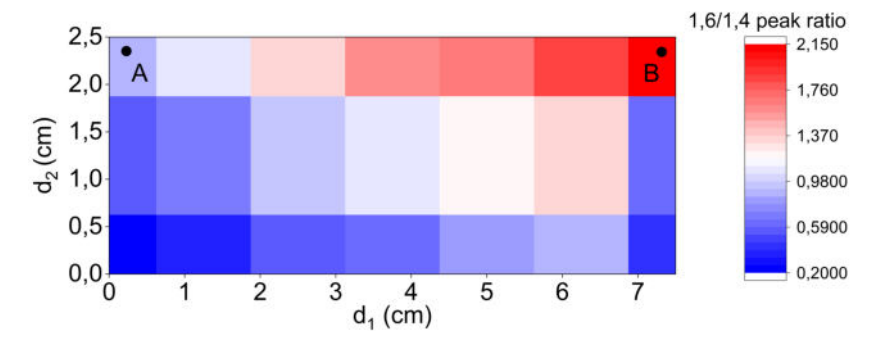
Lastly, one more sample, which surprisingly introduced more complexity to the photoluminescence conundrum, was the 240312 sample, grown on SLG at 300°C, thus under the same conditions as 231213, but for two hours, resulting in a two times thicker (~800nm) layer. Here, for the first time, we witness spectra with two distinct peaks, instead of the usual blurred three- to four-peak conglomerate (Fig. 6.3.12a). The maxima of these peaks approximately fit our recognised energies corresponding to the emission to the  $V_{Cd}$  and the T-E emission; however, a non-negligible 50meV shift from the established by us peak energies is observed. As an aside, peak positions seem to vary alongside their amplitude, which in some sense questions our discretionary assumptions about the origin of these peaks. The key issue, however, is the fact that the intensities of these two peaks vary among different places on the sample. Similarly to the presence of separated peaks itself, this is the first such case observed in the photoluminescence spectra we have studied. To investigate the PL spectrum variations further, we performed systematic spectra measurements as a function of position on the sample surface. Since we all observe two dominant peaks ( $\sim 1.45 \text{eV}$  and  $\sim 1.6 \text{eV}$ ), we calculated their ratio to quantitatively characterise the PL spectrum at each point on the sample. Thus, we can plot a map of the ratio as a function of position on the sample – Figure 6.3.12b. The spectra presented in the plot 6.3.12a correspond to points A and B at the two ends of the sample. For those two points, we measured composition using EDX (as in section 6.3.1). For point A, we obtained In/Cd = 1.83(0.21), and  $\frac{S}{Cd+In} = 1.45(0.03)$ ; for point B: In/Cd= 1.86(0.06), and  $\frac{S}{Cd+In}$  = 1.47(0.04). Therefore, the composition differences between those two points are only within the range of uncertainty.

Such variations of compound properties within a single sample are common and typically result from the geometry of the evaporation chamber, i.e., the positions of the evaporation sources relative to the substrates within the chamber [186, 243]. For the same reason, we also observe variations in layer thickness.

Regardless, the problem of technological deviations, a mechanism behind such behaviour of photoluminescence spectra, remains to be solved. The only parameter distinguishing sample 241312 from the others is twice the thickness resulting from



(a) PL spectra for chosen two points



(b) Map of  $1.6 \,\mathrm{eV}/1.4 \,\mathrm{eV}$  peak intensity ratio as a function of position on the sample.

Figure 6.3.12: Photoluminescence spectra for 240312 sample.

deposition time. Ergo, the bottom layers of the sample spent more time in the chamber than the top layers, which were grown at the very end of the process. Now, what if the annealing process, which we applied to some our samples, does not have to take 72h to fully anneal the sample, but the change induced is mainly done in a shorter time, e.g. 2h? If so, during the relatively longer deposition, the bottom (grown first) layers would experience a phenomenon that one could call *self-annealing*. Thus, during a longer run, we expect to obtain layers with annealing gradient, with the top layer being C24-AS and the bottom being C24-R; especially, when the annealing conditions (temperature, pressure)

are the same as the deposition conditions. However, we did not observe such a significant spectral change in any of the annealed samples, so self-annealing is not the source for this behaviour.

The variation in stoichiometry could cause such effect, as it only needs to induce deviations at the level of defect concentration, thus below the EDX resolution. But if so, we would observe such spectra in all the samples.

Substrate temperature variation, that is to say, a discussion from section 6.3.1 plus the possibility of non-uniform heating, could explain the phenomena, but, again, we would observe such behaviour in all of the samples, and moreover, a difference between 240104 and 240105 samples, and we do not.

The layer thickness itself could stand behind the two-peak spectra, as we observe such demeanour exclusively in the 800nm film. It would also explain the differences between 231213 and 240104 samples, although we neither observe the spectra with distinct peaks, nor their variation there. Perhaps distinct peaks become more distinguishable at higher thicknesses, which naturally amplifies the photoluminescence response, conversely, making it barely visible in thinner films. The origin of those variations is then technological: evaporation chamber geometry can cause atomic flux variations in space, and atomic flux fluctuations during deposition can cause variations in time, resulting in spatial and temporal composition deviations. Actually, the latter can solely explain the observed two peaks in the 240312 sample if one assumes that atomic flux fluctuations become gradually more severe above a particular evaporation time, e.g. above 1h, possibly due to source material run-out. Therefore, longer runs would produce layers with a concentration gradient along the layer thickness. Therefore, the 240312 sample is, in a way, a stack of multiple layers, and the observed spectrum is a response from the sum of those. The same goes for EDX. Hence, the previously rejected stoichiometry is indeed guilty of producing two-peak PL spectra, but such an effect is visible only in thicker CdIn<sub>2</sub>S<sub>4</sub> layers. To verify this hypothesis, one should carry out more detailed point measurements of the composition and, perhaps, measure the composition profile as a function of thickness.

## 6.4 Concluding remarks and future work

From the experimental results elucidated in the preceding sections, one could be incentivised to pursue the definitive resolution, precisely as displayed in Chapter 5. Alas, due to the regrettable paucity of crucial evidence and the speculative nature of certain results, such a comprehensive presentation remains, for the moment, beyond our grasp.

Notwithstanding the speculative nature of our results, these point to peculiar directions for further research. The first is to perform more intricate X-ray diffraction experiments, i.e. a grazing-angle XRD, to acquire more information regarding the samples' crystallinity and predominantly preferred orientation. Moreover, other structural-oriented techniques such as SEM and TEM would benefit such an inquiry.

In section 6.3.1, we debated the potential covering effect of the glass substrates themselves on the deposition temperature. In light of the photoluminescence data, it seems more probable that we are dealing mainly with substrate-related cadmium deficiency, not temperature effects. If one closely relates the increase in the 1.45eV peak amplitude to cadmium deficiency, it becomes evident that the growth on molybdenum enriches the compound with cadmium vacancies. It also seems that the discussed CdS re-evaporation might be weaker for SLG substrates. Connecting this with XRD data, implies, that the strain of the crystal lattice growing on molybdenum may affect the embedding of cadmium into the crystal structure.

Latest photoluminescence measurements demonstrated how important the 1.45eV peak is, which has been overlooked so far. To finally resolve the PL case, more systematic measurements are necessary, especially examination of the effects of various excitation wavelengths on PL spectra. Perhaps, an excitation photoluminescence experiment (akin to the experiments performed in [217]) could provide vital evidence.

Even though the search for a transition between T and V regimes was one of the main goals set at the beginning of this chapter, we have not provided any analysis dedicated to this question. The reality of the matter is that none of those experiments presented can be used to search for this transition. To examine this, one has to perform

a  $\sigma_{DC}(T)$  measurement, which will provide information about the Fermi level position, which, combined with the EDX data, will solve this case.

Similarly, the study on spinel inversion degree remains unfinished. Its continuation, however, requires performing electrical measurements, at least  $\sigma_{DC}(T)$  and  $\Delta\sigma(\lambda,T)$ , to obtain data that enabled us to answer the same questions in chapter 5. Comparing the photoluminescence data with bandgap measurements will verify the conclusions inferred about the 1.66eV peak ratio. As we have more sample material, we will be able to verify and possibly modify or expand the  $CdIn_2S_4$  model. Moreover, the evidence gathered strongly suggests a causal relationship between cadmium content and inversion degree. Similarly, resolving the issue (also omitted) of the 403K temperature requires these measurements to be made. The fact that the layers grown under the 403K are amorphous is probably unrelated to Czaja's spinel inversion.

Likewise, in the case of quenching, which may seem to be leading nowhere, optoelectronic studies of the quenched layers will allow us to examine the research questions<sup>13</sup>.

Summarising, it is imperative to acknowledge that the pivotal goal for producing the thin films was to manufacture neuromorphic devices, with the presented analysis serving as an interim characterisation tool. The culmination of the research presented here and the entire dissertation will be an analysis of devices carried out in subsequent chapters.

<sup>&</sup>lt;sup>13</sup>Preliminary measurements of the transmission coefficients indicate that in the case of quenched layers we indeed deal with severe bandgap decrease.

# Chapter 7

# Memristive devices

Throughout the dissertation, the last three preceding chapters focused mainly on characterising the  $CdIn_2S_4$  compound: we have reviewed and summarised the state of knowledge regarding the compound's optoelectronic properties; investigated it further, developing the  $CdIn_2S_4$  model; and then, went over to technological and structural aspects of the material research by growing series of  $CdIn_2S_4$  thin films. The last chapter constituted a foundation for the paramount goal of this work – both literally and figuratively. We will utilise the thin films analysed in the previous chapter to manufacture the neuromorphic, or in general, memory devices based on  $CdIn_2S_4$ . This chapter will focus on the electrical characterisation of the devices created.

## 7.1 Devices' design

As briefly described in the preceding sections, we devised two potential spinel-based device architectures: a device based on the trap-assisted tunnelling effect; second, a CdIn<sub>2</sub>S<sub>4</sub>-based modulated rectifying junction. Throughout the work, we have manufactured five types of complete devices having the form of a stacked (multilayer) structure (Fig. 7.1.1b), trying to realise those architectures. A complete description of the devices' design, including the justification for the choices made, leading to the final design, cannot be conducted without outlining the devices' development history.

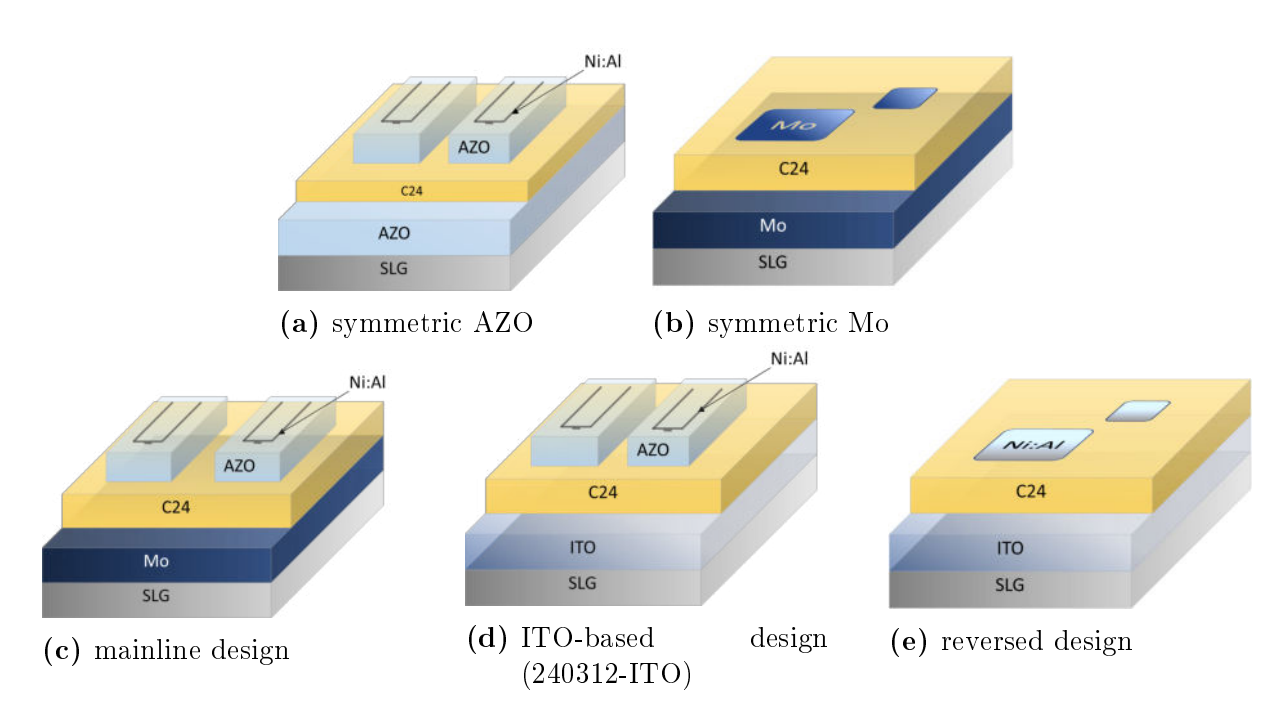


Figure 7.1.1: Devices' designs

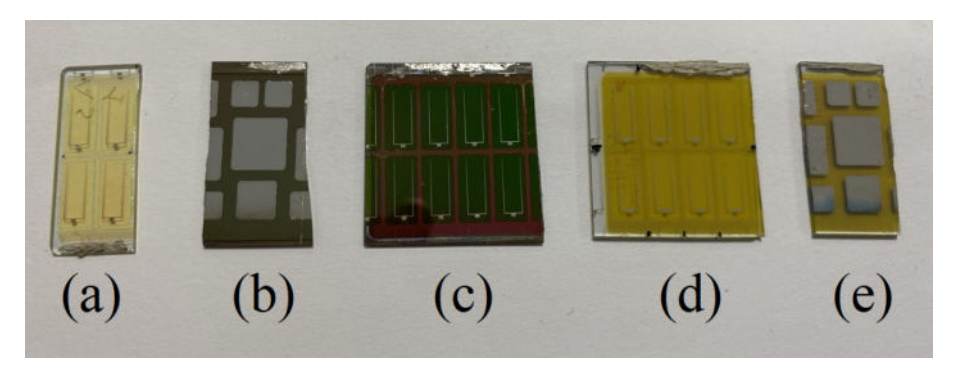


Figure 7.1.2: Picture of the devices: (a) symmetric AZO, (b) symmetric Mo, (c) mainline, (d) ITO-based, (e) reversed design.

#### $First\ shot-240104\ and\ 240105\ series$

We started with an attempt at the realisation of the first concept. The first idea is based on the assumption that the hopping transport in the CdIn<sub>2</sub>S<sub>4</sub> can be controlled by changing the charge state of the metastable defects, therefore, by illumination. For the practical realisation of this concept, one must form a structure akin to the MIM (metal-insulator-metal) structure, i.e., embodying a relatively thin C24 film between

two conductive layers (electrodes), ensuring a sufficiently higher work function for the electrodes, thus obtaining a structure, whose approximate schematic band diagram is shown in Fig. 7.1.4. For sufficiently large barrier height  $\Psi_B$ , the trap-assisted hopping will dominate the electron transport through the structure.

Hence, we have grown the 240104 and 240105 series of 100nm C24 thin films for this application. Before completing the devices, part of the as-grown samples were annealed in vacuum and in sulphur, thus we obtained a series of samples: 240104-AS, 240104-R, 240104-RS, 240105-AS, 240105-R, and 240105-RS<sup>1</sup>. As the electrodes need to be transparent to enable illumination of the internal C24 layer, we deposited a 400nm polycrystalline ZnO:Al layer (AZO), deposited by RF sputtering from a ceramic target (wt.%Al2O3 of 3%). Wide-bandgap AZO acts as a transparent electrode, enabling the illumination of the CdIn<sub>2</sub>S<sub>4</sub> active layer with energies below its bandgap, which correspond to wavelengths higher than ~350nm. A comparison of the photoconductivity response range and the AZO transmission window is shown in Fig. 7.1.4. In order to keep the symmetrical design of the devices, the C24 was grown on the AZO layer, and then, on top, a second AZO film was sputtered through a shadow mask, resulting in defining a series of 45mm<sup>2</sup> cells. Finally, Ni:Al electrodes were deposited using the electron beam evaporation through another shadow mask. A complete symmetric AZO structure is shown in Fig. 7.1.1a.

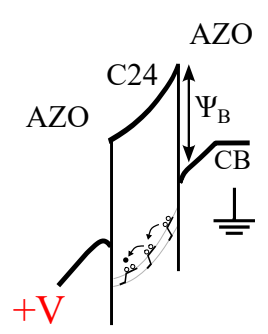


**Figure 7.1.3:** Schematic presentation of the band diagram for the symmetrical AZO structures under bias.

<sup>&</sup>lt;sup>1</sup>Besides creating the devices, 240104 and 240105 layers grown on SLG and Mo were characterised to investigate further the  $CdIn_2S_4$  compound (vide chapter 6).

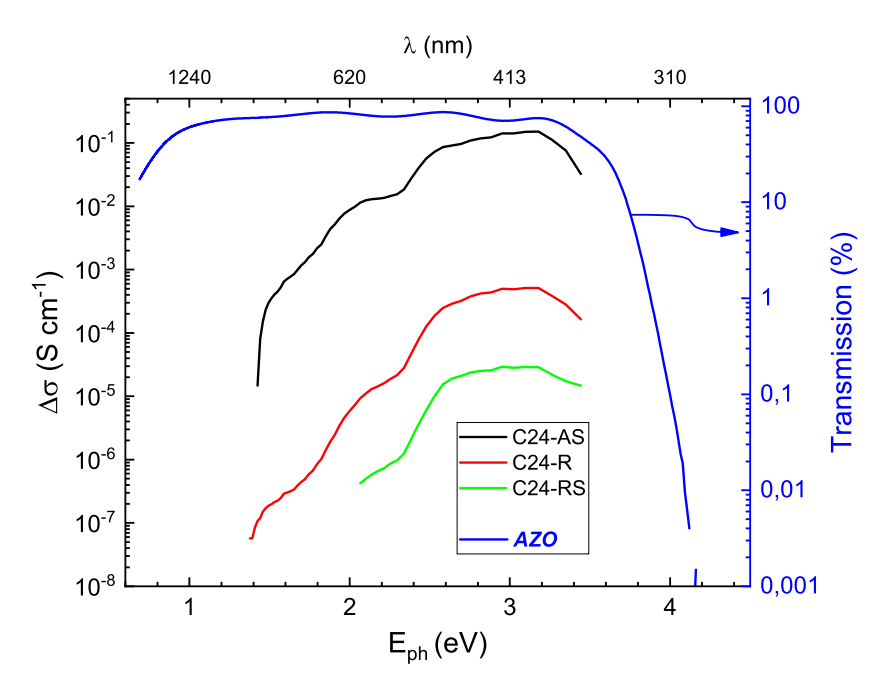


**Figure 7.1.4:** Comparison of CdIn<sub>2</sub>S<sub>4</sub> layers active photoconductivity band and AZO transmission window.

Next to the symmetric AZO structures, we have made **symmetric Mo** (Fig. 7.1.1b) structures: a 240104 and 240105 series grown on SLG/Mo substrates with sputtered Mo top electrode – a dual metal-semiconductor junction designed for electrical measurements without illumination. However, due to molybdenum diffusion into the C24 layer, those structures were shortened ab ovo, thus precluding performing any electrical experiments. In summary, including the samples on SLG substrates, the 240104 and 240105 runs yielded 18 samples in total. A complete list of samples and fabricated devices can be found in the appendix on page 351.

Before proceeding further, let us consider the bulk resistance of the C24 layer within the given structure dimensions. For the 100nm thickness and 45mm<sup>2</sup> cell size, and without accounting for the spreading resistance, the conductivity values of the C24 thin films at room temperature (from table 5.3.2) yield:  $4\Omega$  for C24-RS,  $2.5\Omega$  for C24-R, and only  $660\mu\Omega$  for C24-AS. The  $\Delta\sigma$  increment would introduce only  $0.16m\Omega$  change for C24-AS. Compared to the resistance of the sole AZO and Ni:Al contacts/electrodes, which is, on average,  $2.5\Omega$ , it is readily apparent that the bulk resistance of the C24 layer would

introduce a relatively minor impact on device net resistance. However, it is expected that the predominant factor controlling current would be the tunnelling transport through the barrier; thus, the net resistance would be controlled by the particular transport mechanism.

We have measured the IV characteristics of the symmetric AZO devices at room temperature (Fig. 7.1.5). The measurements were performed in the vertical configuration, between the top Ni:Al electrode and the bottom AZO, with silver paste applied. The bottom electrode was arbitrarily set as ground. The measured characteristics are close to linear, indicating either domination of the ohmic or the trap-assisted hopping transport through the barrier or high series resistance. By approximating the  $\pm 1V$  range by a linear function, we obtained total device resistances (table 7.1.1): For the 240104 series, for the annealed samples, one can observe a trend resembling the annealing of the C48 samples (cf. Fig. 5.3.1). Similarly, the trend in the 240105 series corresponds to the C24 samples. However, checking the resistance of the bottom electrodes after C24 deposition and after annealing reveals that the resistivity of the AZO films increases severely after the concurrent technological processes, up to six orders of magnitude after annealing in sulphur. The resistivity increase is presupposed to be a direct outcome of the AZO degradation during the C24 deposition at elevated temperature, in a sulphur atmosphere, and after similar conditions during the PDT. Consequently, the bottom electrode becomes Zn(O,S), not AZO [243]. As the -R and -RS samples would now have different bottom AZO resistivity, the resistance values from 7.1.1 are believed to be random, or at least only partially related to the C24 layers itself. Moreover, all symmetric AZO devices are almost insensitive to illumination and very weakly temperature dependent. Therefore, we can infer that in these structures, the voltage drop is mainly across the series resistance, and the eventual hopping through C24 controls the current at the minuscule level, in fact, close to zero.

Nevertheless, the asymmetric AZO series has demonstrated the problems and limitations hindering the realisation of the hopping-controlled switching. The C24 and

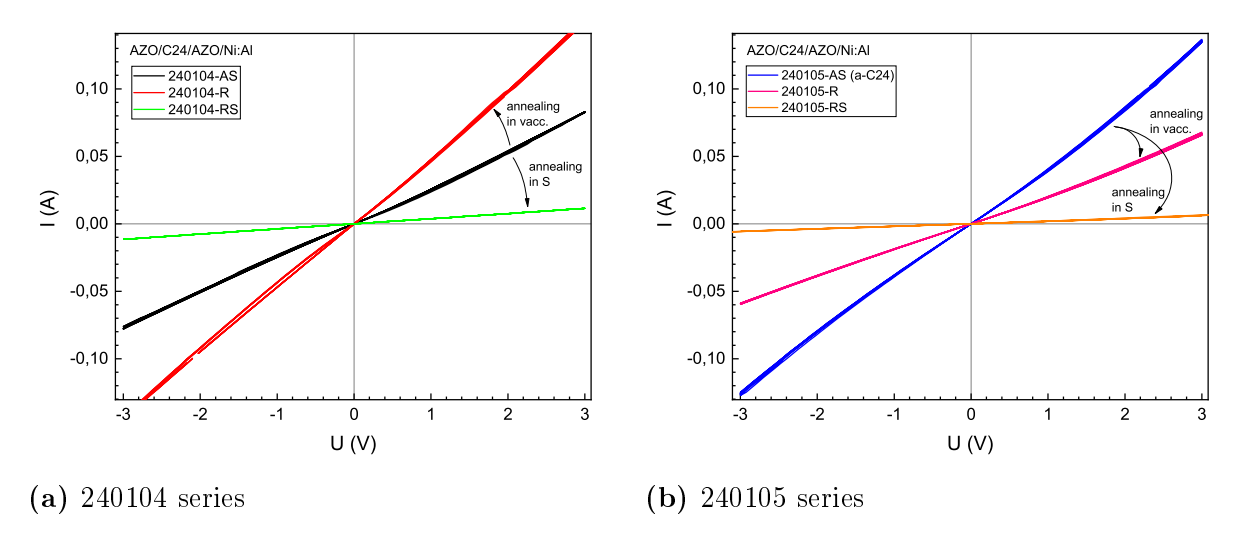


Figure 7.1.5: Current-voltage characteristics of the symmetric AZO devices at room temperature.

**Table 7.1.1:** Calculated total resistance values of the symmetric AZO devices at room temperature.

$_{ m sample}$	$R(\Omega)$
240104-AS	23.88 (0,03)
240104-R	49.16 (0.07)
240104-RS	502.51 (11.36)
240105-AS	37.5 (0.04)
240105-R	20.77 (0.02)
240105-RS	26.25 (0.01)

AZO form, in fact, a double n/n++ junction, probably fully depleted, which is far from the anticipated structure resembling MIM. It transpires that assembling this type of structure with AZO and C24 is rather complicated. Thus, we probably do not deal with the tunnelling-assisted transport; a more detailed description of the C24/AZO interface will be revealed as our work progresses. Summarising, due to the technological difficulties and the C24/AZO interface behaviour, the practical implementation of the intended architecture is currently beyond our reach.

#### Mainline design

Even though symmetric AZO devices turned out to be a miscalculation, as the *first* shot, they pointed us the possibilities and limitations of device design. Those have also shown how important the thermal budget is in the device manufacturing process. After carrying out the described preliminary testing of those devices, we decided to temporarily abandon the hopping architecture and move towards devices based on modulation of the rectifying junctions, which seem to be naturally formed on the C24 interfaces, which used contact materials.

In the next design, we first replaced the bottom AZO with molybdenum as a bottom electrode, eliminating the problems related to the low thermal budget of AZO. The molybdenum is known to have one of the best resilience to sulphur atmosphere among the metals available in the Nantes group [243]. However, it is almost certain that a few-nm-thick MoS<sub>2</sub> layer grows at the Mo/C24 interface [243], which could cause further complications. Next, we increased the C24 thickness to the original 400nm, as the depletion region of the junction is likely to be significantly wider than 100nm. We left the top part - AZO window with Ni:Al electrodes unchanged. The resulting asymmetrical device, the **mainline** design, is shown in Fig. 7.1.1c. At this point – during designing the device and planning the technological processes, we conceived the idea of scanning the  $CdIn_2S_4$  stochiometry in search of the T-V regime transition, described in the preceding chapter, instead of relying on trying to reproduce known samples C24-AS, C24-R and C24-RS, from chapter 5, like we did in the case of 240104 series. Hence, we undertook runs 240130, 2400208, 240311A, and 240311B exclusively with this design. In particular, run 240311A was intended to explore the region of a-C24, and run 240311B – to fine-tune the deposition temperature towards the most efficient devices. From those runs, we obtained the hot, medium and cold samples, as described in the chapter 6. A chosen subset of those samples was subjected to the PDT (annealing, annealing + quenching). In run 240312, we have grown 800nm C24 mainly for optical measurements, and to explore the devices further. In the mainline design, all the electrical measurements were probed between the

Mo bottom electrode and the Ni:Al top electrode, with the Mo electrode arbitrarily set as ground.

During the electrical characterisation of the mainline devices, a suspicion arose that the observed behaviours might originate from the MoS<sub>2</sub> layer, not the C24. To unequivocally dismiss any lingering ambiguities, we manufactured devices without molybdenum: in the 240312 run, besides the mainline design (sample 240312-Mo), we have grown the C24 thin film on ITO substrate, which, similarly to Mo, has acceptable thermal endurance [243]; then, we have finished the ITO/C24 layers with previously used AZO/Ni:Al top electrode, obtaining semi-transparent **ITO-based design** (Fig. 7.1.1d, sample 2410312-ITO). For the same reason, we attempted to reverse the mainline design using the SLG/ITO substrate: we sputtered Ni:Al contacts directly on SLG/ITO/C24 layers, obtaining reversed design (Fig. 7.1.1e). Regretfully, even for the 800nm C24 layer, the top metallisation again shunted the C24 layer by metal diffusion through the device, similar to the symmetric Mo devices<sup>2</sup>.

Given the current state of CdIn<sub>2</sub>S<sub>4</sub> research conducted by us, the mainline design devices represent our peak achievement. The following sections will analyse devices with the mainline design almost exclusively. An explanation of the switching mechanism in these devices and their memory and neuromorphic performance will be described in this and the following last chapters of this dissertation.

## 7.2 Devices' characterisation

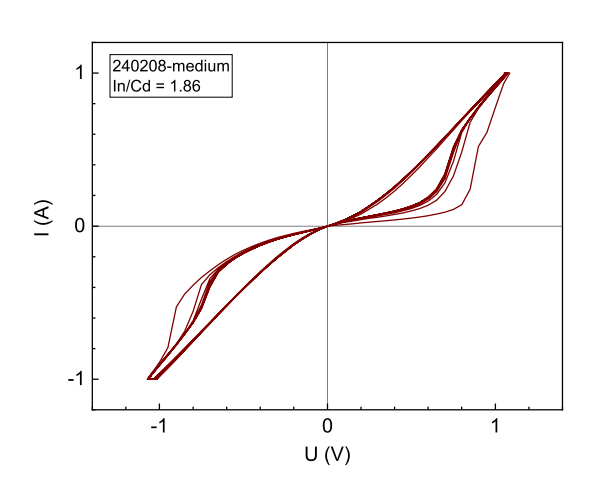
In Fig. 7.2.1a, we have shown the IV characteristics of the 240208-medium sample (as an example) under a triangular voltage waveform stimulation with 4V/s (ten consecutive cycles). Here, for the first time, we witness a pinched hysteresis loop in the  $CdIn_2S_4$ -based device. This plot, we believe, represents the pivotal juncture of this entire work.

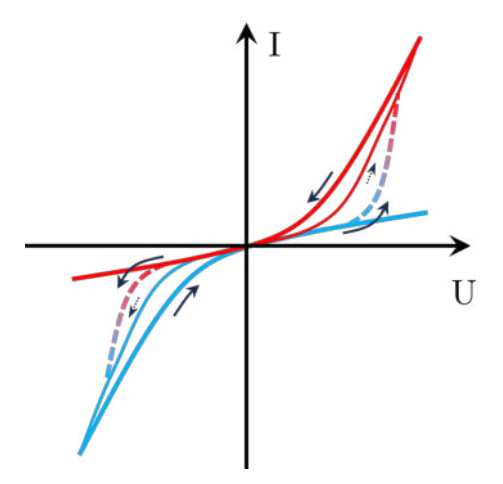
This general pattern of the IV characteristics observed here recurs in most of the devices from the mainline series, which have a global hysteresis loop. By carefully analysing the

<sup>&</sup>lt;sup>2</sup>As it turns out, apart from being a window electrode, the naturally dense AZO also serves a protective function for C24.

shape and the evolution of the IV loops, we have inferred the basic mechanism behind the switching behaviour. By virtue of the evidence presented in this chapter, we shall demonstrate how this interpretation has been reached, and on that very basis, we will characterise the devices. Further matters in this chapter will be organised as follows: first, we shall portray the general observations, a principle of operation of the devices, then we will proceed to a more detailed analysis of the processes governing the devices and a depiction based on the metastable defects, and lastly, we will analyse the impact of the  $CdIn_2S_4$  parameters.

All measurements in this and the next chapter were carried out at a temperature of 300K unless stated otherwise. The measurement of the IV characteristics was typically conducted in 10 complete cycles to examine the reproducibility of the measured hysteresis loop. The bottom Mo electrode in the devices was arbitrarily set to ground.





- (a) IV characteristics of the 240208-medium sample. 10 consecutive sweeps.
- (b) Schematic illustration of the switching resulting in the observed hysteresis on the IV characteristic.

Figure 7.2.1: Exemplary IV characteristics and proposed principle of operation.

#### 7.2.1 General observations

After a most thorough contemplation of the IV curves, the general principle of the devices' operation was made thoroughly clear. The device comprises two rectifying

junctions with opposite polarities: a Schottky junction between Mo and C24, and an n-type isotype junction between C24 and AZO. The direction and evolution of the IV curve are schematically shown in Fig. 7.2.1b. The device and, as a result, its IV characteristics can be considered as two diodes (i.e. electron barriers) connected in opposite directions in series. The electrical hysteresis loop originates from switching between those two diodes with their cathodes facing each other – two conduction regimes: for clarity, we will term them Forward Diode (FD) and Backward Diode (BD) regimes. The regime the device is in depends on which diode controls the conduction (or which barrier is reduced): the FD regime (represented in red on the diagrams) occurs when the diode (barrier) on AZO is reduced, and the state BD regime (blue) occurs when the barrier on molybdenum is reduced<sup>3</sup>. By reduction of the barrier, it is to be understood that a particular barrier becomes measurement-wise transparent for carriers. Hence, those two regimes can be considered as if the device has only one rectifying junction and a certain series resistance. On the diagram 7.2.1b, those regimes are represented by the two traces resembling IV characteristics of the diode. The switching occurs when the device is polarised in such a direction that the diode of the present regime is placed in a state of reverse bias. At a particular voltage region – a switching voltage  $U_{sw}$ , a steep current increase takes place, and the IV trace transits to the opposing regime, diode characteristics. The same occurs symmetrically at the other side of the IV trace (the other diode regime). Thus, when cycled with a symmetrical voltage waveform, the device switches back and forth between BD and FD.

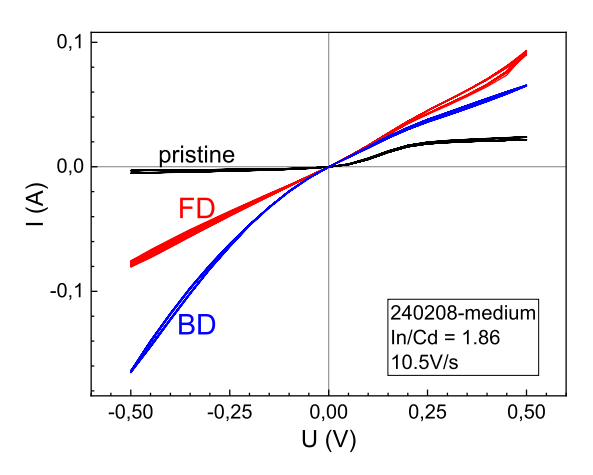
When bias voltage was never applied to the device, or after a sufficiently long time after the last voltage stimulation, the device will be found in the pristine state (Fig. 7.2.2a), where it is neither in BD nor in FD, but in a state that can be considered as *in between* the BD and FD, and be, in effect, a composite of the lower branches of the hysteresis loops of these two states. The device will persist in this state when the bias is kept in the range

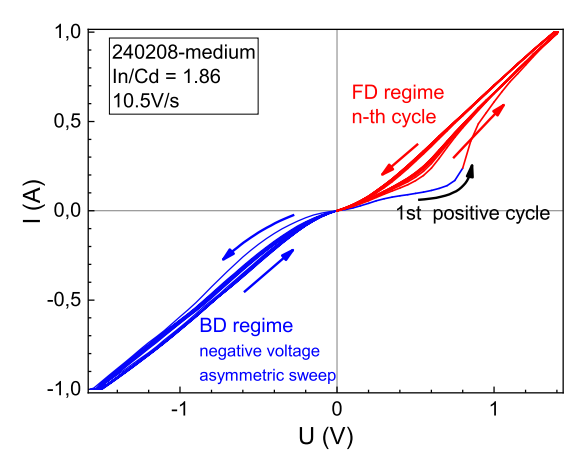
<sup>&</sup>lt;sup>3</sup>The nomenclature is purely conventional and refers to the effective diodes' polarities with respect to the arbitrarily assumed ground. In this way, the author intended to facilitate the understanding of the switching mechanism for the reader, despite the fact that the device can be in an intermediate state between FD and BD, which, as an aside, will become the basis for the neuromorphic operation of these devices.

 $-U_{sw} < U < U_{sw}$ . The IV trace here is, in fact, a superposition of the saturation currents from two Schottky junctions, which is, in essence, precisely the characteristic one would anticipate from a structure of this type.

If switched to the FD or FD regime, the device will persist in the particular regime at low voltage amplitudes, i.e., if it is not biased with a voltage sufficient for the opposite switch process to occur (red and blue traces in Fig. 7.2.2a). This can be considered a binary memory operation of the devices, with the BD and FD (at one chosen polarisation since it is the non-transversal pinched hysteresis loop!) having the meaning of HRS and LRS. As the range of the HRS and LRS states is limited by the switching voltages, the discrimination between these states is consequently constrained by the low current difference between the upper and lower hysteresis branches in this region. This renders the devices quite unsuitable for the role of binary memory. In a finite time at room temperature, the device will relax to the pristine state. It has been observed that a procedure which can accelerate the relaxation is annealing to a temperature ~60°C.

In addition, the reader will notice that the current-voltage values in Fig. 7.2.2a do not precisely match the values from Fig. 7.2.1a or 7.2.2b for the same sample. We will return to this case later.





- (a) Pristine state, and BD-FD regimes at low sweep amplitude (below  $U_{sw}$ ). If not switched back, the device will follow the IV trace of one particular diode regime.
- (b) Asymmetric operation. The device stays in the FD of BD regime without switching, and the local hysteresis loop emerges.

Figure 7.2.2: Example cases of the device operation.

If the stimulating voltage is swept within the range of one regime, i.e. an asymmetric triangular waveform having the lowest voltage point below (or above) the opposite switching voltage, the device would stay within a single regime (Fig. 7.2.2b). The first trace with the opposite polarisation (when the voltage changes sign or reaches the reversing  $U_{sw}$ ) will perform the switching manoeuvre; in the second sweep, the sample will settle on the IV loci of the particular regime (Fig. 7.2.2b). Moreover, during the asymmetric operation, another smaller hysteresis loop would emerge. We will call it a local hysteresis loop, as distinct from the global switching priorly described. The local hysteresis loop can also be observed at lower voltage ranges (as considered in Fig. 7.2.2a), and practically in most of the cyclic IV characteristics. We will discuss this case in more detail later, when the devices' operation is scrutinised from the point of view of electronic processes.

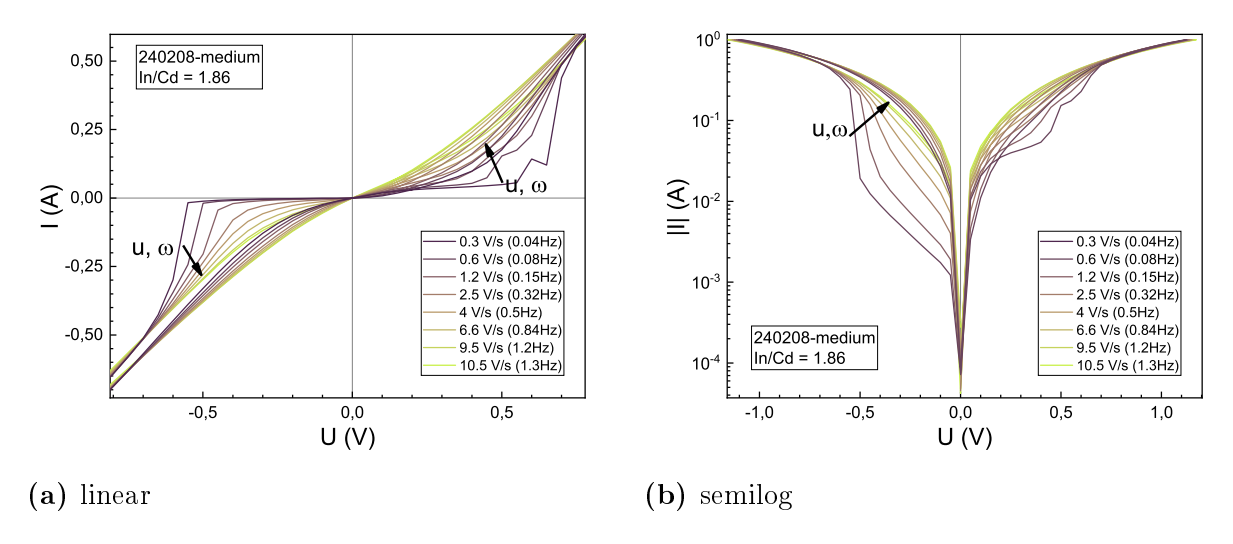


**Figure 7.2.3:** Influence of the sweep speed (frequency) on the shape of the hysteresis loop (one last cycle of each 10 loop scans series), for 240208-medium sample.

When measuring the IV characteristics, we can change the scan triangular waveform frequency, which, for a fixed amplitude, is equivalent to changing the voltage sweep rate  $u \equiv \frac{\mathrm{d}U}{\mathrm{d}t}$ . For the triangular waveform, |u| has a constant value. In Fig. 7.2.3 we have shown the IV characteristics of our exemplary 240208-medium sample for |u| in the  $0.3 \div 10.5 \mathrm{V/s}$  range. As can be observed, the hysteresis loop enlarges with decreasing frequency. It can be further observed that the expansion of the area enclosed by the IV loci upon a decrease in frequency is mainly brought by the lower branch of the hysteresis loop. It

appears to be a consequence of the extension of the region attributable to the saturation current of a reverse-biased diode, id est, shifting the  $U_{sw}$  towards higher voltages. As it was readily observed in previous plots, the  $U_{sw}$  was not a well-defined point on IV loci; however, when decreasing the sweep speed towards conditions that can be considered as quasi steady state — a relatively slow voltage increase, the switching becomes a step-like process (in the observable frequency range). At the same time, the upper branch does not experience such severe changes upon sweep speed/frequency. At this point, however, the means to qualitatively characterise the devices concerning sweep frequency are not yet at hand. Nevertheless, this observation provides irrefutable proof that a particular dynamic switching process occurs, characterised by a specific relaxation time constant, slow enough to be measurable. A future work would be to characterise this phenomenon as a function of temperature. Besides that, it can be further observed that at 0.3V/s the IV loci bear a far closer resemblance to the behaviour of two diodes arranged in a reverse-biased configuration.

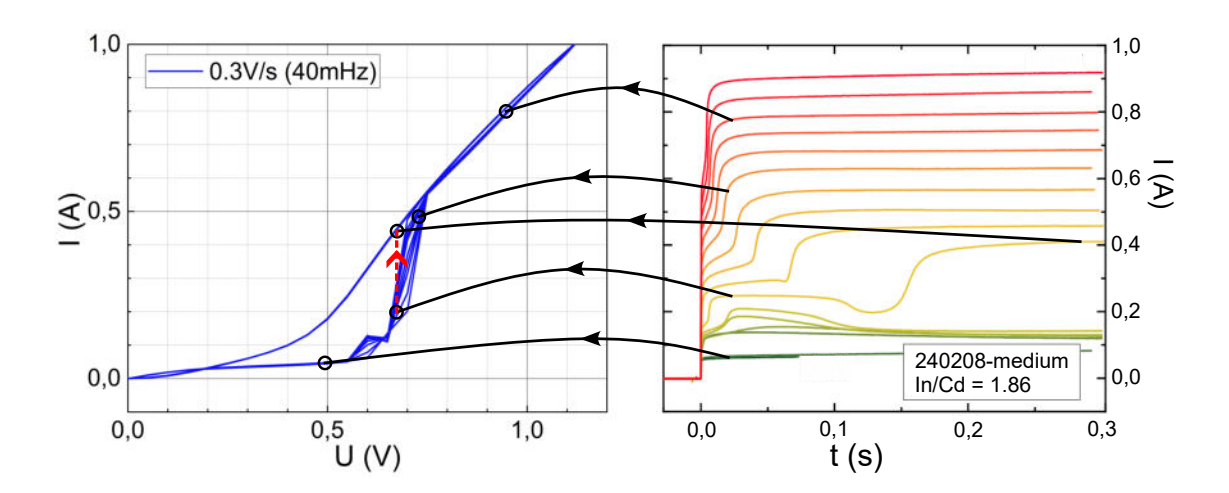


Figure 7.2.4: Transient response of the 240208-medium sample in function of step voltage amplitude in range  $0.25 \div 1.25$ V.

A valuable perspective on the dynamics of the temporal processes present in the devices can be obtained by measuring current kinetics after applying the step-voltage (after turning on bias, i.e., by applying the voltage Heaviside function). This is to be

carried out in an analogous manner to the procedure conducted for the photocurrent kinetics elaborated in chapter 5.4. Figure 7.2.4 shows the example current transients performed on the 240208-medium sample for various step voltages. The current transients can be referenced to particular points on an IV loci of the sample. As can be seen, the kinetics at two extreme voltage regions exhibit rather typical transient responses, with an instantaneous response (low voltages) or with a small time constant (high voltages). Those regions correspond to the linear parts of the IV trace. Conversely, applying a voltage within the switching range (in the region of  $U_{sw}$ ) results in a most intricate current evolution<sup>4</sup>. In one of the current transients presented in Fig. 7.2.4, corresponding to the  $U_{sw}$ , it is even possible to observe the switching kinetics. Actually, such time evolution of the current can partially explain the sweep rate dependency on the IV traces. Inasmuch as the voltage waveform we apply is in fact a staircase function – a composition of a finite number of discrete voltage steps, the observed IV trace will be a direct by-product of probing the current transients at different time windows. A slower sweep rate, thus longer settlement at constant voltage, would result in different current evolution. Thus different apparent IV trace<sup>5</sup>. It stands to reason that steady-state measurements constitute a superior basis for further analysis, since the dynamic factor is thereby eliminated and the results are obtained in a state approaching local equilibrium. Consequently, most of the further IV analyses will be done with a sweep rate of 0.3V/s.

We will now briefly consider the evolution of the IV characteristics when subjected to the influence of two external factors: temperature and illumination. The graphs relevant to this inquiry, again for the sample in question being 240208-medium, are figures 7.2.5 and 7.2.6.

Increasing the temperature causes the closing of the hysteresis loop in a familiar manner, as in the case of the frequency increase: the lower branch of the hysteresis is

<sup>&</sup>lt;sup>4</sup>For someone involved in RF technology, this evolution of kinetics can easily be reminiscent of the response of a mismatched long line and the reflections of the signal pulse as the line approaches steady state.

<sup>&</sup>lt;sup>5</sup>It is to be noted that the analysis of the current transients was the subject of one of the two master's theses aroused from this work, in which the matter is explored in a more detailed manner [255].

observed to converge with the upper. A cursory glance at the semilog plot of the IV characteristics shows that, in fact, the saturation current of the actual reverse-biased diode actually increases. Furthermore, it has to be noted that the switching voltage begins to decrease and blur at elevated temperatures, similar to the case of high sweep frequency. Even a low sweep rate of 0.3V/s does not suffice to secure a clearly discernible  $U_{sw}$ . This observation leads to the inescapable conclusion that the process of switching is thermally activated.

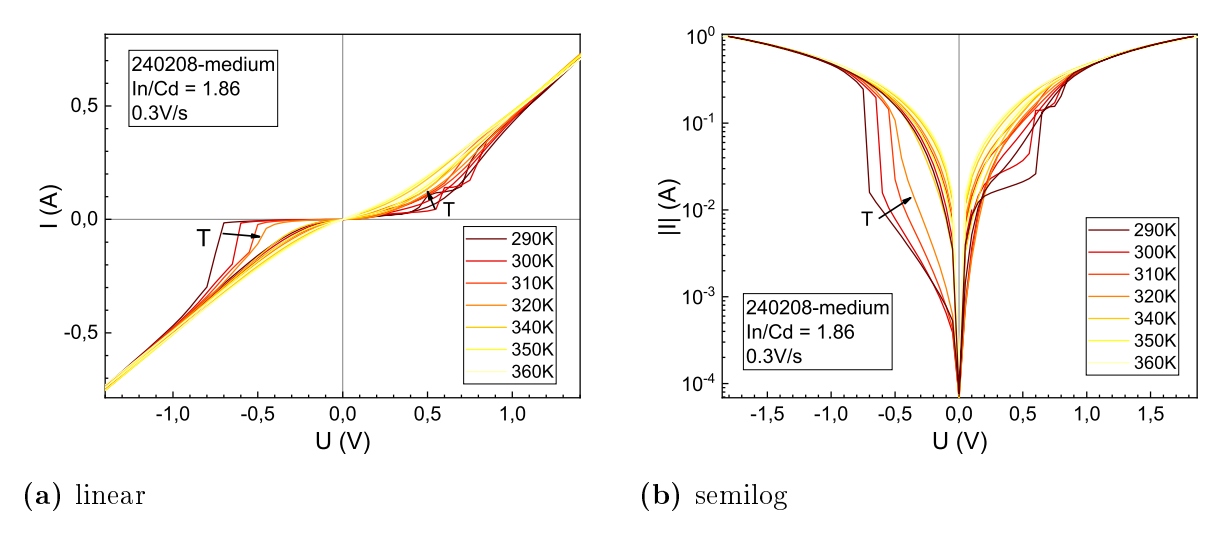


Figure 7.2.5: IV characteristics for 240208-medium sample in function of temperature.

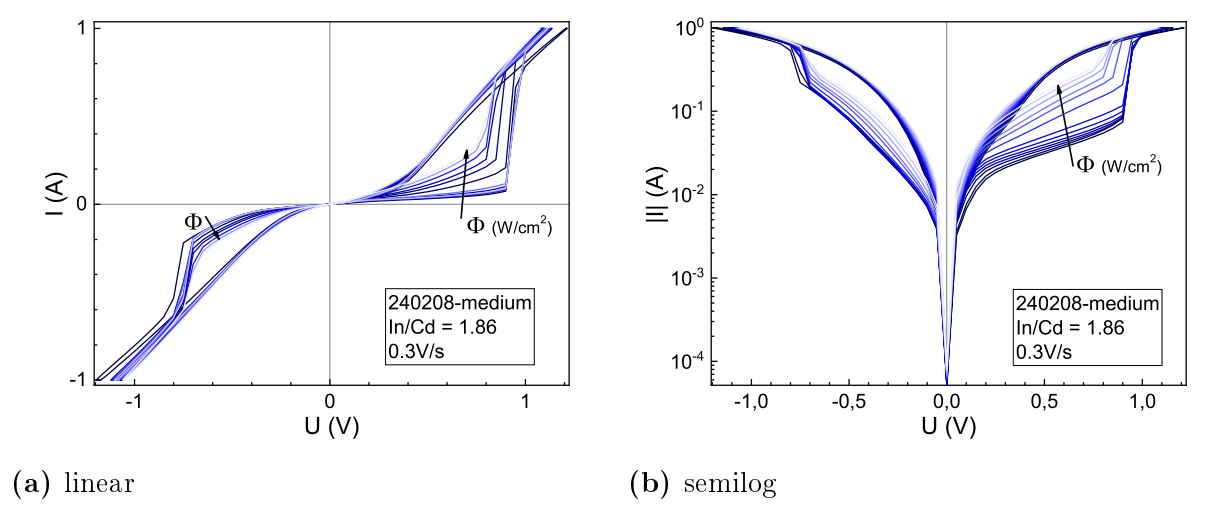


Figure 7.2.6: IV characteristics for 240208-medium sample with 460nm illumination in range  $\Phi = 0.1 \mu \div 1.2 \text{mW/cm}^2$ .

To examine the effects of light, we have illuminated the samples using 460nm (2.7eV) monochromatic light using an LED setup from the previous chapter 5. Illumination of the sample brings a similar result: an increase in current at the lower hysteresis branch, and a decrease in the  $U_{sw}$ ; it has to be noted, however, that we do not observe such severe dispersion of the switching region as in the case of the temperature or frequency. A semilog IV survey shows again that it is mainly the saturation current increase. The upper branch experiences much less evolution under variable illumination than when heated. The more profound analysis of the effects of illumination was carried out in the second of the master's theses derived from this work [256].

To summarise the matter, at this point, it has to be observed that the alteration of the three factors here presented – namely, sweep frequency, temperature, and illumination – gives rise to qualitatively identical changes in the IV characteristics. This alteration consists of an elevation in the lower branch (the *saturation current*), followed by a smaller change in the current of the upper branch; and lastly, a reduction as well as a diffusion of the switching voltage. Henceforth, the hypothetical description of the current transport mechanism – a respective formulation – has to yield the same response under those three factors.

## 7.2.2 Principle of operation

With the general behaviour of the device having been duly scrutinised, it is now time for the inquiry to delve into a deeper level and analyse the operation from the perspective of the double junctions. As the n++ AZO and molybdenum have comparable work functions ( $W_{\rm AZO} \approx 4.2 {\rm eV}$  [243],  $W_{\rm Mo} \approx 4.5 {\rm eV}$  [257]), the heights of the barriers at both junctions are proximate. Assuming the electron affinity of  ${\rm CdIn_2S_4}$  as  $\chi_{C24} \approx 3.5 {\rm eV}$  [225, 226], we have all components to propose a band diagram of the device (Fig. 7.2.7). It is to be presumed that the reader will have long since observed that the device constitutes a most typical back-to-back dual diode structure, widely observed in literature [116, 258, 259]. Here, we marked the FD and BD regimes with corresponding

colours pointing to the barrier minimisation phenomena. Within this band diagram, we can further explain the observed IV characteristics in more detail on the figure 7.2.8:

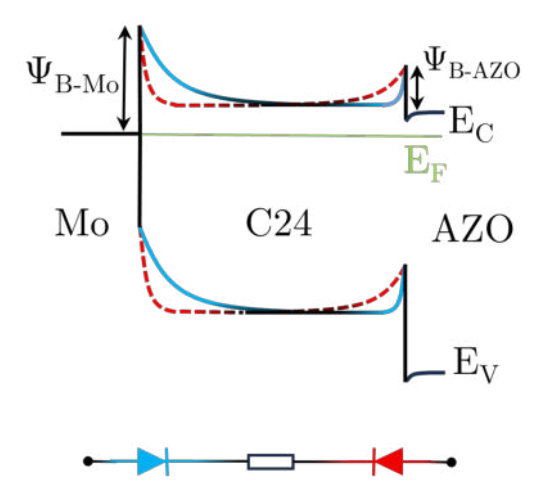


**Figure 7.2.7:** Schematic illustration of the switching process on the band diagram. Red and blue lines mark the band bending corresponding to the FD and BD regimes.

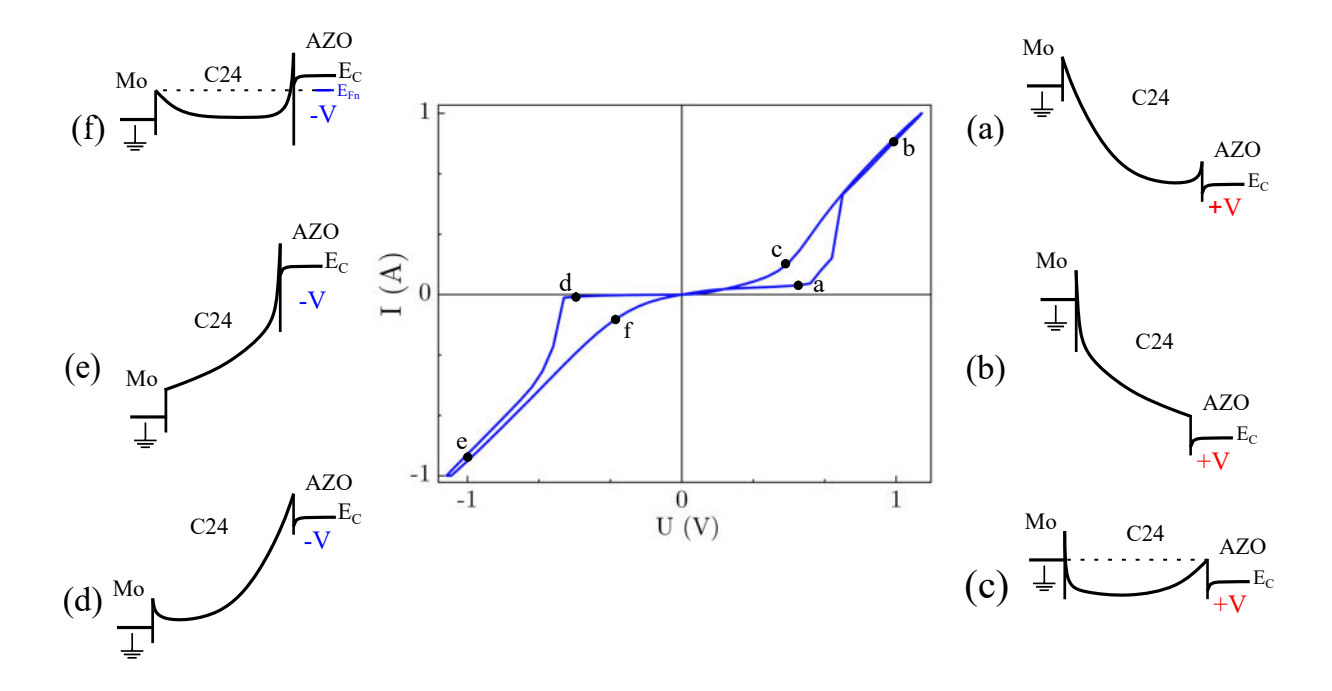


Figure 7.2.8: Phenomenological schematic illustrating the switching mechanism from the band bending point of view.

Starting in the BD regime and with the positive voltage sweep, at low positive voltages on the device, the AZO/C24 junction becomes positively biased, and the C24/Mo negatively. Further increasing the bias, toward the threshold range around  $U_{sw}$ , the opposing barrier (C24/Mo junction) gradually diminishes (point a). When the barrier on molybdenum is finally fully minimised (FD state, point b), the device exhibits close to ohmic resistivity (AZO/C24 junction is strongly forward-biased). It is most probable that tunnelling plays a major role in transport across the reduced barrier at the C24/Mointerface here. At lower voltages in the FD state (during the return), the AZO/C24 barrier begins to dominate, and takes over when the barrier top point becomes higher than the Mo level (point c). When the voltage changes sign, the mirror processes begin, where barriers' roles are swapped; hence, at point d, the stimulation enters the opposite switching voltage range, and the AZO/C24 barrier reduces – the device switches to the BD regime. Simultaneously, the C24/Mo barrier resets. Then, the device reaches a close-to-ohmic state again at point e. At lower voltages, when the top of the C24/Mo barrier extends over the AZO level (point f), the barrier begins to control the conductivity. After that, the complete cycle closes.

It becomes evident that, within the described principle of operation, a voltage-induced barrier reduction mechanism is required to explain the hysteresis phenomena. Moreover, it should be noted that the *switching* event is not instantaneous but requires a finite time/charge for the IV trace to fully get on the alternative path (dotted lines in Fig. 7.2.1b), as was evidenced in our previous analysis. Hence, the frequency evolution of the switching process. The switching time seems to be related to the total current (charge) flow through the device. Therefore, some charging/recharging effect governs the behaviour (this effect will also be a source of the neuromorphic behaviour of the devices). Altering barrier height at one side resets the state on the other, and the device effectively switches between FD and BD.

With the depiction of the barriers in mind, we can now decompose the observed IV characteristic, detailing the individual processes governing electron transport. We can then distinguish three main regions (A, B, C) in the hysteresis half, with their mirror

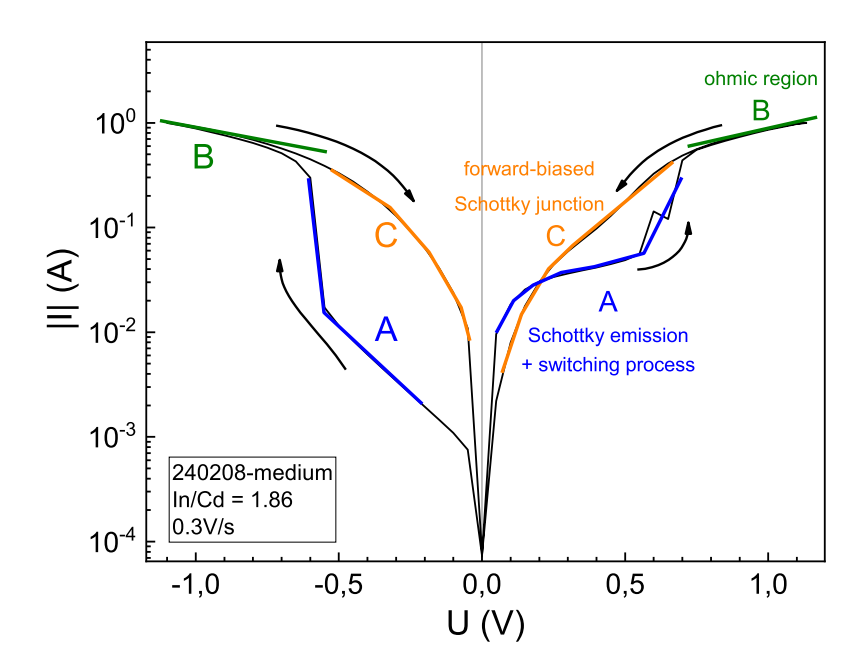


Figure 7.2.9: Characteristic regions of the IV characteristic.

counterparts on the opposite side (Fig. 7.2.9). Contrarily, but in our opinion, for the sake of better understanding, we will explain them in reverse order:

Region C is where the forward-biased junction controls the electrons' transport<sup>6</sup>. The device is fully switched to one of the regimes; thus, we shall observe substantial tunnelling or hopping transport through the reverse barrier. Such process needs to be efficient enough to be invisible on the IV characteristics (large injection) or have a linear electric field dependency, thus manifesting itself as a series resistance. Therefore, the IV characteristic in this region can be described by the equation (3.2.70) with a prospective minor contribution of the series resistance (points  $\bf c$  and  $\bf f$  in Fig. 7.2.8). At the lowest voltage range, we can observe the familiar influence of the -1 factor from the equation (3.2.70). The ideality factor of the forward-biased diode is expected to be significant since the junction deals with the same possible tunnelling/hopping processes as the reverse-bias junction.

In region B, the controlling diode is still forward-biased, and the reverse junction is

<sup>&</sup>lt;sup>6</sup>Since we deal exclusively with n-type semiconductors, we shall consider particularly majority carriers, as the minority carriers would bring only a minor contribution

still reduced (points **b** and **e** in Fig. 7.2.8). The IV characteristics are close to linear. Thus, in this region, the main limiting factor is the bulk resistance of the device. This resistance can originate from the bulk conductivity of the C24 layer, with a possible contribution of the SCLC process. However, it is more likely that such resistance has its source mainly in the contact layers, as it should be remembered that the bulk resistivity of the C24 is still considerably smaller than the resistivity of the rest of the device (as in the case of the *first shot* design), and this part of the IV trace is close to linear, thereby casting a shadow of doubt upon the SCLC transport. Since we are dealing with a C24 layer that is four times larger than that of *first shot* devices while maintaining the same device surface area, the resistance of the C24 layers will be approximately four times larger than the values presented in table 7.1.1. This single observation shows that the main factor limiting the device current is the barriers, not the bulk conductivity.

The IV characteristics of the regions B and C, whose sum constitutes the entire upper branch of the hysteresis loop, can therefore be described by the diode equation with the series resistance  $R_S$ :

$$I = I_S \left[ \exp\left(-\frac{e}{nkT}(U - IR_S)\right) - 1 \right]$$
(7.2.1)

where, as has been previously established,  $R_S$  is to be understood as representing the resistance of the contacts and the entirety of the remainder of the device, and not that of the C24 layer itself. On the other hand, if we neglect the resistance of the junk surrounding the C24 layer and its two junctions, and limit ourselves to analysing only those junctions themselves, there is nothing to prevent us from attributing this series resistance to the transport process through the opposite, reduced barrier. Therefore, we can adopt, for example, the trap-assisted hopping mechanism, e.g. NNH (vide eq. (3.2.76)), thus yielding the equation:

$$I = I_S \exp\left\{-\frac{e}{\eta kT} \left[ U - I\xi \exp\left(\frac{E_m}{kT}\right) \right] \right\} - I_S$$
 (7.2.2)

The ideality factor  $\eta$  would encapsulate the peculiarities of the forward-biased junction. The previously mentioned master's theses showed that in the tested samples  $\eta \sim 10$  [255]. Naturally, the same equation governs the mirror part of the full IV characteristic for the voltages of the opposite polarity.

Region A represents a most perplexing intricacy, yet concurrently holds the most pivotal role in the device operation. Here, the device is still in the regime controlled by the reversely polarised diode, thus one of the processes controlling the current is the thermionic emission over the blocking barrier. Concurrently, the tunnelling/hopping discussed earlier is most likely occurring as well. Lastly, the switching process is observed to take place, which prevails, in essence, throughout the entirety of region A. This process introduces a progressive current increase over time (as in the current kinetics from Fig. 7.2.4), which coincides with the voltage increase at a rate u. Therefore, a non-linear, progressive increase in conductance as a voltage function is observed until the device is brought to a completely switched state. The superposition of these three distinct processes produces the final shape of the IV curve in this region.

Lastly, when illuminated, the applied voltage now drops across the whole layer thickness. Therefore, photogenerated carriers are easily separated and drifted. This photoinduced current contributes to the saturation current of the backward diode in region A. Hence, we observe the current increase in the hysteresis lower branch upon the illumination.

After scrutinising details of the devices' operation, there remains one element indispensable to a complete comprehension of the devices' behaviour, including the hysteresis loop itself; that is to say, the phenomenon of switching. The following section shall present an interpretation of the devices' operation, founded upon the metastable defects.

### 7.2.3 Principle of operation regarding metastability

Herein, we are going to propose a basic explanation of the switching mechanism (and further resulting neuromorphic behaviour) based on interface barrier modulation governed by metastable defect complexes present in  $CdIn_2S_4$ , i.e. the previously examined

V - E (V<sub>S</sub>-Cd<sub>In</sub>) defect complex (vide chapter 5.5). Now, we extend the proposed band diagram of the devices from Figures 7.2.7 and 7.2.8 by including the spatial distribution of metastable complexes below the conduction band. Here, for illustrative purposes, we will represent the metastable defects using a naive depiction – as simple two-state level symbols, used in the literature (Fig. 4.3.1), and in our band diagram (Fig. 5.6.2). Therefore, we will mark the state occupied by the two holes as  $\mathcal{L}$ , and occupied by two electrons as  $\mathcal{L}$ . It would, in point of fact, be more correct to delineate a singular level – one which is, as will shortly become apparent from the switching mechanism, the  $E_{TR}$  of this defect complex. We will place those levels well below the Fermi level, as it takes place for the C24-AS sample (cf. chapter 5). Moreover, as a matter of principle, we acknowledge the existence of a T states distribution, as it plays a crucial role in the compound. We plotted it as a shadow below  $E_C$ .

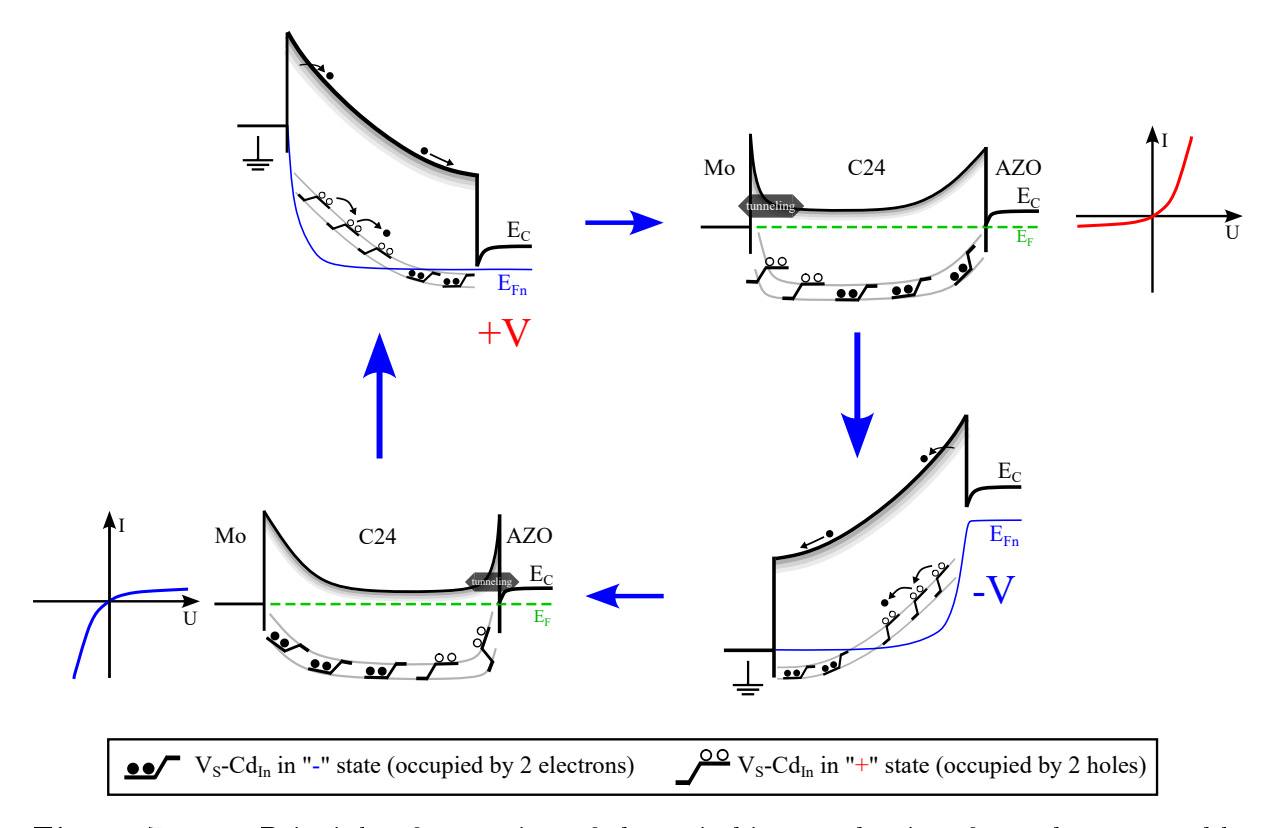


**Figure 7.2.10:** Principle of operation of the switching mechanism from the metastable defects point of view.

The mechanism goes as follows: In the C24 layer, there is some non-uniform spatial distribution of V-E defects in positive and negative charge states. Naturally, the defects' charge participates in the band bending, through contributing to the total  $N_D$  via equation (3.2.67): defects in a positive charge state near one of the barriers increase the electric field and, therefore, decrease the width of the SCR region, thus reducing the barrier width on one of the junctions and enabling the tunnelling or hopping processes of whatever nature they may be, to increase. Sufficiently efficient transport process across the barrier practically short-circuits one of the junctions. The spatial distribution of the defects in the positive charge state can be changed by applying an external electric field. As the quasi-Fermi level for electrons sweeps through the bent  $E_{TR}$ , it has the consequence of part of the states' spatial distribution being above  $E_{Fn}$ , causing the electron emission. Since there is a potential barrier for emission/capture processes of the metastable defects, the occupation change will experience drag, lagging behind the  $E_{Fn}$  changing position. The electrons emitted from the defects would redistribute through hopping or drift, ultimately being captured by the complexes in the positive charge state on the other side of the device.

It is now readily apparent that the operation of the devices is, in fact, quite self-evident, as it is shown in the schematic representation of the cyclic operation in Fig. 7.2.10. The hysteresis loop directly results from the modulation of the spatial distribution function characterising the fraction of the defects in a positive charge state. The BD and FD regimes result from the two extreme cases, where the opposite charge states are fully polarised on the antipodal regions of the C24 layer. The presence of the drag caused by the large capture/emission time constants utterly explains the observed frequency dependence: at high voltage sweep rates, there is a residual concentration of positively charged complexes near each barrier that did not manage to convert on time, thus providing a quiescent pre-charge for the incoming recharging wave. Ergo, at high sweep frequencies and symmetrical operation, the junction does not manage to reset completely, and the hysteresis loop closes. In a similar manner, the temperature can accelerate the conversion process (the capture and emission are thermally activated), resulting in faster operation, thus reducing the effect of drag and closing the hysteresis loop.

At a given applied bias, the decreasing resistivity of the reversely-polarised junction causes a larger voltage drop in the other parts of the device, decreasing the voltage on the junction in question. Thus, the device provides a negative feedback loop on itself, decreasing the conversion speed. This effect is probably one of the processes visible on the current transients (Fig. 7.2.4).

It is patently obvious that the pristine state is characterised by a uniform distribution of complexes in both charge states throughout the thickness of the layer. Consequently, the sample remains in a state intermediate to the BD and FD states until a separating electric field is applied. When the polarising voltage is removed, the spatial occupation of the complexes will persist due to the defects' metastability. After a sufficiently long time, entropy will restore uniform occupation in a function of sample thickness. Annealing accelerates electron emission and thus the diffusion of the charge states.

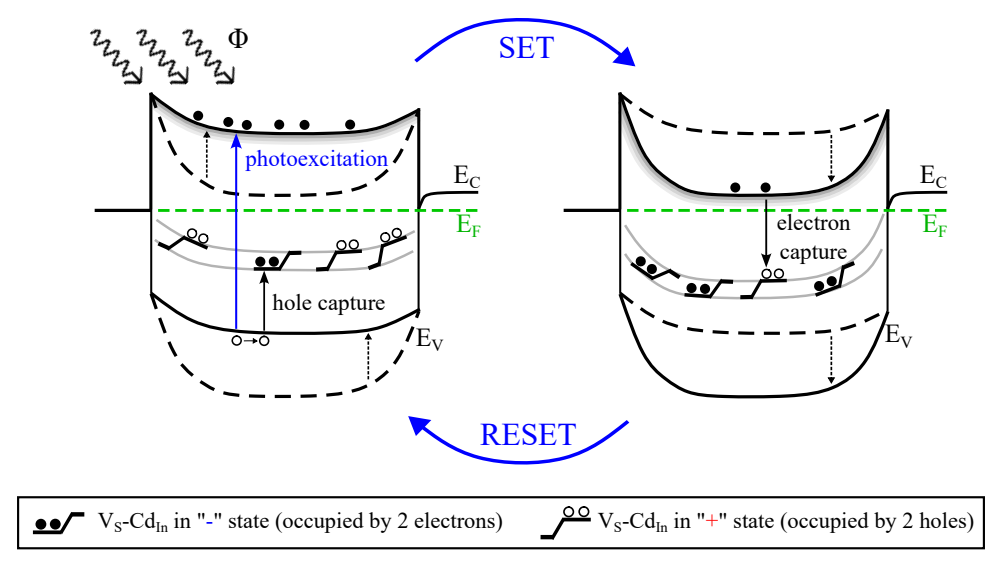


Figure 7.2.11: Principle of operation of the illumination-controlled switching mechanism at 0V bias. Dashed lines show the ending before the particular process took place.

When illuminated, V - E complexes in the negative state capture generated free holes and convert to the positive state. This causes already familiar outcomes, plus induces the PPC and PPS, discussed in more detail in chapter 5.5. Such situation is schematically presented in figure 7.2.11. The separation and collection of photogenerated carriers at an applied voltage will contribute to the freezing of the PPC state even at high temperatures,

above 160K. Thus, if the voltage is not reversed through 0V, the illumination would have a cumulative effect on the total sample conductivity. After removing the illumination and the electric field, the concentration of metastable defects would swiftly decay to the equilibrium value for a given temperature, unless the temperature is high enough for the particular processes to occur efficiently.

The presence of T states would also likely contribute to the switching phenomena. Such a broad density of states located shallowly below the conduction band is a strong candidate for being the effective source of hopping transport across the barrier, both when the given barrier is reduced and when it is not. However, the matter here is adscititiously complicated by the fact that the carriers' lifetime in the T states is also influenced by the V-E complexes, through the quantum gyrator mechanism, outlined in chapter 5.6. Parenthetically, the local hysteresis loop observed in the asymmetrical operation could result from a similar mechanism, but with the T states involved – the variable lifetime of the trapped electrons in T states could bring similar hysteretic effects; however with conversion times, that are not related to large lattice relaxation, but to the classical electronic processes (vide chapter 3.2.3). Nonetheless, this hypothesis is, for now, confined to the domain of obscure speculations.

In the chapter 5.5, we considered electronic processes based on thermally activated carrier emission by the metastable defects. Here, let us write the full set of four complementary conversions for the V-E metastable complex:

$$(V_{\rm S} - {\rm Cd_{In}})^- + 2h \rightarrow (V_{\rm S} - {\rm Cd_{In}})^+$$
 hole capture  
 $(V_{\rm S} - {\rm Cd_{In}})^+ + 2e \rightarrow (V_{\rm S} - {\rm Cd_{In}})^-$  electron capture  
 $(V_{\rm S} - {\rm Cd_{In}})^+ \rightarrow (V_{\rm S} - {\rm Cd_{In}})^- + 2h$  hole emission  
 $(V_{\rm S} - {\rm Cd_{In}})^- \rightarrow (V_{\rm S} - {\rm Cd_{In}})^+ + 2e$  electron emission

After Maciaszek et al. [16, 260, 261], we can write the corresponding time constants analogously as before:

$$\tau_{HC}^{-1} = \nu_{phn}^{-1} (\varsigma_p v_p p)^2 \exp\left(-\frac{\Delta E_{HC}}{kT}\right) \equiv (c_p p)^2 \exp\left(-\frac{\Delta E_{HC}}{kT}\right)$$
(7.2.3a)

$$\tau_{EC}^{-1} = \nu_{phn}^{-1} (\varsigma_n v_n n)^2 \exp\left(-\frac{\Delta E_{EC}}{kT}\right) \equiv (c_n n)^2 \exp\left(-\frac{\Delta E_{EC}}{kT}\right)$$
(7.2.3b)

$$\tau_{HE}^{-1} = \nu_{phn}^{-1} (\varsigma_p \nu_p N_V)^2 \exp\left(-\frac{\Delta E_{HE}}{kT}\right) \equiv (e_p N_V)^2 \exp\left(-\frac{\Delta E_{HE}}{kT}\right) \tag{7.2.3c}$$

$$\tau_{EE}^{-1} = \nu_{phn}^{-1} (\varsigma_n v_n N_C)^2 \exp\left(-\frac{\Delta E_{EE}}{kT}\right) \equiv (e_n N_C)^2 \exp\left(-\frac{\Delta E_{EE}}{kT}\right)$$
(7.2.3d)

Let us now denote the total concentration of the  $V_S$ -Cd<sub>In</sub> metastable complexes as  $N_{V-E}$ , the concentration of complexes in the positive charge state as  $N_+$  and in the negative charge state as  $N_-$ . The concentration of the complexes in the  $(V_S$ -Cd<sub>In</sub>)<sup>+</sup> state is  $N_+ = \mathfrak{f} N_{V-E}$ , where  $\mathfrak{f}$  is the probability of the positive metastable configuration. Compared with [16], we neglect the occupation functions as we consider only one charge state in each configuration. Hence, we can write the equations describing the conversion kinetics:

$$\frac{\mathrm{d}\mathfrak{f}}{\mathrm{d}t} = -\mathfrak{f}(\tau_{EC}^{-1} + \tau_{HE}^{-1}) + (1 - \mathfrak{f})(\tau_{HC}^{-1} + \tau_{EE}^{-1})$$
(7.2.4)

In equilibrium conditions:  $\frac{df}{dt} = 0$ .

Expanding n, p to  $n = N_C \exp\left(-\frac{E_C - E_{Fn}}{kT}\right) p = N_V \exp\left(-\frac{E_{Fn} - E_V}{kT}\right)$ , approximating  $\varsigma_p v_p \approx \varsigma_n v_n$ , and performing few trivial transformations, gives us:

$$\frac{\mathrm{d}f}{\mathrm{d}t} = -f(\varsigma_n v_n n)^2 \exp\left(-\frac{\Delta E_{EC}}{kT}\right) - f(\varsigma_n v_n)^2 \exp\left(\frac{2E_C - \Delta E_{HC}}{kT}\right) \exp\left(\frac{2E_g}{kT}\right) \exp\left(\frac{2e}{kT}U\right) - f(\varsigma_n v_n N_V)^2 \exp\left(-\frac{\Delta E_{HE}}{kT}\right) + f(\varsigma_n v_n N_C)^2 \exp\left(-\frac{\Delta E_{EE}}{kT}\right) + (\varsigma_p v_p p)^2 \exp\left(-\frac{\Delta E_{HC}}{kT}\right) + (\varsigma_n v_n N_C)^2 \exp\left(-\frac{\Delta E_{EE}}{kT}\right) \tag{7.2.5}$$

Here, we also put  $E_{Fn} - E_{Fp} = eU$ . From this equation, it is readily observed that the conversion kinetic is proportional to the applied voltage:

$$\frac{\mathrm{d}\mathfrak{f}}{\mathrm{d}t} \propto -\mathfrak{f}\exp\left(\frac{2e}{kT}U\right) = -\mathfrak{f}\exp\left(\frac{2e}{kT}ut\right) \tag{7.2.6}$$

Consequently, the variable voltage rate u will modulate the conversion kinetics of the metastable defects. In the next step, the influence of the illumination on the kinetics of hole capture could be added, yielding a similar result.

To find the concentration kinetics of free electrons, one would have to incorporate the aforementioned effects with the trapping kinetics and the variable recombination (quantum gyrator effect – the  $e_n$  and  $c_n$  are functions of  $\mathfrak{f}$ ) discussed in the previous chapter. An approximate kinetic equation is:

$$\frac{\mathrm{d}n}{\mathrm{d}t} = -N_{V-E}\mathfrak{f}\tau_{EC}^{-1} + (1-\mathfrak{f})N_{V-E}\tau_{EE}^{-1} + e_n n_t - c_n n p_t + f - \frac{\Delta n}{\tau_n}$$
 (7.2.7)

The aforementioned equations are found to describe, in point of fact, the kinetics of the occupancy of defects and electrons in the spatially uniform approximation. The next step would be to find the dynamics of the spatial distribution f(z,t) of the defect occupancy function and its kinetic. A special case is the point  $z_{TR}$  – the intersection point of the quasi-Fermi level with  $E_{TR}$ , for which  $f(z_{TR}) = \frac{1}{2}$ . Finding:

$$\frac{\mathrm{d}z_{TR}}{\mathrm{d}t} = \frac{\frac{\mathrm{d}\mathfrak{f}(z_{TR},t)}{\mathrm{d}t}}{\frac{\mathrm{d}z}}$$
(7.2.8)

would yield the spatial kinetic for modulation of the  $N_{+}$  concentration.

The spatial distribution of the positively charged complexes controls the current transport, in fact, only indirectly. The apparent conductance of each barrier is controlled by a particular transport mechanism. As previously established, the phenomenon in question is probably a superposition of Schottky emission and some form of hopping or tunnelling, the nature of which is controlled by the thickness of the layer through which this transport takes place. Therefore, to explain the conductivity processes in region A, as distinguished in the previous subsection, one must find the product of changing the

occupation of metastable defects and their influence on the transport process. It should yield an S-shaped dependence of the current at the voltage in the switching region (region A). Jointly with the processes associated with the T states, a remarkably dynamic system defining conductivity in the region A is being formed.

In the simplest case, the density of  $N_{+}$  will modulate the SCR width of the junction (vide eq. 3.2.68), as the resulting compensating donor concentration  $N_{D}$  would be given by:

$$N_D(z,t) = \int_0^d \int_{-\infty}^t N_{V-E}(z)\mathfrak{f}(z,t)dtdz$$
 (7.2.9)

It is then a matter of finding the appropriate kinetics of band bending with the incorporation of overlapping SCRs of the two junctions. It is to be noted that, in essence, a most pertinent model, which describes the impact of metastable defects on the depletion region, has already been developed by Kimerling et al. [262], and applied by Decock et al. [263].

The above equations provide a veil explanation for the influence of external factors upon the IV characteristics, and further highlight their subtle temporal dependencies. Why are IVs different in general, then? It all depends on the time course of the applied voltage. Even 0V pauses between measurements are significant, as they allow for the recharging of occupied defects towards a uniform spatial distribution. Any arbitrary voltage waveform over time will result in a slightly different IV course, meaning the switching voltages and the lower branch of the hysteresis may differ. The upper branch is, in fact, the least susceptible to the  $N_+$  modulation, as it derives from the two extreme cases of the metastable defects distribution. The overall conductivity change results from the integral of applied voltage, or, in other words, from the resulting charge displacement. If one arbitrarily puts  $\varphi = \int U dt$ , one might find the  $\varphi - q$  linkage by solving the equations in this section.

As we now grasp the processes within the device, we can proceed to analyse the impact of the CdIn<sub>2</sub>S<sub>4</sub> layer on the device behaviour. Having the information gathered about the C24 thin films from the previous chapter, and the derived CdIn<sub>2</sub>S<sub>4</sub> model, we can deduce further details regarding the devices.

#### 7.2.4 Influence of the $CdIn_2S_4$

In previous sections, we analysed the characteristics of the 240208-medium sample, which had the In/Cd ratio of 1.86; thus, it was the closest to the C24-AS sample from chapter 5. Herein, we will inspect the effects of modifying the CdIn<sub>2</sub>S<sub>4</sub> layer on the devices. As outlined at the beginning of this chapter, we have manufactured the devices based upon the mainline series of thin films, i.e. runs 240130, 240208, 240311A, 240311B, and run 240312 with double thickness. Indeed, we pursued this matter from many angles; however, we found only a few clear patterns between the devices' behaviour and their deposition temperature or stoichiometry – at least, not as many as we expected. We will therefore now present the superficial results:

The inspection of the IV characteristics shows that the behaviour described in the preceding sections is the general feature of the devices that exhibit the global hysteresis loop. The exemplary IV characteristics are presented in the appendix on page 345. Based on the observation of IV characteristics, it can be inferred that:

The samples grown at the highest temperature (240130, 240208-hot) generally have a steeper characteristic in region C (vide Fig. 7.2.9), which could be interpreted as an outcome of higher  $U_{bi}$ . In consequence, the area defined by the hysteresis loop gets smaller. It is also observed that the series 240311A and 240311B generally lack a global hysteresis loop, exhibiting only a local hysteresis. It is a perplexing finding, given that their deposition parameters partially overlap with those of series 240208 and 240130, which does, in fact, demonstrate a global hysteresis loop. Especially 240311B-hot differs significantly from the samples 240130-hot and 240130-medium despite having the deposition parameters between those of the other two (vide Fig. 6.3.1 or 7.2.12).

A special case is sample 240311A-cold, which has a linear IV characteristic, in which the resistance estimation shows that it is de facto shunted. In this particular instance, however, the matter is of a most uncomplicated nature: SEM imaging (figure on page 342) showed that the C24 layer is significantly discontinuous; therefore, it gets shunted by the AZO layer by filling the cavities. This is, nevertheless, an important conclusion as

it defines the lower temperature limit up to which we are able to obtain a continuous C24 layer.

Let us mark the samples which have a local and local + global hysteresis loop on the composition plot (6.3.1) from chapter 6 - figure 7.2.12. Here, we can distinguish a certain area where we obtained devices with the global hysteresis loop, precisely a range of  $200 \div 320$ °C and of In/Cd in the range  $2 \div 3.25$ . However, the mystery remains: the point In/Cd = 5 (sample 240130-hot).

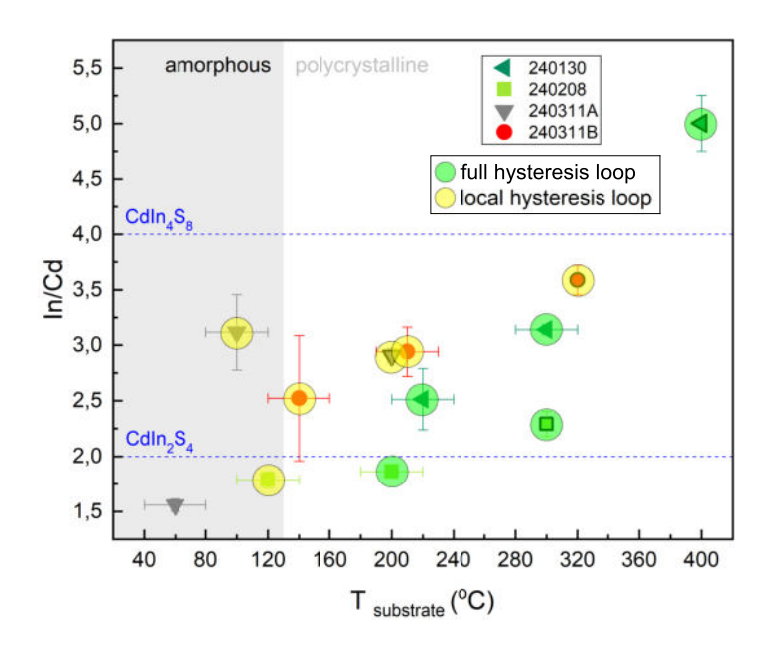


**Figure 7.2.12:** Presence of the hysteresis loop in function of the growth parameters.

We can generally characterise the mainline series by inspecting the switching voltage of the samples with the global hysteresis loop. Aware of the fact that  $U_{sw}$  is, in fact, not a point, we will approximate it from the location where it is best defined, i.e. from characteristics at 300K and 0.3V/s sweep. Analysis of the  $U_{sw}$  for positive and negative voltages showed no trend as a function of temperature and C24 composition for FD $\rightarrow$ BD switching, and relatively small correlation for BD $\rightarrow$ FD (vide appendices on page 346). However, when we plot an absolute difference of the switching voltage, we observe a linear dependency of the stoichiometry (Fig. 7.2.13).

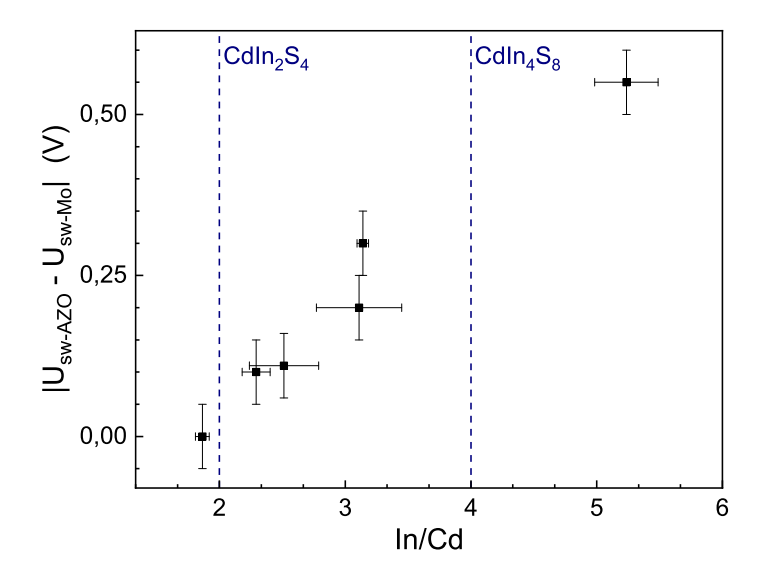


Figure 7.2.13: Difference of the switching voltage in function of stoichiometry

The question now arises: what could be the source of this trend? The difference observed is actually an asymmetry of the junctions on the two sides of the C24 layer. Therefore, the first hypothesis explaining this observation might be simply a difference in barrier height  $\Psi_B$ : a different barrier will result in a different value of current, or total charge flowing at a given constant time for the same excitation voltage waveform, resulting in a different threshold voltage. Precisely, a higher barrier would require more charge to switch, and thus the process would occur at a higher voltage. However, as the  $\Psi_B$  is defined by the metal work function and the electron affinity of the C24, it should remain constant, unless those material properties vary under the variable growth parameters, which is, in fact, possible [264, 265]. Since the work functions of Mo and AZO are slightly different, that would explain the asymmetry.

Through the same causality, the increment in  $U_{sw}$  can be introduced by varying  $U_{bi}$ , although the forward-biased junction limits the current in this case. It would then indicate that we alter the Fermi level position of the C24 (if kept  $\chi_{C24}$  constant). Therefore, this would trace the notional transition from the T to V regime we postulated in the previous chapters. The change of  $U_{bi}$  would also agree with the general observations on the IV characteristics, outlined earlier. However, in this instance, an abrupt transition was

anticipated. The absence of such a transition, therefore, presents one with three outcomes: either the switching process does not allow for the tracing of the T-V transition, or no such transition exists at all – rendering the prior hypothesis false, or the very premise is flawed, and the matter is something else entirely.

As we remember, the stoichiometry change originates from applying a rather heathen method of controlling it, which is the thermally-induced re-evaporation of CdS. Since we also re-evaporate sulphur, one could infer that we increase the concentration of sulphur vacancies. Therefore, the C48 samples would be richer in metastable defects, thus requiring lower  $U_{sw}$ . Despite the likely inverse proportionality, we are dealing here with a trend not in the voltages themselves, but in the difference between the switching voltages, hence the conclusion that in samples deposited at high temperatures, we have a non-uniform distribution of sulphur vacancies in function of layer thickness.

An alternative source of the barrier alteration could lie beyond the C24 layer. We firmly believe that a nanometer-thin layer of  $MoS_2$ , possessing interface passivating properties, forms at the interface between Mo and C24 [243]. Changing the deposition temperature would likely lead to a modification of this layer<sup>7</sup>. This, however, would mean that the trend would be visible not as a function of stoichiometry, but of temperature. Since we do not observe such a trend in temperature, the observed dependency most likely does not originate from the  $MoS_2$  layer. On the other hand, however, a small variation of the barrier switching on the molybdenum side, i.e.  $BD\rightarrow FD$ , may indeed result from the interface passivation.

To resolve this problem, we must return to the structural characterisation and investigate the C24 interfaces more deeply. A C24 lift-off and an XPS measurement would answer several questions, including the MoS<sub>2</sub> case [175, 243]. SEM imaging of the interfaces and further measuring the EDX profile would answer another portion of the questions. Such investigations would also have a beneficial impact on understanding the process of switching itself. For the present, however, the matter remains unresolved.

<sup>&</sup>lt;sup>7</sup>As we remember, atomic fluxes were kept the same, and the stoichiometry difference originates in the form of re-evaporation of the CdS; thus, the only factor altering the MoS layer, which forms at the very beginning of the process, is the substrate temperature.

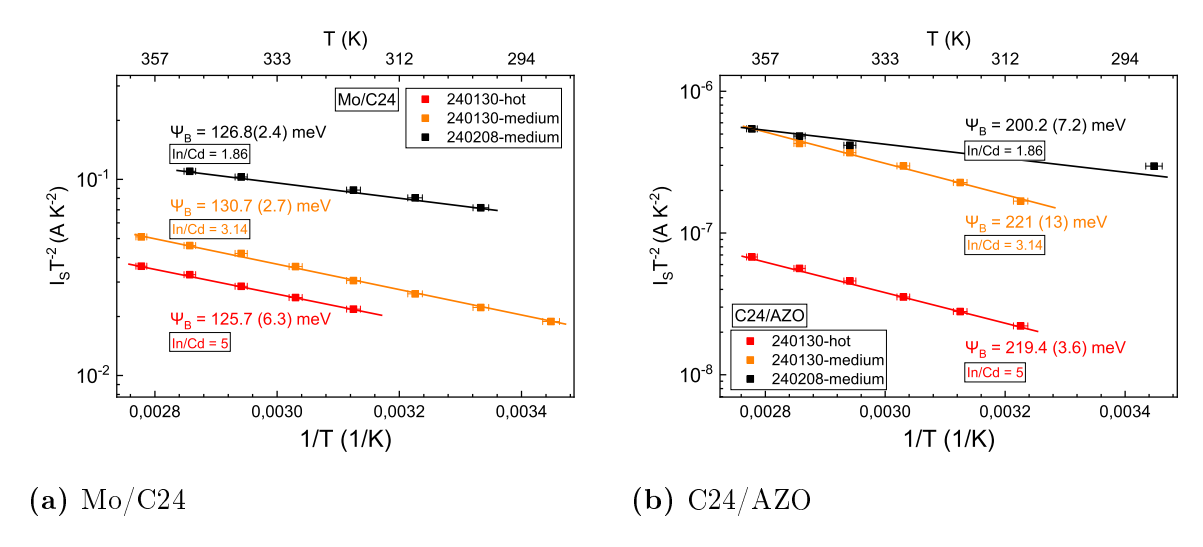


Figure 7.2.14: Barrier heights  $\Psi_B$ , obtained for three mainline samples form the region C (cf. Fig. 7.2.9), for Mo/C24 and C24/AZO junctions.

Having untangled the basic components of the IV characteristics, we can obtain the particular properties of the C24 by analysing their evolution. While matters in region A (Fig. 7.2.9) constitute the most complicated problem, we can further analyse region C, where we deal only with one particular controlling element, the forward-biased Schottky or isotype junction. Assuming the weak dependency of the switching processes on region C (and such an assumption is valid as much as weak is the frequency dependence of this part), we can determine the saturation current from the linear region within the C parts, and obtain values of  $\Psi_{B-Mo}$  and  $\Psi_{B-AZO}$  using the equation (3.2.71). These calculations were one of the issues addressed in one of the master's theses [255]. We have analysed three chosen samples, namely: 240130-hot, 240130-medium and 240208-medium, for which In/Cd equals: 5, 2.5 and 1.86, respectively. For these samples, fitting attempts gave the best results. The obtained Arrhenius plots are presented in Fig. 7.2.14, and the source IV characteristics can be found in the appendix on page 347. As can be seen, the barrier values for Mo/C24 junction are  $\approx 125$ meV, and for the C24/AZO  $\approx 200$ meV. The values obtained are notably small, for a given value of  $\chi_{C24}=3.5\text{eV}$ , the barriers for molybdenum and AZO should, in all likelihood, be in the 0.7–1 eV range. Moreover, such a small difference in the values obtained for samples grown under extreme differences in deposition conditions precludes a significant influence of these conditions, at least within our ability to control them. It should be noted at this point that certain stochastic factors beyond our control can significantly influence the layer growth parameters. Nevertheless, returning to the values themselves, we therefore have a systematic underestimation of some kind. It may, for example, simply result from an erroneously assumed value for the electron affinity of C24 or the work functions of materials forming the contacts. Our assumptions about  $CdIn_2S_4$  electron affinity derive from the calculations in the literature; therefore, we have no serious proof that  $\chi_{C24} = 3.5 \text{eV}$ . The lower value of  $\Psi_B$  may also result from several other factors, including passivating layers (MoS<sub>2</sub>), or interface defects pinning the barrier (and as we already know,  $CdIn_2S_4$  is rich in various types of defects). The barrier-lowering effect associated with the image charge may also be a key element here. Lastly, the very act of determining this barrier may be subject to error resulting from a number of factors: from the approximation error in the used method (which is, from another point of view, relatively trivial), to the influence of metastable defects. Again, this case cannot be resolved without further research.

Continuing to unravel the issues related to post-deposition treatment of the  $CdIn_2S_4$  from chapters 5 and 6, we will also briefly analyse devices based on C24-R and C24-RS layers, i.e. 240208-medium-R and 240208-medium-RS, as well as the devices with C24 layers subjected to quenching: 240208-medium-RQ and 240208-medium-RSQ. The IV characteristics of those devices are shown in the figure 7.2.15. The differences between the samples are essentially identical both with and without quenching. Constructing the device based on the layer annealed in vacuum causes a complete disappearance of the hysteresis effect. Moreover, the IV trace becomes close to linear, indicating that both barriers are mainly reduced or have disappeared completely. It is an observation of great importance. This result shall now be analysed in the context of that which has been previously established regarding the nature of  $CdIn_2S_4$ .

As we have found in chapter 5, annealing in vacuum causes repining the Fermi level from 0.1eV (as grown sample) to the value of  $E_{TR}$  of the V-E metastable complex, which

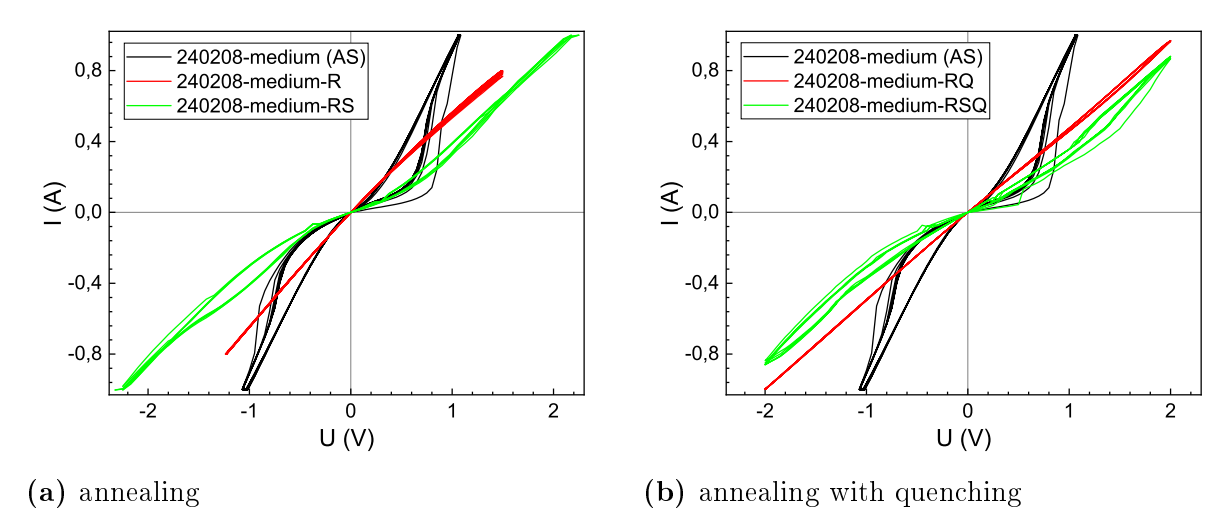


Figure 7.2.15: Comparison of the IV characteristics of the 240208-medium series after annealing procedures. u = 10.5 V/s.

has been found to be 0.4eV below the conduction band. From the junctions' perspective, that would decrease  $U_{bi}$  by approximately 0.3eV, yet it would not explain the change, as the  $\Psi_B$  still persist, assuming the  $\chi_{C24}$  does not change upon annealing.

At this point, we shall discuss what we did not in section 7.2.3, namely the equilibrium concentration of  $N_+$  at 300K. Since in the C24-AS sample  $E_{TR}$  is above  $E_F$ , in the relaxed state at room temperature, most of the metastable complexes will be in a negative charge state. Conversely, in the C24-R sample, half of the complexes are in each charge state. However, due to the highest concentration of species in the C24-AS sample, we have observed the absolute highest magnitude of the effects of PPC and PPS, orders of magnitude stronger than in the C24-R sample. Here, we postulate that the very same relation takes place. Due to the higher value of (1 - f)(z), this sample has a greater prospect of reducing it. Thus, the switching is observed to be the strongest. In the C24-R sample, however, we start with  $\frac{1}{2}f(z)$ , which already brings a reductive effect on the barriers, so we do not observe such a significant switching effect by further increasing f(z). However, the attentive reader will notice that we see absolutely no switching effect in sample 240208-medium-R! Indeed, but we also face a relatively large series resistance in the samples, which, in such a case, could easily cover any minor switching effects. PPC and PPS are orders of magnitude weaker in C24-R compared to the C24-AS sample (cf. Fig.

5.3.5 and 5.4.8). In fact, this could actually explain minuscule switching effects in some of the mainline samples – potentially significant  $R_S$  effectively prevented the observation of weak switching effects there.

A potential alternative explanation for the disappearance of the switching effect could lie in the reduction of the T states upon decreasing the spinel inversion degree. Therefore, the T states not only bring an additional intricacy to the switching process but also serve a crucial, indispensable role in the switching mechanism. Ergo, reducing those species removes the switching. Perhaps the only way to settle which interpretation is correct is to complete the metastable model form section 7.2.3, and perform appropriate numerical simulations. Alternatively, one could produce devices with smaller series resistance, and/or better performance. The issue of the architecture of the devices themselves will be discussed later.

The annealing of samples in sulphur similarly diminishes the global hysteresis loop, but in doing so, it causes the local hysteresis loop to reappear. It also brings back some nonlinear current-voltage relation. This is, in fact, a most perplexing circumstance. Given that annealing in sulphur causes reduction of the concentration of both inversion-related and metastable complexes, it must follow that the local hysteresis loop is a phenomenon altogether separate from metastability and sub-bandgap states, and its provenance is of an entirely different nature. In light of this fact, it is necessary to conduct additional experiments, for we have not yet devised any clear explanation to elucidate this matter.

Using the thin films deposited in the run 240312 (which were grown for 2x longer time, thus having a thickness of ~800nm, and its primary purpose was to serve for optical experiments), we have composed devices 240312-Mo and 240312-ITO; the purpose of which was to investigate the impact of thickness and presumed MoS<sub>2</sub> interfacial layer. The IV characteristics of those devices are shown in Fig. 7.2.16. As can be seen, such devices' modification did not remove the hysteretic effects. However, the behaviour of the devices is found to be distinctly different: In the 240312-Mo sample, we observe, that the hysteresis loop is present only on one side of the IV trace, corresponding to the barrier

(reduction) on the C24/AZO interface (it can be easily distinguished by studying the diagram 7.2.8), and the C24/Mo contact becomes injecting.

Now, the observation that there is no barrier on C24/Mo, and connecting it with the fact that the characteristics of the sample annealed in vacuum (240208-medium-R) are linear, actually brings back the hypothesis of self-annealing. This issue was discussed in the chapter 6.3 regarding the films from, in fact, the very same run (vide Fig. 6.3.12a). Here, the inferred annealing gradient in the 240312-Mo sample can clearly explain such asymmetric IV characteristics: the bottom part of the C24 layer is in fact C24-R, thus forms the same interface as in the 240208-medium-R sample; the top part is the C24-AS, therefore the C24/AZO interface works as in the other samples. It follows that a single-diode device has been fabricated here, quite by chance.

The matters in the 240312-ITO sample are similar. However, here, we observe a uniquely different switching behaviour of the C24/AZO junction: we do not see a hard switching, i.e. transition from region A to B (vide Fig. 7.2.9), but rather a continuous modulation of the transport deficiency limited by the blocking barrier on C24/AZO, i.e. we are moving only within the region A<sup>8</sup>. We can further observe a curious phenomenon of gradually incrementing the current with each consecutive cycle, despite it being symmetrical (so the opposite voltage should, in principle, reset the state). This effect, which is likely due to a slightly different course of the quasi-Fermi level, is, in essence, our very goal for neuromorphic behaviour. That is to say, it results in a gradual increase in conductivity – in other words, potentiation – after applying successive voltage pulses. We do not know the definitive cause behind such behaviours. However, we assume it might be related to the different defect concentrations in the layers, which do not grow on molybdenum, id est, we acknowledge the results of the divagations from the chapter 6.3, regarding the influence of the substrate type on the cadmium content<sup>9</sup>.

<sup>&</sup>lt;sup>8</sup>The association with the collector-emitter characteristic of a bipolar transistor is, in fact, quite correct. This is because the underlying principle is similar: a change in the saturation current of the reverse-biased junction.

 $<sup>^{9}</sup>$ A change in cadmium content affect the concentration and the energy distribution of the T, and E states, effectively changing the dynamics of the T-E recombination, thus possibly influencing the hopping transport process trough the blocking barrier, so the overall switching mechanism.

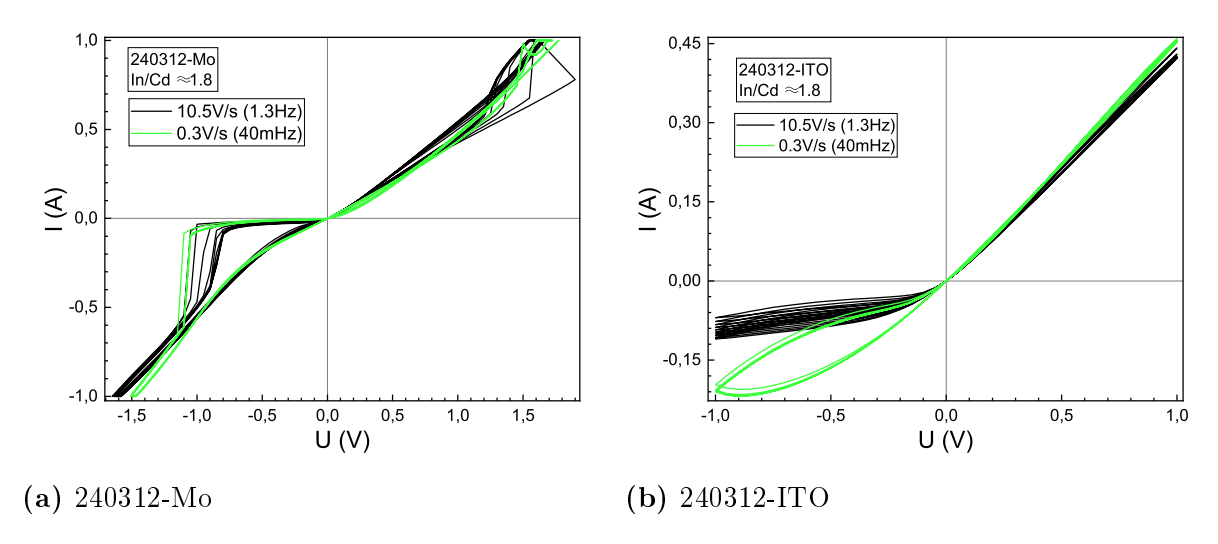


Figure 7.2.16: IV characteristics of samples with 800nm C24 layer

Nevertheless, the 240312-ITO sample conclusively disproves any conjectures that the switching is caused *only* by the MoS<sub>2</sub> layer – the switching behaviour is the inherent property of the Schottky or isotype junction with the CdIn<sub>2</sub>S<sub>4</sub> compound. However, to definitely resolve this matter, further research is necessary.

Lastly, we will present one issue regarding the illumination of the samples. The effect of illumination itself is, in fact, a key element of this inquiry, and it was the subject of one of the master's theses [256]. However, the results of the illumination-related general experiments did not provide any crucial insight for the analysis presented here. However, the effects of illumination on neuromorphic behaviour will be discussed in greater detail in the next chapter. Here, we will show one crucial result of the illumination-related experiments, i.e. the relaxation kinetics of the 240312-ITO sample after the illumination using the 460nm monochromatic light, similar to what was analysed in the chapter 5.4.1 (vide Fig. 5.4.1): In principle, the illumination kinetics showed the typical evolution (vide appendix on page 349). However, in the case of relaxation kinetics for the 240312-ITO (and in a similar manner for 240312-Mo) sample at sufficient negative bias voltages, instead of the typical photocurrent decay, we observe the fast decay, followed by the slow growth (Fig. 7.2.17a).

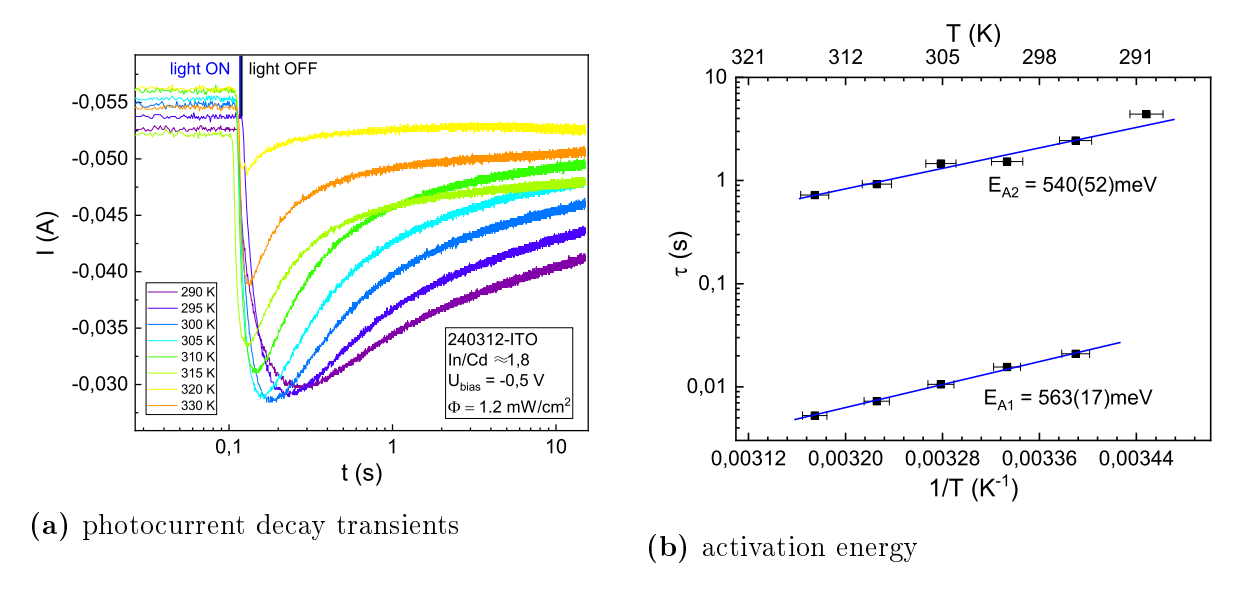


Figure 7.2.17: Photocurrent transients analysis for the sample 241312-ITO

We have observed such an effect on the -0.5V bias, thus in the state where the C24/AZObarrier is in the reverse polarisation. The proposed mechanism is as follows: A significant photocurrent is generated during illumination, contributing to the saturation current. Upon turning off the light, a rapid decrease in photocurrent is observed, resulting from the capture of free electrons. Subsequently, a gradual current increase is seen, which is the result of electrons being emitted from the complexes in negative charge state on the side of the blocking junction, just as was described in the section 7.2.3. This process ultimately leads to a reduction of the barrier and a gradual increase in the dark current - the secondary slow current transient. Assuming the linear dependency between the electron emission processes and the current flowing through the blocking contact, we can directly witness the process of the electron capture by the metastable complexes with time constant  $\tau_{EE}$  (equation (7.2.3d)), giving us a chance to find  $\Delta E_{EE}$  of our metastable defects. Therefore, we measured the kinetics as a function of temperature and performed fitting of the decay and rise parts of the current transients using the  $\xi \exp(\tau^{-1}t)$  function, thus obtaining the Arrhenius plot for activation of those two processes 7.2.17b. The obtained activation energies have values of 563(17)eV and 540(52)eV for the fast and slow processes, respectively, thus making these two activations of proximate value. Therefore, we will put  $\Delta E_{EE} \approx 0.54 \text{eV}$ . The fast process is likely related to some recombination center, 0.6eV

below the conduction band $^{10}$ .

Here, we will bring back the CCD diagram from chapter 5.5. Last time, we calculated the difference between the parabola's nodes by taking the bandgap  $E_g \approx 2.4 eV$ , obtaining 0.7eV. Moreover, we assumed the  $\Delta E_{EC}$  barrier to have some vague value between the measurement-wise (~0.1eV) and the fitting based upon the MPE model.  $\epsilon(+/-)$  was taken from the work of Péan et al. [22]. Hence, we would get  $\Delta E_{EE} = 2E_g - 2\epsilon + \Delta E_{EC} = 1.12 eV$ .

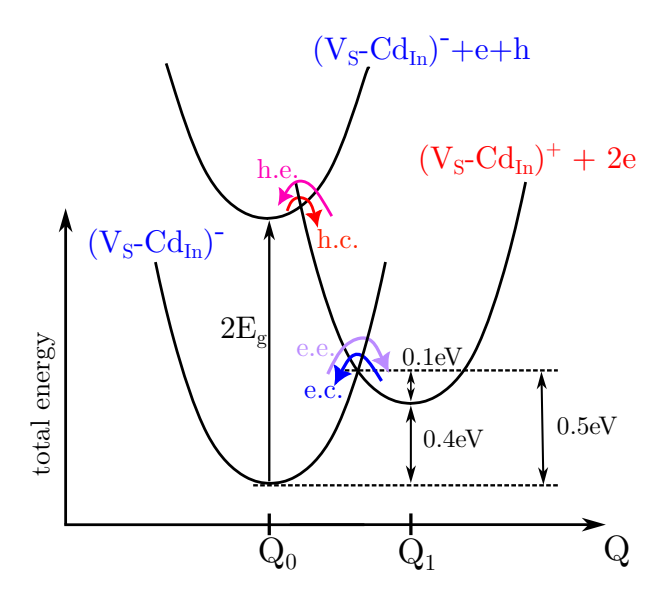


Figure 7.2.18: Modification of the configuration-coordinate diagram proposition for  $V_{\rm S}\text{-Cd}_{\rm In}$  complex from chapter 5.5 We added the complementary processes and modified the barriers' values.

However, if we take the indirect bandgap value for the C24-AS sample at 300K, measured by us (Fig. 5.4.11) – 2.15eV, the value of  $\Delta E_{EC}$  as the activation obtained from the  $\Delta \sigma$  measurement (for C24-R sample, because we cannot observe it in the C24-AS, as explained in the chapter 5.6), from Fig. 5.4.9 – 0.1eV, and we connect it with the value of  $\Delta E_{EE} \approx 0.54 \text{eV}$  it fits together.

The missing values are the barrier for hole capture  $\Delta E_{HC}$  expected to be of a relatively small magnitude, on the order of several to a dozen meV; and the hole emission barrier:  $\Delta E_{HE} = 2\epsilon + \Delta E_{HC} \approx 3.9 \text{eV}$ . Figure 7.2.18 presents the revised CCD diagram for the

 $<sup>^{10}</sup>$ Parenthetically, 0.6V is the depth of the  $V_S$  level below CB, reported in the literature, vide Fig. 4.3.2, and the overall discussion from chapters 4 and 5.

V<sub>S</sub>-Cd<sub>In</sub> metastable complex, having the parameters:

$$\epsilon(+/-) = 1.94 \text{eV}$$
 (7.2.10a)

$$\Delta E_{EC} \approx 0.1 \text{eV}$$
 (7.2.10b)

$$\Delta E_{EE} \approx 0.5 \text{eV}$$
 (7.2.10c)

$$\Delta E_{HC} \approx \text{few meV}$$
 (7.2.10d)

$$\Delta E_{HE} \approx 3.9 \text{eV}$$
 (7.2.10e)

## 7.3 Further insights, summary and future work

Returning to the very matter of the IV characteristics, based on our examination, it is clear that the shape of the IV traces is somewhat more dependent on the batch in which they were created than on the specific deposition parameters (run 240208 vs 240311B). This suggests that the overall behaviour of devices is rather process-wise. In other words, if there are any more subtle dependencies of the CdIn<sub>2</sub>S<sub>4</sub> properties on the devices, other than those we have presented, they are covered by the uncontrollable variation of the deposition parameters. A notable example is the significant variation in layer thickness across a single substrate, which is even visible to the naked eye (Fig. 6.2.1a). The use of shadow masks to define a single device with an area of 45mm<sup>2</sup> yields two single devices to fit side-by-side along the width of the substrate. A significant thickness gradient is thus present across the device itself. Other technological factors, such as spatial variation of composition (vide, sample 240312), will also introduce certain stochastic effects on a large number of samples. Perhaps we should turn to alternative deposition methods, such as the sputtering mentioned in one of the papers [24].

It must be said that even devices from the very same batch yielded slightly different results, not to mention the varying measurements over time. Therefore, the results presented in this chapter are a selection of the most repeatable ones. The most stable of these proved to be sample 240202-medium, which happens to be closest to In/Cd=2, which corresponds to a regular  $CdIn_2S_4$ .

It is important to mention the inconceivably enormous current flowing through the devices during measurement. Values—around 1A are not a mistake—these currents actually flow there. To switch the 240208-medium sample, we require a current ~0.4A; such a requirement prevents us from measuring the samples in the cryogenic setup or performing AC measurements. Parenthetically, when we sweep the devices in the range of ±1A, the power released is ~1W per complete cycle, which is released as the joule heating. Such power surges can contribute to local heating of the structure, which has a relatively low thermal conductivity coefficient. Some differences in individual measurements could therefore be explained by the heating up of the devices.

As mentioned, the series 240311B is particularly curious as it overlaps tightly with the 240130 and 240208, but has practically no hysteresis loop. The reasons may differ and lie in the interface and the bulk. Perhaps it was caused by a narrowly higher sulphur atomic flux, which was set during the runs on 11 March 2024, that resulted in a lower sulphur vacancy concentration. We must remember that we do not have information regarding the sulphur content in samples deposited on molybdenum.

Regarding the CdIn<sub>2</sub>S<sub>4</sub> properties, we do not have information about the Fermi level position, density of T states and inversion degree of the C24 films grown by us. Without that data, we would never be able to find any regularities or patterns in the devices' parameters and further neuromorphic performance. It is a regrettable circumstance that the samples could not be analysed as a function of wavelength due to insufficient illumination power. However, concerning the material characterisation, it is, in any case, generally more prudent to perform such an analysis on the bare thin films, rather than on the device, because of a number of assumptions that make the interpretation of results difficult.

We did not observe any premises for filamentary switching.

Once again, the vague idea of quenching requires more research.

One of the matters we hoped to investigate in the devices was space-charge-limited current. Measuring SCLC would offer the potential to finally investigate the mobility and probe the T states, which have become a recurring theme in our research (vide chapter

3.2.4). However, we could not obtain a slope from the log-log IV plot to be any greater than 1.1 (i.e., the ohmic case), let alone slopes greater than 2 (cf. relation (3.2.65)).

Most importantly, we do not have, in fact, any solid evidence that metastable  $V_{\rm S}\text{-}{\rm Cd_{In}}$  complexes actually govern switching. For the sake of conclusive confirmation, it is a matter of logical necessity to measure these devices below 160K. Alas, the appropriate tools for such a task are currently beyond our reach, due to the large current required to measure the devices properly. The effect of annealing upon the properties of this complex remains, alas, an unknown. For the purposes of this investigation, it has been presumed to have no significant influence.

The presented switching mechanism, based on metastable defects and a change in the width of the SCR, appears to be perfectly suited for investigation by means of CV and AC measurements in general. However, such experiments would presumably be challenging (or enjoyable), as the devices exhibit memory, so certain concerns regarding resetting the device during the measurement would have to be undertaken. For example, we expect that the Mott-Schottky plot would also have a hysteresis loop. In fact, due to modulation of the depleted region, those devices are actually memcapacitors, not memristors (vide chapter 2.1 and [43]).

Regarding possible improvements and the next experimental generations of devices, if we stay with the stacked configuration, the whole device architecture requires major modelling. Starting from the very bottom, an alternative metal for the electrodes must be found, especially with a higher work function to ensure a higher barrier on the interface with the  $CdIn_2S_4$ . Increasing  $\Psi_B$  would simply mitigate the problems of high current densities or the influence of the series resistance. However, learned from experience, we must remember the thermal budget of the lower electrode and the undesirable influence of the sulphur atmosphere during the deposition of the  $CdIn_2S_4$  layers. The next issue would be finding a metal that would form an ohmic junction with spinel without needing post-deposition treatment. Further on, modification of the shadow masks, i.e. simply reducing the surface area of the single device by one order of magnitude: from 45mm² to

4.5mm<sup>2</sup> would straightforwardly reduce the current density of the devices<sup>11</sup>. Finally, we can also further research the influence of the C24 thickness.

Despite the successful switching implementation in junction-based devices, we should reconsider the construction of hopping-based devices. Such devices would operate essentially similarly to those described in this chapter in region A (Fig. 7.2.9). Reconsidering this issue in light of the knowledge gained will be the subject of future research.

#### 7.4 The memristor test

One more aspect should be included before we close this part of the dissertation. The fact that the shape of the hysteresis loop can change continuously (and not as in the case of filamentary switching devices, where the switching occurs in a binary manner), and the general observation that the conductivity of the device depends on the total transferred charge, gives some suggestions of the presence of a genuine R(q) relationship, Moreover, the  $\mathfrak{f}$ , or the resulting  $z_{TR}$  could actually serve as the memristance state function  $\mathcal{Y}_M$  (cf. eq. (2.1.4)). Finally, the presence of a pinched hysteresis loop puts our devices squarely in the running for the title of memristor. It is therefore prudent to conduct the test proposed by Di Ventra and Pershin (mentioned in the chapter 3.3.2) to ascertain if this device is indeed the case.

Di Ventra and Pershin originally proposed a test circuit, as shown in the figure 3.3.3. The idea behind this circuit, as Di Ventra states, lies in the *duality property* of the memristor-capacitor circuit [48]; the capacitor works as a charge tracking device. Although the method is adroit and justifiable, we find this circuit impractical for several reasons: first, the circuit requires encapsulating the device under test with an electronic circuitry that will allow the capacitor to be switched on and off from the circuit in order to measure IV traces during the test. In practical implementation, the authors used a simple relay, probably the most straightforward solution [184]; however, any

<sup>&</sup>lt;sup>11</sup>The use of such shadow masks comes from the fact that we have cleverly adopted for our purposes part of the technology of the Nantes team, typically used to study the solar cells.

additional elements in the system may (and indeed should) raise concerns regarding their influence on the test result, whether by distorting characteristics or even electromagnetic interference. Secondly, the test for an ideal memristor requires an ideal capacitor. The test (and the memristor!) will be only as good as the capacitor used – factors such as ESR or leakage current can effectively ruin the test attempts. The capacitance value selection itself is non-trivial and depends closely on the parameters of the device being tested. Too small capacitance will result in very low current or a short charging time, complicating the measurement. However, from a fundamental point of view, the capacitor serves only to ensure that the total charge flown through our series circuit is zero when excited by a voltage waveform that starts and ends at zero. The capacitor circuit can therefore be successfully replaced by a current source (Fig. 7.4.1). Applying a symmetrical current waveform, i.e. ensuring that the same amount of current flows in both directions, is equivalent to a total transferred charge of zero. The memristor does not know that a capacitor is connected to it; only the total flowing current matters. Such an arrangement constitutes a much more practical solution, as it eliminates the imperfect capacitor and allows the implementation of any measurement waveform<sup>12</sup>.

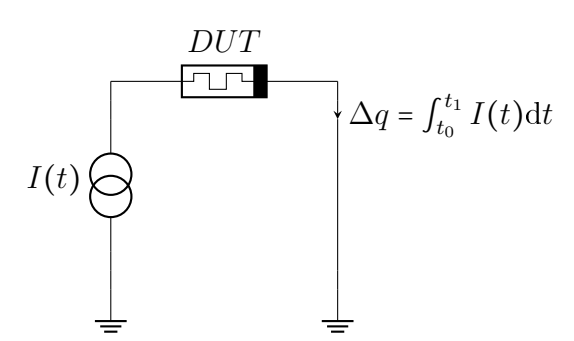


Figure 7.4.1: Modification of the memristor test.

<sup>&</sup>lt;sup>12</sup>If someone really wanted to, it is possible to program modern SMUs with current source functionality to reproduce the exponential dependence of the capacitor charging and discharging current.

method) is shown in Fig. 7.4.3a: the IV characteristic (memristor state) is measured between consecutive triangular current sweeps with various amplitudes, imitating charging/discharging the capacitor through the device. We will apply a triangular waveform for both current and voltage (test) sweeps. The test can be "cut in half" by applying asymmetrical current sweeps, and probing the device in  $(q_0, R_0)$  and  $(q_1, R_1)$  states (vide Fig. 3.3.2) – sequence in Fig. 7.4.2a.

We will test the sample 240208-medium, which is the most stable and repeatable over time. The voltage test sweeps will be limited to  $\pm 0.5V$  to ensure that we will not disrupt overmuch the sample state and, concurrently, we will be able to distinguish differences. We will perform current sweeps in the range  $50 \div 500$ mA, with a 50mA step.

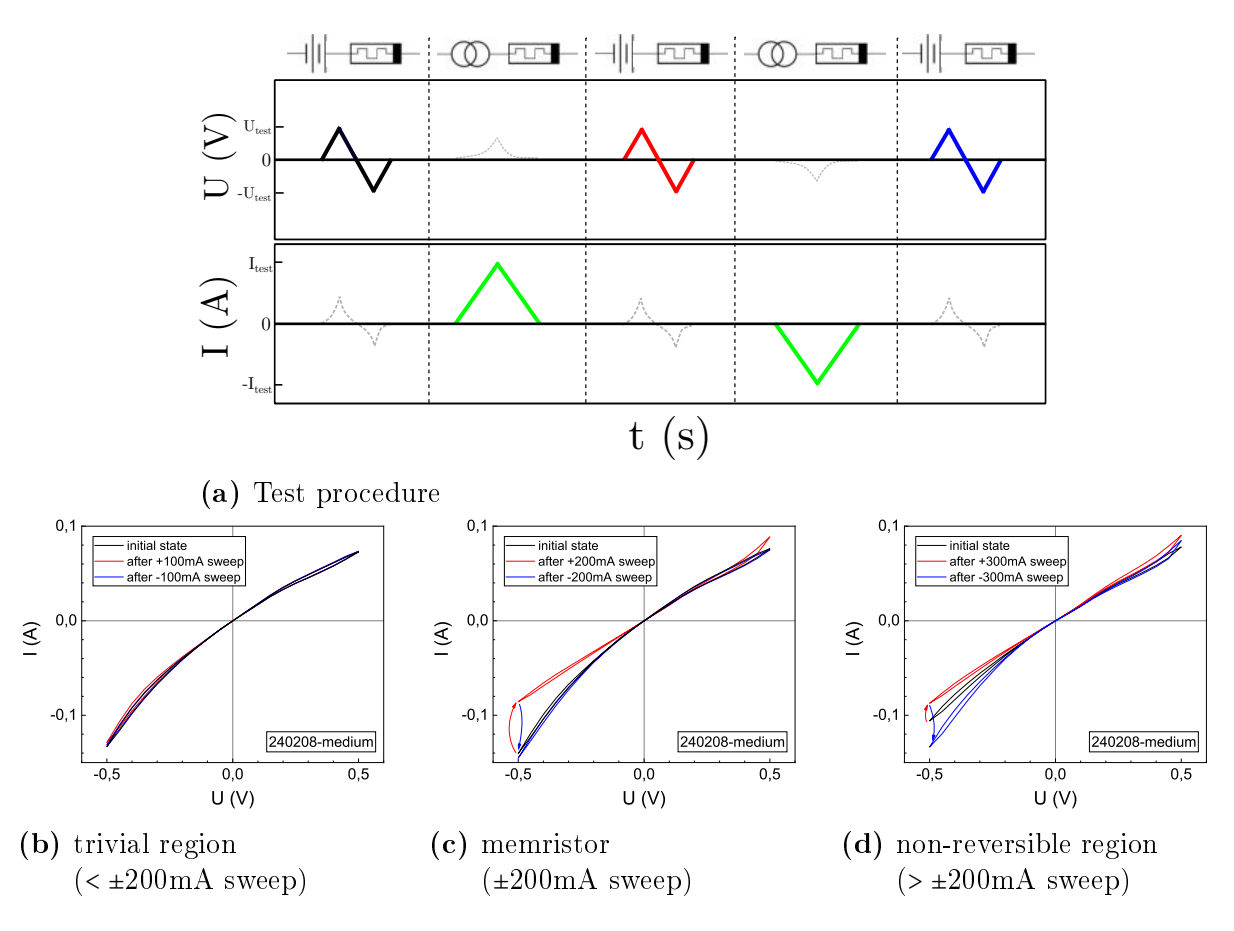


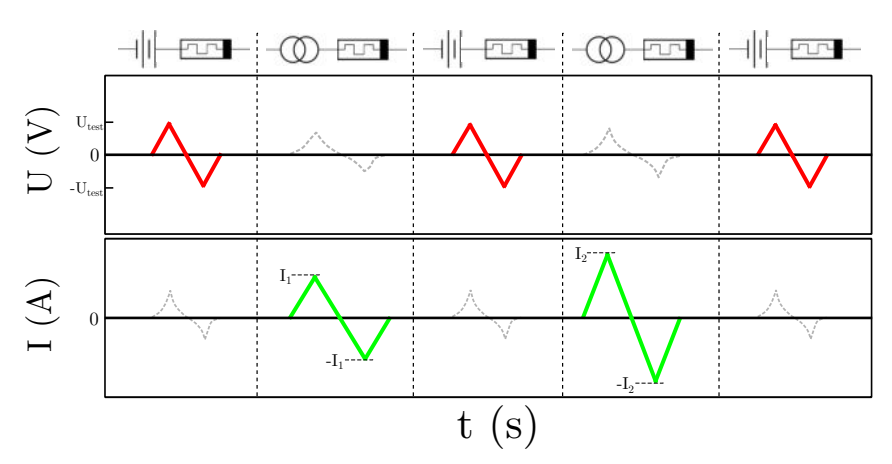
Figure 7.4.2: Memristor test, with the state examination every half cycle, performed for the sample 240208-medium. Black trace – initial state; red trace – after charge transfer  $+\Delta q$ ; blue trace – after  $-\Delta q$ , returning to the original state.

The results of the half-cycle test are shown in Fig. 7.4.2. From the point of view of sample behaviour, the range of applied current can be divided into three areas: first, at current amplitudes below 200mA, where the sweeps do not switch the sample, and the IV traces are identical no matter the total charge transferred (Fig. 7.4.2b). This is the trivial case mentioned in chapter 3.3.2. At  $\pm 200$ mA sweep, we observe the device passing the test – the trace changes after transferring  $\Delta q$  (red trace), and returns to the initial state after  $-\Delta q$  (blue trace). We see the sample in fact switches from the BD to the FD regime and vice versa (Fig. 7.4.2c). The device passes the test also at  $\sim 400$ mA. However, in the third range – above  $\pm 200$ mA the general behaviour becomes non-reversible, thus the device keeps failing the test (Fig. 7.4.2d).

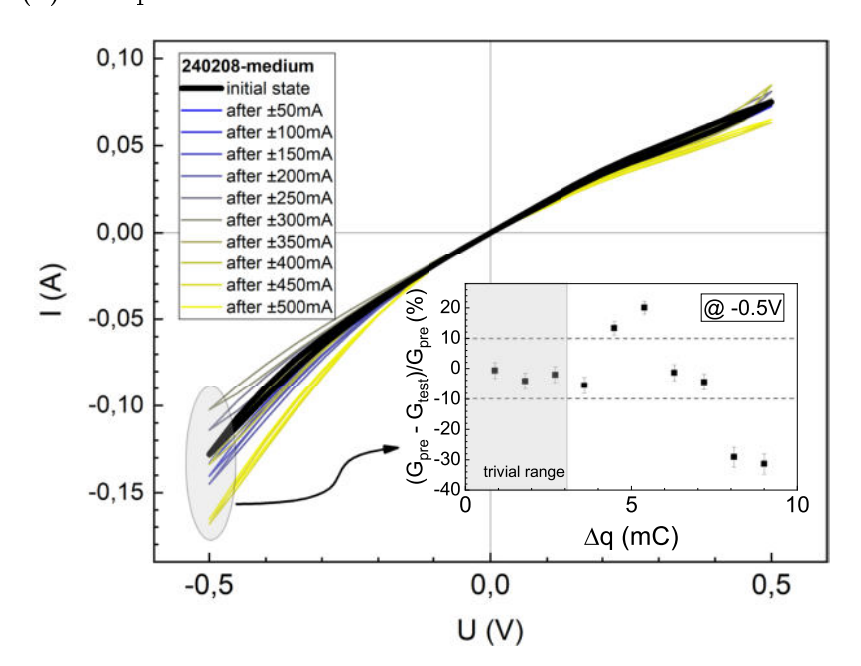
We ran a complete test with a symmetrical voltage waveform, obtaining qualitatively identical results (Fig. 7.4.3) – the device passes the test only in a short range around the current amplitude of 200mA and 400mA. The ±200mA with the given sweep time (~100ms) corresponds to charge of ±3.6mC<sup>13</sup>. Figure 7.4.3b summarises the IV test traces, showing the differences between each sweep. It could be argued that how small a difference makes these characteristics identical. Pershin et al. state that a deviation of 10% is considered satisfactory. [185]. To provide a sensible benchmark for our inquiry, let us calculate the conductivity deviation between consecutive measurements relative to the initial state, approximated at the -0.5V – inset in the figure 7.4.3b. As can be seen, the conductivity change state exceeds significantly the 10% acceptance range above 4mC.

We did not manage, however, to match the working current range to any distinct features of the IV characteristics, nor the particular details of the working mechanism. We also did not test the device with different current waveforms. The key to this problem, perhaps, lies in a more thorough investigation. Nevertheless, a single failed attempt is sufficient to disqualify a device from memristor candidacy. Thus, we conclude that our device is not a *true* memristor.

 $<sup>^{13}</sup>$  Parenthetically, a simple calculation reveals that a charge of 3.6mC at a maximum set voltage of 0.6V would correspond to a test capacitor value at least 6000  $\mu F,$  a value which speaks volumes about the sheer impracticality of implementing the original test.



(a) Test procedure



(b) Measured IV characteristics between consecutive complete current sweeps

Figure 7.4.3: Full memristor test performed at the sample 240208-medium. If the device were a memristor, the IV characteristics would be identical.

# Chapter 8

# Neuromorphic behaviour of the devices

At this point, we arrive at the ultimate goal of this dissertation: the attainment of synaptic behaviour within our devices. Without needless reservation, we must admit that the results presented herein lack a greater systematic regularity, which could be expected for such a broad number of samples available. Here, we will provide a selection of the best results obtained from our set of devices. This, in fact, cherry picking was compelled by nothing other than the considerable instability of the devices under examination, both within the individual cells of a given layer and in the varying behaviour of the same devices over time(!). It was exceedingly difficult to obtain conditions of repeatability for systematic measurements. However, in light of this entire work serving as a proof of concept for the ideas cogitated in this work, the last chapter offers a solid confirmation of the possibility of constructing such devices based upon the compound and the concept of operation in question. Therefore, this paradoxically shortest chapter fully exhausts the assumptions of our chosen research problem. Here, we will therefore present a selection of results demonstrating the devices' neuromorphic behaviour. For the majority of the experiments, the results shall be presented for four samples already known from the previous chapter: 240130-hot, 240130-medium, 240208-medium and 240312-Mo. Moreover, we will also try to do something not so often done in the literature, i.e., we will try to relate the observed time constants to the device parameters, particularly the C24 layer.

### 8.1 Electrical stimulation

We will first begin with the electrical stimulation. From the view of the entire work, it was a rather unexpected outcome that such stimulation was considered, as the assumption was to implement mainly optical stimulation, using hopping-based devices.

#### 8.1.1 Potentiation-depression

As outlined in Chapter 2, the general idea behind neuromorphic devices' operation is accumulating conductance increase through frequent electrical stimulation. As in real neurons, the synaptic connection strength increases with the firing frequency of presynaptic neurons. A complementary process, necessary for the practical implementation of neural networks, is depression, where the strength of the synaptic connection decreases. In practice, such behaviour is studied by applying a train of stimulating pulses, shown in figure 8.1.1.

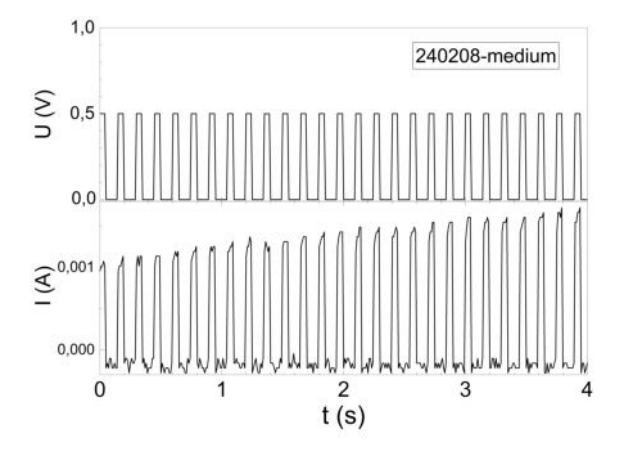


Figure 8.1.1: Potentiation measurement scheme (example for sample 240208-medium) for electrical stimulation, where the synaptic strength is defined as the device conductivity (proportional to current).

In the case of our devices, we need to find electrical stimulation conditions that would allow us to gradually influence f near one of the junctions. Then, we can gradually modify the current flowing through the barrier, thus enhancing the conductivity of the entire device. One may readily deduce that the empirical condition we seek is, in fact, the apparent switching voltage  $U_{sw}$ . Figure 8.1.2 shows the three general cases of the pulse response regarding the pulses' amplitude relative to  $U_{sw}$ . When the pulses are below the  $U_{sw}$ , the device persists in the BD regime (assuming it is not switched), and the current is low (we are on the lower branch of the hysteresis loop). Conversely, for pulses above  $U_{sw}$ , the device immediately switches to FD and stays at the upper hysteresis branch. At the  $U_{sw}$ , we fall into the dynamic region – where we can access the intricate clockwork of  $\frac{\mathrm{d}z_{TR}}{\mathrm{d}t}$  by modulating the duration and frequency of the pulses. Figure 8.1.2 already shows that by carefully trimming the parameters of the pulses, we can achieve a linear increase in the synaptic weight, single-handedly overcoming one of the challenges lingering in the neuromorphic devices.

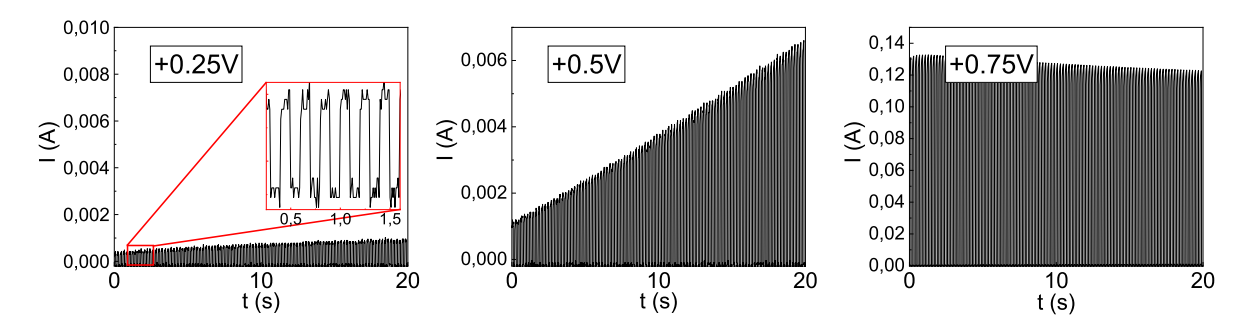
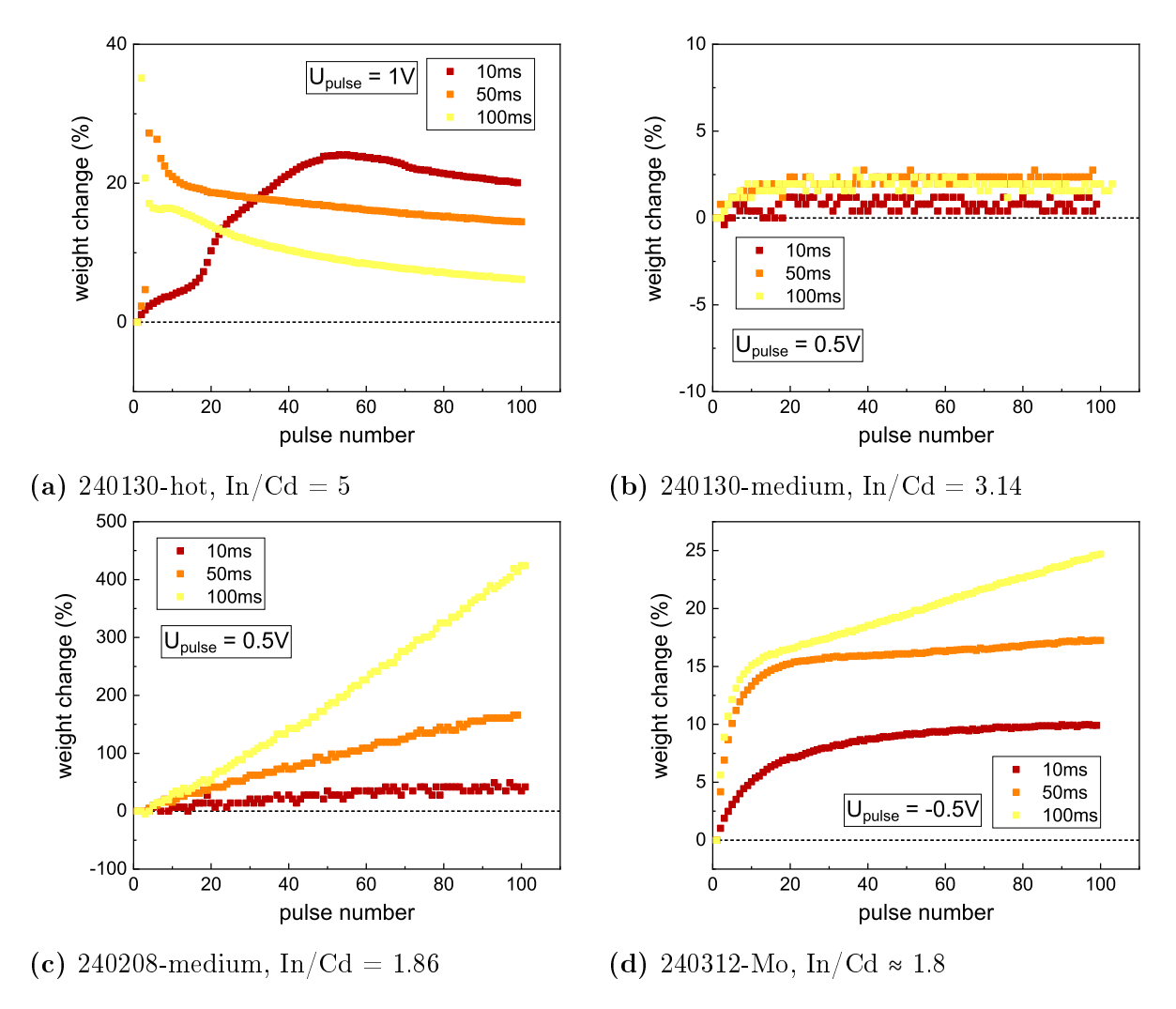


Figure 8.1.2: Potentiation using the 100ms pulses at the frequency 5Hz.

In the figure 8.1.3, we gathered results of the potentiation experiments for the four neuromorphic devices. For each device, we matched the pulse amplitude  $U_{pulse}$  with the appropriate  $U_{sw}$ . We examined three pulse lengths: 10ms, 20ms and 50ms while keeping the pause duration constant at 100ms. Further on, we recalculated the amplitude of the current response as the percentage weight change, relative to the quiescent current (approximated as the current of the first pulse). As it can be observed, we obtained the best results for the samples with In/Cd  $\approx 2$  (those also turned out to be the most stable), yielding close-to-linear weight change with over 400% increase. In the 240130-medium sample, we observed a negligible response, and the potentiation of the 240130-hot sample was significantly unstable.

The described potentiation study, regarding pulse duration, is an approach more oriented towards hardware testing, i.e., for potential pulse calibration to optimise device



**Figure 8.1.3:** Synaptic potentiation experiment. Weight change represent the ratio of the current at each pulse vs the quiescent current.

performance. To investigate neuromorphic properties, more sensitive to stimulation frequency (as the real neurons do), we rearranged gathered measurements to show the frequency dependence more clearly, i.e. we collected the potentiation for a single fixed pulse duration but for different pulse intervals, i.e., for different frequencies. Figure 8.1.4 shows such a comparison for sample 240208-medium, proving the general potentiation dependence of stimulation frequency in our devices.

Alas, since we deal with the double-diode devices, it was nearly impossible to realise the depression action. Both by using only stimulation pulses and the SET-read-RESET approach (vide Fig. 3.3.1). The best we achieved was a condition in which we observed

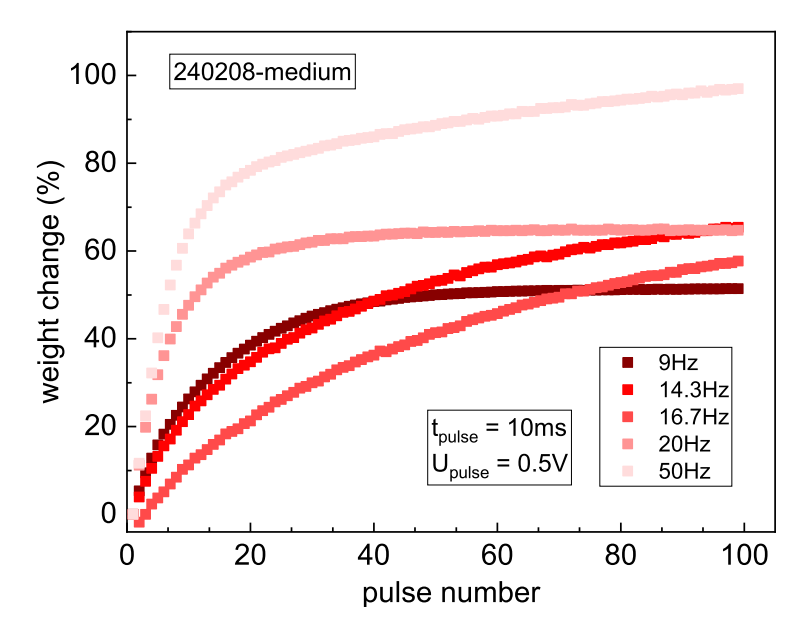


**Figure 8.1.4:** Synaptic weight change vs stimulation frequency for sample 240208-medium.

a spontaneous decrease in synaptic strength over time due to a relaxation of the spatial distribution of  $N_{+}$  concentration towards its uniform distribution; this was essentially independent of the electrical stimulation profile for low pulse amplitudes. The depression was impossible to achieve, because such action requires application of the negative pulses, which, in our case, causes an opposite effect on the junctions. The previously reduced barrier is now forwardly biased, forfeiting the accumulation that was done previously. Meanwhile, the opposing junction is still in the low conductance state. In other words, it is because we have the tangential hysteresis loop, unlike other devices reported in the literature, that usually exhibit transversal hysteresis (with the filamentary devices at the forefront). Therefore, we are confined to only potentiation schemes within the current architecture.

However, there is one case where we obtained a single-diode device: the samples from run 240312. Here, we accidentally created the ohmic contact on one side of the device, which gives us hope of seeing both potentiation and depression. Indeed, after carefully trimming the parameters of the SET, RESET and read pulses, we managed to achieve both potentiation and depression (Fig. 8.1.5) for the separate SET/RESET and read pulses.

We set the pulse voltages so that the SET pulses fall around  $U_{sw}$ , the read pulse within the hysteresis loop, and the RESET pulse on the positive side of the IV characteristics. Having only one junction, we can therefore easily reduce the device's net conductivity by decreasing  $N_{+}$  concentration near the junction, practically realising the depression. This proves the general applicability of this mechanism in neuromorphic devices.

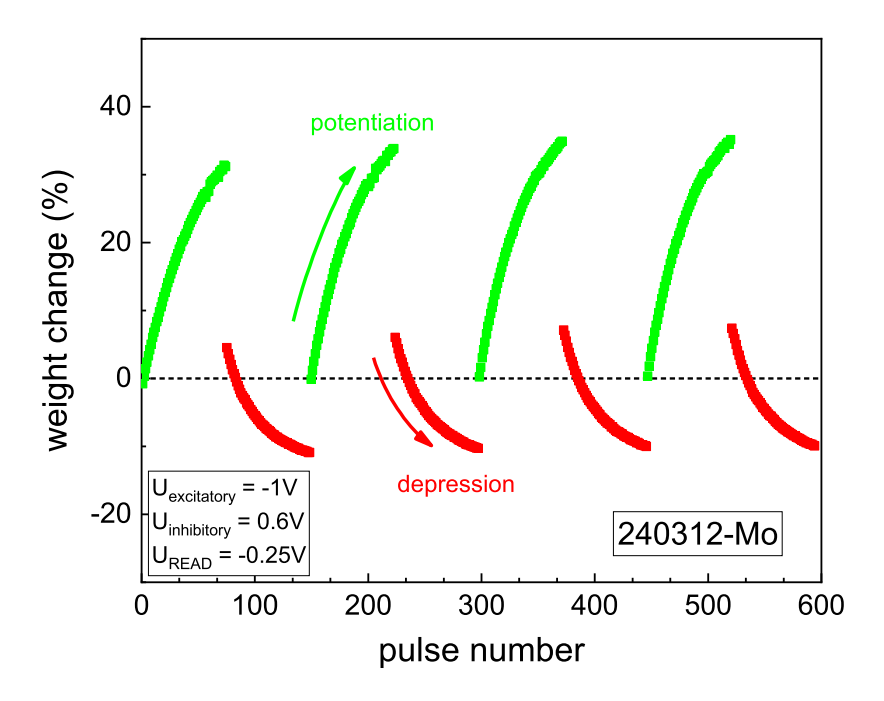


**Figure 8.1.5:** Potentiation and depression in 240312-Mo sample for precisely trimmed set of parameters.

We can observe the aforementioned relaxation of metastable defects towards their uniform distribution in the function of thickness: by first hard-switching the device to the BD or FD, then probing conductance using sufficiently low read pulses to prevent disturbing the state of the barriers with the reading operation. The figure 8.1.6 shows the results of such an experiment. This, in fact, can also be interpreted as the retention of the binary memory, i.e. decay of the particular resistance state (LRS) over time. As can be seen, the most durable retention of the LRS state is achieved in the 240208-medium sample; the 240130-hot and 240130-medium samples reset immediately after the write voltage is turned off to ~10% of the initial conductivity value (into the pristine state); the 240312-Mo sample (most probably due to its larger thickness) exhibits a gradual decay

of the synaptic strength. By fitting the decay curve with the equation (3.3.3), we have obtained time constants: 10.3(0.1)s and 61.4(1.7)s, which could actually be interpreted as the decay constants of short-term and long-term memory: after initial high stimulation, the synapse firstly *forgets*, reducing the strength to the  $\sim 50\%$  of the initial value, then slowly decaying further. Theoretically, a quick rehearsal after the STM state would cause a relearning – quick restoration to the full LRS state (cf. Fig. 2.4.3e).

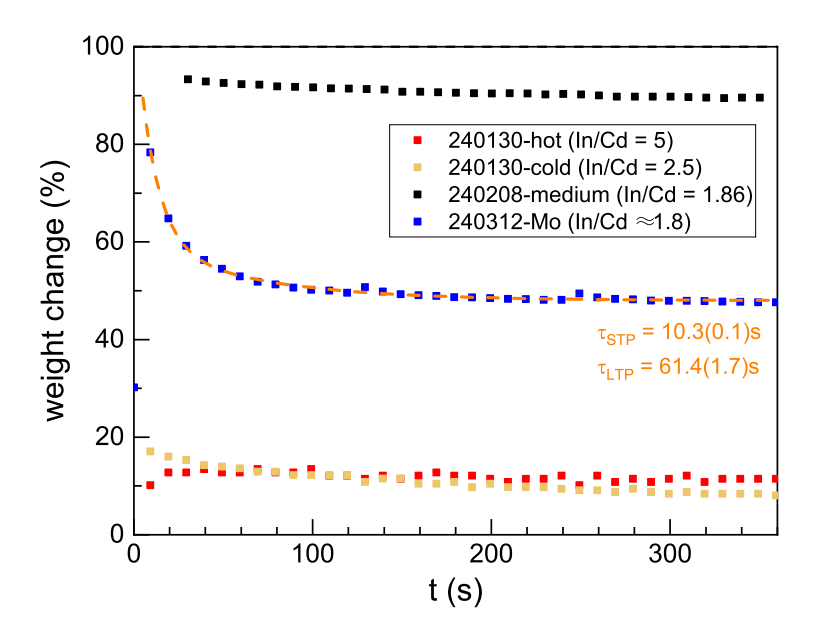


Figure 8.1.6: Decay of the synaptic weight from the maximum value (or the LRS state) over time, calculated as the percentage value of the initial conductivity during the polarisation (stimulation), normalised to the conductivity in the pristine state (0%).

### 8.1.2 Paired-pulse facilitation

Paired-pulse facilitation (PPF) is the next crucial behaviour of the neuromorphic devices, a form of short-term synaptic plasticity (vide chapter 2). Fig. 8.1.7 shows a general testing procedure. We apply two consecutive pulses and analyse the current response of the device to such stimulation in function of time delay  $\Delta t$  between pulses, using the equation (3.3.1). This method of calculation results in the values where 100% means no synaptic change; an increase, i.e., PPF, is above 100%, and a decrease, i.e., paired-pulse

depression, is below 100%. The results for the four samples analysed before are given in the figure 8.1.8. We tested 25ms, 50ms, and 100ms pulses with constant pauses of 100ms. For the sets of data, where the fit was feasible, we provided the fitted time constants using the equation (3.3.3) (double exponential), or using a single exponential function. Once again, the time constants can be interpreted as STP and LTP-related constants. In no case was it possible to fit the KWW curve to the data.

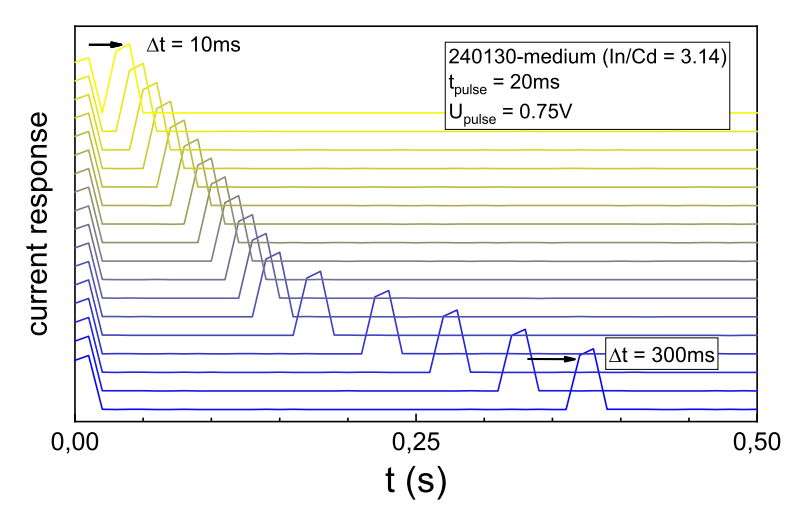


Figure 8.1.7: Paired-pulse facilitation measurement scheme (example for sample 240130-medium)

Due to the large scattering of the obtained results, we will refrain from giving any interpretations related to the specific samples under scrutiny, while giving only general observations, which is that, under certain pulse parameters, it was possible to obtain satisfactory PPF behaviour up to 125% increase for the sample 240130-medium.

The biological interpretation of the PPF phenomenon is usually given as the time dependence of the concentration of neurotransmitters released in the synapse during the firing of neurons. The neurotransmitter injection at the second pulse adds to the residual neurotransmitter concentration remaining after the first pulse. Since neurotransmitter concentrations exhibit exponential decay with time, the PPF as a function of time interval  $\Delta t$  is characterised by the equation (3.3.3).

In our devices, the C24/Mo and C24/AZO junctions take the role of a synapse, and the

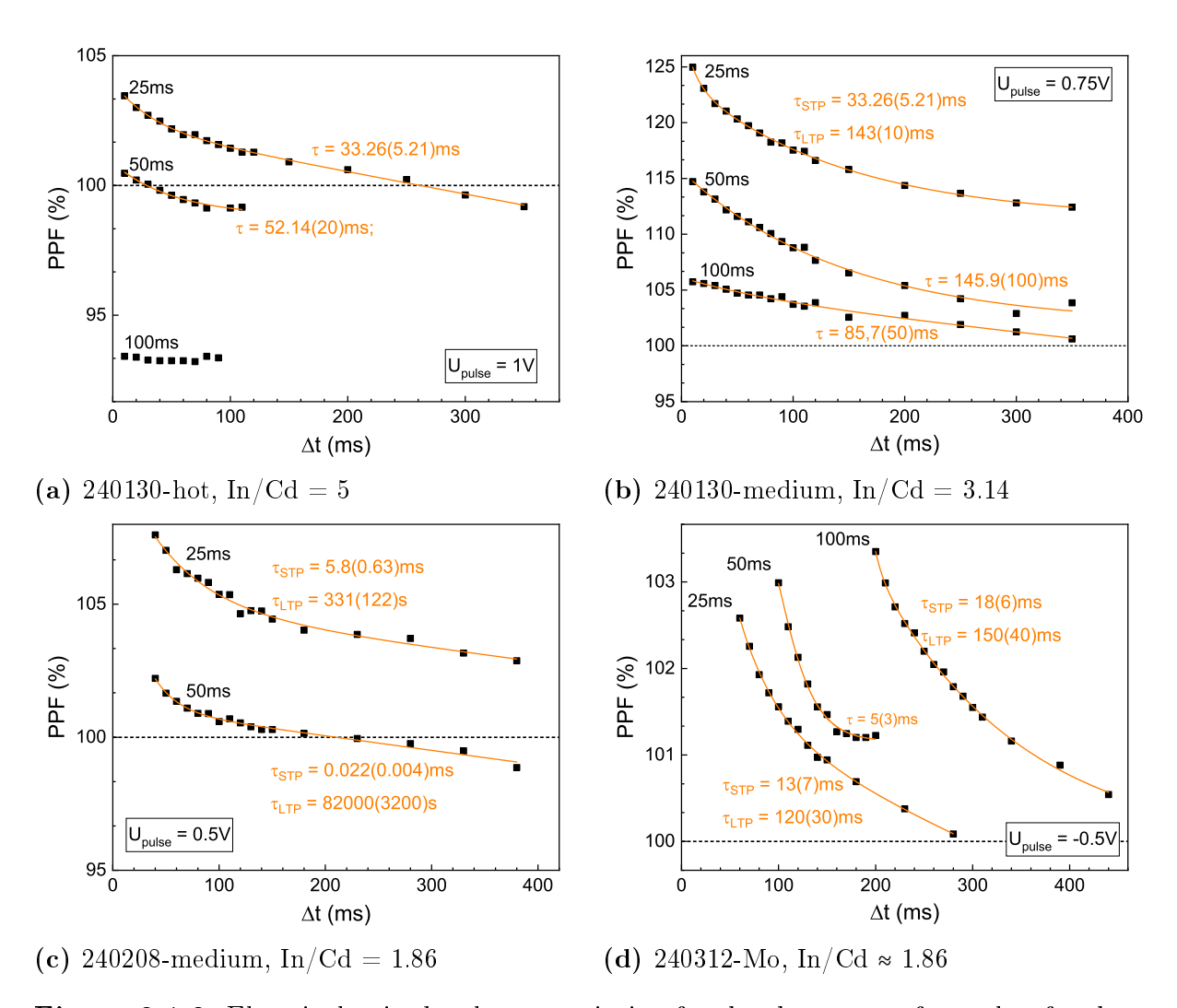


Figure 8.1.8: Electrical paired-pulse potentiation for the chosen set of samples, for three pulse duration times, and with the pulse amplitude  $U_{pulse}$  matching the  $U_{sw}$  for particular sample.

role analogous to a neurotransmitter is played by  $N_+$  – the concentration of our metastable defects in the positive charge state. The operation principle is therefore strikingly similar: after the first pulse, we create some initial  $N_+$  concentration near the blocking junction, which slowly decays over time. The second pulse converts the next portion of the defects, adding to the remnants from the first impulse. Since the  $N_+$  concentration near the junction slowly decays in time, it yields the decremental conductivity change (so also the current) as a function of the inter-spike interval.

In parentheses, it turns out that such a measurement can provide us with information

regarding the defects themselves. By measuring PPF, we are probing the exponential tail of the  $N_{+}$  decay as a function of time.

## 8.2 Optical stimulation

Optical stimulation of neuromorphic devices has been a key focus of our work from the very beginning. In this section, we will demonstrate what we have achieved in this regard based on the devices we have developed. Unfortunately, for reasons outlined earlier, we will limit our research to studies using only supra-bandgap blue light (2.7eV, 460nm).

Firstly, let us outline the general behaviour of the devices upon illumination. In the figure 8.2.1, we show the general process of potentiation using light pulses<sup>1</sup>. At first, the sample is biased with a constant voltage (in this case, 0.25V), generating a certain quiescent current. As expected, applying the light pulses increases the current, which then relaxes to a certain increased value once the optical stimulation is removed. This state will persist until the applied voltage is set to zero. Only applying 0V to the device resets it. This is the process we envisaged in the previous chapter 7.2.3 when analysing the impact of illumination on the operation of devices. Once this is done, voltage can be applied again, and the device is in a fresh state, ready to receive further impulses. This is currently the only known effective method (apart from annealing) to reset the device after optical stimulation.

## 8.2.1 Optical potentiation

Here, we will essentially repeat the previous potentiation experiments, but instead of applying electrical pulses, we will apply optical stimulation. Obviously, such measurements necessitate the application of a constant voltage to the sample under observation. Using the light also differs from its electrical counterpart in such a way that here, we convert the metastable defects in the entire volume of the C24 layer, through the hole capture process, thus reducing both barriers simultaneously. If one were to relate this to electrical

<sup>&</sup>lt;sup>1</sup>For the optical experiments, we have utilised a familiar setup shown in Fig. 3.2.2 (but without the cryostat).

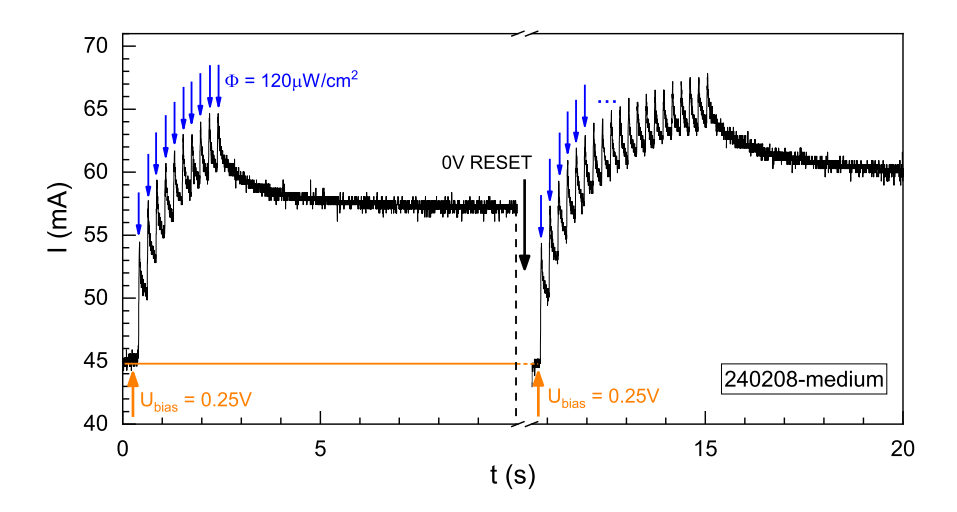


Figure 8.2.1: Optical stimulation of the 240208-medium sample using 460nm light pulses with 120  $\mu W/cm^2$ . The optical pulses are marked by blue arrows.

stimulation, it would be analogous to connecting a third, positively biased virtual electrode directly to the C24 layer.

For the optical potentiation experiment, we have applied constant 50ms light pulses, with a variable time interval. The photon flux was kept at  $\Phi = 1.2 \text{mW/cm}^2$ . The results for the four samples are shown in the figure 8.2.2. As can be seen, we achieve significantly lower weight change compared with the electrical stimulation. It is conceivable, however, that this outcome is a consequence of insufficient available illumination. We can surmise that higher power settings would yield more favourable results. Again, the best performance was achieved for the sample 240208-medium (55%). In the sample 240312-Mo, we observe a low-to-decremental illumination impact<sup>2</sup>.

Let us now extend the scope of our optical potentiation and employ the pulse series depicted in figure 8.2.3a. Here, we applied ten consecutive series with ten single pluses each. As can be observed, each series brings a similar incremental effect. Between the consecutive series, we can note exponential current decay, related to the electron emission

<sup>&</sup>lt;sup>2</sup>This is partly due to the more complex phenomena occurring in the samples from series 240312, which were discussed in chapter 7.2.4 (vide Fig. 7.2.17a).

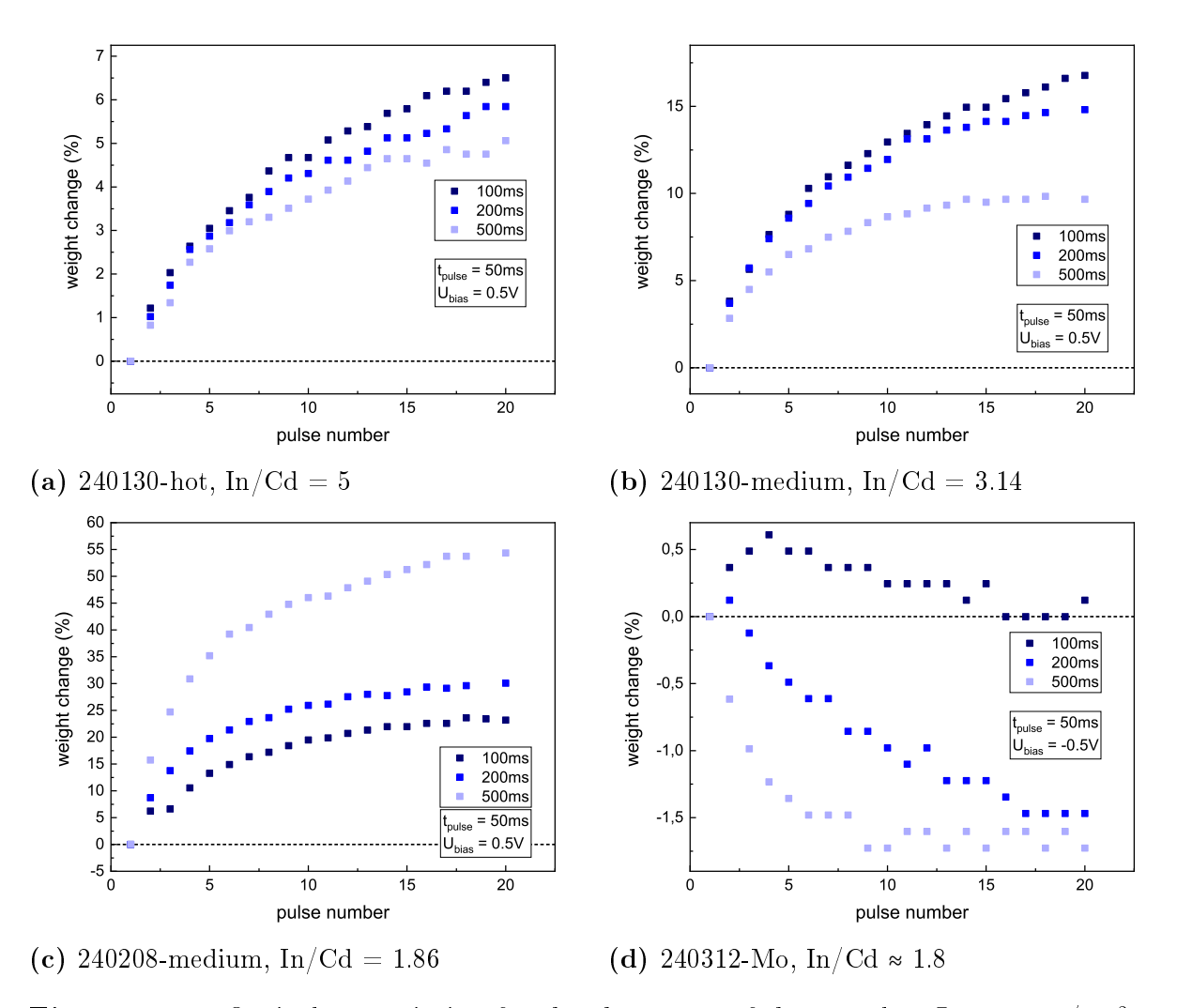
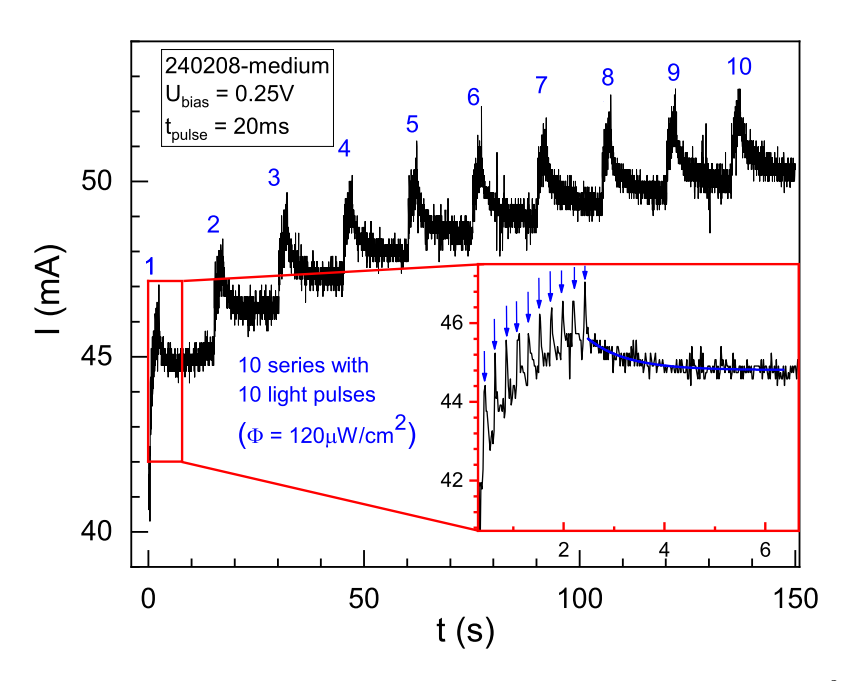


Figure 8.2.2: Optical potentiation for the chosen set of the samples.  $\Phi = 1.2 \text{mW/cm}^2$ .

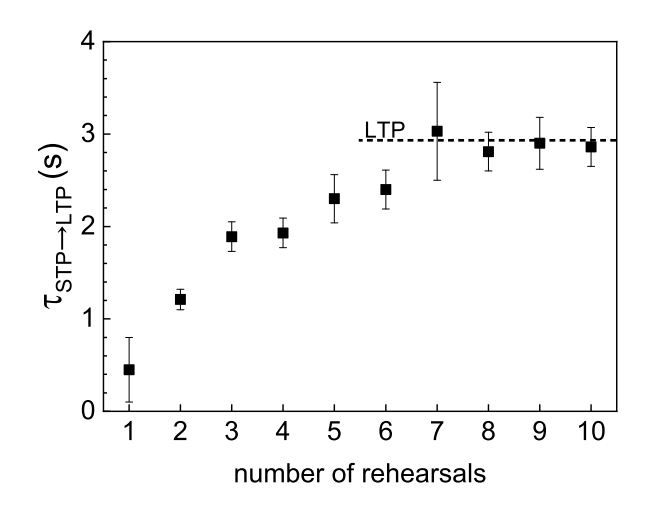
and recombination processes. We may assign the function of learning and relearning to the subsequent series of impulses, with the intervening cessation of activity being a period of forgetting (similarly as in [92] – vide Fig 2.4.3). The tenfold series of impulses themselves would earn the designation of rehearsals<sup>3</sup>. Now, we can fit the exponential decay function to the forgetting parts, and assign the resulting time constants as the memory retention. As shown in figure 8.2.3b, the decay constant saturates at a specific value upon the seventh rehearsal. This particular evolution of the forgetting curve could actually be assigned as the transition from the short-term to the long-term memory.

The presence of such behaviour is most likely owed to the quantum gyrator mechanism.

<sup>&</sup>lt;sup>3</sup>For more details of such inventions, one can check [89] or [180].



(a) Ten series of 20ms optical potentiation pulses.  $\Phi = 10 \mu \text{W/cm}^2$ .



(b) STP-LTP transition.

Figure 8.2.3: Extended scheme of optical potentiation for 240208-medium sample. An short-term→long-term memory transition can be observed.

The conversion of an increasing fraction of metastable defects to the positive charge state reduces the probability of recombining the electrons, and prolongs the duration of their multiple capture and emission by the T states. This is, in essence, a manifestation of the PPS phenomenon, as discussed in Chapter 5. Figure 5.5.3 is essentially an analogue to

the relationship observed herein. This observation practically demonstrates our devices' short-term/long-term plasticity capabilities<sup>4</sup>. It is also worth adding that the observed relaxation times, with an order of magnitude accuracy, coincide with the measurements of photoconductivity kinetics from Chapter 5, which we finally assigned to the T states.

#### 8.2.2 Paired-pulse facilitation

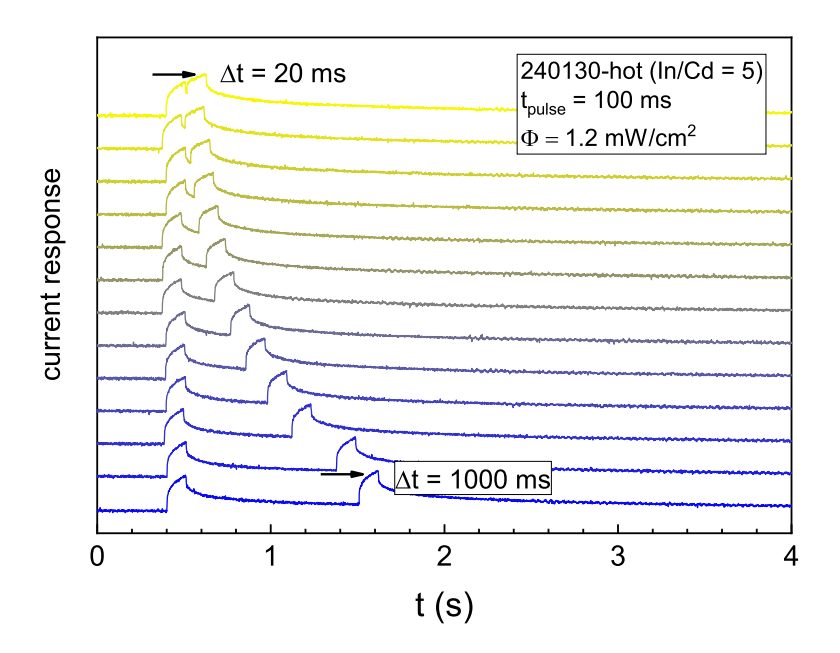


Figure 8.2.4: optical paired-pulse facilitation measurement scheme (example for sample 240130-hot)

In the case of optical stimulation, both the facilitation process and the samples' behaviour do not differ fundamentally from their electrical counterparts, again apart from the requirement to apply a certain biasing voltage. In the case of PPF measurement under optical stimulation, the observation of current changes clearly shows us the operating principle outlined in the analysis of PPF stimulated by electrical impulses (Fig. 8.2.4) – the evolution of the current upon paired optical pulses exquisitely demonstrates the

<sup>&</sup>lt;sup>4</sup>It is possible, on the other hand, that this constitutes a certain over-interpretation, as LTP should not relax at all, or relax very slowly. Moreover, the difference between  $\tau_{STP}$  and  $\tau_{LTP}$ , as well as the value of  $\tau_{LTP}$  itself, ought to be considerably greater. This would be theoretically achievable at lower temperatures, where, one recalls, the relaxation times of metastability will be considerably more prolonged.

outlined principle of neuromorphic behaviour of the devices, as the current delineates the temporal evolution of our neurotransmitters –  $N_{+}$  concentration.

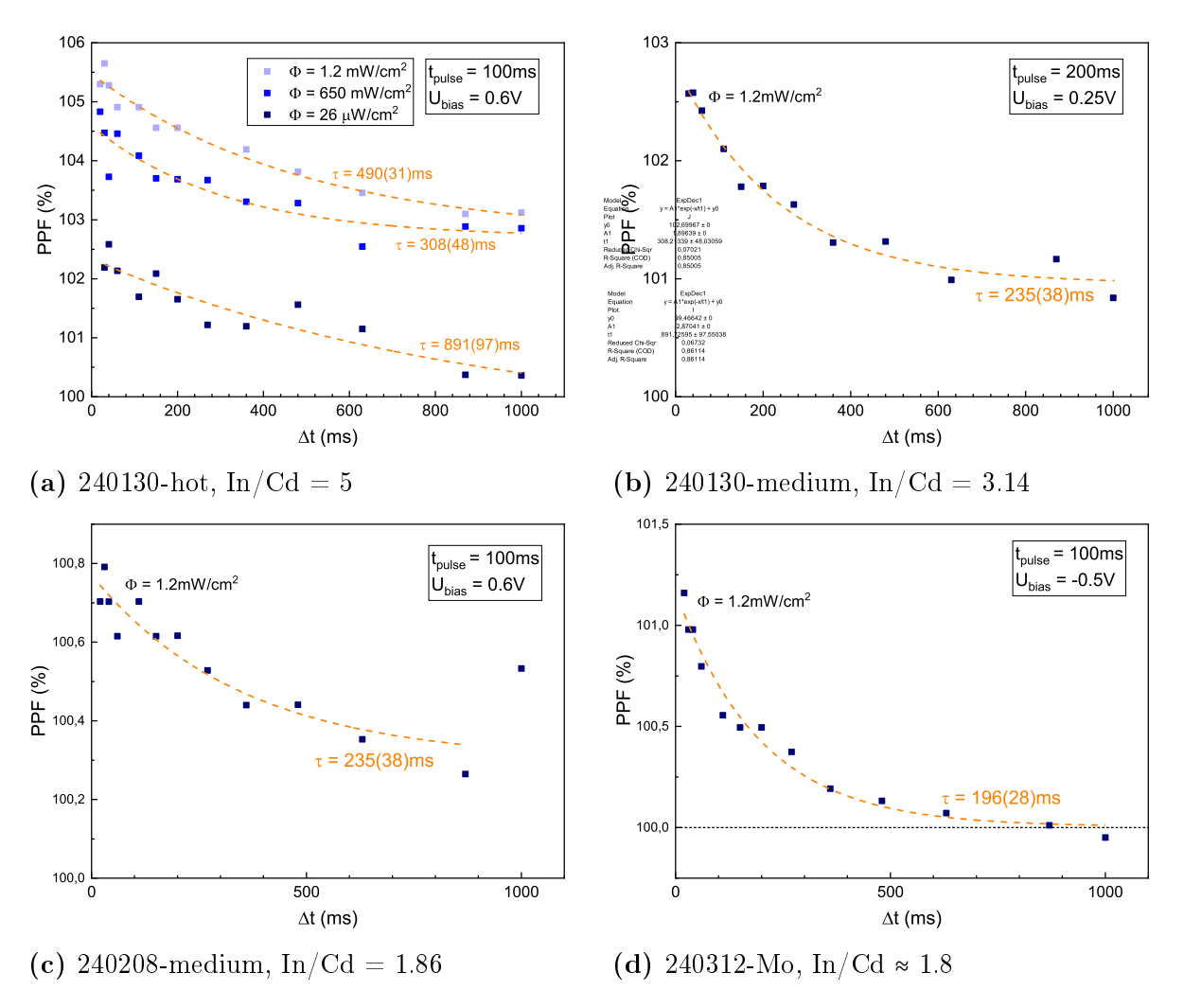


Figure 8.2.5: Optical paired-pulse facilitation for chosen four samples.  $\Phi = 1.2 \text{mW/cm}^2$ ,  $t_{pilse} - 100 ms$ ,  $U_{bias}$  match  $U_{sw}$ .

Nonetheless, the general performance of the devices is considered relatively weak – the best obtained value was only 106% for the sample 240130-hot. An exponential decay function was fitted to part of the data (where it was feasible) to obtain time constant values. Similarly, as was the case with PPF using electrical pulses, we are compelled to abstain from attempting a detailed analysis of the data due to its considerable dispersion.

## 8.3 Summary

This relatively concise chapter can be closed with a single general takeaway message, namely that it is possible, and moreover technically feasible, to construct neuromorphic devices that operate based on metastable defects. However, delineating further research paths for these devices requires an in-depth examination of existing devices. This is no easy task. Let us consider the parameters for optical potentiation: we can manipulate the time duration of pulses, pulse frequency, illumination intensity, illumination wavelength, and bias voltage. It gives us a 5-dimensional matrix of parameters – for one sample at one given temperature. Besides, the devices exhibit significant levels of randomness; thoroughly scanning the stimulation parameters in neuromorphic measurements is therefore a truly Herculean task. This assignment was given as the research problem in the two master's theses mentioned earlier [255, 256].

At this point, we ought to consider what challenges posed to neuromorphic devices our devices address. Undoubtedly, the main success of these devices is the achievement of linear potentiation. Some devices also respond well to voltage pulse stimulation (400% increase in synaptic strength during electrical stimulation, and 55% for optical stimulation). Moreover, we have shown the STP-LTP transition. These results could compete with devices presented in the literature [83, 266]. Perhaps further, more precise setting of stimulation parameters would allow for better performance of the tested devices.

Regarding the latency of the potential neuromorphic devices, they are confined to the switching speed of the metastable defects, i.e.  $\sim \tau_{EC}$ ,  $\tau_{EE}$ , etc.

Other challenges, as well as the device parameters themselves, still leave much to be desired. First and foremost, as mentioned in the previous chapter, reducing the current density in these devices is essential. Secondly, a significant problem affecting many devices reported in the literature and our devices is high variability and unreproducible performance. However, device optimisation outlined in the previous chapter should address these issues.

Unfortunately, we failed to test the STDP learning rule, which is crucial for devices operating in spiking neural networks. It is due to the same concerns as implementing depression. However, to implement STDP, simply removing a single diode is not enough; a device with a transversal hysteresis loop must be constructed.

One issue we have not explored is the response to light stimulation at different wavelengths. Only the effects of stimulation at 460nm were presented. What was additionally studied but not included within this work is stimulation with 640nm light, which yielded promising results. However, realising wavelength-dependent synaptic weights is quite achievable from the perspective of the CdIn<sub>2</sub>S<sub>4</sub> material itself. One need only refer to Figures 5.4.7 and 5.4.10 to see its hidden potential.

Finally, the best performance was obtained for devices with In/Cd = 2, deposited at 300°C. Despite that, it appears that we have come full circle, only to find ourselves precisely where we began. Despite the considerable efforts undertaken, this fact actually makes the  $CdIn_2S_4$  a relatively undemanding material from a technological perspective, i.e. thermal budget or no need for post-deposition treatment.

## Chapter 9

## The Final Conclusions

Alas, we have arrived at the very end of this dissertation. In the last chapter, we will present some general conclusions and final remarks that emerged while analysing the issues addressed in this work. First of all, however, let us return to our research question posed in the first chapter, namely: Is it possible to apply the metastable defects in chalcogenides as a source of memristive behaviour towards building the artificial neuromorphic devices? After conducting appropriate research and a thorough analysis, we conclude that yes, it is possible to use the metastable defects in chalcogenides as a source of memristive behaviour. The intended goal of the work, i.e. to investigate this issue and provide proof of concept for such an implementation, has therefore been achieved. Chapter 8, despite appearing as a mere appendix to this work, clearly emphasises this achievement.

Looking at the presented thesis from a broader perspective, one might conclude that the proposed research topic was only an excuse to research the CdIn<sub>2</sub>S<sub>4</sub>. On the one hand, yes, but on the other, the conducted material investigation and the conclusions drawn constitute a rather complex but *complete recipe* for constructing neuromorphic devices with excellent properties:

Chapters 7 and 8 have shown how crucial T states are for switching. This recurring theme of the sub-bandgap states may be key to device optimisation. Perhaps precise control of the T states, i.e., the degree of spinel inversion, will allow for optimising the

layers to achieve, for example, a linear response to optical potentiation?

Regarding the challenge hindering the development of the light-controlled memristive devices, i.e. realisation of the multi-wavelength device, we have actually shown that our compound could eaisly adress this problem: In the chapter 5, it was shown that it is possible to modulate the strength of the PPS by changing the illumination duration (Fig. 5.5.3). Moreover, we concluded that the metastability can be accessed with any light energy, which causes photogeneration (Fig. 5.4.10). Therefore, if one correlates it with the fact that we have a continuous spectrum with a close to linear (on a logarithmic scale)  $\Delta \sigma - f$  dependence (Fig. 5.4.7), it becomes readily apparent that we have a basically ready recipe for realising a neuromorphic device with broadband continuous wavelength response.

Actually, if the work aimed to show simply the memory properties of the researched material, it would be sufficient to show only figure 5.5.3, as the samples from chapter 5 could actually serve as an example of a *crude* memristive device, whose resistance can be optically modulated. Therefore, we would conclude this dissertation on page 185.

In chapter 5, we developed a  $CdIn_2S_4$  model that successfully predicted some future experimental results. However, this does not imply that the model is free of flaws or open questions. For example: we concluded that in the C48-AS sample, the Fermi level is pinned at 0.4eV below the conduction band, rendering it similar to the sample C24-R. So why do we observe a hysteresis loop in the 240130-hot device, where In/Cd = 5 (thus it corresponds to the C48-AS sample), but in the 240208-medium-R device ( $In/Cd \approx 2$ , i.e. C24-R), we do not?

Regarding the model in general, it is clear that providing only one counterargument is enough to refute a potentially large part of the interpretation<sup>1</sup>. Several unresolved issues were addressed in Chapter 5.7, with mobility being the substantial concern<sup>2</sup>.

<sup>&</sup>lt;sup>1</sup>Which happened about 4 times during its development.

<sup>&</sup>lt;sup>2</sup>Incorporating the mobility, for example, by acknowledging grain boundaries, would certainly add another dimension to the model. Nevertheless, one finds that the model is sufficiently coherent without it, and therefore, by virtue of Occam's razor, there is no pressing need for its inclusion

A major problem with the  $CdIn_2S_4$  compound, which has not been addressed so far, is that the truly metastable state is achieved only at low temperatures. At room temperatures, we are limited by the fast relaxation times of the order of seconds, which were observed in chapter 8, which result from the low barrier heights for relaxation of the metastable  $V_S$ - $Cd_{In}$  complex determined throughout the work. Fortunately, there are other spinels that may possess metastable defects with potentially higher barriers and inversion-dependent properties. One can begin to search for them.

### 9.1 List of open problems

Throughout this work, many unresolved matters and open questions have arisen. Here, we address the role of this work as a *pile of problems* that could trigger further work. Therefore, we present a list:

- 1. Mobility measurement on the samples from chapter 5;
- 2. Raman spectroscopy measurement on the samples from chapter 5;
- Photoluminescence measurement in function of temperature for samples from chapter 5. Excitation photoluminescence and thermally-stimulated luminescence experiments;
- 4. Thorough analysis of PITCS current transients, physical interpretation of the  $\beta$  parameter;
- 5.  $\sigma_{AC}$  measurements in function of temperature for samples from chapter 5, effects of metastability;
- 6. Derivation of the quantum gyrator model and related phenomena: superlinear Lux-Ampere, inductive behaviour of  $\sigma_{AC}$ , compressed exponential current transients. Development of the equivalent circuit from Fig. 5.6.3;
- 7. Further elaboration on the  $\frac{\mathrm{d}n}{\mathrm{d}T}$  curve, development of the equation 5.5.2;

- 8. Ab initio calculations for the V<sub>S</sub>-Cd<sub>In</sub> defect complex;
- 9. Bandgap measurement on the samples from chapter 6, probing the spinel inversion degree in function of deposition temperature;
- 10.  $\sigma(T)$  measurements on the samples from chapter 6 in search for the T-V regime transition;
- 11.  $\Delta\sigma(\lambda)$  and Lux-Ampere measurements on the samples from chapter 6, probing the correlation of the T states and In/Cd ratio;
- 12. Further XRD analysis, GIXRD measurements;
- 13. Investigation of the quenched C24 thin films;
- 14. IV characteristics of the devices from chapter 7 in function of temperature below 160K;
- 15. CV measurements on the devices from chapter 7;
- 16. Examination of the Mo/C24 interfaces in search for the MoS<sub>2</sub> layer;
- 17. Further examination of the 240312 samples, verifying the self-annealing hypothesis;
- 18. Further investigation of the C24/metal interfaces. In particular: examining the nature of contacts in the samples from chapter 5, testing the metals with higher work function for Schottky junctions with high  $\Psi_B$ , investigating the case of metal diffusion into C24 and optimising the deposition process to avoid it;
- 19. Optimisation of the Schottky junction-based memristive devices, devices' architecture modification, developing the single-diode devices;
- 20. Further development of the switching model from chapter 7.2.3, numerical simulations;
- 21. optimisation of the junction-based devices towards better neuromorphic properties;

- 22. Manufacturing the tunnelling-based devices;
- 23. Search for other spinels with metastable defects.

We will not stop researching CdIn<sub>2</sub>S<sub>4</sub>, and in the future, we will probably undertake to solve some of the points on this list ourselves.

### 9.2 Epilogue

As we were describing the model of operation for memristive devices based on metastability in the chapter 7.2.3, it became apparent that we had, in essence, all the pieces of the puzzle before our faces all along. We had great insight into the metastable defects [11,16,261], and modelling their application in the pn junctions modelling [262,263]; and finally, works that unwittingly exploited metastability to develop memory devices, such as the devices developed by Gao et al., woefully similar to ours [92]. One had merely to alter one's perspective on these metastable complexes.

As is often the way of things, unfortunately, we cannot claim to be the first to invent a memristive device founded upon metastability. A device of a nature identical to ours has already been independently discovered and published (but using the trivial CdS) [267,268].

Concerning the memristor in general, regardless of whether it exists or not, we managed to construct a device with memristor characteristics, technically in our second attempt. What does this mean? Was it a cosmic coincidence? An educated guess, based upon assumptions found in the literature? Or memristors are everywhere; one only needs to reach for one. Regarding the last possibility, one could refer to the reports in the literature, where hysteresis phenomena have indeed been observed in thin films [269] and bipolar transistors [270], or in general, in the double-diode structures based on semiconductors rich in defects, akin to our devices. Hence, we postulate that such hysteretic behaviour will emerge in any double-diode structure, such as an npn transistor, formed on highly defective semiconductor material.

A one final word on the matter of the quantum gyrator. The representation of physical processes occurring directly in bulk semiconductor using equivalent circuits is a compelling research topic with prospects for application in other areas. However, though the privilege of naming this mechanism was here usurped, it is to be expected, with a great conviction, that the concept had already been devised. Indeed, electrical circuits of this type can be easily found in the existing literature [34,271,272]. This is nevertheless a non-trivial case, as such a system is frequently presented as an equivalent circuit that serves as a practical realisation of a theoretical electronic element, which is otherwise difficult to obtain – a memristor.

# **Bibliography**

- [1] M. Roser, H. Ritchie, and E. Mathieu, "What is moore's law?," Our World in Data, 2023. https://ourworldindata.org/moores-law. 5
- [2] R. Nussinov, M. Zhang, Y. Liu, and H. Jang, "AlphaFold, Artificial Intelligence (AI), and Allostery," The Journal of Physical Chemistry B, vol. 126, pp. 6372–6383, Sept. 2022. 6
- [3] The Royal Swedish Academy of Sciences, "Press release." https://www.nobelprize.org/prizes/physics/2024/press-release/, 2024. 6
- [4] H. Cheng, M. Zhang, and J. Q. Shi, "A survey on deep neural network pruning: Taxonomy, comparison, analysis, and recommendations," *IEEE Transactions on Pattern Analysis and Machine Intelligence*, 2024. 6, 26
- [5] N. Jegham, M. Abdelatti, L. Elmoubarki, and A. Hendawi, "How Hungry is AI? Benchmarking Energy, Water, and Carbon Footprint of LLM Inference," July 2025. arXiv:2505.09598 [cs]. 6
- [6] C. James O'Donnell, "We did the math on ai's energy footprint. here's the story you haven't heard.," MIT technology review https://www.technologyreview.com/2025/05/20/1116327/ai-energy-usage-climate-footprint-big-tech/, 2025.
- [7] M. Greshko, "Nuclear power for ai: what it will take to reopen three mile island safely," *Nature*, vol. 634, no. 8033, pp. 272–273, 2024. 6

- [8] J. Del Valle, J. G. Ramírez, M. J. Rozenberg, and I. K. Schuller, "Challenges in materials and devices for resistive-switching-based neuromorphic computing," *Journal of Applied Physics*, vol. 124, p. 211101, Dec. 2018. 6, 26, 28, 38, 39, 88
- [9] D. Kudithipudi, "Neuromorphic computing at scale," *Nature*, vol. 637, no. 8047, pp. 801–812, 2025. 7, 8, 28
- [10] S. J. Kim, S. Kim, and H. W. Jang, "Competing memristors for brain-inspired computing," iScience, vol. 24, p. 101889, Jan. 2021. 9, 28, 29, 33, 89
- [11] M. Igalson, M. Bodegård, and L. Stolt, "Reversible changes of the fill factor in the ZnO/CdS/Cu(In,Ga)Se2 solar cells," Solar Energy Materials and Solar Cells, vol. 80, pp. 195–207, Oct. 2003. 8, 287
- [12] M. Igalson and P. Zabierowski, "Transient capacitance spectroscopy of defect levels in CIGS devices," *Thin Solid Films*, vol. 361-362, pp. 371–377, Feb. 2000. 9, 50
- [13] M. Igalson, M. Cwil, and M. Edoff, "Metastabilities in the electrical characteristics of CIGS devices: Experimental results vs theoretical predictions," *Thin Solid Films*, vol. 515, no. 15, pp. 6142–6146, 2025. 9, 48, 50
- [14] M. Igalson, A. Urbaniak, and M. Edoff, "Reinterpretation of defect levels derived from capacitance spectroscopy of CIGSe solar cells," *Thin Solid Films*, vol. 517, pp. 2153–2157, Feb. 2009. 9, 50
- [15] M. Igalson, K. Macielak, A. Urbaniak, N. Barreau, and J. Larsen, "Excitation spectra of defect levels derived from photoinduced current transient spectroscopy
   — a tool for studying deep levels in Cu(In,Ga)Se 2 compounds," Thin Solid Films, vol. 633, pp. 227–230, July 2017. 9, 50
- [16] M. Maciaszek and P. Zabierowski, "Influence of relaxation processes on the evaluation of the metastable defect density in cu(in,ga)se2," *Journal of Applied Physics*, vol. 119, no. 21, p. 215103, 2016. 9, 45, 48, 163, 164, 165, 241, 242, 287

- [17] M. Igalson, M. Maciaszek, K. Macielak, A. Czudek, M. Edoff, and N. Barreau, "Concentration of defects responsible for persistent photoconductivity in cu(in,ga)se2: Dependence on material composition," *Thin Solid Films*, vol. 669, pp. 600–604, 2019. 9, 48
- [18] G. A. Baraff, E. O. Kane, and M. Schlüter, "Theory of the silicon vacancy: An anderson negative- u system," *Physical Review B*, vol. 21, no. 12, pp. 5662–5686, 1980. 9, 45, 48
- [19] D. Lang, DX centers in III-V alloys. CRC Press, 2024. 9, 46, 165
- [20] S. Lany and A. Zunger, "Anion vacancies as a source of persistent photoconductivity in II-VI and chalcopyrite semiconductors," *Physical Review B*, vol. 72, no. 3, p. 035215, 2005. 9, 48, 50
- [21] N. Barreau, A. Frelon, T. Lepetit, E. Gautron, N. Gautier, R. Ribeiro-Andrade, N. Nicoara, S. Sadewasser, P. Zabierowski, L. Arzel, L. Choubrac, S. Harel, C. Deudon, C. Latouche, S. Jobic, M. Caldes, L. Assmann, P. Tsoulka, E. V. Péan, J. Lorthioir, F. Geschier, I. Braems, M. Moret, O. Briot, and G. Ouvrard, "High efficiency solar cell based on full PVD processed cu(in,ga)se 2 /cdin 2 s 4 heterojunction," Solar RRL, vol. 1, no. 11, p. 1700140, 2024. 10, 95, 202
- [22] E. V. Péan, N. Barreau, J. Vidal, C. Latouche, and S. Jobic, "Theoretical investigation of CdIn<sub>2</sub>S<sub>4</sub>: A possible substitute for CdS in CuIn<sub>1-x</sub>ga<sub>x</sub>se<sub>2</sub>-based photovoltaic devices," *Physical Review Materials*, vol. 1, no. 6, p. 064605, 2017. 10, 96, 98, 102, 103, 111, 112, 113, 159, 171, 256
- [23] Y. Seki, S. Endo, and T. Irie, "Low-frequency photocurrent oscillations in cdin 2 s 4 single crystals," *Japanese Journal of Applied Physics*, vol. 19, no. 9, p. 1667, 2022. 10, 104
- [24] Y. Seki, S. Endo, and T. Irie, "Switching phenomena in cdin2s4 thin films," Il Nuovo Cimento D, vol. 2, no. 6, pp. 1846–1851, 1983. 10, 96, 104, 187, 257

- [25] A. Charlebois and E. Fortin, "Gain excitation spectrum and acceptor density in cdin 2 s 4," Journal of Applied Physics, vol. 66, no. 7, pp. 3220–3223, 1989. 10, 98, 101, 106, 107, 143, 144, 174
- [26] A. N. Georgobiani, A. N. Gruzintsev, S. A. Ratseev, V. E. Tezlevan, I. M. Tiginyanu, and V. V. Ursaki, "Luminescence and photoconductivity caused by antisite defects in cdin2s4 single crystals," Crystal Research and Technology, vol. 21, no. 2, pp. 259–263, 1986. 10, 98, 100, 101, 102, 106, 113, 143, 152
- [27] L. Chua, "Memristor-the missing circuit element," *IEEE Transactions on Circuit Theory*, vol. 18, no. 5, pp. 507–519, 1971. 13
- [28] L. Chua, *Handbook of Memristor Networks*. Cham: Springer International Publishing, 2019. 14, 16
- [29] L. Chua and Sung Mo Kang, "Memristive devices and systems," *Proceedings of the IEEE*, vol. 64, no. 2, pp. 209–223, 1976. Publisher: Institute of Electrical and Electronics Engineers (IEEE). 15
- [30] L. Chua, "Memristor, Hodgkin-Huxley, and Edge of Chaos," Nanotechnology, vol. 24, p. 383001, Sept. 2013. 16
- [31] L. Chua, "If it's pinched it's a memristor," Semiconductor Science and Technology, vol. 29, Oct. 2014. 17
- [32] D. Biolek, Z. Biolek, V. Biolkova, and Z. Kolka, "Some fingerprints of ideal memristors," in 2013 IEEE International Symposium on Circuits and Systems (ISCAS2013), (Beijing), pp. 201–204, IEEE, May 2013. 17
- [33] D. Biolek, Z. Biolek, and V. Biolkova, "Pinched hysteretic loops of ideal memristors, memcapacitors and meminductors must be 'self-crossing'," *Electronics Letters*, vol. 47, pp. 1385–1387, Dec. 2011. 17

- [34] A. Isah and J.-M. Bilbault, "Review on the Basic Circuit Elements and Memristor Interpretation: Analysis, Technology and Applications," Journal of Low Power Electronics and Applications, vol. 12, p. 44, Aug. 2022. 17, 288
- [35] D. B. Strukov, G. S. Snider, D. R. Stewart, and R. S. Williams, "The missing memristor found," *Nature*, vol. 453, pp. 80–83, May 2008. 17, 30, 34, 35
- [36] R. Williams, "How we found the missing memristor," IEEE Spectrum, vol. 45, pp. 28–35, Dec. 2008. 17
- [37] A. Theodorakakos, S. G. Stavrinides, E. Hatzikraniotis, and R. Picos, "A non-ideal memristor device," in 2015 International Conference on Memristive Systems (MEMRISYS), (Paphos, Cyprus), pp. 1–2, IEEE, Nov. 2015. 18
- [38] M. D. R. Cantero, P. L. Perez, N. Scarinci, and H. F. Cantiello, "Two-dimensional brain microtubule structures behave as memristive devices," *Scientific Reports*, vol. 9, no. 1, p. 12398, 2019. 18
- [39] F. Corinto and A. Ascoli, "Memristive diode bridge with LCR filter," Electronics Letters, vol. 48, no. 14, 2012. 18
- [40] S. Peotta and M. Di Ventra, "Superconducting Memristors," *Physical Review Applied*, vol. 2, Sept. 2014. Publisher: American Physical Society (APS). 18
- [41] D. Lin, L. Chua, and S.-Y. Hui, "The First Man-Made Memristor: Circa 1801 [Scanning Our Past]," *Proceedings of the IEEE*, vol. 103, pp. 131–136, Jan. 2015. 18
- [42] G. Gandhi, V. Aggarwal, and L. Chua, "Coherer is the elusive memristor," in 2014 IEEE International Symposium on Circuits and Systems (ISCAS), (Melbourne VIC, Australia), pp. 2245–2248, IEEE, June 2014. 18
- [43] M. D. Ventra, Y. V. Pershin, and L. O. Chua, "Circuit elements with memory: memristors, memcapacitors and meminductors," *Proceedings of the IEEE*, vol. 97, no. 10, pp. 1717–1724, 2009. 18, 259

- [44] K. Sun, J. Chen, and X. Yan, "The Future of Memristors: Materials Engineering and Neural Networks," Advanced Functional Materials, vol. 31, p. 2006773, Feb. 2021. 18, 28
- [45] F. Z. Wang, L. Li, L. Shi, H. Wu, and L. O. Chua, " $\phi$  memristor: real memristor found," *Journal of Applied Physics*, vol. 125, no. 5, 2019. 18
- [46] Y. V. Pershin and M. D. Ventra, "Comment on " $\phi$  memristor: Real memristor found" by f. z. wang, l. li, l. shi, h. wu, and l. o. chua [j. appl. phys. 125, 054504 (2019)]," 2021. 19
- [47] F. Z. Wang, "Reply to" comment on phi memristor: Real memristor found", arxiv: 1909.12464," arXiv preprint arXiv:2104.09357, 2021. 19
- [48] M. Di Ventra and Y. V. Pershin, Memristors and Memelements: Mathematics, Physics and Fiction. Springer Nature, 2023. 19, 20, 90, 260
- [49] S. Vongehr and X. Meng, "The missing memristor has not been found," Scientific Reports, vol. 5, no. 1, p. 11657, 2015. 19
- [50] K. M. Sundqvist, D. K. Ferry, and L. B. Kish, "Memristor equations: Incomplete physics and undefined passivity/activity," Fluctuation and Noise Letters, vol. 16, no. 4, p. 1771001, 2017. 19
- [51] I. Abraham, "The case for rejecting the memristor as a fundamental circuit element," Scientific Reports, vol. 8, no. 1, p. 10972, 2018. 19
- [52] B. Tellini, M. Bologna, K. J. Chandía, and M. Macucci, "Revisiting the memristor concept within basic circuit theory," *International Journal of Circuit Theory and Applications*, vol. 49, no. 11, pp. 3488–3506, 2021. 19, 20
- [53] K. M. Sundqvist, D. K. Ferry, and L. B. Kish, "Second law based definition of passivity/activity of devices," *Physics Letters A*, vol. 381, no. 39, pp. 3364–3368, 2017. 19

- [54] D. Jeltsema and A. van der Schaft, "Ideal memcapacitors and meminductors are overunity devices," *Scientific Reports*, vol. 10, no. 1, p. 16688, 2020. 19
- [55] B. Mouttet, "The memristor and the scientific method," 2012. 20
- [56] H. M. Upadhyaya and S. Chandra, "Polarity-dependent memory switching effects in the ti/cd<sub>x</sub> pb<sub>1-x</sub> s/ag system," Semiconductor Science and Technology, vol. 10, no. 3, pp. 332–338, 2011. 20, 33
- [57] T. W. Hickmott, "Low-frequency negative resistance in thin anodic oxide films," Journal of Applied Physics, vol. 33, no. 9, pp. 2669–2682, 1962. 20
- [58] F. Argall, "Switching phenomena in titanium oxide thin films," Solid-State Electronics, vol. 11, no. 5, pp. 535–541, 1968. 20
- [59] F. A. Azevedo, L. R. Carvalho, L. T. Grinberg, J. M. Farfel, R. E. Ferretti, R. E. Leite, W. J. Filho, R. Lent, and S. Herculano-Houzel, "Equal numbers of neuronal and nonneuronal cells make the human brain an isometrically scaled-up primate brain," *Journal of Comparative Neurology*, vol. 513, pp. 532–541, Apr. 2009. 21
- [60] R. Yang, H. Huang, and X. Guo, "Memristive Synapses and Neurons for Bioinspired Computing," Advanced Electronic Materials, vol. 5, p. 1900287, Sept. 2019. 22, 23, 28, 29, 88, 89
- [61] M. Bear, B. Connors, and M. A. Paradiso, Neuroscience: Exploring the brain, enhanced edition: Exploring the brain. Jones & Bartlett Learning, 2020. 24
- [62] A. L. Hodgkin and A. F. Huxley, "A quantitative description of membrane current and its application to conduction and excitation in nerve," The Journal of Physiology, vol. 117, pp. 500–544, Aug. 1952. 24
- [63] L. Chua, V. Sbinev, and H. Kim, "Hodgin-huxley axon is made of memristors," International Journal of Bifurcation and Chaos, vol. 22, p. 1230011, Mar. 2012. 25

- [64] Y. V. Pershin, S. La Fontaine, and M. Di Ventra, "Memristive model of amoeba learning," *Physical Review E*, vol. 80, no. 2, p. 021926, 2009. 25
- [65] J. Von Neumann, The computer and the brain. Yale Univer. Press, 1958. 26
- [66] History of Data Science, "Ai winter: The highs and lows of artificial intelligence." https://www.historyofdatascience.com/ai-winter-the-highs-and-lows-of-artificial-intelligence/, 2021. 26
- [67] Y. Chen, H. H. Li, C. Wu, C. Song, S. Li, C. Min, H.-P. Cheng, W. Wen, and X. Liu, "Neuromorphic computing's yesterday, today, and tomorrow – an evolutional view," *Integration*, vol. 61, pp. 49–61, Mar. 2018. 26
- [68] Z. Du, D. D. Ben-Dayan Rubin, Y. Chen, L. He, T. Chen, L. Zhang, C. Wu, and O. Temam, "Neuromorphic accelerators: a comparison between neuroscience and machine-learning approaches," in *Proceedings of the 48th International Symposium* on Microarchitecture, (Waikiki Hawaii), pp. 494–507, ACM, Dec. 2015. 26
- [69] I. Schlag, K. Irie, and J. Schmidhuber, "Linear transformers are secretly fast weight programmers," in *International conference on machine learning*, pp. 9355–9366, PMLR, 2021. 26
- [70] Q. Fournier, G. M. Caron, and D. Aloise, "A practical survey on faster and lighter transformers," *ACM Computing Surveys*, vol. 55, no. 14s, pp. 1–40, 2023. 26
- [71] G. Amin Vahdat, "Ironwood: The first google tpu for the age of inference." https://blog.google/products/google-cloud/ironwood-tpu-age-of-inference/, 2025. 27
- [72] Apple, "Apple unleashes m1." https://www.apple.com/pl/newsroom/2020/11/apple-unleashes-m1/, 2020. 27
- [73] M. Davies, N. Srinivasa, T.-H. Lin, G. Chinya, Y. Cao, S. H. Choday, G. Dimou, P. Joshi, N. Imam, S. Jain, Y. Liao, C.-K. Lin, A. Lines, R. Liu, D. Mathaikutty, S. McCoy, A. Paul, J. Tse, G. Venkataramanan, Y.-H. Weng, A. Wild, Y. Yang, and

- H. Wang, "Loihi: A Neuromorphic Manycore Processor with On-Chip Learning," *IEEE Micro*, vol. 38, pp. 82–99, Jan. 2018. 27
- [74] F. Akopyan, J. Sawada, A. Cassidy, R. Alvarez-Icaza, J. Arthur, P. Merolla, N. Imam, Y. Nakamura, P. Datta, G.-J. Nam, B. Taba, M. Beakes, B. Brezzo, J. B. Kuang, R. Manohar, W. P. Risk, B. Jackson, and D. S. Modha, "TrueNorth: Design and Tool Flow of a 65 mW 1 Million Neuron Programmable Neurosynaptic Chip," *IEEE Transactions on Computer-Aided Design of Integrated Circuits and Systems*, vol. 34, pp. 1537–1557, Oct. 2015. 27
- [75] C. Sung, H. Hwang, and I. K. Yoo, "Perspective: A review on memristive hardware for neuromorphic computation," *Journal of Applied Physics*, vol. 124, p. 151903, Oct. 2018. 27, 28, 29, 37, 38
- [76] J. Wang, N. Ilyas, Y. Ren, Y. Ji, S. Li, C. Li, F. Liu, D. Gu, and K. Ang, "Technology and Integration Roadmap for Optoelectronic Memristor," Advanced Materials, vol. 36, p. 2307393, Mar. 2024. 27
- [77] K. M. Kim, D. S. Jeong, and C. S. Hwang, "Nanofilamentary resistive switching in binary oxide system; a review on the present status and outlook," *Nanotechnology*, vol. 22, p. 254002, June 2011. 27, 32, 34
- [78] G. C. Adam, A. Khiat, and T. Prodromakis, "Challenges hindering memristive neuromorphic hardware from going mainstream," *Nature Communications*, vol. 9, no. 1, p. 5267, 2018. 27, 28, 37, 39
- [79] D. R. Muir and S. Sheik, "The road to commercial success for neuromorphic technologies," *Nature Communications*, vol. 16, no. 1, p. 3586, 2025. 28
- [80] L. Hu, J. Yang, J. Wang, P. Cheng, L. O. Chua, and F. Zhuge, "All-Optically Controlled Memristor for Optoelectronic Neuromorphic Computing," Advanced Functional Materials, vol. 31, p. 2005582, Jan. 2021. 29

- [81] J. Mao, L. Zhou, X. Zhu, Y. Zhou, and S. Han, "Photonic memristor for future computing: A perspective," Advanced Optical Materials, vol. 7, no. 22, p. 1900766, 2022. 29, 32
- [82] C. Yang, B. Sun, G. Zhou, T. Guo, C. Ke, Y. Chen, J. Shao, Y. Zhao, and H. Wang, "Photoelectric Memristor-Based Machine Vision for Artificial Intelligence Applications," ACS Materials Lett, vol. 5, pp. 504–526, Jan. 2023. 29
- [83] M. E. Pereira, R. Martins, E. Fortunato, P. Barquinha, and A. Kiazadeh, "Recent progress in optoelectronic memristors for neuromorphic and in-memory computation," *Neuromorphic Computing and Engineering*, vol. 3, p. 022002, June 2023. 29, 38, 88, 280
- [84] T. Li, Y. Li, Y. Wang, Y. Liu, Y. Liu, Z. Wang, R. Miao, D. Han, Z. Hui, and W. Li, "Neuromorphic Photonics Based on Phase Change Materials," *Nanomaterials*, vol. 13, p. 1756, May 2023. 29
- [85] X. Shan, C. Zhao, X. Wang, Z. Wang, S. Fu, Y. Lin, T. Zeng, X. Zhao, H. Xu, X. Zhang, et al., "Plasmonic optoelectronic memristor enabling fully light-modulated synaptic plasticity for neuromorphic vision," Advanced Science, vol. 9, no. 6, p. 2104632, 2022. 29
- [86] P. Roy, S. Kunwar, D. Zhang, D. Chen, Z. Corey, B. X. Rutherford, H. Wang, J. L. MacManus-Driscoll, Q. Jia, and A. Chen, "Role of Defects and Power Dissipation on Ferroelectric Memristive Switching," Advanced Electronic Materials, vol. 8, p. 2101392, June 2022. 31, 33
- [87] E. Lim and R. Ismail, "Conduction Mechanism of Valence Change Resistive Switching Memory: A Survey," *Electronics*, vol. 4, pp. 586–613, Sept. 2015. 32, 82, 85
- [88] Y. Wang, J. Yang, Z. Wang, J. Chen, Q. Yang, Z. Lv, Y. Zhou, Y. Zhai, Z. Li, and S.-T. Han, "Near-infrared annihilation of conductive filaments in quasiplane

- mose2/bi2se3 nanosheets for mimicking heterosynaptic plasticity," *Small*, vol. 15, no. 7, p. 1805431, 2019. 32
- [89] P. Thakkar, J. Gosai, H. J. Gogoi, and A. Solanki, "From fundamentals to frontiers: a review of memristor mechanisms, modeling and emerging applications," *Journal of Materials Chemistry C*, vol. 12, no. 5, pp. 1583–1608, 2024. 33, 35, 84, 85, 89, 276
- [90] H. Tan, G. Liu, X. Zhu, H. Yang, B. Chen, X. Chen, J. Shang, W. D. Lu, Y. Wu, and R.-W. Li, "An optoelectronic resistive switching memory with integrated demodulating and arithmetic functions," *Advanced Materials*, vol. 27, no. 17, pp. 2797–2803, 2015. 33, 184, 185
- [91] Y.-F. Wang, Y.-C. Lin, I.-T. Wang, T.-P. Lin, and T.-H. Hou, "Characterization and Modeling of Nonfilamentary Ta/TaOx/TiO2/Ti Analog Synaptic Device," *Scientific Reports*, vol. 5, p. 10150, May 2015. 33
- [92] S. Gao, G. Liu, H. Yang, C. Hu, Q. Chen, G. Gong, W. Xue, X. Yi, J. Shang, and R.-W. Li, "An oxide schottky junction artificial optoelectronic synapse," ACS Nano, vol. 13, no. 2, pp. 2634–2642, 2019. 33, 35, 36, 185, 276, 287
- [93] T. You, N. Du, S. Slesazeck, T. Mikolajick, G. Li, D. Bürger, I. Skorupa, H. Stöcker, B. Abendroth, A. Beyer, K. Volz, O. G. Schmidt, and H. Schmidt, "Bipolar Electric-Field Enhanced Trapping and Detrapping of Mobile Donors in BiFeO 3 Memristors," ACS Applied Materials & Interfaces, vol. 6, pp. 19758–19765, Nov. 2014. 33
- [94] S. Li, B. Li, X. Feng, L. Chen, Y. Li, L. Huang, X. Fong, and K.-W. Ang, "Electron-beam-irradiated rhenium disulfide memristors with low variability for neuromorphic computing," npj 2D Materials and Applications, vol. 5, p. 1, Jan. 2021. 33
- [95] Y. Tian, L. Jiang, X. Zhang, G. Zhang, and Q. Zhu, "Trap-assisted transition between schottky emission and fowler-nordheim tunneling in the

- interfacial-memristor based on bi2s3 nano-networks," *AIP Advances*, vol. 8, no. 3, p. 035105, 2018. 33
- [96] Y. Matveyev, K. Egorov, A. Markeev, and A. Zenkevich, "Resistive switching and synaptic properties of fully atomic layer deposition grown TiN/HfO2/TiN devices," *Journal of Applied Physics*, vol. 117, Jan. 2015. 33
- [97] D. Li, B. Wu, X. Zhu, J. Wang, B. Ryu, L. Wei, and X. Liang, "MoS2 Memristors Exhibiting Variable Switching Characteristics toward Biorealistic Synaptic Emulation," 1, no. 12, p. 9240–9252, 2018. 33
- [98] Y. Qiao, T. Hirtz, F. Wu, G. Deng, X. Li, Y. Zhi, H. Tian, Y. Yang, and T.-L. Ren, "Fabricating Molybdenum Disulfide Memristors," ACS Applied Electronic Materials, vol. 2, pp. 346–370, Feb. 2020. 33
- [99] J. Yang, L. Hu, L. Shen, J. Wang, P. Cheng, H. Lu, F. Zhuge, and Z. Ye, "Optically driven intelligent computing with ZnO memristor," *Fundamental Research*, July 2022. 33, 34
- [100] S. Kvatinsky, E. G. Friedman, A. Kolodny, and U. C. Weiser, "TEAM: ThrEshold Adaptive Memristor Model," *IEEE Transactions on Circuits and Systems I: Regular Papers*, vol. 60, pp. 211–221, Jan. 2013. 34
- [101] I. Abraham, "An Advection-Diffusion Model for the Vacancy Migration Memristor," IEEE Access, vol. 4, pp. 7747–7757, 2016. 34
- [102] T. Chang, S.-H. Jo, K.-H. Kim, P. Sheridan, S. Gaba, and W. Lu, "Synaptic behaviors and modeling of a metal oxide memristive device," *Applied Physics A*, vol. 102, pp. 857–863, Mar. 2011. 34
- [103] C. Funck and S. Menzel, "Comprehensive model of electron conduction in oxide-based memristive devices," ACS Applied Electronic Materials, vol. 3, no. 9, pp. 3674–3692, 2021. 35, 185

- [104] T. Tomohiro Kanno, ""spin-memristor"." https://www.tdk.com/en/news\_center/press/20241002 01.html, 2024. 37
- [105] Alex Nugent, ""knowm inc."." https://knowm.com/, 2025. 37
- [106] I. Yoo, B. Kang, Y. Park, M. Lee, and Y. Park, "Interpretation of nanoscale conducting paths and their control in nickel oxide (nio) thin films," Applied Physics Letters, vol. 92, no. 20, 2008. 37
- [107] J. Coutinho, V. P. Markevich, and A. R. Peaker, "Characterisation of negative- U defects in semiconductors," Journal of Physics: Condensed Matter, vol. 32, no. 32, p. 323001, 2020. 41, 44, 45, 50
- [108] P. Bräunlich, P. Kelly, and J. P. Fillard, "Thermally stimulated luminescence and conductivity," in *Thermally Stimulated Relaxation in Solids* (P. Bräunlich, ed.), vol. 37, pp. 35–92, Springer Berlin Heidelberg, 1979. Series Title: Topics in Applied Physics. 43, 50, 52
- [109] C. H. Henry and D. V. Lang, "Nonradiative capture and recombination by multiphonon emission in GaAs and GaP," *Physical Review B*, vol. 15, pp. 989–1016, Jan. 1977. 47
- [110] P. W. Anderson, "Model for the electronic structure of amorphous semiconductors," Physical Review Letters, vol. 34, no. 15, pp. 953–955, 1975. 48
- [111] M. Levinson, "Charge-state-controlled structural relaxation of the EL 2 center in GaAs," *Physical Review B*, vol. 28, pp. 3660–3662, Sept. 1983. 48
- [112] R. Kiliulis, V. Rinkevičius, J. Storasta, and J. Vaitkus, "Influence of the EL2 → EL2\* transition on photoconductivity and thermally stimulated processes in semi-insulating GaAs," *Physica Status Solidi (a)*, vol. 127, pp. 415–422, Oct. 1991. 48, 50

- [113] D. J. Chadi and K. J. Chang, "Theory of the atomic and electronic structure of DX centers in GaAs and al x ga 1 x as alloys," *Physical Review Letters*, vol. 61, no. 7, pp. 873–876, 1988. 48
- [114] P. M. Mooney, "Electrical properties of DX centers in GaAs and AlGaAs," Radiation Effects and Defects in Solids, vol. 111-112, no. 1, pp. 281-298, 1989. 48, 50
- [115] Z. Rivera-Alvarez, L. Hernandez, M. Becerril, A. Picos-Vega, O. Zelaya-Angel, R. Ramiirez-Bon, and J. Vargas-Garciia, "Dx centers and persistent photoconductivity in cdte-in films," *Solid State Communications*, vol. 113, no. 11, pp. 621–625, 2000. 48
- [116] S. O. Kasap, ed., Photoconductivity and Photoconductive Materials. Wiley, 1 ed., 2022. 49, 68, 76, 77, 78, 79, 80, 232
- [117] D. Redfield and R. Bube, "Metastable Defects and Stretched Exponentials," MRS Proceedings, vol. 325, p. 335, 1993. 49
- [118] J.-P. Bouchaud, "Anomalous relaxation in complex systems: from stretched to compressed exponentials," May 2007. arXiv:0705.0989 [cond-mat]. 49
- [119] Z. W. Wu, W. Kob, W.-H. Wang, and L. Xu, "Stretched and compressed exponentials in the relaxation dynamics of a metallic glass-forming melt," *Nature Communications*, vol. 9, p. 5334, Dec. 2018. 49
- [120] K. Trachenko and A. Zaccone, "Slow stretched-exponential and fast compressed-exponential relaxation from local event dynamics," *Journal of Physics: Condensed Matter*, vol. 33, p. 315101, Aug. 2021. 49
- [121] P. K. Giri and Y. N. Mohapatra, "Nonexponentiality in photoinduced current transients in undoped semi-insulating gallium arsenide," *Journal of Applied Physics*, vol. 78, no. 1, pp. 262–268, 1995. 49, 75

- [122] J. Y. Lin, A. Dissanayake, G. Brown, and H. X. Jiang, "Relaxation of persistent photoconductivity in al 0.3 ga 0.7 as," *Physical Review B*, vol. 42, no. 9, pp. 5855–5858, 1990. 49, 50
- [123] V. Brinzari, "Mechanism of band gap persistent photoconductivity (PPC) in SnO 2 nanoscrystalline films: Nature of local states, simulation of PPC and comparison with experiment," Applied Surface Science, vol. 411, pp. 437–448, July 2017. 49
- [124] K. Shimakawa, Y. Yano, and Y. Katsuma, "Origin of the non-exponential photocurrent decay in amorphous semiconductors," *Philosophical Magazine B*, vol. 54, no. 4, pp. 285–299, 1986. 49, 70, 183
- [125] J. Nelson, "Continuous-time random-walk model of electron transport in nanocrystalline TiO 2 electrodes," *Physical Review B*, vol. 59, no. 23, pp. 15374–15380, 1999. 49, 71, 149, 181
- [126] O. Edholm and C. Blomberg, "Stretched exponentials and barrier distributions," *Chemical Physics*, vol. 252, pp. 221–225, Jan. 2000. 49
- [127] H. J. Queisser, "Nonexponential Relaxation of Conductance near Semiconductor Interfaces," Physical Review Letters, vol. 54, pp. 234–236, Jan. 1985. 49
- [128] K. Shimakawa, A. Kolobov, and S. Elliott, "Photoinduced effects and metastability in amorphous semiconductors and insulators," Advances in Physics, vol. 44, pp. 475–588, Dec. 1995. 50
- [129] P. Giri, "Metastablility of interstitial clusters in ion-damaged silicon studied by isothermal capacitance transient spectroscopy," *Defect and Diffusion Forum*, vol. 210-212, pp. 1–14, 2002. 50, 75
- [130] D. C. Look, Chapter 2 The Electrical and Photoelectronic Properties of Semi-Insulating GaAs, vol. 19. Elsevier, 1983. 51

- [131] B. Šantić, N. Radić, and U. Desnica, "Calculation of the glow curve shape—application to the thermally stimulated currents (tsc)," *Solid state communications*, vol. 79, no. 6, pp. 535–538, 1991. 52
- [132] A. Jonscher, "Frequency-dependence of conductivity in hopping systems," *Journal of Non-Crystalline Solids*, vol. 8-10, pp. 293–315, 1972. 53, 55
- [133] S. Elliott, "A.c. conduction in amorphous chalcogenide and pnictide semiconductors," *Advances in Physics*, vol. 36, no. 2, pp. 135–217, 1987. 53, 135
- [134] M. Pollak and G. Pike, "Ac conductivity of glasses," Physical Review Letters, vol. 28, no. 22, p. 1449, 1972. 54
- [135] G. E. Pike, "ac conductivity of scandium oxide and a new hopping model for conductivity," *Physical Review B*, vol. 6, no. 4, pp. 1572–1580, 1972. 55
- [136] M. Pollak and T. H. Geballe, "Low-frequency conductivity due to hopping processes in silicon," *Physical Review*, vol. 122, no. 6, pp. 1742–1753, 1961. 55
- [137] S. R. Elliott, "The mechanism for a.c. conduction in chalcogenide semiconductors: Electronic or atomic?," *Philosophical Magazine B*, vol. 40, no. 6, pp. 507–511, 1979. 55, 56
- [138] S. Elliott, "On the super-linear frequency dependent conductivity of amorphous semiconductors," *Solid State Communications*, vol. 28, no. 11, pp. 939–942, 1978.

  56
- [139] K. S. Gilroy and W. A. Phillips, "An asymmetric double-well potential model for structural relaxation processes in amorphous materials," *Philosophical Magazine B*, vol. 43, no. 5, pp. 735–746, 1981. 56, 135
- [140] Y. B. James Ross MacDonald, Impedance Spectroscopy Theory, Experiment, and Applications. Wiley, 2005. 57

- [141] G. G. Raju, Dielectrics in electric fields. CRC Press, second edition ed., 2017. 57
- [142] C.-T. Sah, "The equivalent circuit model in solid-state electronics—part i: The single energy level defect centers," *IEEE*, vol. 55, no. 5, pp. 654–671, 1967. 57, 60
- [143] C.-T. Sah, "The equivalent circuit model in solid-state electronics-part ii: The multiple energy level impurity centers," *IEEE*, 1967. 57
- [144] C.-T. Sah, "The equivalent circuit model in solid-state electronics-part iii: Conduction and displacement currents," *IEEE*, vol. 13, no. 12, pp. 1547–1575, 1970. 57, 176
- [145] D. Moia, "Equivalent-circuit modeling of electron-hole recombination in semiconductors and mixed ionic-electronic conductors," *Physical Review Applied*, vol. 23, no. 1, p. 014055, 2025. 58, 60, 176
- [146] E. Von Hauff, "Impedance spectroscopy for emerging photovoltaics," *The Journal of Physical Chemistry C*, vol. 123, no. 18, pp. 11329–11346, 2019. 58
- [147] O. Khaldi and F. Jomni, "Understanding the physical origin of negative capacitance (NC) in high-k oxides: Experimental and ab-initio approach," Chemical Physics Letters, vol. 781, p. 138964, 2021. 58
- [148] F. Ebadi, N. Taghavinia, R. Mohammadpour, A. Hagfeldt, and W. Tress, "Origin of apparent light-enhanced and negative capacitance in perovskite solar cells," *Nature Communications*, vol. 10, no. 1, p. 1574, 2019. 58
- [149] M. Ershov, H. Liu, L. Li, M. Buchanan, Z. Wasilewski, and A. Jonscher, "Negative capacitance effect in semiconductor devices," *IEEE Transactions on Electron* Devices, vol. 45, no. 10, pp. 2196–2206, 1998. 58
- [150] I. Mora-Seró, J. Bisquert, F. Fabregat-Santiago, G. Garcia-Belmonte, G. Zoppi,
  K. Durose, Y. Proskuryakov, I. Oja, A. Belaidi, T. Dittrich, R. Tena-Zaera, A. Katty,
  C. Lévy-Clément, V. Barrioz, and S. J. C. Irvine, "Implications of the negative

- capacitance observed at forward bias in nanocomposite and polycrystalline solar cells," *Nano Letters*, vol. 6, no. 4, pp. 640–650, 2006. 58
- [151] C. Gonzales, A. Guerrero, and J. Bisquert, "Transition from capacitive to inductive hysteresis: A neuron-style model to correlate I - V curves to impedances of metal halide perovskites," The Journal of Physical Chemistry C, vol. 126, no. 32, pp. 13560–13578, 2022. 58
- [152] M. Berruet, J. C. Pérez-Martínez, B. Romero, C. Gonzales, A. M. Al-Mayouf, A. Guerrero, and J. Bisquert, "Physical model for the current-voltage hysteresis and impedance of halide perovskite memristors," ACS Energy Letters, vol. 7, no. 3, pp. 1214–1222, 2022. 58
- [153] L. J. Bennett, A. J. Riquelme, J. A. Anta, N. E. Courtier, and G. Richardson, "Avoiding ionic interference in computing the ideality factor for perovskite solar cells and an analytical theory of their impedance-spectroscopy response," *Physical Review Applied*, vol. 19, no. 1, p. 014061, 2023. 58
- [154] B. D. Tellegen, "The gyrator, a new electric network element," *Philips Res. Rep*, vol. 3, no. 2, pp. 81–101, 1948. 59
- [155] R. H. Bube, Photoconductivity of Solids. John Wiley & Sons inc, 1960. 62, 65, 66,152, 153, 178, 181
- [156] J. Singh and K. Shimakawa, Advances in amorphous semiconductors. No. 5 in Advances in condensed matter science, Taylor & Francis, 1. publ ed., 2003. 64, 66, 70, 71
- [157] A. Rose, Concepts in photoconductivity and allied problems. Krieger, rev. ed., with corrections and new material ed., 1978. 64, 65, 66, 67, 70, 76
- [158] J. G. Simmons and G. W. Taylor, "Nonequilibrium steady-state statistics and associated effects for insulators and semiconductors containing an arbitrary

- distribution of traps," *Physical Review B*, vol. 4, no. 2, pp. 502–511, 1971. 65, 70
- [159] R. H. Bube, "Large-signal photoconductivity in semiconductors," *Solid-State Electronics*, vol. 27, no. 5, pp. 467–473, 1984. 65, 146
- [160] R. H. Bube, "A new mechanism for superlinear photoconductivity with relevance to amorphous silicon," *Journal of Applied Physics*, vol. 74, no. 8, pp. 5138–5143, 1993. 65, 146
- [161] C. Main, F. Dick, S. Reynolds, W. Gao, and R. Gibson, "Sublinear photoconductivity in n-type a-si:h analysis and computer modelling," *Journal of Non-Crystalline Solids*, vol. 198-200, 1996. 67, 69
- [162] S. K. Ram, S. Kumar, R. Vanderhaghen, B. Drevillon, and P. Rocca I Cabarrocas, "Recombination traffic in highly crystallized undoped microcrystalline si films studied by steady state photoconductivity," *Thin Solid Films*, vol. 511-512, pp. 556-561, 2006. 69
- [163] Y. Vygranenko, M. Fernandes, M. Vieira, G. Lavareda, C. Nunes De Carvalho, P. Brogueira, and A. Amaral, "Photoconductivity kinetics of indium sulfofluoride thin films," *The European Physical Journal Applied Physics*, vol. 89, no. 1, p. 10302, 2020. 69
- [164] F. Hooge and D. Polder, "Conditions for superlinear intrinsic photoconductivity," Journal of Physics and Chemistry of Solids, vol. 25, no. 9, pp. 977–984, 1964. 70
- [165] F. Cardon and R. H. Bube, "Theory of superlinear photoconductivity in CdS and related materials," *Journal of Applied Physics*, vol. 35, no. 11, pp. 3344–3351, 1964.
  70
- [166] R. H. Bube and D. Redfield, "Variation of photoconductivity with doping and optical degradation in hydrogenated amorphous silicon," *Journal of Applied Physics*, vol. 66, no. 7, pp. 3074–3081, 1989. 70, 146

- [167] S. Agarwal, Y. N. Mohapatra, and V. A. Singh, "Temperature-time duality and deep level spectroscopies," *Journal of Applied Physics*, vol. 77, no. 7, pp. 3155–3161, 1995.
  75
- [168] A. Rose, "Space-Charge-Limited Currents in Solids," Physical Review, vol. 97, pp. 1538–1544, Mar. 1955. 76, 77
- [169] P. Zhang, "Space-charge limited current in nanodiodes: Ballistic, collisional, and dynamical effects," Journal of Applied Physics, 2021. 77
- [170] P. Mark and W. Helfrich, "Space-Charge-Limited Currents in Organic Crystals,"

  Journal of Applied Physics, vol. 33, pp. 205–215, Jan. 1962. 77
- [171] M. A. Lampert, "Volume-controlled current injection in insulators," Reports on Progress in Physics, vol. 27, pp. 329–367, Jan. 1964. 77, 78
- [172] R. H. Bube, "Trap Density Determination by Space-Charge-Limited Currents," Journal of Applied Physics, vol. 33, pp. 1733–1737, May 1962. 78
- [173] D. K. Schroder, Semiconductor Material and Device Characterization. Wiley, 1 ed., Oct. 2005. 79, 80, 81
- [174] E. H. Rhoderick, "Metal-semiconductor contacts," *IEE Proceedings I (Solid-State and Electron Devices)*, vol. 129, no. 1, pp. 1–14, 1982. 79, 82
- [175] L. Assmann, J. Bernède, A. Drici, C. Amory, E. Halgand, and M. Morsli, "Study of the Mo thin films and Mo/CIGS interface properties," Applied Surface Science, vol. 246, pp. 159–166, June 2005. 80, 248
- [176] M. Oldham, W.G., "n-n Semiconductor heterojunctions," *Solid-State Electronics*, vol. 6, pp. 121–132, Mar. 1963. 81
- [177] Y.-C. Yeo, T.-J. King, and C. Hu, "Direct tunneling leakage current and scalability of alternative gate dielectrics," Applied Physics Letters, vol. 81, pp. 2091–2093, Sept. 2002. 82

- [178] J. G. Simmons, "Poole-Frenkel Effect and Schottky Effect in Metal-Insulator-Metal Systems," Physical Review, vol. 155, pp. 657–660, Mar. 1967. 82
- [179] N. F. Mott and E. A. Davis, Electronic processes in non-crystalline materials. International series of monographs on physics, Oxford: Clarendon Press, 2nd ed ed., 1979. 83
- [180] R. Tetzlaff, ed., Memristors and Memristive Systems. New York, NY: Springer New York, 2014. 85, 89, 276
- [181] D. Ielmini, Resistive Switching. Wiley-VCH, 2016. 85
- [182] C. Li, X. Zhang, P. Chen, K. Zhou, J. Yu, G. Wu, D. Xiang, H. Jiang, M. Wang, and Q. Liu, "Short-term synaptic plasticity in emerging devices for neuromorphic computing," iScience, vol. 26, p. 106315, Apr. 2023. 89
- [183] L. O. Chua, R. Tetzlaff, and A. Slavova, eds., Memristor Computing Systems. Cham: Springer International Publishing, 2022. 89
- [184] J. Kim, Y. V. Pershin, M. Yin, T. Datta, and M. Di Ventra, "An experimental proof that resistance-switching memory cells are not memristors," Advanced Electronic Materials, vol. 6, no. 7, p. 2000010, 2020. 91, 260
- [185] Y. V. Pershin, J. Kim, T. Datta, and M. D. Ventra, "An experimental demonstration of the memristor test," *Physica E: Low-dimensional Systems and Nanostructures*, vol. 142, p. 115290, 2022. 91, 263
- [186] D. M. Mattox, Handbook of physical vapor deposition (PVD) processing. Oxford, UK: William Andrew, 2nd ed ed., 2010. 92, 93, 211
- [187] J. Liu, Z. Wei, and W. Shangguan, "Defects engineering in photocatalytic water splitting materials," *ChemCatChem*, vol. 11, no. 24, pp. 6177–6189, 2019. 95
- [188] Q. Xu, L. Zhang, B. Cheng, J. Fan, and J. Yu, "S-scheme heterojunction photocatalyst," *Chem*, vol. 6, no. 7, pp. 1543–1559, 2020. 95

- [189] B. Kale, J.-O. Baeg, S. Lee, H. Chang, S.-J. Moon, and C. Lee, "Cdin2s4 nanotubes and "marigold" nanostructures: A visible-light photocatalyst," Advanced Functional Materials, vol. 16, no. 10, pp. 1349–1354, 2006. 95
- [190] M. A. Mahadadalkar, S. B. Kale, R. S. Kalubarme, A. P. Bhirud, J. D. Ambekar, S. W. Gosavi, M. V. Kulkarni, C.-J. Park, and B. B. Kale, "Architecture of the cdin2s4 /graphene nano-heterostructure for solar hydrogen production and anode for lithium ion battery," RSC Advances, vol. 6, no. 41, pp. 34724–34736, 2016. 95
- [191] D. Li, "Cdin2s4/g-c3n4 heterojunction photocatalysts: enhanced photocatalytic performance and charge transfer mechanism," *RSC Advances*, vol. 7, no. 1, pp. 231–237, 2017. 95
- [192] C. Ling, "Solvothermal synthesis of cdin 2 s 4 photocatalyst for selective photosynthesis of organic aromatic compounds under visible light," Scientific Reports, vol. 7, no. 1, pp. 27–27, 2017. 95
- [193] S. Chandrasekaran, C. Bowen, P. Zhang, Z. Li, Q. Yuan, X. Ren, and L. Deng, "Spinel photocatalysts for environmental remediation, hydrogen generation, CO 2 reduction and photoelectrochemical water splitting," *Journal of Materials Chemistry A*, vol. 6, no. 24, pp. 11078–11104, 2018. 95
- [194] Q. Zhang, J. Wang, X. Ye, Z. Hui, L. Ye, X. Wang, and S. Chen, "Self-assembly of CdS/cdin 2 s 4 heterostructure with enhanced photocascade synthesis of schiff base compounds in an aromatic alcohols and nitrobenzene system with visible light," ACS Applied Materials & Interfaces, vol. 11, no. 50, 2019. 95
- [195] X. Weiwei, "Ion sputtering—assisted double-side interfacial engineering for cdin 2 s 4 photoanode toward improved photoelectrochemical water splitting," Advanced Materials Interfaces, vol. 7, no. 6, p. 1901947, 2020. 95
- [196] Y. Chen, Q. Hu, M. Yu, X. Gong, S. Li, S. Wang, H. Yu, and Z. Li, "In situ construction of a direct z-scheme cdin 2 s 4 /TiO 2 heterojunction for improving

- photocatalytic properties," CrystEngComm, vol. 23, no. 29, pp. 5070–5077, 2021.
- [197] Y.-X. Tan, Z.-M. Chai, B.-H. Wang, S. Tian, X.-X. Deng, Z.-J. Bai, L. Chen, S. Shen, J.-K. Guo, M.-Q. Cai, C.-T. Au, and S.-F. Yin, "Boosted photocatalytic oxidation of toluene into benzaldehyde on cdin <sub>2</sub> s <sub>4</sub> -CdS: Synergetic effect of compact heterojunction and s-vacancy," ACS Catalysis, vol. 11, no. 5, pp. 2492–2503, 2021.
- [198] C. Yuan, X. Zou, F. He, Y. Dong, Y. Cui, H. Ge, and Y. Hou, "Constructing an s-scheme heterojunction between cdin 2 s 4 and an in 2 o 3 catalyst for enhanced photocatalytic activity," Advanced Energy and Sustainability Research, vol. 3, no. 8, p. 2200012, 2022. 95
- [199] C. Zhang, J. Qin, C. Yang, and Y. Hu, "Sulfur-vacancy-rich ZnS/cdin2s4 heterojunction for efficient photocatalytic selective oxidation of toluene to benzaldehyde," *Journal of Photochemistry and Photobiology A: Chemistry*, vol. 444, 2023. 95
- [200] N. Zhang, Z. Xing, Z. Li, and W. Zhou, "Sulfur vacancy engineering of metal sulfide photocatalysts for solar energy conversion," *Chem Catalysis*, vol. 3, no. 1, p. 100375, 2023. 95
- [201] Y. Wu, X. Deng, R. Cui, M. Song, X. Guo, X. Gong, J. He, and P. Chen, "Electronic configuration inversion in cdin2s4 for efficient photocatalytic hydrogen peroxide generation coupled with selective benzylamine oxidation," *Journal of Colloid and Interface Science*, vol. 656, pp. 528–537, 2024. 95
- [202] T. Lepetit, Influence of KF post deposition treatment on the polycrystalline Cu(In, Ga)Se2/CdS heterojunction formation for photovoltaic application. Ecole Polytechnique de l'Université de Nantes, 2015. 96
- [203] M. Mousavi-Kamazani, M. Salavati-Niasari, M. Goudarzi, and Z. Zarghami, "Hydrothermal synthesis of cdin2s4 nanostructures using new starting reagent for

- elevating solar cells efficiency," Journal of Molecular Liquids, vol. 242, pp. 653–661, 2017. 96
- [204] W. Fan, H. Yao, Y. Wang, J. Zhu, X. Lv, and S. Ban, "Synthesis of titanium-doped cdin2s4 thin film and its photoelectric properties for intermediate band solar cells," Optik, vol. 265, 2022. 96, 98
- [205] M. Ueno, S. Endo, and T. Irie, "Memory effects of cdin 2 s 4 single crystal," Japanese Journal of Applied Physics, vol. 13, no. 3, pp. 580-580, 1974. 96, 104, 105, 139
- [206] P. Kistaiah, K. Satyanarayanamurthy, and K. V. K. Rao, "Lattice thermal expansion of spinel cdln2s4," *Journal of Materials Science Letters*, 1982. 96
- [207] Y. Seminovski, P. Palacios, P. Wahnón, and R. Grau-Crespo, "Band gap control via tuning of inversion degree in cdin2s4 spinel," Applied Physics Letters, vol. 100, no. 10, p. 102112, 2012. 97, 98, 112, 159, 191
- [208] N. Joshi, "Detection of partial inverse spinel structure in cdin2s4 by fourier transform spectroscopy," Journal of Physics and Chemistry of Solids, vol. 41, no. 9, pp. 943–945, 1980. 97, 112
- [209] F. Meloni, G. Mula, and G. Pegna, "Structural stability in the spinel compound cdin2s4," *Il Nuovo Cimento D*, vol. 2, no. 6, pp. 1736–1741, 1983. 97
- [210] W. Czaja, "An apparent landau-type second order transition in the spinel cdin2s4," Physik der Kondensierten Materie, vol. 10, no. 4, pp. 299–316, 1970. 97, 112, 135
- [211] C. Haas, "Phase transitions in crystals with the spinel structure," Journal of Physics and Chemistry of Solids, vol. 26, no. 8, pp. 1225–1232, 1965. 97, 112
- [212] S. I. Radautsan, I. P. Molodyan, N. N. Syrbu, V. E. Tezlevan, and M. A. Shipitka, "Optical and photoelectrical properties of cdin2s4," *Physica Status Solidi* (b), vol. 49, no. 2, pp. K175–K179, 1972. 98

- [213] E. Grilli, M. Guzzi, A. Anedda, F. Raga, and A. Serpi, "Fundamental optical constants of cdin2s4," Solid State Communications, vol. 27, no. 2, pp. 105–111, 1978. 98
- [214] W. Czaja and L. Krausbauer, "Photoluminescence of cdin2s4 and mixed crystals with in2s3 as related to their structural properties," physica status solidi (b), vol. 33, no. 1, pp. 191–199, 1969. 98, 99, 102, 106, 113
- [215] H. Nakanishi, S. Endo, and T. Irie, "Optical properties of cdin2s4 single crystals," Le Journal de Physique Colloques, vol. 36, pp. C3-163-C3-168, 2024. 98
- [216] H. Nakanishi, S. Endo, and T. Irie, "Magnetoresistance of cdin2s4 single crystals," Il Nuovo Cimento D, vol. 2, no. 6, pp. 1886–1890, 1983. 98
- [217] E. Grilli, M. Guzzi, P. Cappelletti, and A. V. Moskalonov, "Photoluminescence of cdin2s4 single crystals recombination process and localized levels," *Physica Status Solidi* (a), vol. 59, no. 2, pp. 755–765, 1980. 98, 99, 106, 107, 112, 113, 117, 143, 147, 159, 175, 182, 214
- [218] A. N. Georgobiani, A. N. Gruzintsev, Z. P. Ilyukhina, V. E. Tezlevan, and I. M. Tiginyanu, "Photoconductivity and non-equilibrium carrier recombination in cdin2s4 single crystals," *Physica Status Solidi* (a), vol. 82, no. 1, pp. 207–212, 1984. 98, 100, 101, 106, 107, 113, 152
- [219] O. V. Kulikova, L. L. Kulyuk, S. I. Radautsan, S. A. Ratseev, E. E. Strumban, V. E. Tezlevan, and V. I. Tsitsanu, "Influence of defect generation processes in cdin2s4 single crystals on the photoluminescence and raman scattering spectra," Physica Status Solidi (a), vol. 107, no. 1, pp. 373–377, 1988, 98, 100, 106, 143
- [220] S. N. Mustafaeva, M. M. Asadov, and D. T. Guseinov, "X-ray electric properties of cdin2s4 monocrystal," *Inorganic Materials: Applied Research*, vol. 1, no. 4, pp. 293–296, 2010. 98, 102

- [221] S. Charbonneau, E. Fortin, and A. Anedda, "Saturation photoconductivity in cdin2s4," *Physical Review B*, vol. 31, no. 4, pp. 2326–2329, 1985. 98, 102, 106, 107, 175
- [222] S. Endo and T. Irie, "Transport properties of cdin2s4 single crystals," Journal of Physics and Chemistry of Solids, vol. 37, no. 2, pp. 201–209, 1976. 98, 102, 178, 179
- [223] R. Sawant, K. Rajpure, and C. Bhosale, "Determination of cdin2s4 semiconductor parameters by (photo)electrochemical technique," *Physica B: Condensed Matter*, vol. 393, no. 1, pp. 249–254, 2007. 98, 175
- [224] C. Guillot-Deudon, M. T. Caldes, A. Stoliaroff, L. Choubrac, M. Paris, C. Latouche, N. Barreau, A. Lafond, and S. Jobic, "Crystal chemistry, optical-electronic properties, and electronic structure of cd<sub>1-x</sub> in<sub>2+2 x/3</sub> s<sub>4</sub> compounds (0 < x < 1), potential buffer in CIGS-based thin-film solar cells," *Inorganic Chemistry*, vol. 57, no. 20, pp. 12624–12631, 2018. 98, 112, 137, 190
- [225] S. Guo, Y. Li, C. Xue, Y. Sun, C. Wu, G. Shao, and P. Zhang, "Controllable construction of hierarchically cdin2s4/cnfs/co4s3 nanofiber networks towards photocatalytic hydrogen evolution," *Chemical Engineering Journal*, vol. 419, p. 129213, 2021. 98, 179, 232
- [226] C. Li, Y. Zhao, X. Liu, P. Huo, Y. Yan, L. Wang, G. Liao, and C. Liu, "Interface engineering of co9s8/cdin2s4 ohmic junction for efficient photocatalytic h2 evolution under visible light," *Journal of Colloid and Interface Science*, vol. 600, pp. 794–803, 2021. 98, 179, 232
- [227] M. Springford, "The luminescence of some ternary chalcogenides and mixed binary systems of group III-VI compounds: The nature of luminescence centres in group III-VI compounds," Proceedings of the Physical Society, vol. 82, no. 6, pp. 1029–1037, 1963. 99

- [228] W. K. Unger, H. Meuth, J. C. Irwin, and H. Pink, "Photoluminescence and resonant raman scattering in cdin2s4 and znin2s4," *Physica Status Solidi* (a), vol. 46, no. 1, pp. 81–87, 1978. 99
- [229] H. Nakanishi, H. Miyashita, S. Endo, and T. Irie, "Photoluminescence and photoconduction in the system (cdin <sub>2</sub> s <sub>4</sub> ) <sub>1-x</sub> -(in <sub>2</sub> s <sub>3</sub> ) <sub>x</sub>," *Japanese Journal of Applied Physics*, vol. 20, no. 8, p. 1481, 2023. 100, 101, 107, 112, 113, 143, 152
- [230] R. Horiba, H. Nakanishi, S. Endo, and T. Irie, "Growth and properties of vacuum deposited cdin2s4 films," *Surface Science*, vol. 86, pp. 498–503, 1979. 101, 107, 112
- [231] I. A. Damaskin, S. L. Pyshkin, S. I. Radautsan, and V. E. Tazlavan, "Multi-quantum photoconductivity in cdln2s4," *Opto-electronics*, vol. 5, no. 5, pp. 405–410, 1973. 101
- [232] A. Anedda, L. Garbato, F. Raga, and A. Serpi, "Photoconductivity and trap distribution in cdin2s4," *Physica Status Solidi* (a), vol. 50, no. 2, pp. 643–650, 1978. 101, 102, 106, 107, 113, 143, 145, 152
- [233] T. Takizawa, H. Takeuchi, and K. Kanbara, "Time-dependent photoconductivity in cdin 2 s 4," Japanese Journal of Applied Physics, vol. 27, no. 2, p. L234, 2023. 101, 175
- [234] A. Serpi, M. Tapiero, and J. P. Zielinger, "Investigation of photoelectronic processes in cdin2s4 by photoinduced current transient spectroscopy," *physica status solidi* (a), vol. 93, no. 1, pp. 241–249, 1986. 102, 106
- [235] Y. Seki, S. Endo, and T. Irie, "Science university of tokyo negative resistance in cdin2s4 single crystals," physica status solidi (a), vol. 71, no. 2, pp. 365–370, 1982. 104, 139
- [236] J. Mohamed, C. Sanjeeviraja, and L. Amalraj, "Influence of substrate temperature on physical properties of (111) oriented cdin <sub>2</sub> s <sub>4</sub> thin films by nebulized spray pyrolysis technique," *Journal of Asian Ceramic Societies*, vol. 4, no. 2, pp. 191–200, 2016. 112

- [237] H. Neumann, W. Kissinger, F. Lévy, H. Sobotta, and V. Riede, "Electrical and infrared optical properties of cdin2s4 single crystals grown by chemical transport," Crystal Research and Technology, vol. 24, no. 11, pp. 1165–1169, 1989. 113, 178, 179
- [238] R. H. Bube, G. A. Dussel, C. Ho, and L. D. Miller, "Determination of electron trapping parameters," *Journal of Applied Physics*, vol. 37, no. 1, pp. 21–31, 1966. 129, 145
- [239] S. N. Mustafaeva, M. M. Asadov, and D. T. Guseinov, "Frequency-dependent dielectric properties and electrical conductivity of cdin2s4 single crystals," *Inorganic Materials*, vol. 47, no. 8, pp. 844–846, 2011. 137
- [240] H. Brandstätter, I. Hanzu, and M. Wilkening, "Myth and reality about the origin of inductive ps in impedance spectra of lithium-ion electrodes a critical experimental approach," *Electrochimica Acta*, vol. 207, pp. 218–223, 2016. 138
- [241] H. B. DeVore, "Spectral distribution of photoconductivity," *Physical Review*, vol. 102, no. 1, pp. 86–91, 1956. 152
- [242] K. Sato, Y. Yokoyama, and T. Tsushima, "Photoconductivity and photoluminescence spectra of cdin2s4:cr," *Journal of the Physical Society of Japan*, vol. 42, no. 2, pp. 559–563, 1977. 152
- [243] N. Barreau. Private conversations, 2024. 179, 195, 211, 221, 223, 224, 232, 248
- [244] R. Street, G. Davies, and A. Yoffe, "The square law dependence with frequency of the electrical conductivity of as2se3," *Journal of Non-Crystalline Solids*, vol. 5, no. 3, pp. 276–278, 1971. 180
- [245] M. Sayer and A. Mansingh, "Ohmic contacts and dielectric relaxation in transition metal phosphate glasses," *Journal of Non-Crystalline Solids*, vol. 31, no. 3, pp. 385–393, 1979. 180

- [246] T. R. Anantharaman and C. Suryanarayana, "Review: A decade of quenching from the melt," *Journal of Materials Science*, vol. 6, no. 8, pp. 1111–1135, 1971. 183
- [247] P. Dutta, "Bulk growth of crystals of iii–v compound semiconductors," *Elsevier*, 2011. 190
- [248] A. Jaber, S. Alamri, M. Aida, M. Benghanem, and A. Abdelaziz, "Influence of substrate temperature on thermally evaporated CdS thin films properties," *Journal* of Alloys and Compounds, vol. 529, pp. 63–68, July 2012. Publisher: Elsevier BV. 196
- [249] A. K. Varshneya and J. C. Mauro, "Thermal conductivity and acoustic properties of glass," *Elsevier*, pp. 283–291, 2019. 197
- [250] M. Rubin, "Optical properties of soda lime silica glasses," *Solar Energy Materials*, vol. 12, pp. 275–288, Sept. 1985. Publisher: Elsevier BV. 198
- [251] A. Bernasconi, M. Dapiaggi, C. Milanese, M. Alloni, and A. Pavese, "Structure of soda-lime-aluminosilicate glasses as revealed by in-situ synchrotron powder diffraction experiments," *Journal of Non-Crystalline Solids*, vol. 568, p. 120932, Sept. 2021. Publisher: Elsevier BV. 199
- [252] J. H. Seo, "Electrochemical Analysis of Sputtered Molybdenum Thin Films on Glass Substrates in Various Acid Solutions," *Journal of the Korean Physical Society*, vol. 50, p. 1193, Apr. 2007. 200
- [253] G. F. Harrington and J. Santiso, "Back-to-Basics tutorial: X-ray diffraction of thin films," *Journal of Electroceramics*, vol. 47, pp. 141–163, Dec. 2021. 200
- [254] O. Sakata and M. Nakamura, "Grazing Incidence X-Ray Diffraction," Springer Series in Surface Sciences, pp. 165–190, 2013. ISSN: 0931-5195. 203
- [255] M. Andrzejewski, "Badanie wpływu stechiometrii warstw  $CdIn_2S_4$  na mechanizmy przełączania w strukturach memrystorowych  $Al/ZnO/CdIn_2S_4/Mo$ ," master's

- thesis, Faculty of Physics, Warsaw University of Technology, Warsaw, Poland, July 2025. 230, 236, 249, 280
- [256] G. Szczepanik, "Badanie wpływu oświetlenia na pętlę histerezy i efekty pamięciowe w strukturach memrystorowych opartych na półprzewodniku CdIn<sub>2</sub>S<sub>4</sub>," master's thesis, Faculty of Physics, Warsaw University of Technology, Warsaw, Poland, July 2025. 232, 254, 280
- [257] W. M. Haynes, CRC handbook of chemistry and physics. CRC press, 2016. 232
- [258] A. J. Chiquito, C. A. Amorim, O. M. Berengue, L. S. Araujo, E. P. Bernardo, and E. R. Leite, "Back-to-back Schottky diodes: the generalization of the diode theory in analysis and extraction of electrical parameters of nanodevices," *Journal of Physics:* Condensed Matter, vol. 24, p. 225303, June 2012. 232
- [259] J. Osvald, "Back-to-back connected asymmetric Schottky diodes with series resistance as a single diode," physica status solidi (a), vol. 212, pp. 2754–2758, Dec. 2015. 232
- [260] M. Maciaszek and P. Zabierowski, "Quantitative analysis of the persistent photoconductivity effect in Cu(In,Ga)Se2," Journal of Applied Physics, vol. 123, p. 161404, Apr. 2018. 241
- [261] K. Macielak, M. Maciaszek, M. Igalson, P. Zabierowski, and N. Barreau, "Persistent Photoconductivity in Polycrystalline Cu(In,Ga)Se<sub>2</sub> Thin Films: Experiment Versus Theoretical Predictions," *IEEE Journal of Photovoltaics*, vol. 5, pp. 1206–1211, July 2015. 241, 287
- [262] L. C. Kimerling, "Influence of deep traps on the measurement of free-carrier distributions in semiconductors by junction capacitance techniques," Journal of Applied Physics, vol. 45, pp. 1839–1845, Apr. 1974. 244, 287

- [263] K. Decock, P. Zabierowski, and M. Burgelman, "Modeling metastabilities in chalcopyrite-based thin film solar cells," *Journal of Applied Physics*, vol. 111, p. 043703, Feb. 2012. 244, 287
- [264] J. Lindahl, J. Keller, O. Donzel-Gargand, P. Szaniawski, M. Edoff, and T. Törndahl, "Deposition temperature induced conduction band changes in zinc tin oxide buffer layers for Cu(In,Ga)Se2 solar cells," Solar Energy Materials and Solar Cells, vol. 144, pp. 684–690, Jan. 2016. 247
- [265] V. V. Kutwade, K. P. Gattu, M. E. Sonawane, D. A. Tonpe, M. K. Mishra, and R. Sharma, "Contribution in PCE enhancement: numerical designing and optimization of SnS thin film solar cell," *Journal of Nanoparticle Research*, vol. 23, p. 146, July 2021. 247
- [266] Y. Sun, H. Wang, and D. Xie, "Recent Advance in Synaptic Plasticity Modulation Techniques for Neuromorphic Applications," Nano-Micro Letters, vol. 16, p. 211, Dec. 2024. 280
- [267] H. Yin, A. Kumar, J. M. LeBeau, and R. Jaramillo, "Defect-Level Switching for Highly Nonlinear and Hysteretic Electronic Devices," *Physical Review Applied*, vol. 15, p. 014014, Jan. 2021. 287
- [268] J. Dong and R. Jaramillo, "Modeling defect-level switching for nonlinear and hysteretic electronic devices," *Journal of Applied Physics*, vol. 135, p. 224501, June 2024. 287
- [269] J. G. Simmons, "New conduction and reversible memory phenomena in thin insulating films," Proceedings of the Royal Society of London. Series A. Mathematical and Physical Sciences, vol. 301, pp. 77–102, Oct. 1967. 287
- [270] multple authors, "Weird loopy transistors causing strange (loopy) voltage/current diagrams." https://ibm-1401.info/WeirdParts.html, 2007. 287

- [271] D. Biolek, V. Biolkova, Z. Kolka, and Z. Biolek, "Passive Fully Floating Emulator of Memristive Device for Laboratory Experiments," *Advances in Electrical and Computer Engineering*, 2015. 288
- [272] J. Kalomiros, S. G. Stavrinides, and F. Corinto, "A two-transistor non-ideal memristor emulator," in 2016 5th International Conference on Modern Circuits and Systems Technologies (MOCAST), (Thessaloniki, Greece), pp. 1–4, IEEE, May 2016. 288

## Author's disseminations

### **Publications**

Jakub Zdziebłowski, Nicolas Barreau, and Paweł Zabierowski. "Interface Barrier-Modulated Neuromorphic Behavior in Mo/CdIn2S4/ZnO-Al Structures Based on Metastable Defects." ACS Applied Electronic Materials 2025.

https://doi.org/10.1021/acsaelm.5c00800

Jakub Zdziebłowski, Marek Pawłowski, Cezariusz Jastrzębski, Nicolas Barreau, and Paweł Zabierowski. "Influence of Post Deposition Treatment on Optoelectronic Properties of  $CdIn_2S_4$ " Preprint available at SSRN 5272894.

https://papers.ssrn.com/sol3/Delivery.cfm?abstractid=5272894

### Oral presentations

Jakub Zdziebłowski, Nicolas Barreau, and Paweł Zabierowski. "Switching phenomena in CdIn<sub>2</sub>S<sub>4</sub> related to defects induced by spinel inversion" *EMRS Fall Meeting 2024*, Warsaw, Poland, 2024.

https://www.european-mrs.com/meetings/2024-fall/symposia-program

### **AUTHOR'S DISSEMINATIONS**

### Poster presentations

Jakub Zdziebłowski, Nicolas Barreau, and Paweł Zabierowski. "Switching phenomena in CdIn<sub>2</sub>S<sub>4</sub>-based neuromorphic structures" *EuroSOI-ULIS 2024*, Athens, Greece, 2024. https://eurosoi-ulis2024.eventsadmin.com/i/Program

Jakub Zdziebłowski, Nicolas Barreau, and Paweł Zabierowski. "CdIn<sub>2</sub>S<sub>4</sub>-Based Memory Devices with Neuromorphic Capabilities" *MRS Fall Meeting 2024*, Boston, Massachusetts, 2024.

https://www.mrs.org/meetings-events/annual-meetings/archive/meeting/presentations/view/2024-fall-meeting/2024-fall-meeting-4149312

### Contributions

Paweł Zabierowski, Jakub Zdziebłowski, and Nicolas Barreau. "Defect engineering in CdIn<sub>2</sub>S<sub>4</sub> spinel for photocatalytic applications" 29th PhotoIUPAC, Valencia, Spain, 2024.

Mateusz Andrzejewski, Gabriela Szczepanik, Jakub Zdziebłowski, Nicolas Barreau, and Paweł Zabierowski. "Metastable Defects Driving Neuromorphic Behaviour in CdIn<sub>2</sub>S<sub>4</sub> Memristive Devices" *EuroSOI-ULIS 2025*, Warsaw, Poland, 2025.

Gabriela Szczepanik, Mateusz Andrzejewski, Jakub Zdziebłowski, Nicolas Barreau, and Paweł Zabierowski. "Switching mechanism based on metastable defects towards all optically controlled memristive devices" *EuroSOI-ULIS 2025*, Warsaw, Poland, 2025.

## Acknowledgements

I would like to express my sincere gratitude to my supervisor, Paweł Zabierowski, for your guidance, help, availability at different times of the day and night, and the countless hours spent on the discussion about the experiments' results and the anfractuosity of the spinel. Thank you for disposing your time to do all this.

To Marek Maciaszek, thank you for your unmatched insight into the metastable defects. Specifically, for the invaluable help in elucidating the metastability phenomena in  $CdIn_2S_4$ , and in constructing the configuration-coordination diagram of the  $V_S-Cd_{In}$  metastable defect complex.

I would like to also thank Marek Pawłowski and Cezariusz Jastrzębski. Your participation in our discussions, your support and experimental expertise is something we did not forget.

To Nicolas Barreau. I am still in awe of how much time you have committed to my research, for which I am incredibly grateful. Your participation was essential in achieving the results presented in this work. I look forward to continued productive collaboration with our increasingly younger team.

Special thanks to Gabi and Mati for joining the team, your help, your valuable data, and the differential diagnosis, we conducted together.

To Fabien, Léo, Thamer, and Eugène. Thank you for your invaluable help and companionship during my stay in Nantes. Without you, my time spent in Nantes would me way more miserable, and the chapter six of this work would certainly not come into existence in the present form.

To my dear colleagues from near and far corners of the academy: Aleksander, Ania, Przemek, Aniela, Maciek, Eryk, Zuza, Julianna, Klaudia, et al. Thanks for keeping me sane during my struggles with the research and teaching life, and for visiting me sometimes while I was locked up in the dark lab room for two years.

To my stellar friends: Basia and Grzegorz, Wiktoria and Bartosz, Paulina and Jakub, Zu and Wojtek, Michał, Kamil. Thank you for understanding the hardships of PhD student's life and sincerely supporting me throughout this long trek.

I would like to thank my dear parents and sister for always being close when I needed you. Thank you, Grandfather, for your support, hospitality, advice regarding the scientific life, and your wisdom.

I express my gratitude and respect to You, dear reader, and I hope reading this somewhat lengthy dissertation was enlightening, engaging, or inspiring for you.

I won't thank myself, it took too long to solve the spinel puzzle because of me. You should have read those papers you kept on your desktop for half a year.

# List of Symbols

A	surface area (general)	$[{ m cm}^2]$
$\alpha$	optical absorption coefficient	$[1/\mathrm{cm}]$
a	lattice constant	$[ m \AA]$
$\beta$	KWW function streching exponent factor	
c	speed of light	$[\mathrm{m/s}]$
$c_n, c_p$	${\rm electron/hole\ capture\ coefficient}$	$[{ m cm^3/s}]$
C	electrical capacitance	[F]
$\gamma$	index of the power (Lux-Ampere)	
d	layer thickness (general)	[nm]
e	elementary charge	[C]
$e_n, e_p$	electron/hole emission coefficient	$[{ m cm^3/s}]$
$\epsilon, E_{TR}$	transition energy for metastable level	[eV]
$arepsilon_0$	vacuum permittivity	$[\mathrm{F/m}]$
$\varepsilon$	relative dielectric permittivity	
$\eta$	diode ideality factor	
heta	XRD diffraction angle	[°]
$\vartheta$	thermally generated carriers	$[1/\mathrm{cm^3 s}]$
$E_A$	activation energy (general)	[eV]
$\Delta E_{}$	energy barrier related to lattice relaxation	[eV]
$E_C, E_V$	conduction band, valence band	[eV]
$E_{Dn}, E_{Dp}$	${\rm demarcation\ level\ for\ electrons/holes}$	[eV]

## LIST OF SYMBOLS

$E_F$	Fermi level	[eV]
$E_{Fn}, E_{Fp}$	quiasi-Fermi level for electrons/holes	[eV]
$E_g, E_{dir}, E_{indir}$	bandgap (general), direct/indirect bandgap	[eV]
$E_m$	barrier height (hopping model)	[eV]
$E_{ph}$	photon energy	[eV]
$E_t$	trap energy level	[eV]
$E_R$	lowering of the bound state energy in MPE	[eV]
F	electric field	[V/cm]
f	photogeneration	$[1/{ m cm^3 s}]$
f	occupation function	
$\Phi$	photon flux	$[\mathrm{W/m^2}]$
arphi	magnetic flux	[Wb]
g	degeneracy factor	
G	electrical conductance	[S]
$\chi$	electron affinity	[eV]
h	Planck constant	[Js]
$\hbar$	reduced Planck (Dirac) constant	[Js]
I	electric current	[A]
$I_S$	saturation current	[A]
$I_0$	quiescent current	[A]
$j,\ j_n,\ j_p$	electric current density,	$[\mathrm{mA/cm^2}]$
	electron/hole current density	
ι	TATS window parameter	
k	Boltzmann constant	$[{ m eV/K}]$
l	index of the power (SCLC)	
L	electrical inductance	[H]
$\lambda$	wavelength	[nm]
M	memristance	$[\Omega]$
$m_e$	electron mass	[kg]

## LIST OF SYMBOLS

$\mu, \mu_n, \mu_p$	mobility, free electron/hole mobility	$[{ m cm^2/Vs}]$
$\nu$	attempt to escape frequency (general)	[1/s]
$ u_{phn}$	phonon frequency	[1/s]
$N_C, N_V$	conduction/valence band density of states	$[1/\mathrm{cm}^3]$
$N_t$	density of trapping states	$[1/\mathrm{cm}^3]$
$N_D$	density of donor impurities	$[1/\mathrm{cm}^3]$
$N_+,\ N$	density of metastable defects	$[1/\mathrm{cm}^3]$
	in positive/negative charge state	
$N_{V-E}$	total density metastable ( $V_S$ - $Cd_{In}$ complexes	$[1/\mathrm{cm}^3]$
n,p	total free electron/hole concentration	$[1/\mathrm{cm}^3]$
$n_0, p_0$	$free\ electron/hole\ concentration\ (thermally\ excited)$	$[1/\mathrm{cm}^3]$
$\Delta n,\Delta p$	$photogenerated\ electron/hole\ concentration$	$[1/\mathrm{cm}^3]$
$n_t, p_t$	${\it electron/hole\ occupied\ traps\ concentration}$	$[1/\mathrm{cm}^3]$
$n_r, p_r$	${\rm electron/hole\ occupied}$	$[1/\mathrm{cm}^3]$
	recombination centers concentration	
ξ	unimportant scale parameter	[]
Q	configurational coordinate	[]
q	electric charge	[C]
R	electrical resistance	$[\Omega]$
ho	electrical resistivity	$[\Omega \mathrm{cm}]$
r	heating rate	[K/min.]
S	Huang-Rhys factor	
s	index of the power (impedance spectroscopy)	
$\sigma$	electrical conductivity (general)	$[\mathrm{S/cm}]$
$\sigma_0,\sigma_{light}$	$conductivity\ when\ relaxed/illuminated$	$[\mathrm{S/cm}]$
$\sigma_{AC}$	AC electrical conductivity	$[\mathrm{S/cm}]$
$\Delta \sigma$	photoinduced electrical conductivity	$[\mathrm{S/cm}]$
$\varsigma,\ \varsigma_n,\ \varsigma_p$	capture cross section (general),	$[\mathrm{cm}^2]$
	${\it electron/hole\ capture\ cross\ section}$	

## LIST OF SYMBOLS

$\mathfrak{T},\mathfrak{R}$	transmission/reflection coefficient	
$T^{'}$	absolute temperature	[K]
$T^*$	band-tails characteristic temperature	[K]
$T_C, T_V$	CB, VB sub-bandgap states characteristic temperature	[K]
$T_{eff}$	effective temperature in MPE model	[K]
$T_m$	TSC peak temperature	[K]
t	time	[s]
au	time constant (general)	[s]
$ au_0$	transient (response) time constant	[s]
$ au_n, au_p$	free electron/hole lifetime	[s]
$ ilde{ au}$	relaxation time distribution	[s]
Υ	dielectric susceptibility	$[\mathrm{C/m^2}]$
U	voltage (general)	[V]
$U_{bi}$	built-in voltage	[V]
$U_{sw}, U_{tr}$	switching voltage, SCLC crossover voltage	[V]
u	voltage sweep rate	[V/s]
$v_n, v_p$	electron/hole thermal velocity	$[\mathrm{cm/s}]$
$v_d^n, v_d^p$	electron/hole drift velocity	$[\mathrm{cm/s}]$
$\Psi_B$	barrier height (general)	[eV]
$\Psi_T$	barrier height in tunnelling transport mechanisms	[eV]
$\omega$	angular frequency	[1/s]
w	synaptic weight	[%]
$W_M,W_S$	metal/semiconductor work function	[eV]
X	electrical reactance	$[\Omega]$
X	spinel inversion degree	
y	state variable	[]
$\mathcal{Y}_M$	memristance state function	[]
z	distance (general)	[nm]
Z	electrical impedance	$[\Omega]$

# List of Figures

1.0.1	progression of neuromorphic computing systems	7
1.0.2	levels of complexity of the biological and neuromorphic system	9
2.1.1	memristor symbol	13
2.1.2	four electrical circuit elements	14
2.1.3	pinched hsteresis loops	17
2.2.1	typical synaptic plasticity observed in biology	22
2.2.2	biological neurons	24
2.3.1	crossbar SNN with memristor synapses	28
2.3.2	idea of neuromorphic vision	29
2.4.1	types of resistive switching mechanisms	31
2.4.2	schematic operation mechanism of the device presented by Gao et al	35
2.4.3	neuromorphic behaviour of the device presented by Gao et al	36
2.5.1	roadmap for manufacturing challenges	37
3.1.1	exemplary schematic CCD diagram vs electronic energy levels	43
3.1.2	CCD diagram of the Si DX center in $\mathrm{Al}_x\mathrm{Ga}_{1-x}\mathrm{As}$	44
3.1.3	illustrations of aspects of metastable defects	45
3.2.1	gyrator circuit	61
3.2.2	setup for $\Delta \sigma$ spectra measurement	74
3.2.3	idea of $\Delta\sigma$ spectra measurement	74
3.2.4	isotype heterojunction schematic	81
3.2.5	transport mechanisms in the MIM structures	84
3.3.1	neuromorphic behaviour experimentation	87

3.3.2	schematic of $R(q)$ in the memristor
3.3.3	schematic of the memristor test circuit
3.4.1	thermal evaporation method
4.2.1	visualization of the $CdIn_2S_4$ crystal structure
4.2.2	direct and indirect bandgap as a function of inversion degree 97
4.2.3	PL comparison made by Nakanishi et al
4.2.4	defect formation energy of complex defects
4.2.5	PL comparison made by Nakanishi et al
4.3.1	various band diagrams from the literature
4.3.2	band diagram created from existing literature on $CdIn_2S_4$ 108
5.1.1	samples used in primary $CdIn_2S_4$ investigation
5.2.1	C24 photoluminescence spectra
5.2.2	C48 photoluminescence spectra
5.2.3	PL peaks ratio
5.2.4	effects of changing the chopper frequency on the PL spectrum 120
5.3.1	$\sigma_{DC}(T)$ measurement for C24/C48 samples
5.3.2	$\sigma_{DC}$ Arrhenius plot for C24 and C48 samples
5.3.3	calculated Fermi Level position for C24 samples
5.3.4	C24 IV characteristics
5.3.5	C24 TSC – summary
5.3.6	C24-AS, C24-R TSC measurements
5.3.7	C24-R TSC peaks analysis
5.3.8	$\sigma(\omega)$ conductivity for C24
5.3.9	$\sigma_{AC}$ conductivity for C24 with various illumination
5.3.10	Nyquist plots for C24 at low light
5.4.1	C24-R kinetics at various light intensities at 300K
5.4.2	TATS analysis for various light intensity at 300K for C24-R sample 140
5.4.3	photoconductivity in function of photogeneration

5.4.4	sub-bandgap states schematic diagram	144
5.4.5	$\Delta\sigma(f) \ N_{tot} \ {\rm profiles} \ \ldots \ldots \ldots \ldots \ldots$	145
5.4.6	slope of the Lux-Ampere characteristics vs temperature	148
5.4.7	C24-R dark photoconductivity spectra	151
5.4.8	photoconductivity in function of wavelength for C24 samples	153
5.4.9	Arrhenius plot for $\Delta \sigma$ for C24 samples	155
5.4.10	various pre-illumination Arrhenius plots for $\Delta \sigma$	156
5.4.11	temperature-bandgap dependence for C24 samples	158
5.5.1	summary of the PPC phenomenon in the C24 samples	160
5.5.2	CCD diagram proposition for the $V$ – $E$ complex	162
5.5.3	saturation of metastable photosensitivity in sample C24-R	166
5.5.4	Arrhenius plot for $\Delta \sigma$ at 2eV	166
5.5.5	Arrhenius plot for $\Delta \sigma$ at 2eV	168
5.6.1	recombination diagram for C24 samples	173
5.6.2	the final $CdIn_2S_4modelbanddiagram$	174
5.6.3	quantum gyrator circuit	177
5.7.1	$CdIn_2S_4 mobility$ in the literature $\ \ \ldots \ \ \ldots \ \ \ldots \ \ \ldots$	179
5.8.1	two propositions of $CdIn_2S_4$ -based devices	184
6.2.1	photo of deposited thin films	195
6.3.1	$In/Cd\ ratio\ vs\ deposition\ temperature  .\ .\ .\ .\ .\ .$	197
6.3.2	XRD of the 231213 and 240105 samples	199
6.3.3	XRD of the 240311A samples	200
6.3.4	XRD of the 231213 and 240208-hot	201
6.3.5	231213, 240104 and 240105 PL spectra	204
6.3.6	1.66eV PL peak ratio for the 240104 and 240105 series	205
6.3.7	SLG vs Mo samples PL spectra comparison	206
6.3.8	mainline series PL spectra	208
6.3.9	1.45eV PL peak ratio for the mainline series	208
6.3.10	1.66eV PL peak ratio for the mainaline series	209

6.3.11	PL analysis of the quenched C24 samples
6.3.12	240312 PL spectra
7.1.1	devices' design
7.1.2	photo of the devices
7.1.3	band diagram of the symmetric AZO structures
7.1.4	$CdIn_2S_4 \Delta \sigma$ vs ZnO transmission window
7.1.5	IV characteristics of asymmetric AZO devices
7.2.1	basic principle of operation of the devices
7.2.2	example cases of the device operation
7.2.3	sweep frequency dependence in 240208-medium sample
7.2.4	transient response of the 240208-medium sample
7.2.5	IV characteristics of 240208-medium in function of temperature 231
7.2.6	IV characteristics of 240208-medium in function of illumination 231
7.2.7	schematic illustration of the band bending
7.2.8	phenomenological schematic illustrating the switching mechanism 233
7.2.9	IV trace characteristic regionss
7.2.10	principle of operation of the switching mechanism
7.2.11	principle of operation of the light-controlled switching
7.2.12	hysteresis in function of the growth parameters
7.2.13	difference of $U_{sw}$ in function of stoichiometry
7.2.14	Arrhenius plots of junction barriers
7.2.15	IV characteristics of 240208-medium after PDT
7.2.16	IV characteristics of samples with 800nm C24 layer
7.2.17	240312-ITO double process kinetics
7.2.18	modified CCD diagram proposition for the $V$ – $E$ complex
7.4.1	modification of the memristor test
7.4.2	initial memristor test
7.4.3	full memristor test

8.1.1	potentiation measurement scheme	266
8.1.2	amplitude comparison for the electrical potentiation potentiation $\dots$ .	267
8.1.3	synaptic potentiation	268
8.1.4	240208-medium frequency-dependent potentiation	269
8.1.5	240312-Mo potentiation and depression	270
8.1.6	binary state retention	271
8.1.7	PPF measurement scheme	272
8.1.8	electrical PPF	273
8.2.1	optical stimulation and reset processes	275
8.2.2	optical potentiation for chosen set of samples	276
8.2.3	optical potentiation	277
8.2.4	optical PPF measurement scheme	278
8.2.5	optical PPF	279

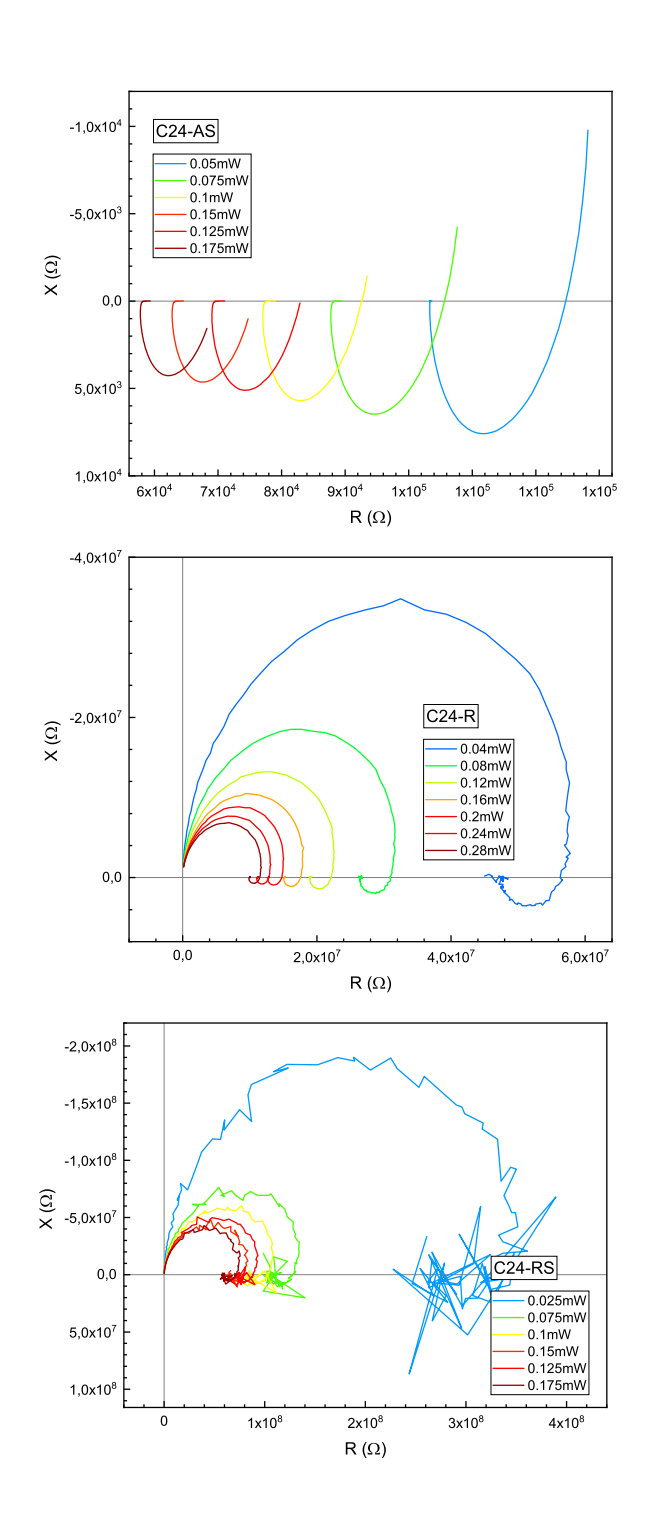
# List of Tables

5.2.1 fitted PL peak values
5.3.1 calculated conductivity parameters for C24 and C48 samples 128
5.3.2 conductivity values calculated from IV for C24 samples
5.4.1 Lux-Ampere slope analysis for C24 samples
5.5.1 MPE model fit parameters for C24 series
6.3.1 calculated lattice constants from XRD
7.1.1 resistance values for symmetric AZO devices

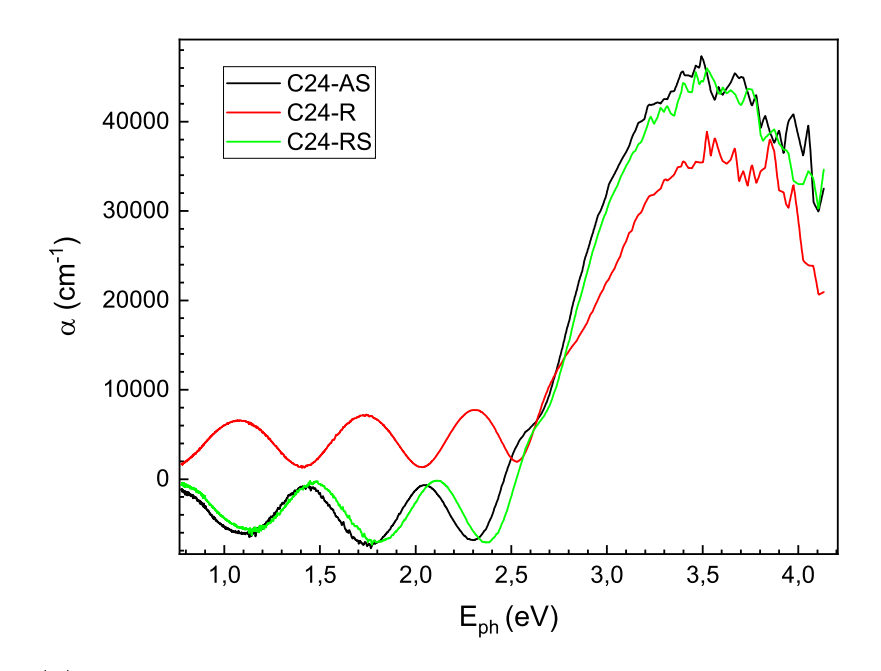
# List of Appendices

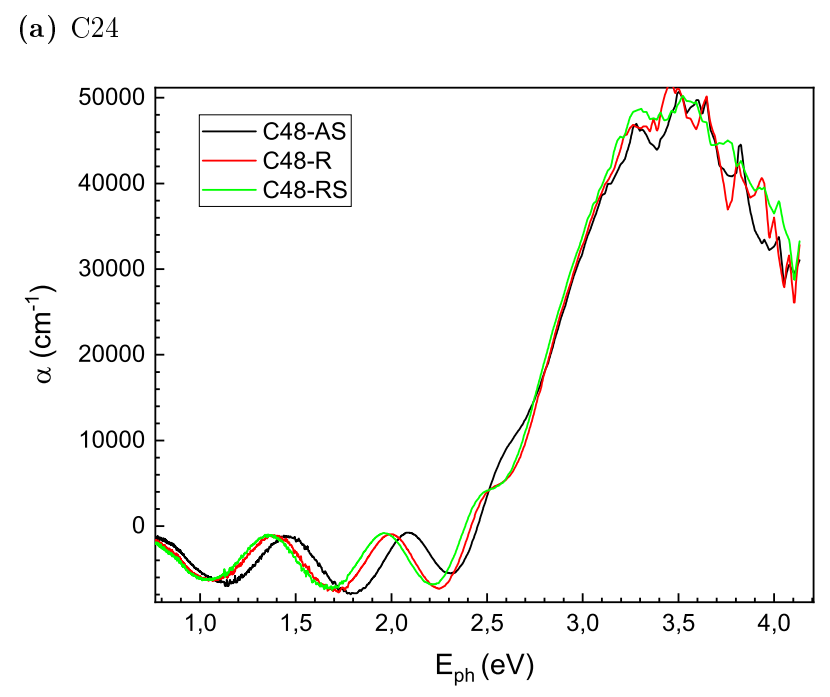
Nyquist plots of C24 samples under 460nm illumination	336
Absorption coefficient of C24 and C48 samples	337
Transient parameters of the PITCS/Lux-Ampere relaxation kinetics of C24 samples 3	338
Exemplary photocurrent kinetics in function of temperature and excitation energy	
for C24-R sample	339
TATS analysis of the photocurrent transients in function of temperature and	
excitation wavelength for C24-R sample	340
Fitting the bandgap values for C24 samples	341
SEM images	342
X-ray diffractograms	343
Photoluminescence spectra	344
IV characteristics of the mainline devices	345
Switching voltages of the mainline devices	346
IV characteristics of the mainline devices in function of temperature	347
IV characteristics of the mainline devices under 460nm illumination	348
Exemplary photocurrent kinetics in function of illumination power for 240130-hot	
and 240208-medium samples	349
List of runs	350
List of samples	351

Appendix: Nyquist plots of C24 samples under 460nm illumination.



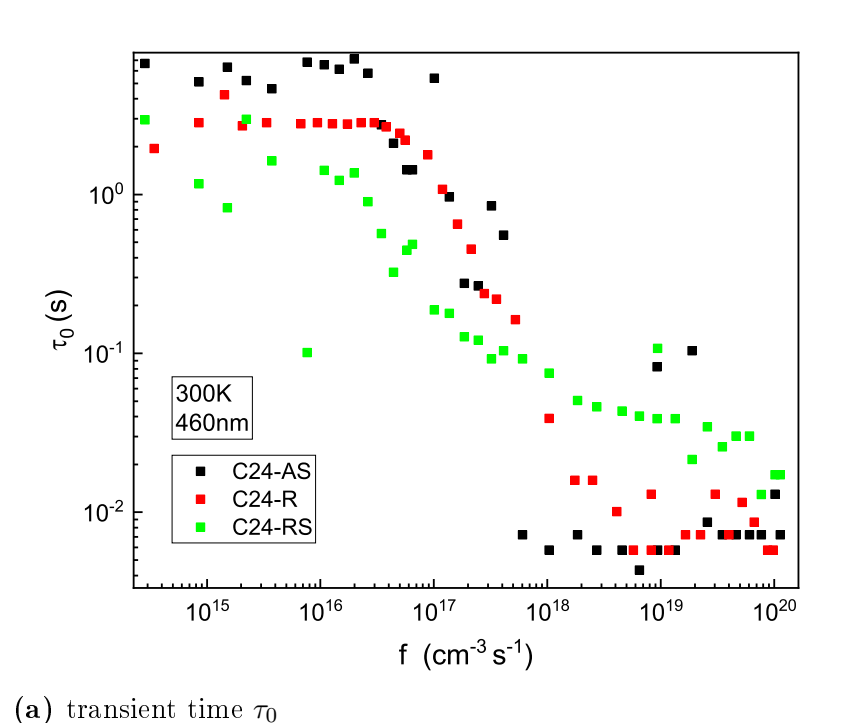
# Appendix: Absorption coefficient of C24 and C48 samples

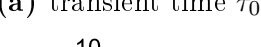


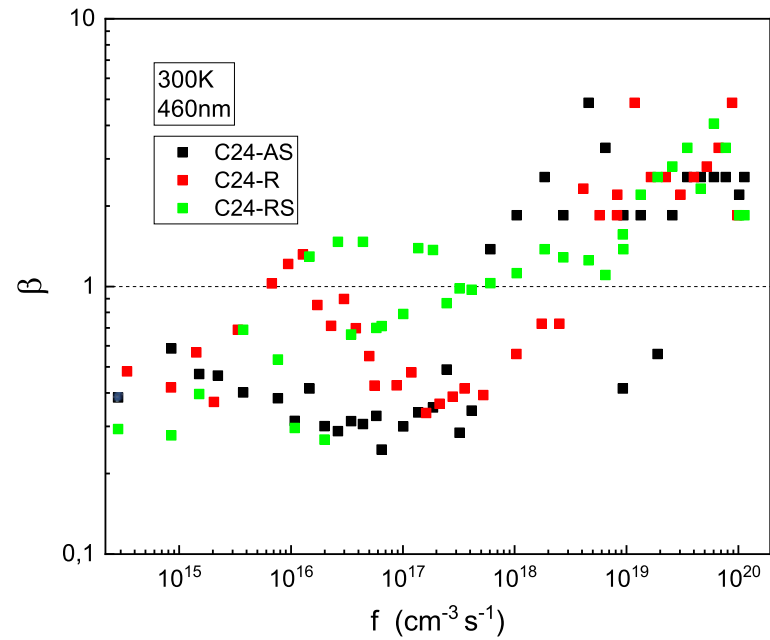


**(b)** C48

Appendix: Transient parameters of the PITCS/Lux-Ampere relaxation kinetics of C24 samples

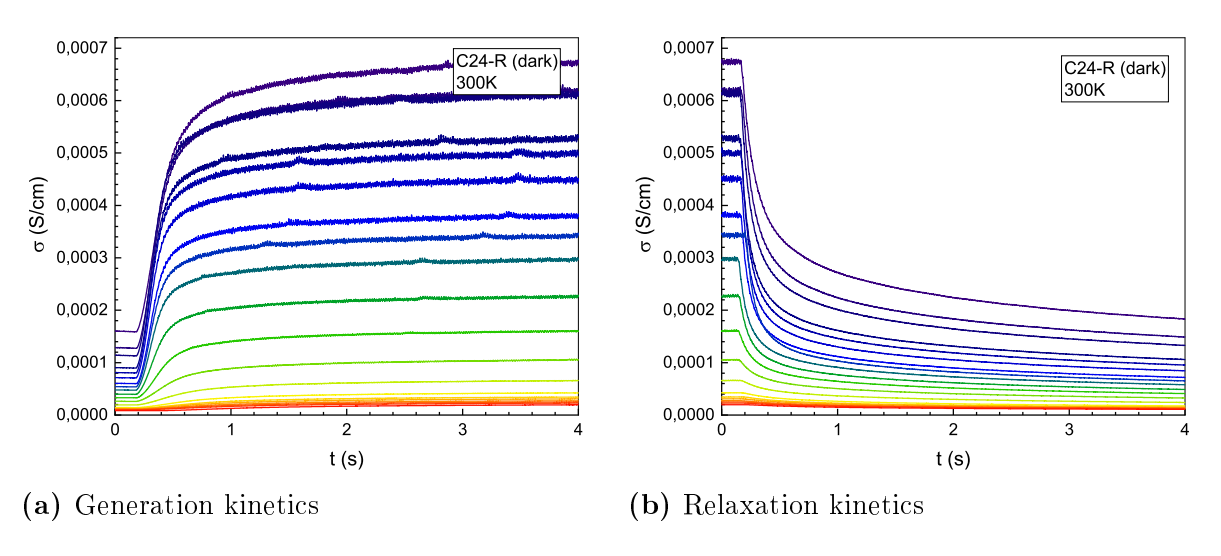




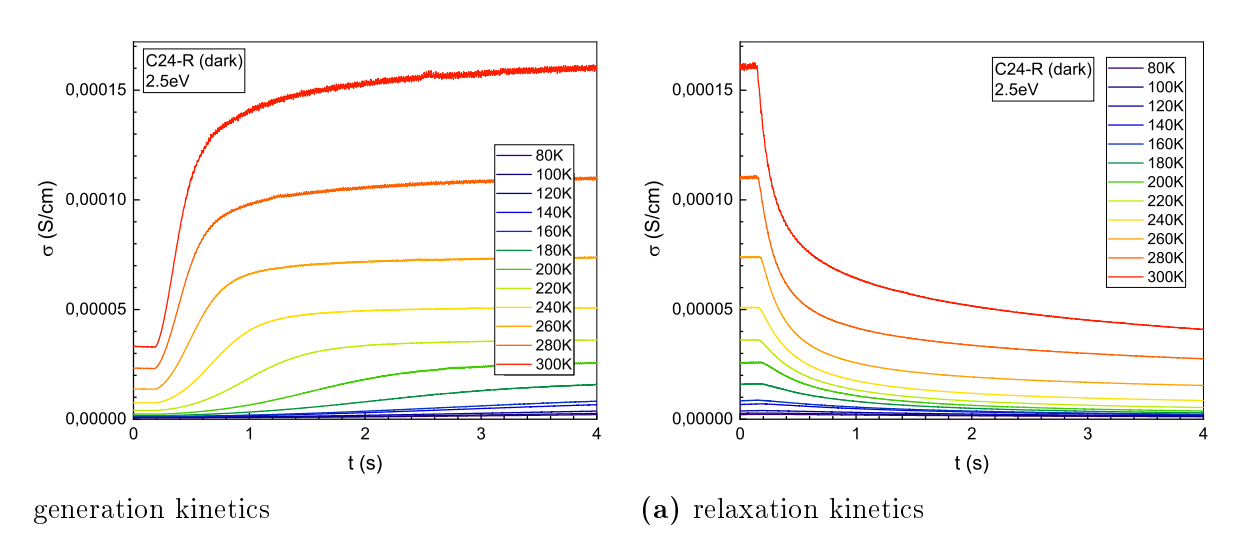


(b)  $\beta$  coefficient

# Appendix: Exemplary photocurrent kinetics in function of temperature and excitation energy for C24-R sample

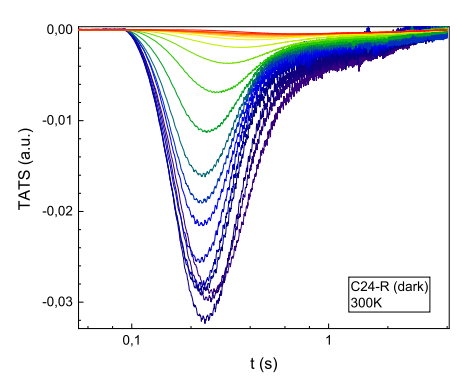


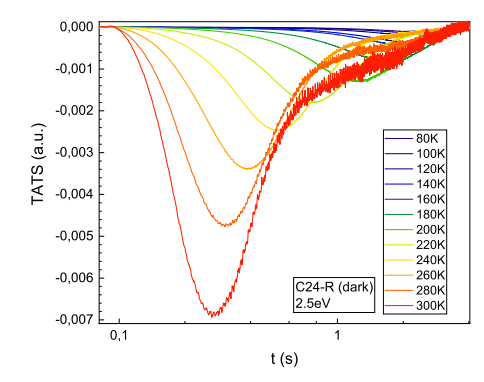
C24-R kinteics vs  $E_{ph}$  in range of 2÷3eV at 300K.



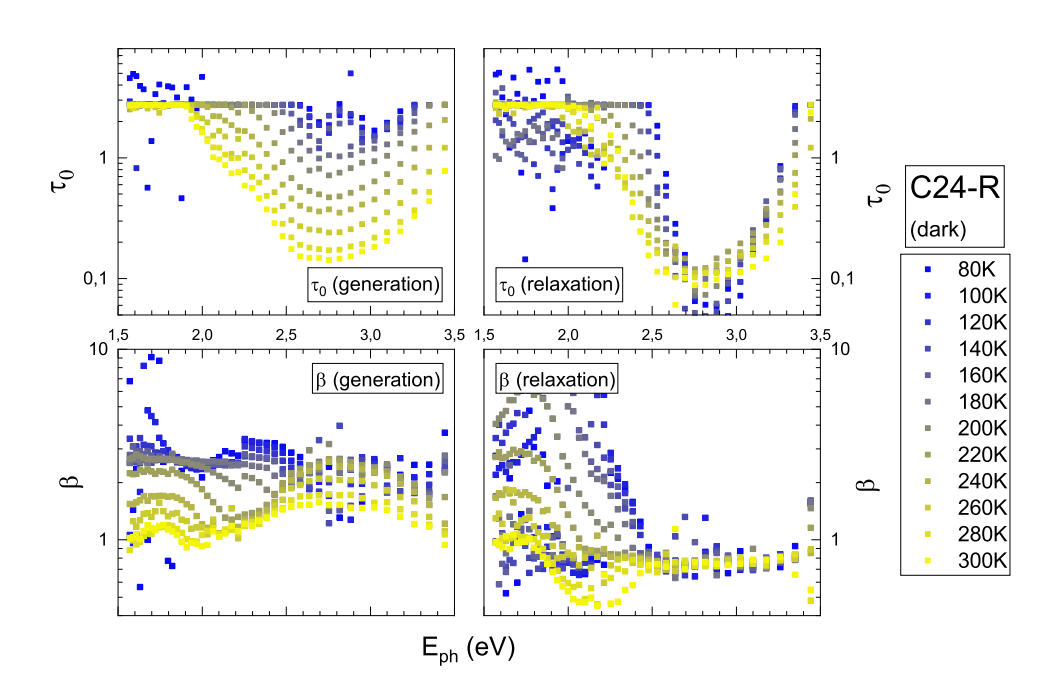
C24-R kinetics for 500nm excitation in function of temperature

Appendix: TATS analysis of the photocurrent transients in function of temperature and excitation wavelength for C24-R sample.



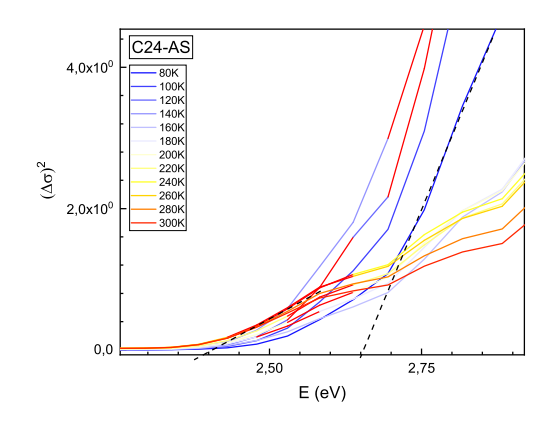


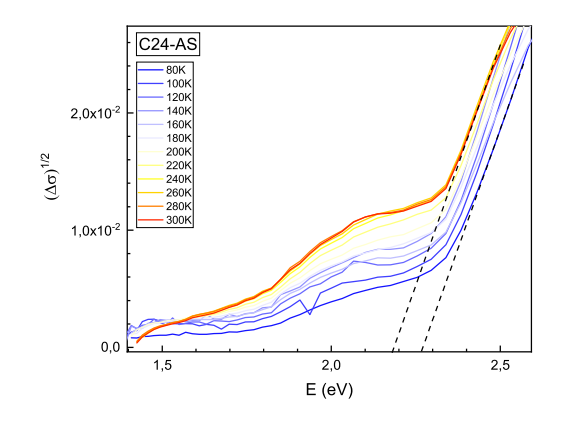
- (a) 300K, multiple excitation energies.
- (b) 2.5eV, multiple temperatures.

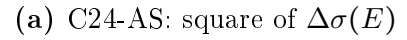


TATS parameters

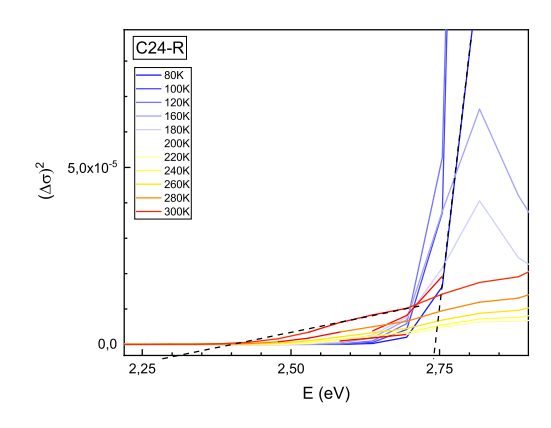
## Appendix: Fitting the bandgap values for C24 samples

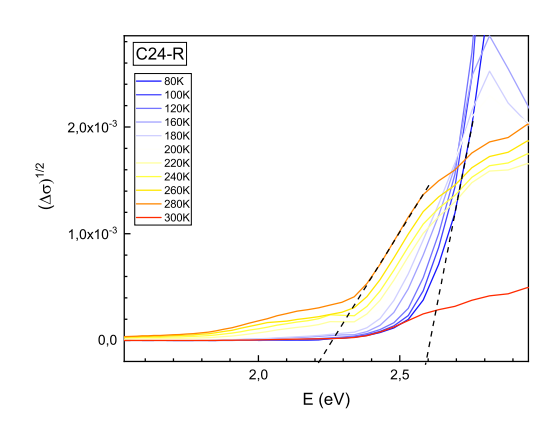






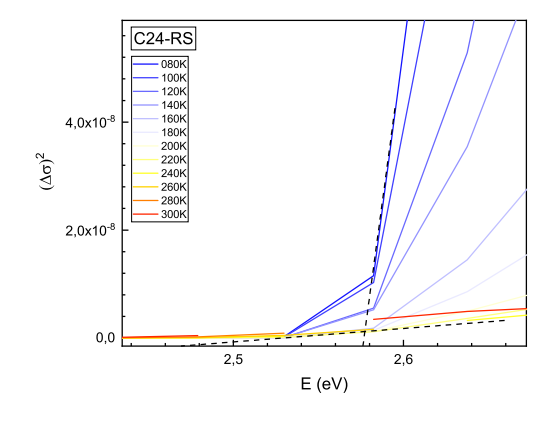
(b) C24-AS: square root of  $\Delta \sigma(E)$ .

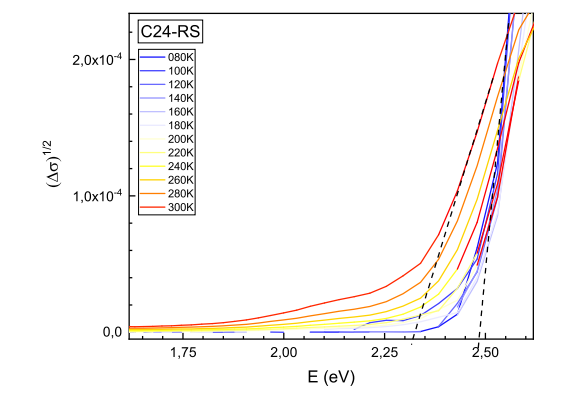




(c) C24-R: square of  $\Delta \sigma(E)$ 

(d) C24-R: square root of  $\Delta \sigma(E)$ .

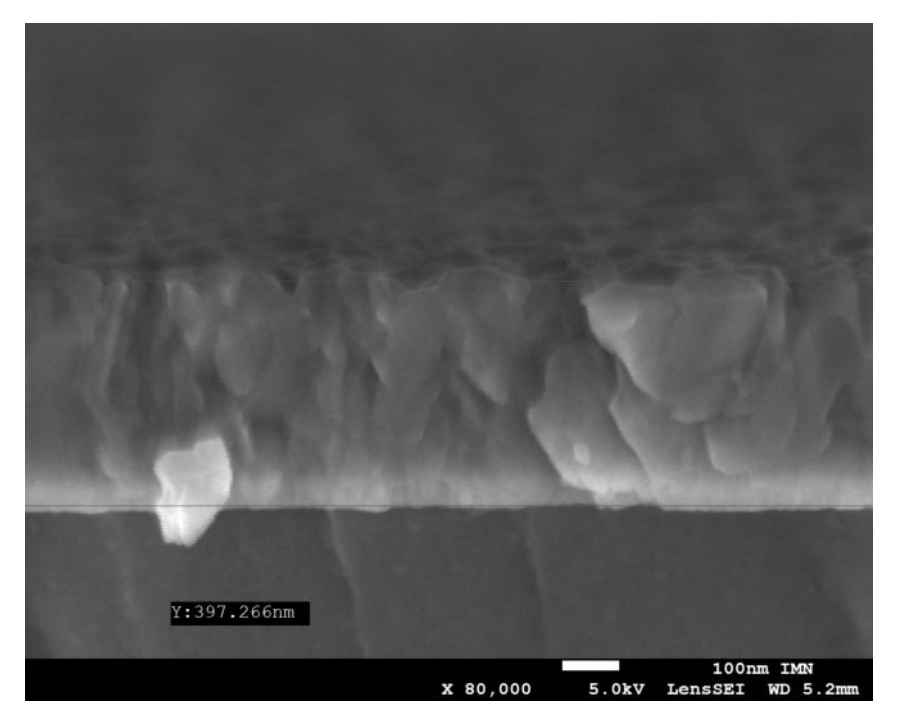




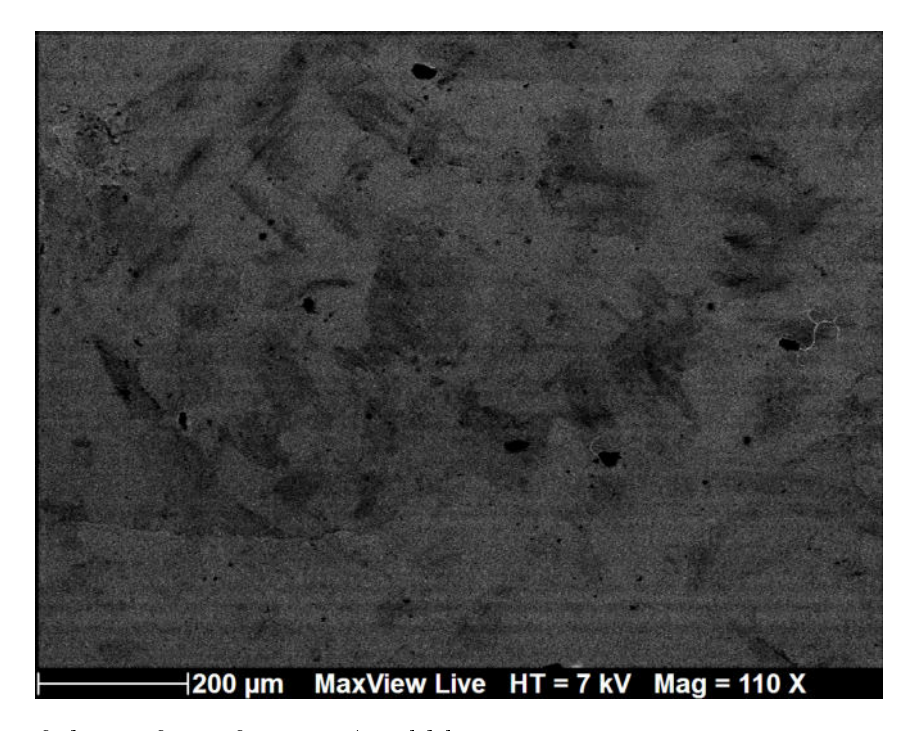
(e) C24-RS: square of  $\Delta \sigma(E)$ 

(f) C24-RS: square root of  $\Delta \sigma(E)$ .

## Appendix: SEM images

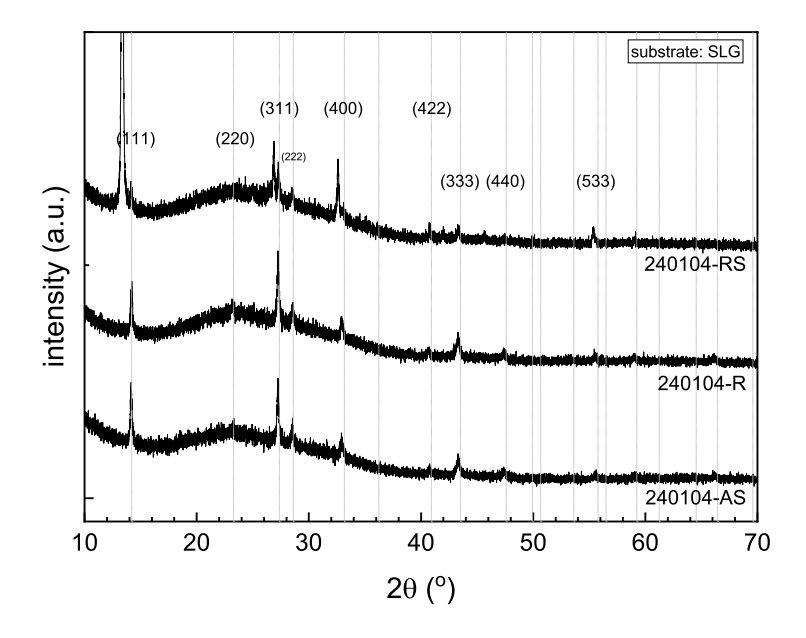


SEM image of the 231213 layer cross section (reference C24-AS).

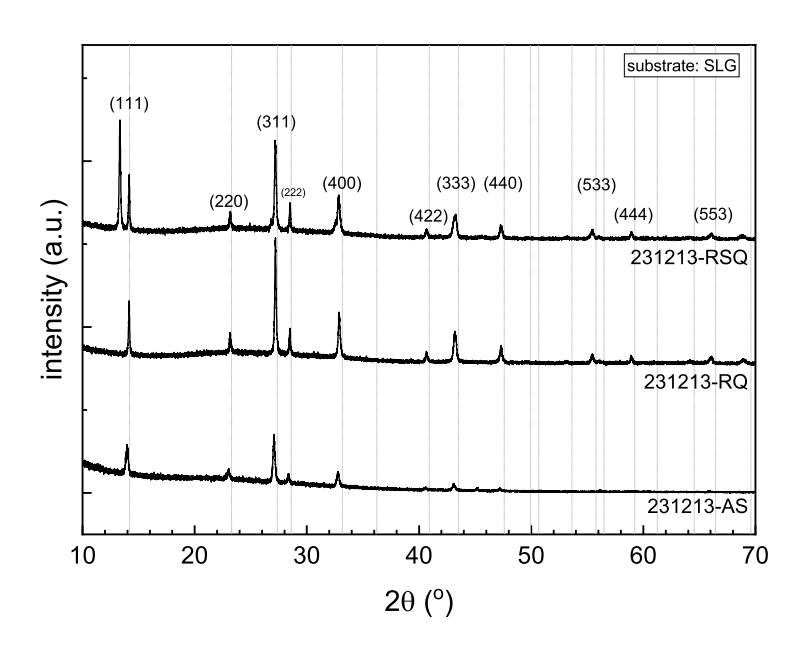


SEM image of the surface of 240311A-cold layer.

## Appendix: X-ray diffractograms

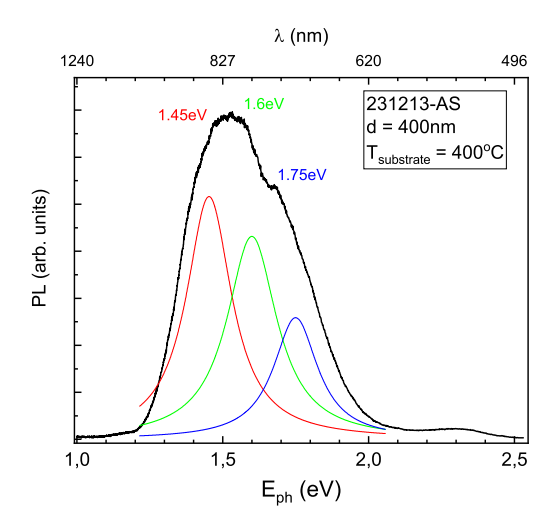


XRD diffractograms of the 240104 samples (in as grown state and after annealing).

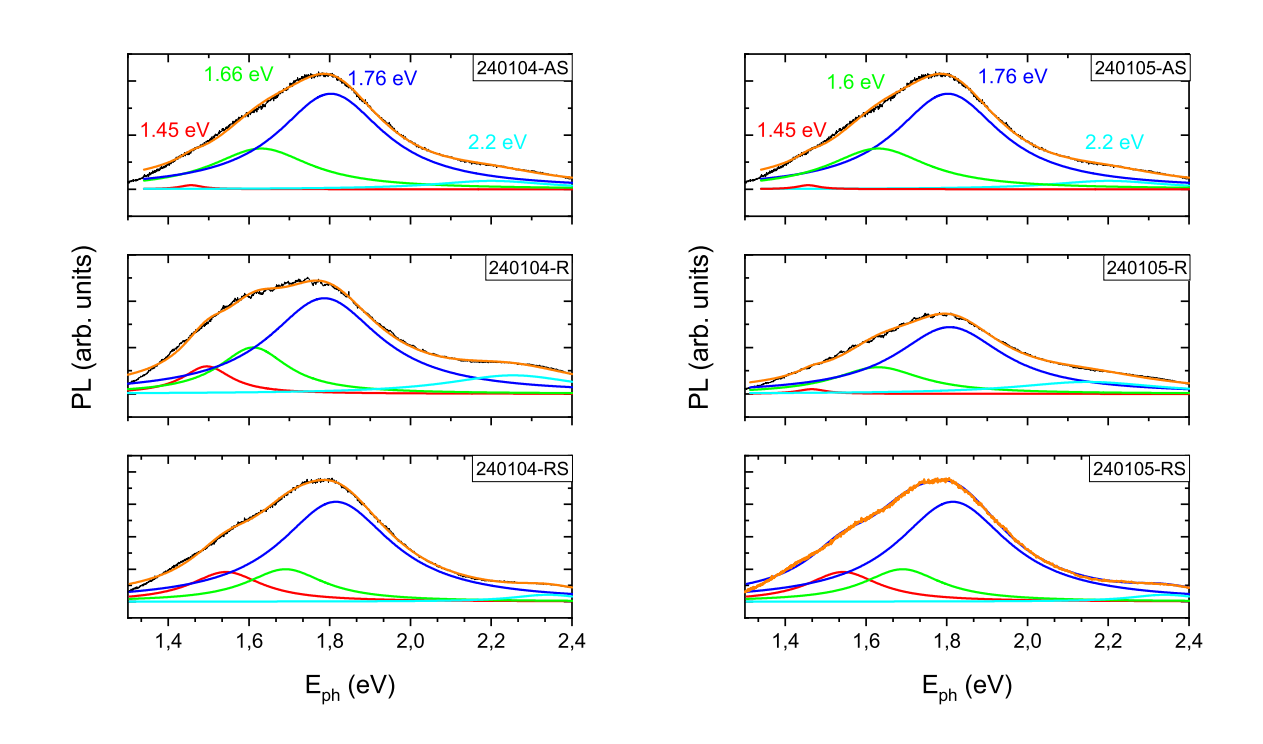


XRD diffractograms of the 231213 samples (in as grown state and after annealing with quenching).

## Appendix: Photoluminescence spectra



Photoluminescence of the 231213-AS sample

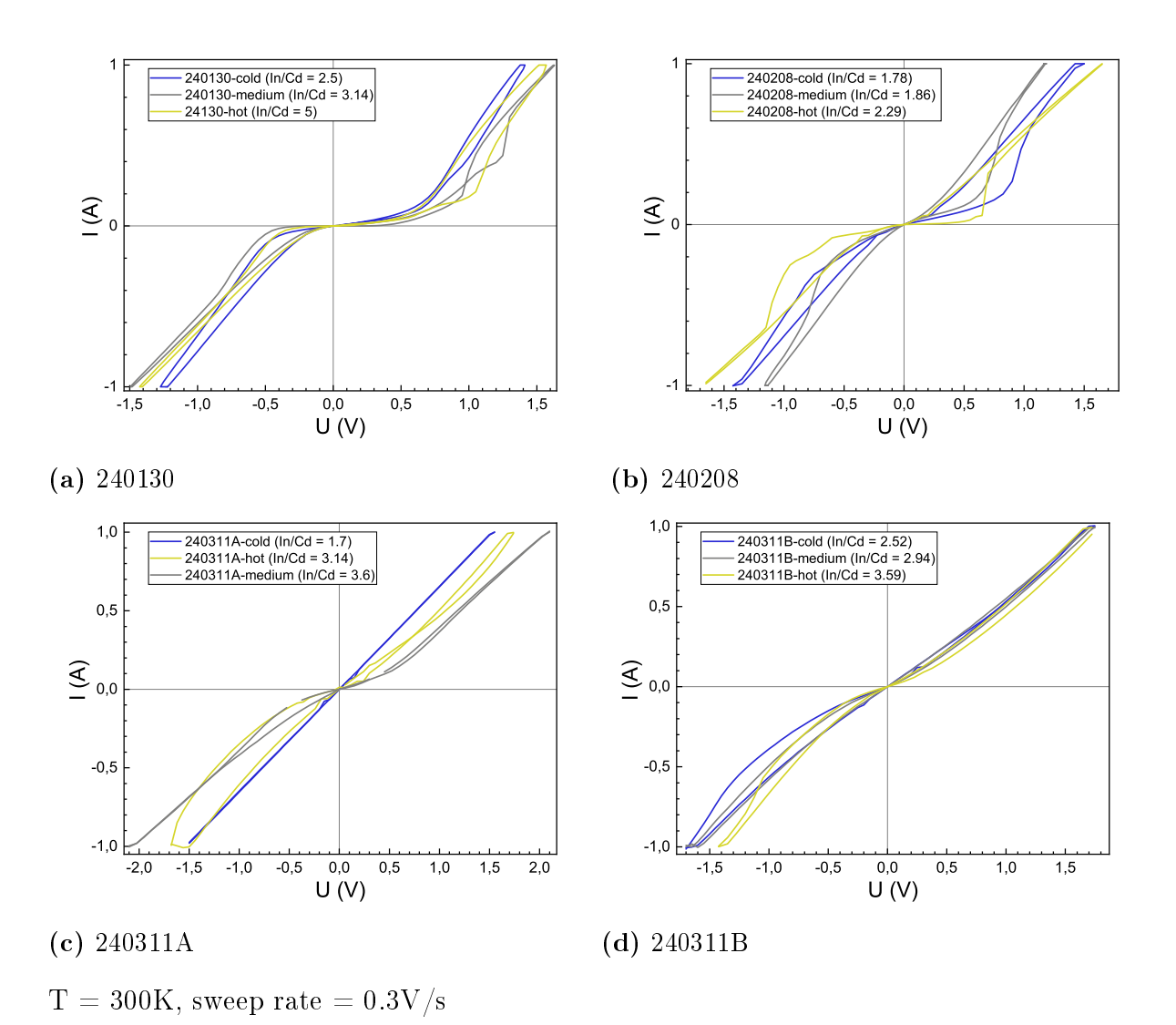


Photoluminescence of 240104 and 240105 series.

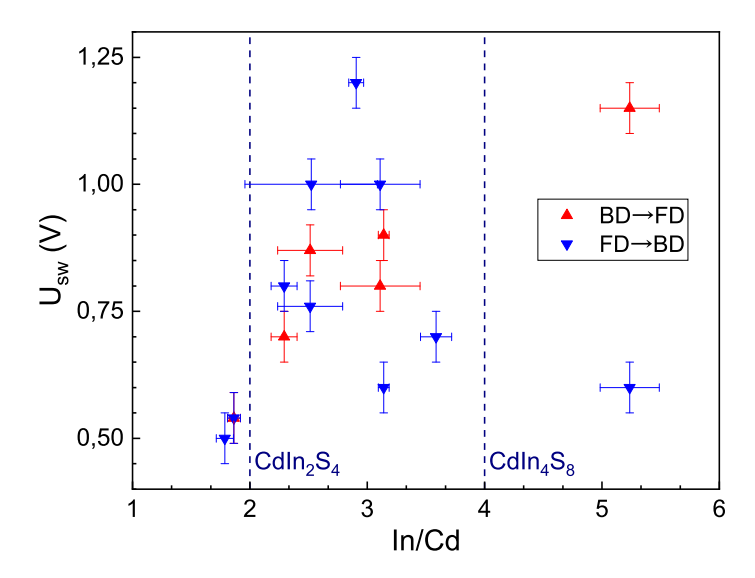
(a) 240104 series PL spectra

(b) 240105 series PL spectra

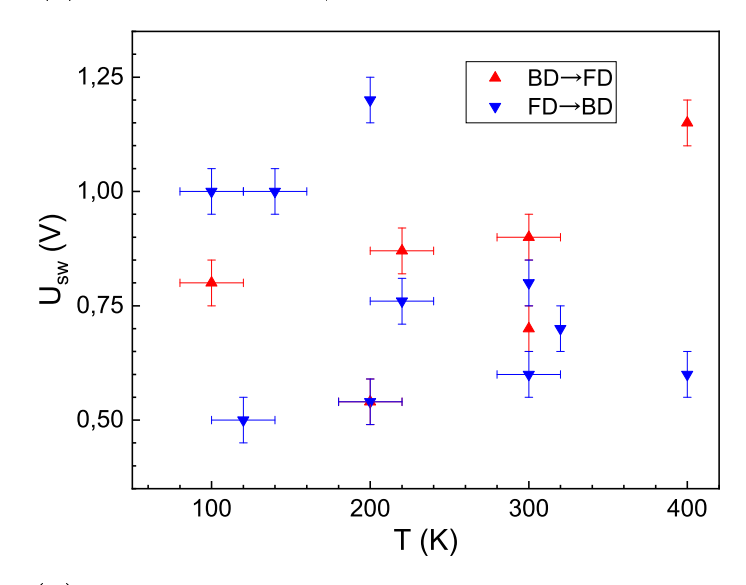
## Appendix: IV characteristics of the mainline devices



## Appendix: Switching voltages of the mainline devices



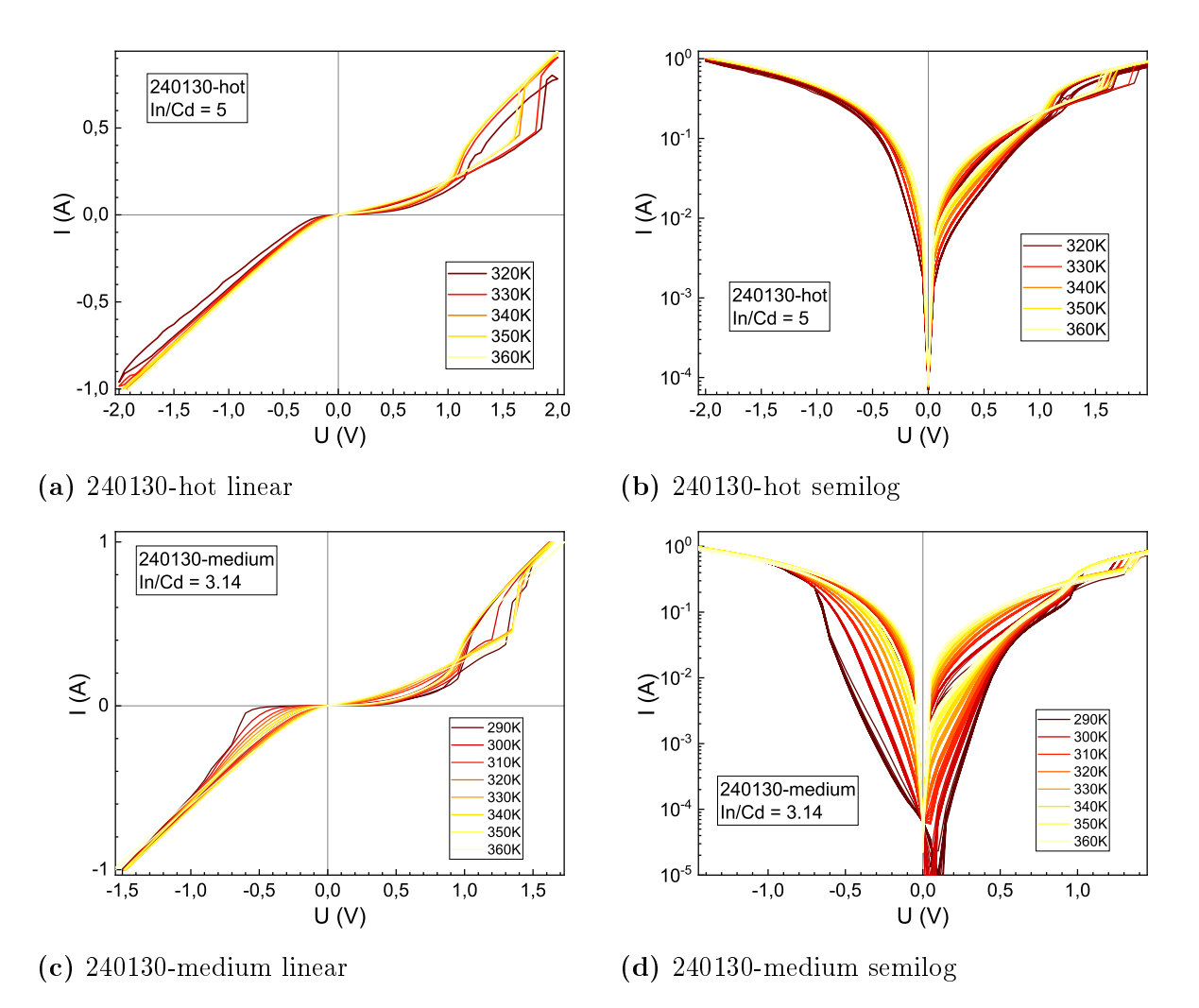
(a) as a function of In/Cd ratio



(b) as a function of temperature

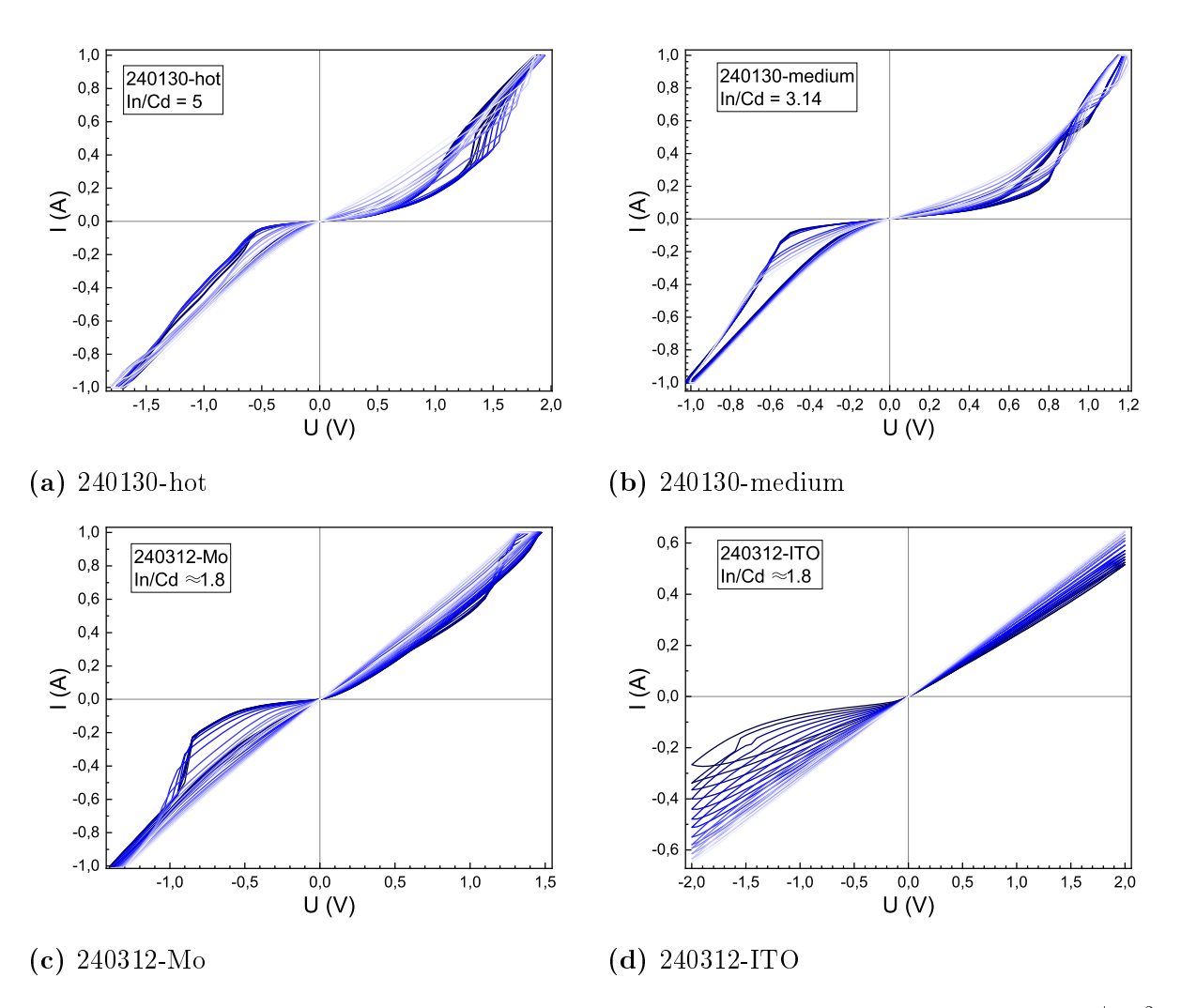
Dependency of the switch voltage between BD and FD regimes for the manufactured devices.

# Appendix: IV characteristics of the mainline devices in function of temperature



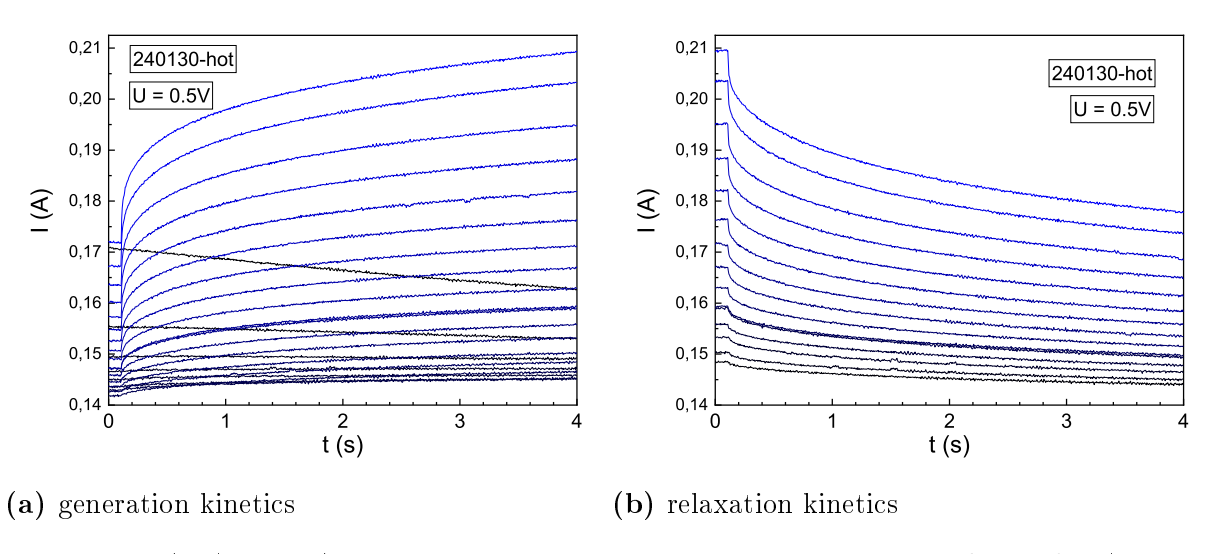
IV characteristics of the devices at temperatures in range 290÷350K, with 0.3V/s sweep rate.

# Appendix: IV characteristics of the mainline devices under 460nm illumination

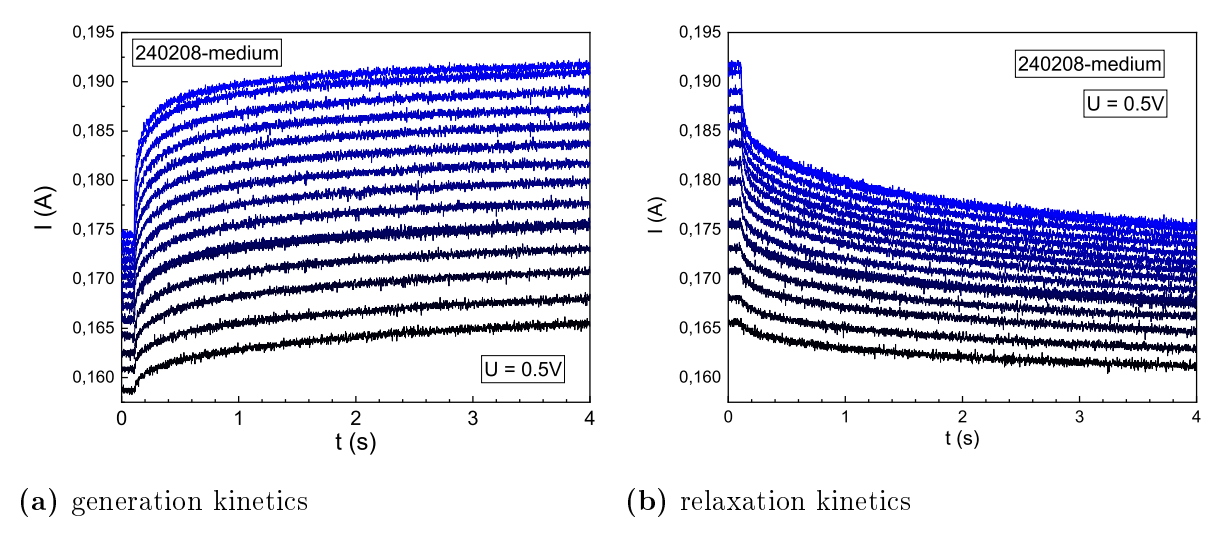


IV characteristics of the devices under 460nm illumination in range  $\Phi$  =0.1  $\mu\div1.2 mW/cm^2,$  with 0.3 V/s sweep rate.

Appendix: Exemplary photocurrent kinetics in function of illumination power for 240130-hot and 240208-medium samples



240130-hot (In/Cd = 5) kinetics vs illumination power in range of  $10^{-6} \div 10^{-3} \mathrm{W/cm^2}$ 



240208-medium (In/Cd = 1.86) kinetics vs illumination power in range of  $10^{-6} \div 10^{-3} \rm W/cm^2$ 

## Appendix: List of runs

				1S	substrates:	i.	sdus	substrate covers:	vers:
No.	run	thickness (nm)	temp. (°C)	slot 1	slot 2	slot 3	slot 1	slot 2	slot 3
1	231213	400	300	SLG	SLG	STG	-	ı	1
2	240104	001	007	STS	$_{ m OM}$	OuZ	-	-	-
8	240105	130	<130	STS	$_{ m OM}$	OuZ	ı	-	1
7	240130	400	400	оМ	Мо	оМ	SLG/Mo (1mm)	I	SLG/Mo (3mm)
5	240208	400	300	Mo	Mo	Mo	SLG/Mo (1mm)	ı	SLG/Mo (3mm)
9	240311A	400	200	Мо	Мо	Mo	SLG/Mo (1mm)	ı	SLG/Mo (3mm)
9	240311B	400	320	Мо	Мо	оМ	SLG/Mo (1mm)	I	SLG/Mo (3mm)
8	240312	008	008	STS	$_{ m OM}$	OLI	-	-	-
6	240321	20	400	Mo, Si, ITO	Mo, Si, ITO	Mo, Si, ITO	SLG + SLG/Mo (Imm)	STS	SLG + SLG/Mo (3mm)
10	240322	100	400	Mo, Si, ITO	Mo, Si, ITO	Mo, Si, ITO	SLG + SLG/Mo (lmm)	STG	SLG + SLG/Mo (3mm)

## Appendix: List of samples

		C24				
No.	name	thickness	origin	PDT	device structure	comments
		(mm)				
1	C24-AS	400	231213	euou	$\mathrm{SLG/C24}$	C24-AS ref.
				annealing in vacuum		
2	C24-RQ	400	231213	@300°C, 72h	$\mathrm{SLG/C24}$	ı
				+ quenching		
				annealing in sulphur		
3	C24-RSQ	400	231213	@300°C, 72h	$\mathrm{SLG}/\mathrm{C24}$	ı
				+ quenching		
4	240104-AS	100	240104	euou	$\mathrm{SLG/C24}$	C24-AS
5	240104-R	100	240104	annealing in vacuum @300°C, 72h	$\mathrm{SLG/C24}$	C24-R
9	240104-RS	100	240104	annealing in sulphur @300°C, 72h	SLG/C24	C24-RS
2	240104-AS (moly)	100	240104	none	${ m SLG/Mo/C24/Mo}$	shorted (diffusion)
8	240104-R (moly)	100	240104	annealing in vacuum @300°C, 72h	${ m SLG/Mo/C24/Mo}$	shorted (diffusion)
6	240104-RS (moly)	100	240104	annealing in sulphur @300°C, 72h	${ m SLG/Mo/C24/Mo}$	shorted (diffusion)
10	240104-AS (AZO)	100	240104	none	SLG/AZO/C24/AZO/Ni:Al.	I
111	240104-R (AZO)	100	240104	annealing in vacuum @300°C, 72h	SLG/AZO/C24/AZO/Ni:Al.	1

## Appendices

No.	name	thickness	origin	PDT	device structure	comments
12	240104-RS (AZO)	100	240104	annealing in sulphur @300°C, 72h	SLG/AZO/C24/AZO/Ni:Al.	ı
13	240105-AS	130	240105	none	${ m SLG/C24}$	a-C24
14	240105-R	130	240105	annealing in vacuum @300°C, 72h	SLG/C24	ı
15	240105-RS	130	240105	annealing in sulphur @300°C, 72h	SLG/C24	ı
16	240105-AS (moly)	130	240105	попе	${ m SLG/Mo/C24/Mo}$	shorted (diffusion)
17	240105-R (moly)	130	240105	annealing in vacuum @300°C, 72h	${ m SLG/Mo/C24/Mo}$	shorted (diffusion)
18	240105-RS (moly)	130	240105	annealing in sulphur @300°C, 72h	${ m SLG/Mo/C24/Mo}$	shorted (diffusion)
19	240105-AS (AZO)	130	240105	euou	SLG/AZO/C24/AZO/Ni:Al.	I
20	240105-R (AZO)	130	240105	annealing in vacuum @300°C, 72h	SLG/AZO/C24/AZO/Ni:Al.	i
21	240105-RS (AZO)	130	240105	annealing in sulphur @300°C, 72h	SLG/AZO/C24/AZO/Ni:Al.	ı
22	240130-C24-hot	400	240130	auou	SLG/Mo/C24/AZO/Ni:Al.	I
23	240130-hot-Al.	400	240130	none	SLG/Mo/C24/Ni:Al.	shorted (diffusion)
24	240130-hot-R	400	240130	annealing in vacuum @300°C, 72h	SLG/Mo/C24/AZO/Ni:Al.	ı

## Appendices

No.	name	thickness	origin	PDT	device structure	comments
25	240130-hot-RS	400	240130	annealing in sulphur @300°C, 72h	SLG/Mo/C24/	destroyed while hammering the ampule
26	240130-medium	400	240130	none	SLG/Mo/C24/AZO/Ni:Al.	ı
22	240130-cold	400	240130	euou	SLG/Mo/C24/AZO/Ni:Al.	ı
28	240208-hot	400	240208	none	SLG/Mo/C24/AZO/Ni:Al.	ı
29	240208-medium	400	240208	none	SLG/Mo/C24/AZO/Ni:Al.	I
30	240208-medium-Al.	400	240208	none	${ m SLG/Mo/C24/Ni:Al.}$	shorted (diffusion)
31	240208-medium-R	400	240208	annealing in vacuum @300°C, 72h	SLG/Mo/C24/AZO/Ni:Al.	shorted (diffusion)
32	240208-medium-RS	400	240208	annealing in sulphur @300°C, 72h	SLG/Mo/C24/AZO/Ni:Al.	1
33	240208-medium-RQ	400	240208	annealing in vacuum @300°C, 72h + quenching	SLG/Mo/C24/AZO/Ni:Al.	1
34	240208-medium-RSQ	400	240208	annealing in sulphur @300°C, 72h + quenching	SLG/Mo/C24/AZO/Ni:Al.	r
35	240208-cold	007	240208	euou	SLG/Mo/C24/AZO/Ni:AI.	I
98	240311A-hot	400	240311A	none	SLG/Mo/C24/AZO/Ni:AI.	I
37	240311A-medium	400	240311A	none	SLG/Mo/C24/AZO/Ni:Al.	I
38	240311A-cold	400	240311A	none	SLG/Mo/C24/AZO/Ni:AI.	ı

## Appendices

No.	name	thickness	origin	PDT	device structure	comments
39	240311B-hot	400	240311B	none	SLG/Mo/C24/AZO/Ni:Al.	ı
40	240311B-medium	400	240311B	none	SLG/Mo/C24/AZO/Ni:Al.	ı
41	$240311\mathrm{B-cold}$	400	240311B	none	SLG/Mo/C24/AZO/Ni:Al.	1
42	240312-SLG	800	240312	none	$\mathrm{SLG}/\mathrm{C24}$	1
43	240312-Mo	800	240312	none	SLG/Mo/C24/AZO/Ni:Al.	ı
44	240312-Mo-A1.	008	240312	none	${ m SLG/Mo/C24/Ni:AI.}$	shorted (diffusion)
45	240312-ITO-	008	240312	none	SLG/ITO/C24/AZO/Ni:Al.	1
46	240312-ITO-Al.	008	240312	none	SLG/ITO/C24/Ni:Al.	-
47	Н1	09	240321	none	m SiO2/C24	
48	$1 \mathrm{M}$	09	240321	none	m SiO2/C24	
49	10	09	240321	none	m SiO2/C24	
50	$1 \mathrm{H} (\mathrm{JJ})$	20	240321	none	m SiO2/C24	
51	(1) M1	09	240321	none	m SiO2/C24	
52	1C (JJ)	09	240321	none	m SiO2/C24	
53	$1\mathrm{H-Mo}$	09	240321	none	${ m SLG/Mo/C24}$	
54	oIVI-IVI	20	240321	none	m SLG/Mo/C24	future use
55	$1\mathrm{C-Mo}$	09	240321	none	m SLG/Mo/C24	
56	OLI-H1	20	240321	none	${ m SLG/ITO/C24}$	
57	1M-ITO	20	240321	none	${ m SLG/ITO/C24}$	
58	1C-ITO	50	240321	none	${ m SLG/ITO/C24}$	
59	2H	100	240322	none	m SiO2/C24	
09	2M	100	240322	none	SiO2/C24	

No.	name	thickness	origin	PDT	device structure	comments
61	2C	100	240322	none	m SiO2/C24	
62	1H (JJ)	100	240322	none	m SiO2/C24	
63	1M (JJ)	100	240322	əuou	m SiO2/C24	
64	1C (JJ)	100	240322	əuou	m SiO2/C24	
65	$_{ m 2H-Mo}$	100	240322	əuou	${ m SLG/Mo/C24}$	
99	2M-Mo	100	240322	əuou	${ m SLG/Mo/C24}$	
67	2C-Mo	100	240322	euou	${ m SLG/Mo/C24}$	
89	2H-ITO	100	240322	euou	$\mathrm{SLG/ITO/C24}$	future use
69	2M-ITO	100	240322	euou	${ m SLG/ITO/C24}$	
70	2C-ITO	100	240322	none	${ m SLG/ITO/C24}$	